UNIVERSIDAD DEL PAÍS VASCO
EUSKAL HERRIKO UNIVERSITATEA

DOCTORAL THESIS

Theoretical study of the linear and nonlinear optical response of plasmonic tunneling gaps

Author:

**Garikoitz
AGUIRREGABIRIA**

Supervisors:

**Dr. Rubén ESTEBAN
Prof. Javier AIZPURUA**

*A thesis submitted in fulfilment of the requirements
for the degree of Philosophiae Doctor, Ph.D.*

in the

Theory of Nanophotonics Group
Centro de Física de Materiales

July, 2018

Resumen

La nanoóptica es una rama de la óptica en la que se utilizan estructuras dieléctricas y/o metálicas cuyas dimensiones oscilan entre decenas y cientos de nanómetros para controlar y manipular la luz. Una de las características que hace que estos sistemas sean interesantes es su capacidad de concentrar la luz en volúmenes muy pequeños, lo que provoca que las interacciones entre la luz y la materia se intensifiquen. El campo de la nanoóptica ha experimentado una gran expansión en los últimos años debido a importantes avances en las técnicas de fabricación y caracterización de estructuras dieléctricas y metálicas, lo que ha permitido el diseño de dispositivos con los que manipular la luz de forma muy precisa.

Las nanoestructuras metálicas presentan especial interés debido a su capacidad de concentrar la luz en volúmenes inferiores al límite de difracción debido a la excitación de resonancias plasmónicas (también llamados modos plasmónicos o simplemente plasmones). Estas resonancias son consecuencia de la hibridación del campo electromagnético con las oscilaciones de la densidad electrónica del metal. Además de concentrar la luz en volúmenes muy reducidos, las resonancias plasmónicas se caracterizan por provocar un fuerte aumento del campo electromagnético en la zona cercana a la superficie de las partículas. La variación de la forma de las partículas, el material del que están compuestas, o el medio material que las rodea permite sintonizar de manera controlada la frecuencia de la resonancia plasmónica de dichas partículas. Por ejemplo, si consideramos una nanopartícula cilíndrica de tipo varilla es posible ajustar la longitud de onda a la que se excitan los plasmones si se fija el radio del cilindro y se varía su longitud. De la misma forma, manteniendo fijas las dimensiones de la partícula cilíndrica y afilando sus extremos conseguiremos concentrar e intensificar el campo electromagnético cercano en la proximidad de dichas puntas. Por todo esto, las nanopartículas plasmónicas destacan como sistemas muy versátiles con los que construir dispositivos nanoópticos.

Uno de los sistemas plasmónicos que ofrece gran versatilidad para ajustar las propiedades de las resonancias plasmónicas, permitiendo a la vez localizar eficazmente y aumentar fuertemente la intensidad del campo cercano, son los dímeros formados por dos nanopartículas separadas por una distancia muy pequeña, donde se forma una cavidad o *gap*. Gracias a la interacción entre las cargas eléctricas acumuladas en las superficie de las partículas de la zona del *gap*, se produce una hibridación de las resonancias plasmónicas de ambas partículas dando lugar a unas nuevos modos plasmónicos (*Bonding Plasmons* (BP)). Al variar la distancia entre las partículas, la interacción entre ambas se modifica y su produce un cambio en la frecuencia de resonancia de los BP, así como en la intensidad de los campos en la zona del *gap*. Como norma general, cuanto menor es la distancia más intenso y localizado es el campo cercano en el *gap* que separa las partículas. Esta propiedad permite alcanzar campos cercanos muy intensos y localizados en la zona del *gap*, lo que supone una

propiedad muy interesante desde un punto de vista práctico, por ejemplo para su utilización en técnicas de espectroscopia de campo cercano. Sin embargo el aumento del campo a medida que se cierra el *gap* no continúa de forma indefinida. Cuando la distancia que separa las nanopartículas plasmónicas alcanza dimensiones subnanométricas, la naturaleza cuántica de los electrones se manifiesta y permite el traspaso de electrones entre las partículas debido al tuneleo cuántico, el cual es un proceso prohibido en una descripción clásica. Esta transferencia de electrones provoca que la acumulación de cargas en la superficie de cada partícula disminuya (apantallamiento) y, por lo tanto, que los campos cercanos en el *gap* se reduzcan drásticamente.

En esta tesis estudiamos de forma minuciosa sistemas plasmónicos formados por dos o más partículas separadas por *gaps* (sub-)nanométricos, centrándonos en tres aspectos principales. Por un lado estudiamos como la morfología exacta del *gap* es capaz de modificar la estructura modal de dímeros o cadenas de nanopartículas, por ejemplo dando lugar a la aparición de modos de *gap* no radiantes. Por otro lado, estudiamos como el tuneleo cuántico afecta a diferentes modos plasmónicos excitables en trímeros (sistemas compuestos por tres esferas plasmónicas situadas en una configuración triangular) y dímeros caracterizados por diferentes tipos de terminaciones en el gap. Estas diferentes geometrías nos permiten excitar e investigar los efectos cuánticos en modos eléctricos (los más comunes en plasmónica) así como en otros modos menos comunes como los modos de *gap* no radiantes, los magnéticos y los oscuros. Además, el proceso del tuneleo cuántico es un efecto altamente no-lineal en el que pequeñas variaciones en la barrera de potencial producen grandes variaciones en la corriente eléctrica. Por lo tanto también estudiamos las posibles ventajas que ofrece el efecto túnel para generar efectos ópticos no-lineales en dímeros de partículas plasmónicas. A continuación detallamos brevemente los resultados obtenidos.

En el capítulo 1 revisamos la metodología teórica que empleamos durante la tesis. Usar un formalismo teórico puramente cuántico es la opción más directa dado que el foco principal de esta tesis es el estudio de sistemas plasmónicos con *gaps* muy pequeños donde los efectos cuánticos cobran especial relevancia. La metodología *Time-Dependent Density Functional Theory* (TDDFT) permite estudiar sistemas metálicos describiendo la dinámica de la densidad electrónica dentro de un formalismo cuántico riguroso. Además el TDDFT nos permite estudiar de forma directa la respuesta óptica no-lineal al ser una metodología basada en la descripción temporal de los sistemas físicos. Por lo tanto, se utiliza el TDDFT para calcular la respuesta no-lineal de partículas y dímeros plasmónicos. Sin embargo, debido a limitaciones computacionales, esta metodología se suele aplicar en cálculos de sistemas plasmónicos de tamaño reducido (mucho menores que los utilizados en experimentos típicos). Por ello, también implementamos el *Quantum Corrected Model* (QCM), un modelo semi-clásico que nos permite introducir el efecto del tuneleo cuántico entre partículas metálicas a frecuencias ópticas de forma efectiva en simulaciones que resuelven las ecuaciones clásicas de Maxwell. El QCM se basa en introducir un material ficticio

con una conductividad que reproduce fielmente las propiedades del efecto túnel en *gaps* muy pequeños. La conductividad de este material ficticio se calcula realizando simulaciones cuánticas para un sistema simplificado. El QCM nos permite estudiar el efecto de las corrientes túnel en la respuesta óptica lineal de partículas plasmónicas de tamaño realista, que serían imposibles de calcular utilizando la metodología TDDFT.

En el capítulo 2 nos centramos en estudiar cómo la morfología del *gap* afecta a la respuesta óptica lineal de dímeros formados por partículas con simetría cilíndrica. En primer lugar se consideran cilindros de oro de 100 nm de longitud y 50 nm de diámetro. Se utilizan dos configuraciones diferentes para la terminación del extremo del *gap*, por un lado una terminación esférica y por otro una terminación plana. Antes de estudiar el rango de distancias de separación entre los cilindros para las cuales el efecto de túnel cuántico tiene relevancia, se analiza la respuesta clásica con el fin de entender la estructura modal del sistema.

En el caso del dímero con terminaciones esféricas se encuentra una respuesta óptica muy similar a la que fue analizada anteriormente por otros grupos que estudiaron la interacción entre dos esferas. Empezando con las partículas bien separadas, a medida que se cierra el *gap* (siempre manteniendo la distancia del *gap* $d_{\mathrm{gap}} \gtrsim 0.5$ nm) se observa, tanto en el campo lejano como en el campo cercano, que la energía de resonancia de los modos plasmónicos BP se modifica hacia valores cada vez más bajos (*redshift*). Al mismo tiempo, el campo cercano que se obtiene en el centro del *gap* al excitar la resonancia BP se intensifica fuertemente a medida que la distancia del *gap* es reducida.

En el caso de los cilindros con terminaciones planas en el *gap* se observa que para distancias de *gap* grandes, se mantienen las mismas tendencias que en el caso anterior. En cambio, para distancias de *gap* reducidas se obtienen diferencias notables. Por ejemplo, las resonancias plasmónicas del sistema con terminaciones planas presentan una saturación del *redshift* para *gaps* muy pequeños. Esta saturación se puede explicar con un modelo sencillo en el que representamos el dímero como un circuito eléctrico RC en serie. Al reducir la distancia del *gap*, la capacitancia diverge produciendo un cortocircuito para *gaps* muy pequeños. La frecuencia de saturación corresponde con la frecuencia de resonancia de un cilindro de doble longitud que los cilindros que forman el dímero. Concentrándonos ahora en el campo cercano producido por las partículas con terminaciones planas en el *gap* se obtiene que, además de los modos presentes en el campo lejano, emerge un nuevo grupo de modos para distancias reducidas que muestran un *redshift* muy pronunciado a medida que el *gap* se cierra. Estos modos se pueden identificar como *Transverse Cavity Plasmons* (TCPs), los cuales pueden entenderse como resonancias tipo Fabry-Pérot que se forman por la interferencia de plasmones que se propagan en una dirección paralela a las superficies planas del *gap*. Observamos que los modos BP y los TCP de la estructura de dímeros cilíndricos están desacoplados, lo cual permite ajustar su frecuencia de resonancia de manera independiente variando

diferentes parámetros de la estructura (longitud, d_{gap}, ...). Esto nos permite ajustar las propiedades ópticas de campo lejano sintonizando los BPs de forma adecuada y por otro lado, controlar la distribución espacial del campo cercano en la zona del *gap* gracias a la sintonización TCPs.

Una vez entendida la respuesta óptica para *gaps* plasmónicos donde el tuneleo cuántico no entra en juego, reducimos el *gap* de $d_{\text{gap}} = 0.5$ nm hasta que las partículas contactan, $d_{\text{gap}} = 0$ nm, e incluso empiezan a superponerse $d_{\text{gap}} < 0$ nm. El efecto de la corriente túnel se introduce en nuestras simulaciones mediante el QCM. Como primer paso, se verifica que el tuneleo de electrones afecta a la respuesta del dímero con terminaciones esféricas de manera plenamente consistente con el análisis del dímero de esferas. Es decir, una vez que el tuneleo empieza a ser relevante, se observa que los BPs se difuminan y desaparecen, al mismo tiempo que el traspaso de carga eléctrica provoca la aparición de *Charge Transfer Plasmons* (CTPs). Los CTPs aparecen antes de que se produzca el contacto físico entre las partículas, un efecto puramente cuántico ya que clasicamente no es posible que los electrones atraviesen la región dieléctrica entre las partículas. A medida que el *gap* se cierra (aumentando la conductividad túnel) crece la intensidad de estos CTPs y la frecuencia de la resonancia se desplaza hacia valores mas altos (*blueshift*). Además, dado que las cargas acumuladas en las superficies que forman el *gap* son las responsables de producir intensos campos cercanos, el incremento de la corriente eléctrica viene acompañado por una fuerte reducción del campo cercano en el *gap*.

La gran influencia del tuneleo cuántico en *gaps* esféricos contrasta fuertemente con los resultados obtenidos para el dímero con terminaciones planas en el *gap*. Como se ha descrito anteriormente, el *redshift* de la resonancia BP satura a la frecuencia de un cilindro de longitud doble (equivalente a tener $d_{\text{gap}} = 0$ nm). Tal como se ha indicado anteriormente, un *gap* suficientemente pequeño se comporta como un cortocircuito por el que la corriente de desplazamiento fluye libremente. Añadir la corriente eléctrica túnel a esta corriente de desplazamiento no afecta a los BPs, los cuales determinan el campo lejano. Por lo tanto la señal emitida por nuestra estructura para d_{gap} muy pequeño no se ve afectada por el cierre del *gap*. En cambio, se observa que la disminución de la intensidad de los campos cercanos en el centro del *gap* es incluso más abrupta que para el caso de las terminaciones esféricas, lo cual es debido a la mayor superficie plana donde el tuneleo es posible.

Finalmente, para comprobar si los resultados obtenidos son robustos o solo son aplicables a una configuración particular extendemos nuestro estudio al caso de estructuras cilíndricas de diferentes formas. En general, se encuentra que muchas las propiedades asociadas a la presencia de terminaciones planas en el *gap* y la forma en la que la respuesta óptica se ve afectada por el efecto túnel es robusta con respecto a la forma global de la partícula. Por tanto, el estudio realizado en el capítulo 2 nos permite concluir la importancia de considerar la morfología exacta de la zona del *gap* a la hora de diseñar sistemas plasmónicos donde la distancia que separa las partículas plasmónicas sea muy reducida.

En el capítulo 3 se estudia la respuesta óptica lineal de sistemas plasmónicos compuestos por más de dos partículas y que por lo tanto presentan varios *gaps*. En la primera parte del capítulo se estudia el efecto que tiene el tuneleo en la compleja estructura modal que poseen los trímeros triangulares formados por tres nanopartículas esféricas de plata. Este trabajo se realiza en colaboración con el grupo experimental de Jennifer Dionne en la Universidad de Stanford. En la segunda parte se estudian las ventajas que ofrecen las terminaciones planas a la hora de diseñar dispositivos plasmónicos altamente versátiles basados en agregados autoensamblados.

Los trímeros triangulares ofrecen la posibilidad de excitar modos plasmónicos con carácter eléctrico (similares a los estudiados en el capítulo 2), con carácter magnético, así como modos oscuros. Los modos magnéticos se caracterizan por presentar unas corrientes de desplazamiento circulares que producen campos magnéticos netos en el centro del trímero, dando lugar a una distribución de los campos electromagnéticos similar a la de un dipolo magnético. Los modos oscuros son aquellos que presentan una distribución de momentos dipolares en cada partícula de manera que el momento dipolar total resultante es cero, y por lo tanto, no es posible excitarlos usando luz convencional. Es posible estudiar estos modos mediante cálculos y experimentos que utilizan un haz de electrones que permite excitar todas las resonancias de interés, así como caracterizarlas midiendo la cantidad de energía que pierde el haz al pasar a poca distancia de la estructura plasmónica. Además, este mismo haz de electrones permite modificar la distancia entre las partículas con la resolución necesaria para estudiar los efectos que surgen debido al establecimiento de una corriente túnel para separaciones de $d_{\mathrm{gap}} \lesssim 0.5$ nm.

La comparación de los resultados de simulaciones puramente clásicas, con cálculos que incorporan el tuneleo de electrones (usando el QCM) y con los resultados experimentales nos permite llegar a las siguientes conclusiones. Con respecto a los modos eléctricos (BP) se observa un comportamiento equivalente al encontrado en el capítulo 2: la corriente túnel provoca el apantallamiento y posterior desaparición de los modos BP seguido de la aparición de modos CTP antes de que se produzca el contacto físico entre las partículas. En el caso de los modos magnéticos se observa que el efecto túnel también les afecta de manera similar. Al reducir la distancia de los *gaps* la frecuencia de resonancia de los modos magnéticos sufre un *redshift* para posteriormente desvanecerse una vez que la corriente túnel es suficientemente intensa. Una vez que las partículas que forman el trímero entran en contacto, emerge un modo magnético CTP a muy bajas energías. A diferencia del caso en el que las partículas del trímero estaban separadas, en esta situación las cargas eléctricas pueden describir trayectorias circulares libremente, creando así el momento dipolar magnético en el centro del trímero. La energía de resonancia del modo magnético CTP sufre un *blueshift* a medida que aumenta la superposición entre las partículas. Los modos magnéticos son afectados, por tanto, por la corriente túnel de manera muy similar a los modos eléctricos BP convencionales. Finalmente cuando se analiza la

evolución de los modos oscuros observamos que la energía a la que se produce la resonancia no varía al modificar la distancia de los *gaps* que separan las partículas.

De manera significativa, mientras que los cálculos puramente clásicos son capaces de reproducir fielmente los resultados experimentales de los modos oscuros, esto no se produce para los modos magnéticos y eléctricos, los cuales requieren incluir el efecto de la corriente túnel para explicar la evolución experimental. Por lo tanto podemos concluir que la influencia del efecto túnel en cada modo plasmónico depende de su distribución de cargas.

En el capítulo 2 se ha estudiado cómo las terminaciones planas en el *gap* presentan una respuesta óptica diferente a la de las terminaciones esféricas. Por lo tanto, la presencia de caras planas podría ser beneficiosa para el control de la respuesta de agregados autoensamblados. Especialmente interesantes son los agregados en los que la distancia entre las partículas es de un tamaño del orden de 1 nm ya que, como hemos explicado anteriormente, esos *gaps* tan reducidos producen un campo cercano muy intenso. Esta característica puede ser especialmente relevante en técnicas de espectroscopia, donde los campos cercanos intensos son los responsables de generar una mayor eficiencia de la interacción entre la luz y las moléculas o sustancias a analizar. Estudios previos han demostrado cómo la respuesta óptica de estos sistemas puede calcularse a menudo de forma bastante precisa asumiendo que la respuesta óptica lineal del agregado es una combinación de las respuestas de las distintas cadenas que lo forman. Por lo tanto, en la segunda parte del capítulo 3 analizamos la respuesta óptica lineal de cadenas plasmónicas en función del tamaño de la zona plana en las terminaciones del *gap*. Las partículas están separadas por *gaps* de 1 nm, con lo que el campo cercano en el *gap* puede alcanzar valores muy altos cuando la cadena es iluminada en resonancia. Observamos que la utilización de partículas con caras planas en el *gap*, en vez de partículas esféricas, mejora considerablemente la capacidad de ajustar la resonancia plasmónica de la cadena mediante el aumento del número de partículas que la componen. En el caso de partículas esféricas se encuentra que hay una variación máxima de la longitud de onda de unos 200 nm en la posición espectral de la resonancia en función del número de partículas en la cadena, mientras que, usando partículas con caras totalmente planas en el *gap*, se encuentra que la resonancia plasmónica se puede ajustar en un rango de unos 800 nm. Este hecho se puede entender usando de nuevo conceptos de circuitos RC similares a los descritos en el capitulo 2. Cuando la separación entre las partículas es muy pequeña, el *gap* entre caras planas corresponde a una capacitancia muy grande y por tanto casi a una situación de cortocircuito, con lo que la cadena se asemeja a una partícula cilíndrica continua. Aumentar el número de partículas corresponde a aumentar la longitud del cilindro, y por tanto a disminuir la energía del modo.

Otro resultado relevante es que el uso de caras planas no reduce demasiado la intensidad de los campos cercanos en el *gap* pero los distribuye en un volumen mayor, lo cual puede ser beneficioso para técnicas de espectroscopia de

campo cercano donde se estudien capas moleculares en las que la posición de las moléculas que se quieren estudiar no se pueda controlar con precisión.

Por último, en el capítulo 4 se estudia la generación de efectos ópticos no-lineales usando esferas de aluminio, dímeros de esferas de aluminio y dímeros de cilindros de sodio. Para este estudio se utiliza el formalismo cuántico TDDFT, el cual nos permite tratar la dinámica no-lineal de la densidad electrónica de las nanopartículas sin imponer ningún parámetro. Nos concentramos en la generación de luz armónica: cuando se ilumina el sistema con un pulso de luz intenso de frecuencia ω, la respuesta no-lineal da lugar a la emisión de luz a frecuencias múltiples $n\omega$ ($n = 2, 3, ...$). Las nanopartículas metálicas son particularmente interesantes para la generación de efectos no lineales ya que los intensos campos cercanos producidos por la resonancia plasmónica aumentan fuertemente la eficiencia del proceso no-lineal. En general todos los metales presentan procesos ópticos no-lineales pero, dependiendo de las simetrías internas y de la geometría del sistema, algunos de estos procesos no-lineales pueden estar prohibidos. Por ejemplo, sistemas compuestos por partículas metálicas centrosimétricas, como las esferas y los dímeros estudiados en esta tesis, no presentan efectos no-lineales de segundo orden, es decir, no pueden emitir luz a frecuencias armónicas pares.

En la primera parte del capítulo 4 se estudia cómo al polarizar una nanopartícula esférica de aluminio con un campo eléctrico estático es posible romper la condición de centrosimertría y producir luz en armónicos pares. Estos armónicos pares provienen de las propiedades no-lineales impares de orden mayor. Por ejemplo, el segundo armónico proviene de un efecto no-lineal de orden 3 que, al mezclar el campo electromagnético incidente a frecuencia ω con el campo estático de polarización, produce una emisión a 2ω, lo que permite la posibilidad de controlar de forma activa la intensidad de la emisión a frecuencias armónicas pares. Al aumentar el campo de polarización aumentamos la emisión de luz a esta frecuencia.

También se estudia cómo la generación de luz armónica es especialmente eficaz cuando la frecuencia de emisión coincide con la resonancia plasmónica del sistema. En este contexto, una ventaja extra que ofrecen las partículas esféricas de aluminio es que su resonancia plasmónica se encuentra en el ultravioleta, con lo que estos sistemas podrían ser útiles para la generación de luz en este rango del espectro electromagnético. En concreto se demuestra cómo, eligiendo una frecuencia de iluminación tal que el cuarto armónico esté en resonancia con el modo plasmónico de la esfera, se consigue aumentar un orden de magnitud la intensidad de la emisión en este armónico.

En la segunda parte del capítulo 4 se investiga cómo afecta el tuneleo de electrones a la generación de luz armónica. Para ello se utiliza un dímero de nanoesferas de aluminio y un dímero de cilindros de sodio. Estos dos materiales están caracterizados por tener unas densidades electrónicas muy distintas y por tanto, sus respectivas resonancias plasmónicas se encuentran a frecuencias muy diferentes. Esto nos permite estudiar los efectos del tuneleo en dos situaciones

distintas: por un lado la situación en que la frecuencia de iluminación y la frecuencia armónica están lejos de la resonancia plasmónica y, por otro lado, la situación en que la iluminación no está en resonancia, pero la frecuencia armónica coincide con un modo plasmónico BP. Para estudiar el efecto de las corrientes túnel monitorizamos la intensidad del tercer armónico para diferentes frecuencias de iluminación a medida que se cierra el *gap* que separa las dos partículas que forman el dímero.

En primer lugar se estudia el caso en el que tanto la iluminación como el correspondiente armónico se encuentran por debajo de la frecuencia de resonancia BP. Cuando la distancia entre las partículas es relativamente grande se observa cómo a medida que se cierra el *gap*, la generación de luz armónica aumenta progresivamente gracias al aumento del campo cercano. Cuando la distancia se reduce por debajo de los $\approx 4 - 6$ Å (dependiendo del material utilizado) se observa un cambio relativamente brusco en la tendencia caracterizado por un aumento de la emisión armónica, aún más rápido al seguir cerrando el *gap*. Analizando la corriente no-lineal a través del *gap* y su correlación con el momento dipolar inducido, es posible demostrar que la corriente de túnel no-lineal es la principal responsable del cambio brusco observado en el aumento de la intensidad emitida a estas frecuencias armónicas. Finalmente, una vez que el *gap* se reduce por debajo de los $\approx 2 - 4$ Å (dependiendo del material utilizado) la intensidad del tercer armónico decae fuertemente.

En el caso de que para cierta separación entre partículas d_{gap} la frecuencia armónica esté en resonancia con algún modo plasmónico, se produce, en general, la mayor intensidad de luz armónica. Este efecto se observa claramente en el caso del dímero formado por cilindros de sodio. Si se ilumina el dímero de forma que para distancias de *gap* grandes la frecuencia del tercer armónico coincida con la del modo BP, se observa cómo al reducir la distancia d_{gap}, el modo BP sufre un *redshift*, lo que hace que la condición de resonancia deje de cumplirse, y por lo tanto la emisión de luz en el tercer armónico sea menos intensa.

Un último resultado relevante obtenido en esta parte del capitulo 4 está relacionado con la comparación entre la emisión armónica absoluta y la emisión armónica relativa, definida como la emisión del dímero normalizada por la emisión de un dímero equivalente de partículas no interaccionantes. Los cálculos realizados revelan que la condición (frecuencia de iluminación y distancia de *gap*) de emisión absoluta máxima no coincide necesariamente con la condición de emisión relativa máxima. Por lo tanto, a la hora de diseñar un dispositivo nanoplasmónico de generación de armónicos es importante diferenciar claramente cuál es la emisión que se necesita maximizar (absoluta o relativa).

El uso de una metodología rigurosamente cuántica en el capítulo 4 nos ha permitido demostrar la posibilidad de controlar de forma activa la emisión de luz a frecuencias armónicas pares. Además, la sintonización de la frecuencia armónica con la resonancia plasmónica del sistema produce un fuerte aumento en la eficiencia de la emisión. Finalmente nuestro estudio revela que para dímeros separados por *gaps* pequeños la respuesta no-lineal cambia en función

de la distancia del *gap* con tres regímenes bien diferenciados. Para distancias relativamente grandes, el aumento de la emisión armónica viene dominado por el aumento del campo cercano. Para distancias donde el efecto túnel cobra importancia observamos que las corrientes no-lineales dominan e incrementan fuertemente la emisión. Por último, cuando el *gap* se reduce por debajo de los $\approx 2 - 4$ Å se produce un fuerte decaimiento de la respuesta óptica no-lineal.

En resumen, el estudio presentado en esta tesis desvela aspectos fundamentales de las propiedades lineales y no-lineales de *gaps* (sub)nanométricos mediante una combinación de cálculos clásicos y cuánticos basados en metodologías avanzadas en nanoóptica.

Acknowledgements

I want to thank my supervisors, Javier Aizpurua and Rubén Esteban, for giving me the opportunity to join such an stimulating team of people that are part of the Theory of Nanophotonics Group. I joined the group to work on the final project of my Master's degree and from that day they have continuously supported and helped me to grow as a researcher. From the very beginning they showed me a complete availability to discuss as many doubts as I had, as many times as I needed. Little by little they have shaped and polished my abilities to make me develop my full potential. They also encouraged me to travel to conferences to present and defend my work in front of the community.

Javier and Rubén have also showed me that being a good supervisor goes beyond the ability to teach technical knowledge. I can confirm that they really care for their students. Whenever I had a personal difficulty I could talk with them and they did their best to help me. Thank you.

During the PhD I had the opportunity to travel to the Institut des Sciences Moléculaires d'Orsay to work with Andrei G. Borisov and Dana Codruta Marinica. This collaboration gave me the opportunity to learn the WPP method, which was a big challenge for me. I have to thank Andrei and Codruta for the time and patience they put in teaching me the WPP and all the quantum physics related to it. Apart from project-related discussions, the many conversations we had over lunch and coffee broadened my view into science. Andrei's and Codruta's contribution has been really important to make me become the researcher I am today. I addition to their technical training, I greatly appreciate their welcoming and generous personalities, which made feel very happy during all my stays at ISMO.

I also would like to thank all the collaborators of the different projects. Garnett W. Bryant from the National Institute of Standards and Technology, whose insight was key for the work related to the effect of gap morphology. Jennifer Dionne and her group at Stanford University, thanks to whom I collaborated for the first time with an experimental group, which allowed me to grasp the hard work that is required to do cutting-edge experiments. From J. Dionne's group Aitzol García-Etxarri deserves a special mention. As the link between the two groups, he advised me about the calculations and clarified all the experiment-related issues.

I would like to acknowledge all the research centres and funding agencies that supported my research during these years, the Material Physics Center (MPC), the Donostia International Physics Center (DIPC), the Spanish Council for Scientific Research (CSIC), the University of the Basque Country (UPV/EHU), the Ministry of Economy, Industry and Competitiveness (MINEICO) of the Spanish government, the Department of Education of the

As I mentioned, the Theory of Nanophotonics Group is an amazing team of people that makes every person that joins the group feel at home. Therefore here is my big THANK YOU to all the past and present members of the group for always keeping the "good vibes" and for the constructive criticism atmosphere that is present in all of our group meetings, which make us become better scientists: Nerea, Alberto, Aitzol, Mario, Yao, Luca, Angela, Ameen, Mikolaj, Tomas, Andrea, Mattin, Alvaro, Antton.

Ameen and Mikolaj were the students that welcomed me to the group. From the very first moment they made me feel part of the team and helped me with the first steps into research. Specially I have to thank Mikolaj for the support he gave me through my first scripts and calculations and for all the advice he gave me during the time we shared in Donostia.

Mario and I learned the WPP simultaneously, and this created a bond. I have really enjoyed all the philosophical conversations we had.

The Monday cakes of Tomas deserve to be acknowledged here. Many, many weeks started with joy because of his baking ability.

Finally I want to thank Iñigo Aldazabal for introducing me to Python and HPC. He always gave me good advice on how I could try to improve my scientific computing skills.

Llegar hasta aquí y poder defender una tesis doctoral no habría sido posible sin mi familia. Tengo la suerte de tener una familia que siempre me ha apoyado de forma incondicional y me ha ayudado todo lo posible para que consiguiera avanzar en el camino que yo decidiera. Tengo tantas cosas que agradecer que la verdad no se hacerlo como os merecéis. Así que no voy a hacer una lista de motivos por los que os estoy agradecido pero si voy a puntualizar una cosa que considero importante. Todo lo que he aprendido de vosotros y lo que me ha hecho llegar a ser quien soy lo he aprendido de vuestro ejemplo.

Por último tengo que agradecerle a Nagore todo su apoyo durante este proceso. No ha sido fácil y, sinceramente, creo que no lo habría conseguido sin tenerte a mi lado. Has compartido mi ilusión, me has animado en los momentos duros haciéndome ver que son parte del proceso y, sin duda, me has ayudado crecer como persona. Básicamente me has hecho la vida más bonita e interesante, ¿qué más se puede pedir?. De verdad, gracias.

Contents

Abbreviations

ALDA Adiabatic Local Density Approximation.

BDP Bonding Dipolar Plasmon.

BEM Boundary Element Method.

BP Bonding Plasmon.

BQP Bonding Quadrupolar Plasmon.

CTP Charge Transfer Plasmon.

DFT Density Functional Theory.

DP Dipolar Plasmon.

EELS Electron Energy-Loss Spectroscopy.

EFIEHG Electric Field-Induced Even-Harmonic Generation.

EM electromagnetic.

FGH Fourier-Grid Hamiltonian.

JM Jellium Model.

KS Kohn-Sham.

LAP Longitudinal Antenna Plasmon.

LCP Longitudinal Chain Plasmon.

LSP Localized Surface Plasmon.

LSPP Localized Surface Plasmon Polariton.

PAT Photo-Assisted electron Transport.

QCM Quantum Corrected Model.

RE resonant enhancement.

SO Split-Operator.

SPP Surface Plasmon Polariton.

static STM static Scanning Tunneling Microscopy.

STEM Scanning Transmission Electron Microscopy.

TCP Transverse Cavity Plasmon.

TDDFT Time-Dependent Density Functional Theory.

TDKSE Time-Dependent Kohn-Sham Equation.

TDSE Time-Dependent Schrödinger Equation.

TE tunneling enhancement.

WKB Wentzel-Kramers-Brillouin.

WPP Wave Packet Propagation.

Introduction

Optics is a very transversal field in physics. In addition to the ongoing research on the classical and quantum properties of optical fields, light, and in general electromagnetic (EM) fields, are used in most branches of natural sciences as a tool to carry out a wide variety of experimental interrogations to matter. Using light for such a broad research scope is possible because of the many types of interactions that can take place between light fields and the material system under study. These light-matter interactions might result in a change of the properties of the light beam after the interaction takes place, or in the emission of particles, typically electrons. Similarly, a system that has been excited non-optically might emit photons when it de-excites to the ground state. Therefore, understanding the underlying mechanisms of such rich range of interactions between EM fields and matter is of high relevance.

The object of interest of this thesis is particularly focused on the optical response of systems of small dimensions. Optical microscopes are one of the most direct ways to investigate objects that are too small to be observed by the naked eye, but the capabilities of the techniques necessary to retrieve information from microscopic systems exceed imaging. For example, infrared absorption spectroscopy measures which infrared frequencies of the EM spectrum are absorbed by a substance, allowing to characterize vibrational fingerprints of the sample. With this information at hand, it is possible to infer the chemical composition of the substance.

From micro to nanophotonics

The ability to manipulate and concentrate light at the (sub-)micrometre scale opens new possibilities to study small physical systems or to miniaturize optoelectronic devices in progressively smaller regions. To that end, many types of dielectric microphotonic devices have been developed thanks to the improvements of fabrication processes that allow to engineer structures sustaining the desired properties to a high degree of precision. One example of such class of devices are photonic crystals[1], which provide a control of the propagation of light inside a structure by imprinting a periodic pattern in a dielectric that creates a band structure for photons in a similar way as the position of the atoms in a crystal determine the electronic energy bands. The photonic energy band structure can present band gaps that forbid the propagation of certain wavelengths in the crystal in all (absolute bandgap) or particular directions. If, for example, an adequate 1-dimensional defect is created in the photonic crystal,

the energy band structure is modified in that region so that specific frequencies corresponding to the band gap can now propagate, thus creating a photonic waveguide that can be used to design photonic devices. Dielectric photonics is also an appropriate framework to develop microresonators such as Fabry-Perot micro pillars, with high quality factors (long-lived photonic states), able to manipulate and concentrate light very efficiently at very precise frequencies.

Dielectric microphotonic devices can be used to manipulate light and enhance light-matter interactions at the micro and submicrometer scale but they are limited by the diffraction-limit, which establishes that the minimum volume at which light of wavelength λ can be confined is of the order of $(\lambda/2n)^3$, where n is the refractive index of the dielectric. In order to beat the diffraction limit and to obtain nanometric confinement, Surface Plasmon Polaritons (SPPs) emerge as a powerful excitation in metals capable of confining light due to the response of the conduction electrons. A SPP is a resonant electronic density wave that is excited at metal/dielectric interfaces due to the hybridization of the oscillations of the conduction electrons in the metal (surface plasmons) with EM fields at visible and near-infrared frequencies. Propagating SPPs are able to strongly confine optical fields in the region near a flat metal-dielectric interface extending a few tens of nanometres in the direction normal to the interface.

Furthermore, if a metallic nanoparticle is resonantly excited, the SPP, in this case called Localized Surface Plasmon Polariton (LSPP), confines the optical fields induced by the surface charge density oscillations at the metal surface to a very small volume around the nanoparticle. The resonance wavelength as well as the distribution of the fields around the nanoparticle can be tailored by modifying the size, shape and material of the particle or the environment surrounding the nanoparticle, which is a major advantage for designing the optical response of plasmonic nanodevices and thus tailor their properties for eventual applications in nanooptics. The strongly localized fields can be used to enhance light-matter interactions[2,3] beyond the capabilities of dielectric structures. We describe propagating SPPs and LSPPs in more detail in Secs. I-IV of this introduction.

The typical sizes of plasmonic nanoparticles (also called optical nanoantennas) are in the range of a few tens to hundreds of nanometres. Many fabrication challenges arise in order to create nanoparticles with high control in their shape, position on a substrate, or composition. Over the last decades much research activity has focused on improving and exploring new fabrication techniques, which has allowed to achieve remarkable precision in top-down fabrication approaches[4–6], and large versatility in bottom-up ones[7–9].

From a theoretical perspective, a big effort has been devoted to the development of theoretical frameworks and computational tools to accurately solve Maxwell's equations near metallic nanoparticles for a large variety of complex nanostructures. Theoretical and computational effort has allowed in two decades to obtain the response of progressively more complicated objects, evolving from symmetric objects such as spherical particles and dimers[10,11] to

Far-field

Near-field

Linear

a)

b)

Nonlinear

c)

d)
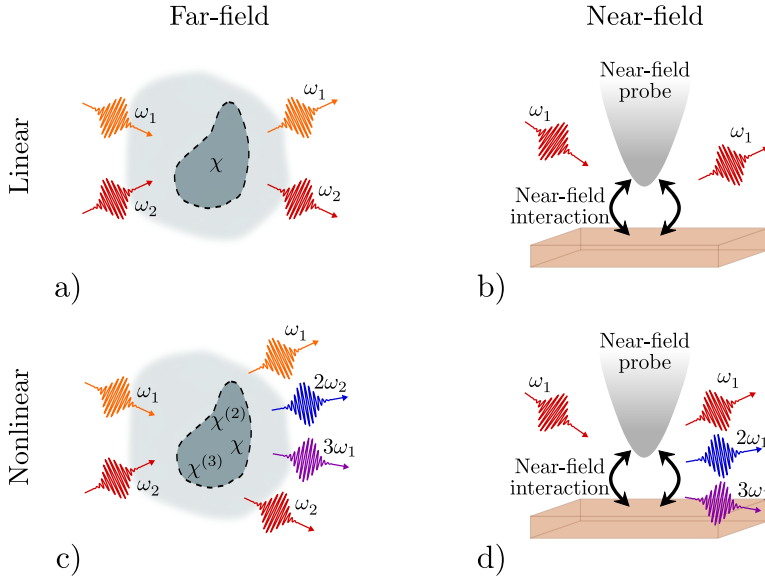
FIGURE 1: Examples of different types of light-matter interactions. Schematics of far-field (left column) and near-field (right column) configurations. Linear (top row) and nonlinear (bottom row) light-matter interactions are shown. (a) Far-field configuration presenting a linear interaction where two pulses of frequency ω_1 and ω_2 are scattered elastically by a sample and thus, the resulting light after the interaction has the same frequency as the incident. (b) Near-field configuration presenting linear light-matter interaction where a near-field probe is illuminated by light of frequency ω_1, which is elastically scattered. (c) Far-field configuration presenting a nonlinear interaction where two pulses of frequency ω_1 and ω_2 interact with a sample and the scattered field has components at ω_1, ω_2 and linear combinations of such frequencies. (d) Near-field configuration presenting a nonlinear interaction where a near-field probe is illuminated by a pulse of frequency ω_1 and the scattered field has components at ω_1 and multiples such frequency.

much more complex interacting objects showing extreme geometries and large number of particles[12,13].

With such large number of systems under study, it is not surprising that light-matter interactions can be analysed and organized according to different criteria. We emphasize in Fig. 1 two of those criteria that will be of particular relevance in this thesis: whether the interaction between light and matter is linear or nonlinear and, whether the process under study relies on the far-field or near-field response.

Linear and nonlinear light matter interactions

When light with electric field $\mathbf{E}(t)$ illuminates a material, both bounded and conduction charges of the latter, oscillate as a response to the electric field and create a microscopic polarization, $\mathbf{P}(t)$, which in the lowest linear order of approximation takes the form

$$\mathbf{P}(t) = \chi \mathbf{E}(t) \ , \tag{1}$$

where χ is the dielectric susceptibility of the material that for simplification we assume as an scalar factor independent of the spectrum of the incoming light (a more complex χ is discussed in Ch. 4). The assumption that the polarizability of the material is proportional to the first power of the electric field corresponds to the approximation that the light-matter interaction is linear. If the system is illuminated by two lasers of different frequency ω_1 and ω_2 and with corresponding electric field amplitude $\mathbf{E_1}$ and $\mathbf{E_2}$ (see Fig. 1a), Eq. (1) is transformed into

$$\mathbf{P}(t) = \chi \mathbf{E_1} \cos(\omega_1 t) + \chi \mathbf{E_2} \cos(\omega_2 t) \ , \tag{2}$$

which indicates that the material responds separately to each frequency. These components of the microscopic polarization scatter light at the initial frequencies ω_1 and ω_2, but not at any new frequency, as sketched in Fig. 1a.

The linear approximation in Eq. (1) can be extended to higher order contributions to the microscopic polarization, where higher powers of the electric field need to be considered[14]:

$$\mathbf{P}(t) = \chi \mathbf{E}(t) + \chi^{(2)} \mathbf{E}^2(t) + \chi^{(3)} \mathbf{E}^3(t) + \dots \ , \tag{3}$$

where χ is the linear dielectric susceptibility as in Eq. (1) and $\chi^{(n)}$ are the nonlinear dielectric susceptibilities of order $n = 2, 3, \dots$ (assuming again that they are independent of the spectrum of the incoming light). As the nonlinear order increases, the associated contribution to the total polarization decreases rapidly, so that very intense EM fields are needed to trigger a noticeable nonlinear response. These nonlinearities give rise to a wide variety of phenomena that are extensively studied and exploited in optics[14].

Figure 1c sketches a typical nonlinear process that can take place when a material is illuminated with light at two different frequencies ω_1 and ω_2. The nonlinear response in Eq. (3) mixes the illumination frequencies and produces a polarization which shows oscillations at a linear combination of all the frequencies involved. To illustrate the origin of the combination of frequencies let us assume that the material is illuminated by a z-polarized optical field whose electric field can be expressed as:

$$\mathbf{E}(t) = \big(E_1 \cos(\omega_1 t) + E_2 \cos(\omega_2 t)\big)\hat{e}_z \ , \tag{4}$$

where $\hat{e}_z$ is the unit length vector along the z-direction.

Inserting Eq. (4) into Eq. (3) and focusing only on the nonlinear term of order $n = 2$ one obtains that the z-component of the polarization can be expressed as:

$$
\begin{aligned}
\mathrm{P}_z^{(2)}(t) &= \chi^{(2)}\big(E_1^2 \cos^2(\omega_1 t) + E_2^2 \cos^2(\omega_2 t) + 2E_1 E_2 \cos(\omega_1 t)\cos(\omega_2 t)\big) \\
&= \chi^{(2)}\Big(E_1^2 \frac{1}{2}\big[1 + \cos(2\omega_1 t)\big] + E_2^2 \frac{1}{2}\big[1 + \cos(2\omega_2 t))\big] \\
&\quad + E_1 E_2 \big[\cos((\omega_1 - \omega_2)t) + \cos((\omega_1 + \omega_2)t)\big]\Big) \,,
\end{aligned}
\tag{5}
$$

that is, we obtain contributions at $2\omega_1$ and $2\omega_2$ from the first two terms (second harmonic generation) and a contribution that oscillates at the sum and difference of frequencies, $\omega_1 + \omega_2$ and $\omega_1 - \omega_2$. These terms in combination with the linear ones previously outlined, and those coming from higher orders of $\chi^{(n)}$ add up to create the total polarization of the material. Thus, nonlinear light-matter interactions can generate oscillations of the polarization at a large variety of frequencies corresponding to $|\ell\omega_1 \pm m\omega_2|$, where $\ell + m$ are equal to the maximum nonlinear order n considered for the response $\chi^{(n)}$.

Far-field and near-field mediated interactions

Let us explore next the differences between far-field and near-field optical responses. In far-field optical processes the excitation of the material as well as the detection of the scattered/emitted light from the material is carried out far (tens of wavelengths to centimetres/metres away) from the sample. If the material under study is composed by many constituents (different plasmonic nanoparticles or a gas of molecules for example), the constituents are assumed to be well separated so that the main interaction between them consists of long-range dipolar interactions mediated by propagating EM fields. Figure 1a,c sketches typical linear and nonlinear far-field processes. Traditional telescopes, optical microscopes and standard spectroscopy, among others, are instruments and techniques that relay on the far field.

On the other hand, in optical processes mediated by the near field, the constituents of the sample under study are located close enough to be sensitive to short-range interactions mediated by induced evanescent fields. Notice that in applications that rely on the near field, the sample can be excited from the far field and, after the near-field interaction, the scattered fields can be collected in the far field. In this situation, however, the signal scattered can not be explained without taking into account the near-field light-matter interaction.

In this thesis we are interested in the study of fundamental far-field and near-field properties of LSPPs, in both the linear and nonlinear regimes. Usually, plasmonic systems are theoretically studied by solving classical Maxwell's equations, an approach valid to describe many nanoscale systems in optics. However, recent developments in fabrication and experimental techniques have

allowed to place plasmonic nanoparticles in extremely close proximity so that quantum processes such as nonlocal dynamical screening[15–20] and quantum tunneling[16,21–29] can have an influence in the response of the system. In those cases, the classical framework is not valid anymore and semiclassical or full quantum-mechanical frameworks need to be employed to correctly account for all the details of the optical response. In this thesis we focus on how electron tunneling across sub-nanometric gaps modifies the linear and nonlinear optical response of plasmonic cavities, and how harmonic light emission can be actively controlled.

In the following sections of this introduction we review the basic properties of plasmon resonances, as the main building block of the results of this thesis.

I   Surface plasmon polaritons

As we have just described, SPPs are resonances that emerge at metal/dielectric interfaces due to the hybridization of the electromagnetic field with the electronic density of the metal[30,31]. One option to study the properties of SPP resonances is to model the metal using a dielectric permittivity obtained experimentally. On the other hand, a very common approach that allows to understand the main physical phenomena while maintaining good accuracy for energies below d-band excitations (particularly in infrared spectrum) is to use the Drude model, which describes the conduction electrons of the metal as a non-interacting free electron gas. The frequency-dependent relative dielectric permittivity of a metal, $\varepsilon_m(\omega)$, within the Drude model is expressed as:

$$\varepsilon_m(\omega) = \varepsilon_\infty - \frac{\omega_p^2}{\omega(\omega + i\gamma_p)} \ , \tag{6}$$

where γ_p is the damping coefficient that accounts for the losses in the metal, ε_∞ is the background screening that accounts phenomenologically for the polarisability of bounded d-electrons (the damping related to these contributions is not included in the Drude model) and ω_p is the plasma frequency of the metal, which is defined as:

$$\omega_p = \sqrt{\frac{ne^2}{\varepsilon_0 m_e}} \ , \tag{7}$$

with n being the electronic density of the metal, e the electron charge, ε_0 the dielectric permittivity of vacuum and m_e the effective electron mass.

It can be shown that, if a planar metal/dielectric interface is illuminated by a monochromatic plane wave, the continuity of the electromagnetic field at the interface leads to a dispersion relation for the component parallel to the
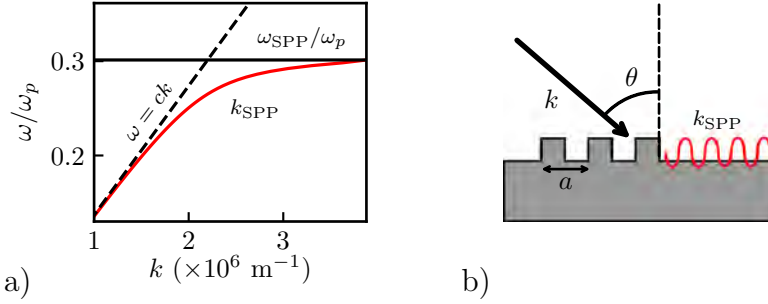
FIGURE 2: (a) Dispersion relation of propagating SPP (red line) at a gold/vacuum interface. The gold is modelled within the Drude model (Eq. (6)) with parameters[32] $\omega_p = 9.06$ eV, $\gamma_p = 0.07$ eV and $\varepsilon_\infty = 9.84$ eV and the vacuum relative permittivity is $\varepsilon_d = 1$. The light cone is represented as a black dashed line and the horizontal black line marks the SPP frequency, which satisfies $\varepsilon_m(\omega_{\mathrm{SPP}}) = -\varepsilon_d$. (b) Sketch of a metal/dielectric interface where a propagating SPP is being excited thanks to a grating of periodicity a imprinted on the metal. The grating is illuminated by a planewave with wave-vector k at an angle θ with respect to the direction normal to the surface.

metal/dielectric interface of the wave-vector of the propagating SPP[30,31]:

$$k_{\mathrm{SPP}} = \sqrt{\frac{\varepsilon_m(\omega)\varepsilon_d}{\varepsilon_m(\omega) + \varepsilon_d}} \frac{\omega}{c} . \qquad (8)$$

Here ε_d is the relative permittivity of the dielectric, c is the speed of light in vacuum and $k = \omega/c$ is the electromagnetic plasmon wave-vector in vacuum.

Figure 2a shows the dispersion relation (Eq. (8)) of a propagating SPP (red line) in a gold/vacuum planar interface. The gold is modelled within the Drude model (Eq. (6)) with parameters[32] $\omega_p = 9.06$ eV, $\gamma_p = 0.07$ eV and $\varepsilon_\infty = 9.84$ eV. The black dashed line is the light cone, which represents the dispersion relation of a plane wave of frequency ω propagating in vacuum. For small energies (small ω), the SPP dispersion line follows very closely the light cone but, as the energy increases k_{SPP} strongly deviates from the light cone towards the asymptote at ω_{SPP}, which produces a large mismatch between the illumination wave-vector and k_{SPP}. Finally, the solid black line marks the so called SPP frequency, ω_{SPP}, that is defined as the frequency for which the denominator on the right-hand side of Eq. (8) is zero ($\varepsilon_m(\omega_{\mathrm{SPP}}) = -1$ in our case). An advantage of a SPP wave-vector component parallel to the interface much larger than the light cone is that strongly evanescent fields are generated at the interface, in the direction perpendicular to the surface.

To excite a propagating SPP, the component of the illumination wave-vector parallel to the interface should be equal to k_{SPP}. However, Eq. (8) and Fig. 2a
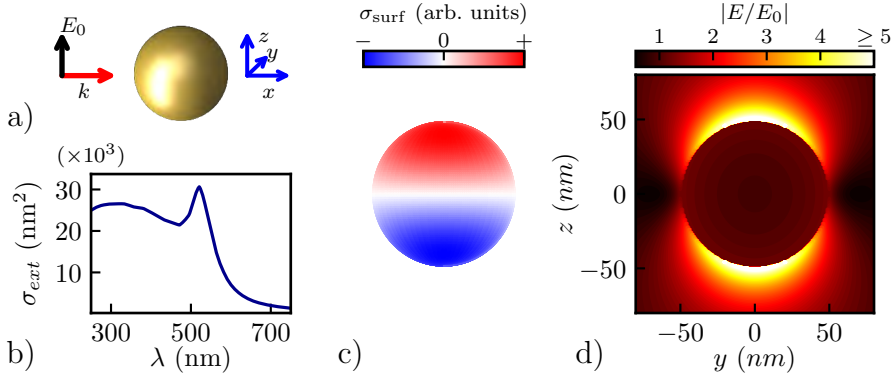
FIGURE 3: Properties of LSPs. Optical response of a gold nanosphere of diameter $D = 100$ nm. (a) The nanoparticle is illuminated along the direction k by linearly polarized light with amplitude E_0. The direction of propagation (k) and the polarization are given by the red and black arrows respectively. (b) Extinction cross-section σ_{ext} as a function of the illumination wavelength λ. (c) Surface charge distribution of the Dipolar Plasmon (DP) mode orthogonally projection onto the $x = 0$ plane. (d) Near-field enhancement ($|E/E_0|$) at the wavelength of the resonance, $\lambda_{DP} = 521$ nm.

show that, for any given frequency, the wave-vector of a propagating SPP is larger than that of an electromagnetic wave propagating on the dielectric material (vacuum in this case). Therefore, propagating SPPs cannot be excited by direct illumination of a flat metal/dielectric interface (assuming that this is the only flat interface in the system[33,34]). One way to provide the extra momentum that is needed to launch a propagating SPP is presented in Fig. 2b. A grating with periodicity a is patterned on the metal surface, such that it provides the extra momentum, $a/2\pi$, that is needed to match the illumination and SPP wave-vectors. A propagating SPP is excited when the grating is illuminated at an incidence angle, θ, with respect to the normal direction such that the component of the k-vector parallel to the metal surface satisfies $k\sin(\theta) + m(a/2\pi) = k_{SPP}$, where m is and integer.

Contrary to propagating SPPs, the Localized Surface Plasmons (LSPs) (commonly used short-hand notation for LSPPs) that are supported by small nanoparticles can be excited in a straightforward manner by direct illumination. Figure 3 shows different aspects of the optical response of a gold spherical nanoparticle of diameter $D = 100$ nm. In this and following figures of the introduction we use the experimental permittivity of gold[35] and the Boundary Element Method (BEM) as a Maxwell's equations solver[10,36,37] to obtain the results. The nanoparticle is illuminated by a plane wave propagating in the x-direction and polarized along the z-direction, as sketched in Fig. 3a. Figure 3b shows the extinction cross section as a function of the wavelength of the incoming field. The resonance located at $\lambda_{DP} = 521$ nm is the Dipolar Plasmon (DP)

mode of the sphere, as confirmed by the surface charge distribution obtained when illuminating the spherical nanoparticle at λ_{DP}, as shown in Fig. 3c. In the plot we use an orthogonal projection in which each point on the $x > 0$ hemisphere surface of the particle is projected onto the $x = 0$ plane using a line orthogonal to this plane. A clear dipolar pattern can be observed with charges of opposite sign at the top and bottom hemispheres of the nanoparticle (red positive charges and blue negative ones). These charges oscillate resonantly at the frequency of the illumination. The near-field enhancement map (total field amplitude at each point normalized to the amplitude of the incident field, $|E/E_0|$) associated to this mode is plotted in Fig. 3d. A large enhancement and strong localization of the near-fields around the nanoparticle can be clearly observed. Importantly, the near fields are localized into a region much smaller than the wavelength of the excitation source. In the example plotted in Fig. 3d we can observe that the regions of strong fields extends a few tens of nanometres around the nanoparticle. Much larger localization is possible for smaller particles and for optimized structures such as the dimers discussed below.

To gain further insight, we consider the case of a metallic sphere with permittivity $\varepsilon_m(\omega)$ embedded in a dielectric medium ε_d. The radius R of the sphere is much smaller than the wavelength of light ($R << \lambda$). For such small sphere, the response can be calculated analytically using the dipolar approximation within the so-called electrostatic approximation. The dipole moment induced at the nanoparticle by a homogeneous electric field $\mathbf{E_0}$ can be obtained from the nanoparticle's polarisability[31], α, as:

$$\mathbf{p} = \varepsilon_d \alpha \mathbf{E_0} \ , \tag{9}$$

where α is given by

$$\alpha = 4\pi\varepsilon_0 R^3 \frac{\varepsilon_m(\omega) - \varepsilon_d}{\varepsilon_m(\omega) + 2\varepsilon_d} \ . \tag{10}$$

The DP resonance is excited for a frequency ω_{DP} that satisfies the condition $\varepsilon_m(\omega_{DP}) = -2\varepsilon_d$. If the metal is modelled as a lossless Drude metal without background screening, $\gamma_p = 0$ and $\varepsilon_\infty = 1$, in Eq. (6), we obtain

$$\omega_{\text{DP}} = \frac{\omega_p}{\sqrt{1 + 2\varepsilon_d}} \ . \tag{11}$$

If the surrounding medium is vacuum ($\varepsilon_d = 1$), ω_{DP} in Eq. (11) becomes $\omega_{\text{DP}} = \omega_p/\sqrt{3}$, which is valid for perfect Drude-like metals but is not a complete description for some of the most typical plasmonic materials such as gold (Au) and silver (Ag) in the visible range of the spectrum. In the case of gold[32], which has a plasma frequency $\omega_p \approx 9$ eV, Eq. (11) predicts that the DP wavelength would be at $\lambda_{\text{Au}} \approx 240$ nm while the experimental value is at $\lambda_{\text{Au}} \approx 520$ nm. The reason for this discrepancy is that the description neglects the effect of the background polarisability of bound d-electrons and the damping of the

material to obtain Eq. (11). When the background polarisability of d-electrons is included the optical properties of noble-metal particles are well reproduced.

The discussion so far has been centred in spherical particles, but the two key characteristics observed in Fig. 3 qualitatively hold for nanoparticles of arbitrary shape. Plasmonic resonances of generally present sub-wavelength localization and strong near-field enhancements. On the other hand, the exact resonance frequency of the plasmon modes and distribution of the near field of such resonances depends strongly on the material, the shape of the nanoparticle and the dielectric response of the surrounding medium[38,39]. This great tunnability of the plasmon properties is a key reason why plasmonic nanoparticles are so relevant in nanophotonics. The ability to tune the resonances of a nanosystem allows to engineer the optical properties at the nanoscale, tailoring them for specific technological purposes where photonic modes are needed

Much research has been carried out in the last decades in the understanding of these LSP resonances and in the development of techniques to fabricate, characterize and exploit plasmonic nanoparticles[3,8,40]. A system of particular interest consists of two nanoparticles that are positioned in close proximity, where the interaction between the modes of each nanoparticle gives rise to new hybridized plasmonic modes. These coupled plasmonic modes further localize and enhance the near field between the nanoparticles. The present thesis focuses on the study of linear and nonlinear properties of coupled plasmonic particles forming extremely (nanometre and subnanometre) narrow gaps between their surfaces. Thus, we describe next the main properties of dimers of metallic nanoparticles.

II   Bonding plasmon resonances

When two nanoparticles are set in close proximity, the Coulomb interaction between the charges associated to the LSP modes of both particles produces a hybridization of the modes forming Bonding Plasmon (BP) resonances (and anti-Bonding Plasmon resonances) in a similar way as atomic orbitals hybridize when forming a molecule[41–43]. The situation where there is no electron transfer between the nanoparticles and Coulomb forces dominate the interaction is often described as a capacitive regime, which we describe below. Otherwise, in the conductive regime, electrons can flow from one particle to the other. The conductive regime is explained in detail in Sec. III.

Plasmonic dimers have stimulated intense research due to their advantages over single nanoparticles. The accumulation of charges at facing metallic surfaces across the gap leads to a significant increase of the localization and enhancement of the near field in the gap region in comparison to the single nanoparticle case[44,45]. In addition, the strong Coulomb interaction between these charges shifts the spectral position of the BP resonances, making them
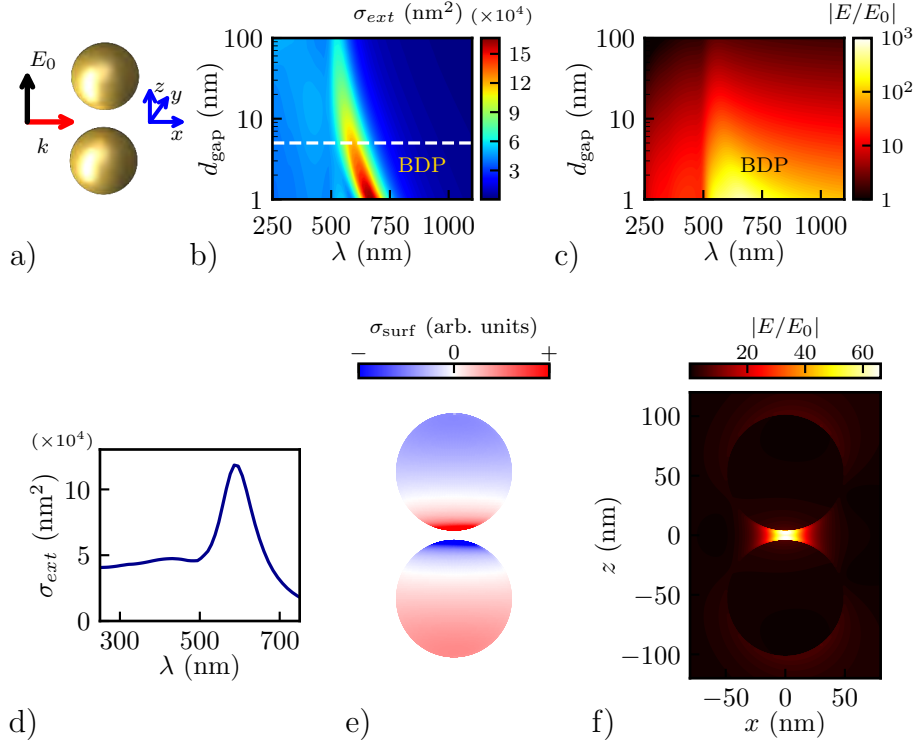
FIGURE 4: Properties of BDPs. Optical response of a dimer of gold spheres of diameter $D = 100$ nm. (a) Scheme of the dimer illuminated by a plane wave propagating along the x-axis, polarized along the dimer axis and with amplitude E_0 and momentum k. (b) Extinction cross-section σ_{ext} and (c) near-field enhancement $|E/E_0|$ at the centre of the gap as a function of wavelength, λ, and gap distance, d_{gap}. (d) Spectrum of the optical response of the dimer for $d_{\mathrm{gap}} = 5$ nm. The spectrum corresponds to the white dashed line in (b). (e) Orthogonal projection of the surface charge distribution on the dimer at the BDP wavelength and (f) near-field enhancement at $d_{\mathrm{gap}} = 5$ nm and $\lambda = 586$ nm corresponding to the BDP in (d).

very sensitive to the gap separation distance[16,45]. These properties allow optimizing the response of single molecules deposited at the gap between particles[2], thus sensing minuscule amounts of substances[6] or boosting nonlinear effects[46].

Figure 4 illustrates the sensitivity of the plasmonic response to the separation between the nanoparticles, d_{gap}. As sketched in Fig. 4a, a dimer of gold spheres of diameter $D = 100$ nm is illuminated by a plane-wave that propagates along the x-axis with momentum k and with field amplitude E_0 polarized along the dimer axis (z-axis). In Fig. 4b we plot the evolution of the extinction cross-section σ_{ext} as the gap between the spheres is closed from

$d_\mathrm{gap} = 100$ nm to $d_\mathrm{gap} = 1$ nm. σ_{ext} presents one peak which corresponds to the Bonding Dipolar Plasmon (BDP), a resonance that is a consequence of the hybridization of the DPs of each nanoparticle[41–43]. The extinction cross-section σ_{ext} in Fig. 4b shows how, as the gap is closed, the resonance wavelength of the BDP shifts to larger wavelengths (redshifts) and the resonance increase its intensity. For very narrow gaps, a small variation on the gap width produces a large change in the resonance wavelength (notice that the d_gap-axis is set in logarithmic scale).

In Fig. 4c we plot the field enhancement, $|E/E_0|$, at the centre of the gap ($x = y = z = 0$ nm) for the same wavelengths and gap distances. The redshift of the BDP mode as the gap is closed can again be observed. Furthermore, we observe that the field enhancement at the BDP wavelength grows 2 orders of magnitude from $d_\mathrm{gap} = 100$ nm to $d_\mathrm{gap} = 1$ nm, reaching values of $|E/E_0| \sim 580$.

To clearly observe the properties of the BDP we calculate next the surface charge distribution and the near-field enhancement around the nanoparticles for a separation distance $d_\mathrm{gap} = 5$ nm. Figure 4d shows the extinction cross-section of the dimer for this separation (white dashed line in Fig. 4b). The spectrum is characterized by the BDP resonance centred at a wavelength $\lambda = 586$ nm. In Fig. 4e we plot an orthogonal projection of the surface charge distribution associated to the BDP. Both spheres present a dipolar pattern with charges of opposite sign accumulated at the top/bottom hemisphere. However, if we compare these results with the charge distribution of a single sphere in Fig. 3c, we observe the increased localization of charges of opposite sign at the gap surface regions. The resulting strong increase in the near-field enhancement and efficient localization of the fields in the gap region is verified in the near-field enhancement map of Fig. 4f.

The BDP is a key resonance in nanooptics as it often emerges in many architectures which show metallic gaps. On top of structures fabricated using lithography and particles united by molecular linkers that exhibit this kind of junctions, scanning probe microscopies, such as tunneling microscopy, often generate metallic cavities where BDPs are formed at the gaps, assisting in enhanced microscopy and spectroscopy. For this reason, the BDP is often referred as a "gap plasmon".

III   Charge-transfer plasmon resonances

When electric charges can be transferred between two nanoparticles forming a dimer, Charge Transfer Plasmon (CTP) modes can be excited. CTPs are present, for example in particles at physical contact in a merging process. However, CTPs can also be excited if the particles are well separated but electrons can still flow from one particle to another due to other means of transport, for example through a conductive molecular layer formed between the nanoparticles[47,48], or *via* electron tunneling through the gap[21,22].
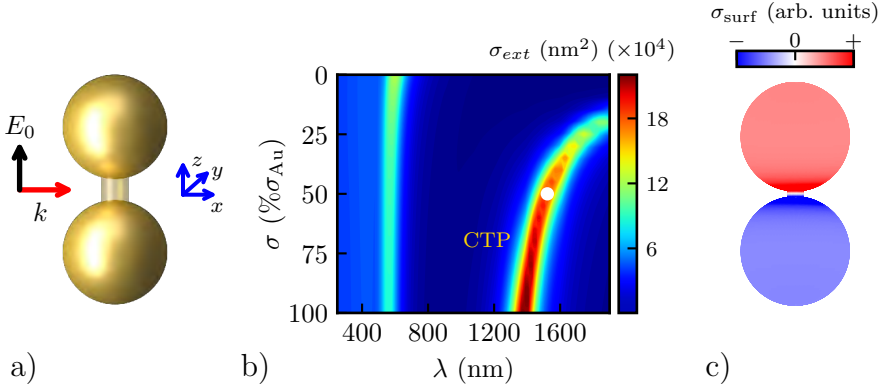
FIGURE 5: Properties of the CTP. Classical optical response of a dimer of gold spheres of diameter $D = 100$ nm. The spheres are electrically connected with a material of variable conductivity. (a) Schematics of the connected dimer illuminated by a plane-wave travelling along the x-axis and polarized along the dimer symmetry axis. (b) Extinction cross-section σ_{ext} as a function of wavelength and conductivity of the material placed at the gap, given as a percentage of the conductivity of gold. (c) Orthogonal projection on the $x = 0$ plane of the surface charge distribution of the dipolar CTP for a conductance of the interparticle material $\sigma = 0.5\sigma_{Au}$ and $\lambda = 1522$ nm. The white dot in (b) marks the (σ, λ) point where the surface charge map in (c) has been calculated.

The spectral position of CTPs is very sensitive to the properties of the charge transfer channel. Contrary to BPs, each nanoparticle forming the dimer gets net charge due to the electrons that are transferred between the particles back and forth at each optical cycle. We first follow closely the work of O. Pérez-González and co-workers[47] to study how a conductive junction linking two metallic nanoparticles modifies the optical response of the system. Figure 5 shows the optical response of a dimer of gold spherical particles of diameter $D = 100$ nm, with a gap distance $d_{gap} = 4$ nm and being joined by a metallic cylinder of $R = 7$ nm that is placed at the centre of the gap and contacts the two particles (Fig. 5a). The dimer is illuminated by a plane wave that propagates along the x-axis and that is polarized along the dimer symmetry axis (z-axis). We vary the conductivity σ of the linking cylinder to study the effect of electron transfer on the optical response of the dimer. The conductivity is calculated as a percentage of the conductivity of gold using Eq. (A.11) of Appendix A, and the experimental permittivity of Ref. [35]. Figure 5b shows the extinction cross-section of the dimer as we increase the conductivity of the metallic junction from $\sigma(\omega) = 0$ (top of the figure) to the value of the conductivity of gold $\sigma(\omega) = \sigma_{Au}(\omega)$ (bottom of the figure). Initially, the conductivity of the junction is approximately 0 and, consistent with the results of the previous section, only the BDP is excited around $\lambda \sim 600$ nm. As we increase the

conductivity the charges accumulated at the metallic surfaces of the gap get screened and, thus, the BDP weakens and slightly blueshifts due to the weaker Coulomb interaction. When the conductivity of the junction increases to the point where it allows enough electrons to flow between the nanoparticles (in our case $\sigma \approx 0.15\sigma_{\mathrm{Au}}$) the lowest-order CTP is excited at large wavelengths. With further increasing of the conductivity of the junction, this low-energy CTP resonance blueshifts until it saturates to the $\lambda \sim 1380$ nm DP wavelength of the gold dumbbell structure, which is obtained when the gap cylinder is made of gold.

The charge distribution in Fig. 5c demonstrates that when exciting the CTP each nanoparticle acquires net charge. We plot the surface charge density of the lowest-energy CTP when the conductivity of the junction is $\sigma(\omega) = 0.5\sigma_{\mathrm{Au}}(\omega)$ (condition marked as a white dot in Fig. 5b). A dipolar pattern in the charge distribution is observed with the top and bottom spheres exhibiting opposite net charge.

Figure 5 considers the behaviour of CTPs in the theoretical case in which the conductivity of the junction is increased continuously. However, the results are general and can be used to understand realistic experimental situations where a generic change of conductivity is produced. For example, if conductive molecules are placed at the gap, the number of molecules would determine the effective conductivity and therefore the position and strength of the lowest-energy CTP[48,49].

Another situation in which charge can be transferred between two nanoparticles is when they reach physical contact. Figure 6 shows the classical optical response of a dimer of $D = 100$ nm gold spheres as the gap separating them is closed from the capacitive regime $d_{\mathrm{gap}} > 0$ to the conductive regime $d_{\mathrm{gap}} < 0$. Negative d_{gap} means that the centres of the spheres are separated by $2R - |d_{\mathrm{gap}}|$ and therefore are physically touching. Figure 6a illustrates the geometry, which is illuminated by a plane wave polarized along the dimer's symmetry axis (z-axis). We notice that for $d_{\mathrm{gap}} \lesssim 0.5$ nm electron tunneling might also affect the optical response but we focus here in the classical prediction leaving the treatment of this quantum effect for Sec. IV. Figure 6b shows the extinction cross-section as a function of gap distance (d_{gap}) and wavelength (λ), where the results for $d_{\mathrm{gap}} > 1$ nm repeat the values already shown in Fig. 4b. For smaller but positive distances the redshift is more pronounced, diverging as the gap vanishes. Furthermore, for the smallest separations, along with the BDP, a higher-order BP is clearly observed at smaller λ, which also redshifts for closing d_{gap}.

For negative d_{gap} we find a set of CTP modes that strongly blueshift as the merging process takes place. For perfect spheres, the contact point at $d_{\mathrm{gap}} = 0$ nm is 0-dimensional so that charges cannot yet be transferred. As the distance, d_{gap}, is further reduced the contact area between the particles increases rapidly enabling the transport of charges across the contact region, therefore producing the strong blueshift. In the classical calculations described
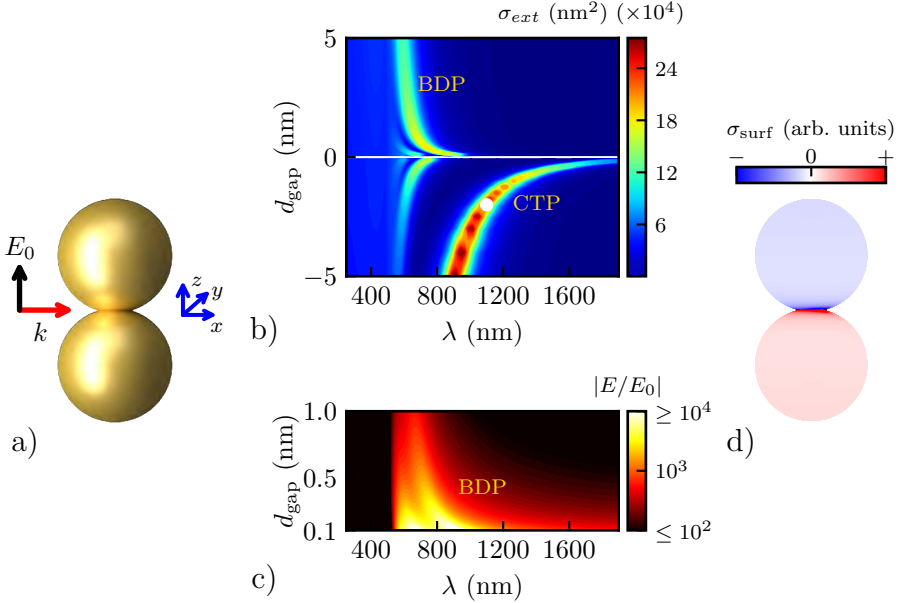
FIGURE 6: Properties of a merging dimer. Classical optical response of a merging dimer of gold spheres of diameter $D = 100$ nm. (a) Schematics of an overlapping dimer illuminated by a plane-wave travelling along the x-axis and polarized along the dimer symmetry axis. (b) Extinction cross-section σ_{ext} as a function of wavelength and separation distance (for $d_{\text{gap}} \geq 0.1$ nm and $d_{\text{gap}} \leq -0.1$ nm). (c) Near-field enhancement $|E/E_0|$ at the centre of the gap for very small positive gaps ($0.1 \leq d_{\text{gap}} \leq 1.0$ nm) (d) Orthogonal projection on the $x = 0$ plane of the surface charge distribution of the dipolar CTP for $d_{\text{gap}} = -2$ nm and $\lambda = 1100$ nm. The white dot in (b) marks the point where the surface charge map in (d) has been calculated.

here the electrons cannot cross the gap before contact, even for vanishing distances, and thus the transition from bonding to charge-transfer modes is discontinuous[45]. In Fig. 6d the surface charge distribution of the lowest-energy CTP at $d_{\text{gap}} = -2$ nm and $\lambda = 1100$ nm (white dot in Fig. 6b) demonstrates that the mode has the same dipolar character as in the previous case of a conductive bridge (Fig. 5c).

For completeness, we plot in Fig. 6c the near-field enhancement in the centre of the gap, focusing on the case of ultra-narrow gaps, 0.1 nm $\leq d_{\text{gap}} \leq 1$ nm. We observe that the near-field enhancement at the BDP resonance wavelength continuously grows as the gap is closed finding the strongest fields for the smallest d_{gap}. We discuss in the next section how this unrealistic field enhancement is quenched by the emergence of tunneling of electrons across the gap.

IV   Effect of electron tunneling on the plasmonic response

The classical formalism used to obtain the optical response of a plasmonic dimer in Fig. 4 is appropriate to reproduce the physics of interacting plasmonic systems typically used in experimental situations, where the metallic particles are separated by distances of several nanometres. However, when plasmonic nanoparticles are separated by ultra-narrow gaps, smaller than ~ 0.5 nm, the quantum nature of the electrons in the metal becomes relevant and requires a more sophisticated treatment. For example, in the classical results in Fig. 6b we observed an unphysical divergence of the resonant frequency of both the BDP and the lowest-energy CTP close to $d_{\mathrm{gap}} = 0$ nm. However, following the quantum nature of electrons in a gap, where the Fermi levels of both particles are shifted by the optical potential acting at the gap, at ultra-narrow gaps, $d_{\mathrm{gap}} \leq 0.5$ nm, a tunneling current will be established between the nanoparticles. We discussed in Sec. III how charge transfer can strongly affect the plasmonic response, and thus one can expect tunneling to have a similar impact.

More in detail, in a classical formalism the boundary that separates the metal and the surrounding material is perfectly defined and the electrons are completely bounded by it to be inside the particle. Therefore, it is impossible that charge transfer occurs before physical contact of the nanoparticles if no conducting material is placed at the gap. In a quantum mechanical description of the electron gas, the electrons of each sphere are not tightly bounded by any well-defined boundary (given for example by the outermost atoms that form the particle) and the electrons show a finite probability to be found outside, as the electron wave-function decays gradually. When the gap separating a plasmonic dimer reaches subnanometric distances, the electronic clouds of each individual nanoparticle can slightly overlap and electrons can tunnel through the gap during each half of the optical period in one and another direction. Therefore, tunnelling can occur at optical frequencies[21-23], enabling the formation of CTPs before physical contact. Quantum tunneling thus play a similar role as the conductive junctions shown in Fig. 5.

To illustrate how the gap distance between the nanoparticles affects the tunneling currents let us assume the simple Wentzel-Kramers-Brillouin (WKB) model[50,51] to describe the tunneling probability of an electronic wavefunction across a square potential barrier of fixed height ϕ_0. Within the WKB approximation the tunneling probability, T, follows an exponential decay with the width of the potential barrier (d_{gap}) i.e. $T(d_{\mathrm{gap}}) \propto \exp(-d_{\mathrm{gap}}/\delta)$, where δ is a decay length that depends on the barrier height and the energy of the wavefunction. Figure 7b shows the normalized tunneling probability as a function of gap distance for two semi-infinite gold planes. The exponential behaviour of $T(d_{\mathrm{gap}})$ with the gap separation implies that once the plasmonic dimer enters into the tunneling regime i.e. for a distance such that $d_{\mathrm{gap}}/\delta \sim 1$, the electron
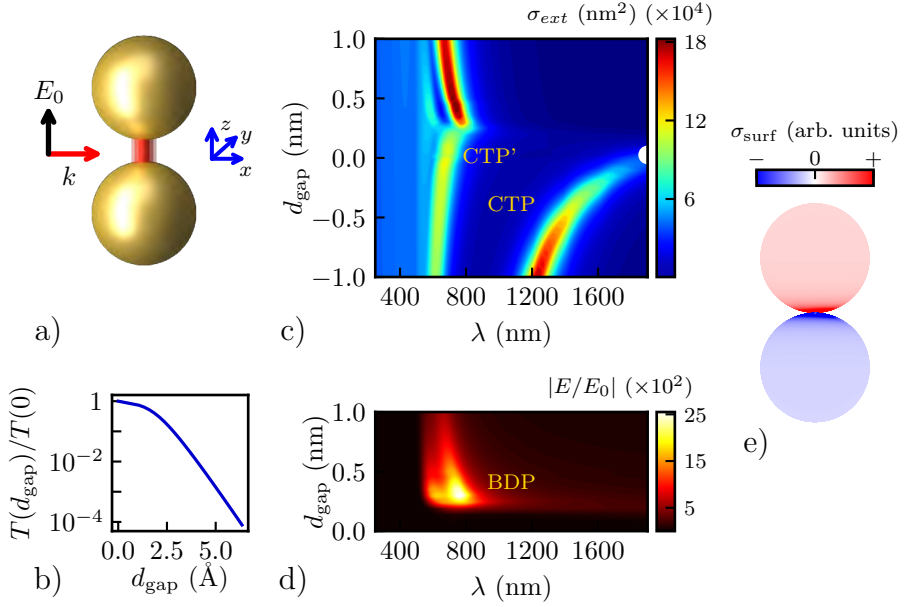
FIGURE 7: Optical response of a dimer when electron tunneling is considered. The dimer is formed by two gold spheres of diameter $D = 100$ nm separated by a gap d_{gap}. Once d_{gap} is reduced bellow 0.5 nm the Quantum Corrected Model (QCM) is used to describe electron tunneling. (a) Schematics of the dimer in the tunneling regime. The incident electromagnetic plane-wave is travelling along the x-axis and it is polarized along the dimer symmetry axis (z-axis). The red cylinder between the spheres corresponds to the effective material within the QCM. (b) Normalized tunneling probability, T, as a function of the separation distance for two gold semi-infinite planes. (c) Extinction cross-section σ_{ext} as a function of wavelength and gap distance d_{gap} of the dimer system. The white dot in (c) marks the point where the surface charge map in (e) has been calculated. (d) Near-field enhancement at the centre of the gap, $|E/E_0|$, as a function of wavelength and gap distance d_{gap}. (e) Orthogonal projection on the $x = 0$ plane of the surface charge distribution of the dipolar CTP for wavelength $\lambda = 1900$ nm and $d_{\text{gap}} = 0.025$ nm.

current is very sensitive to d_{gap} and grows rapidly as the gap is closed. For these ultra-narrow, positive, gap distances CTPs can be excited.

Figure 7 shows the evolution of the optical response of a dimer of gold spheres of diameter $D = 100$ nm as the gap is closed when the possibility of electron transfer is considered. We focus on ultra-narrow gaps -1 nm $\leq d_{\mathrm{gap}} \leq 1$ nm, where the coupling in the dimer changes from capacitive, $d_{\mathrm{gap}} \gtrsim 0.5$ nm (negligible charge transfer), to conductive, $d_{\mathrm{gap}} \lesssim 0.5$ nm (charge transfer plays a key role). For the latter, the electron transfer can originate from tunneling ($d_{\mathrm{gap}} > 0$ nm) or from the conductivity at the physical contact of the two nanoparticles ($d_{\mathrm{gap}} \leq 0$ nm). Tunneling can be included using the Quantum Corrected Model (QCM), according to which an effective conductive material (in red in Fig. 7a) is placed at the gap to effectively account for the tunneling conductivity (the QCM is explained in detail in Sec. 1.1).

The extinction cross-section as a function of the gap distance d_{gap} and wavelength λ is plotted in Fig. 7c. For $d_{\mathrm{gap}} \gtrsim 0.5$ nm we observe the same classical response as in Fig. 6b, with BPs redshifting as the gap closes. Once the gap distance is reduced to the distances where electrons can tunnel across the gap ($d_{\mathrm{gap}} \lesssim 0.4$ nm), the charges accumulated at the dimer's gap surfaces diminish (screening) and the BPs fade away for $d_{\mathrm{gap}} \sim 0.3$nm. The BDP peak at this distance is found at ~ 770 nm, giving a maximum redshift of $\lambda_{\mathrm{BDP}}(d_{\mathrm{gap}} = 0.3$ nm$) - \lambda_{\mathrm{BDP}}(d_{\mathrm{gap}} = 100$ nm$) \sim 250$ nm. As the distance is further reduced, the tunneling current becomes strong enough and CTPs emerge before physical contact. Notably, in contrast to classical calculations, the high-order CTP emerges around $d_{\mathrm{gap}} \approx 0.2$ nm and $\lambda \approx 720$ nm and the lowest-order CTP can be excited at $d_{\mathrm{gap}} \approx 0.025$ nm and $\lambda \approx 1900$ nm. We will describe in Ch. 2 how the lowest-order CTP can appear for larger d_{gap} for specific gap geometries. As the conduction across the gap becomes larger, similarly to the results shown in Fig. 5b and Fig. 6b, the CTPs blueshift, without discontinuity at $d_{\mathrm{gap}} = 0$ nm (in contrast to the results of the classical calculation in Fig. 6b).

Furthermore, Fig. 7d shows that electron tunneling also strongly affects the near-field enhancement at the gap. The decrease of the accumulation of surface charge density at opposite surfaces across the gap screens the near field, which decreases from a maximum value at the BDP wavelength of $|E/E_0| \approx 2550$ at $d_{\mathrm{gap}} = 0.3$ to $|E/E_0| \approx 74$ at $d_{\mathrm{gap}} = 0.15$ nm.

To demonstrate the transfer of charge *via* quantum tunneling for positive distances, Fig. 7e shows the surface charge density of the lowest-energy CTP for a separation of $d_{\mathrm{gap}} = 0.025$ nm and wavelength $\lambda = 1900$ nm. This mode displays a dipolar charge distribution with the top sphere charged positively and the bottom sphere negatively, in a similar manner as in the case of the linked dimer in Fig. 5b, where the nanoparticles were electrically connected.

The role of conductance in a metallic gap, particularly the role of tunneling, in the response of plasmonic systems with narrow gaps has been emphasized in this introduction. Typical plasmonic set-ups are designed to maximize the

near-field in the gap region, thus the quenching of $|E/E_0|$ due to tunneling (Fig. 7d) could be perceived as a major disadvantage. On the other hand, tunneling may be beneficial in many other applications. For example, the sensitivity of tunneling to the details of the potential barrier between particles may find applications for new sensing schemes. Furthermore, the dependence of the tunneling barrier on the application of an intense laser, an electrical bias, or a polarization field, introduces nonlinearities that can be advantageous in the design of novel optoelectronic devices.

The main objective of this thesis is to study how the properties of the tunneling gap influence the linear and nonlinear optical response of plasmonic nanocavities. After introducing in Ch. 1 the theoretical formalisms that are used throughout the thesis to perform the calculations, in Ch. 2 we investigate how the morphology of the gap can strongly influence the linear optical response of plasmonic gap antennas. In Ch. 3 we study the influence of tunneling in the linear plasmonic response of metamolecules that sustain a wide variety of non-conventional resonances as well as the effect of gap morphology in the tunability of linear chains of plasmonic nanoparticles as examples of more complex interacting plasmonic systems. Finally, in Ch. 4, we study the effect of tunneling in the nonlinear response of plasmonic gaps, relevant for situations of intense incident fields. The active control of the nonlinear response thanks to the application of DC polarizing fields is also analysed in this last chapter.

Chapter 1

Theoretical Methods

1.1 Semiclassical optical response in plasmonic gaps: the Quantum Corrected Model (QCM)

In principle, only fully quantum mechanical methods can wholly address the optical response of nanostructures by properly considering nonlocal effects and electron tunneling across subnanometric interparticle gaps. We consider one of the most extended quantum mechanical frameworks to tackle these effects, the Time-Dependent Density Functional Theory (TDDFT), in Sec. 1.2. However, as a result of the computational cost, full *ab-initio* methods are limited to small systems composed by a maximum of a few thousands of electrons. Typical sizes of experimental plasmonic nanostructures range from tens of nanometers to micrometers, thus being often much larger than the systems that can be treated *ab-initio*. Nonlocality has been addressed within some approximated models such as the hydrodynamic approach[17–20,52–54] that allows to tackle large plasmonic systems, but these types of models do not incorporate electron tunneling between particles that can completely alter the response. Therefore, it is desirable to develop a simple model that can incorporate the effect of tunneling in plasmonic systems.

The Quantum Corrected Model (QCM)[24,25,55] is a semiclassical model, developed by the Theory of Nanophotonics Group in San Sebastián in close collaboration with A.G. Borisov and D.C. Marinica from the Approches théoriques en dynamique quantique group at the Institut des Sciences Moléculaires d'Orsay, in which the effect of electron tunneling in the optical response is introduced by means of an effective conductive material placed in the subnanometric gap. This effective material is built using the tunneling conductivity obtained from full quantum mechanical calculations for a much simpler system. During the last few years, the QCM has proven its validity in both theoretical[25–27,56] and experimental studies[21–23], gaining broad acceptance in the plasmonic community. During this thesis, we implemented the QCM to describe the far-field and near-field optical response of cylindrically symmetric gap-antennas with faceted gaps (Ch. 2) and of trimer metamolecules (Sec. 3.1) to study how tunneling

affects the plasmonic response of different types of modes (magnetic, electric, dark and cavity modes)[23,56]. We describe the QCM in detail in the following.

1.1.1 QCM for Drude metals surrounded by vacuum

In this section we study how to incorporate electron tunneling *via* the QCM for a system composed by a dimer of metallic nanoparticles (plasmonic gap-antenna) surrounded by vacuum. A more general situation is described in Sec. 1.1.2. Figure 1.1 shows the situation under consideration. The plasmonic gap-antenna is composed by two metallic nanoparticles characterized by a relative dielectric permittivity ε_m and surrounded by vacuum (ε_0). When the minimum inter-particle gap separation (d_{gap}) is small enough to allow electron tunneling between the nanoparticles, the QCM prescribes the use of an effective material that must be placed between the particles to reproduce the effect of charge transfer across the gap. Furthermore, as the gap morphology is usually not perfectly flat, we divide the gap into several regions, describing each one by means of an effective material with a permittivity which depends on the mean separation l characterizing the separation in that particular region. The different effective materials described within the QCM are representatively shown in different tones of red and labelled ε_{gi} in Fig. 1.1b.

Metallic nanoparticles can be modelled by means of a dielectric permittivity. The value of the permittivity can be obtained from experimental work[35,57], from simple theoretical models such as the local Drude description of the dielectric permittivity[30,31] or more sophisticated nonlocal models[17–20]. The Drude model description in particular, which treats metals as a non-interacting free electron gas, describes reasonably well the main features of the plasmonic response in the infrared part of the spectrum.

Within the Drude model, the frequency-dependent permittivity of a metallic particle is given by

$$\varepsilon_m(\omega) = 1 - \frac{\omega_p^2}{\omega(\omega + i\gamma_p)} \ , \tag{1.1}$$

where ω_p is the plasma frequency of the metal and γ_p is the damping coefficient (intrinsic losses).

In order to build an effective material that accounts for tunneling in the gap we will use a Drude-like effective gap dielectric function ε_g that is gap-distance dependent. Previous work has shown that the tunneling gap has resistive character[25], corresponding to a permittivity that is approximately purely imaginary (the tunneling current and the oscillating field are in phase). Considering that the tunneling is resistive is an approximation and a more exact solution should consider a complex conductivity[27]. The dependence on the separation distance across the gap, l, is inserted *via* the damping coefficient
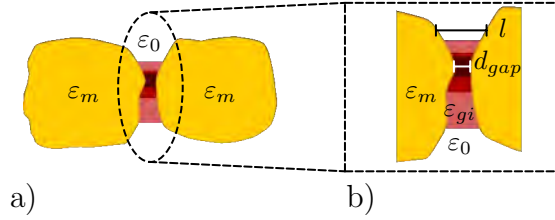
FIGURE 1.1: (a) Two plasmonic nanoparticles with permittivity ε_m embedded in vacuum (ε_0) are separated by a subnanometric gap where the effective material defined by the QCM is inserted (in red). (b) Zoom to the gap where due to the different local gap distances (l) several QCM effective materials (ε_{gi}) are used. The minimum local gap distance is labeled by d_{gap} and it defines the gap size.

$\gamma_g(l)$ of the Drude permitivity. Taking this into account we define:

$$\varepsilon_g(\omega, l) = 1 - \frac{\omega_p^2}{\omega(\omega + i\gamma_g(l))} \ , \tag{1.2}$$

where we use the same plasmon frequency (ω_p) as for the metal that composes the gap-antenna. $\gamma_g(l)$ must be much larger than ω_p for ε_g to be resistive.

In order to create an adequate permittivity function for the gap $\varepsilon_g(\omega, l)$, which depends on the gap separation l, three conditions have to be fulfilled:

- For zero gap distance ($l = 0$) the permittivity of the effective material must be equal to the permittivity of the metal: $\varepsilon_g(\omega, l = 0) = \varepsilon_m(\omega)$.

- For large separation distances ($l \to \infty$) the permittivity of the gap material must be equal to the one of the surrounding vacuum $\varepsilon_g \to 1$.

- $\varepsilon_g(\omega, l)$ has to correctly reproduce the charge transfer across the gap associated with the tunneling current.

The first two conditions are easily verified by imposing $\gamma_g(l) \to \gamma_p$ for $l \to 0$ and $\gamma_g(l) \to \infty$ for $l \to \infty$.

We thus focus next on the third condition to correctly describe the transfer of charge across the plasmonic gap due to tunneling. To do so, it is useful to consider the conductivity of the gap $\sigma_g(\omega, l)$ and its relationship with the permittivity $\varepsilon(\omega)$. According to Appendix A:

$$\varepsilon(\omega) = 1 + i\frac{\sigma(\omega)}{\varepsilon_0 \omega} \ . \tag{1.3}$$

In principle we could obtain directly $\sigma_g(\omega, l)$ from full quantum-mechanical calculations and directly apply Eq. (1.3) to obtain the permittivity of the gap, which would immediately verify the three aforementioned conditions. However, we use a computationally simpler approach. Using Eq. (1.2) and Eq. (1.3) we

can relate the distance-dependent damping coefficient of the effective material $\gamma_g(l)$ with the tunneling conductivity. We consider that the frequency dispersion of the tunneling conductivity is negligible and thus use the static tunneling conductivity $\sigma(\omega = 0, l) \rightarrow \sigma_0(l)$ obtaining

$$\gamma_g(l) = \frac{\varepsilon_0 \omega_p^2}{\sigma_0(l)} \ , \tag{1.4}$$

where the static conductivity $\sigma_0(l)$ can be calculated *ab-initio* for a much simpler gap system.

Furthermore, $\sigma_0(l)$ does not need to be known for all distances if we assume that it depends exponentially on l, based on the exponential dependence of the tunneling current with separation distance in static Scanning Tunneling Microscopy (static STM) measurements[51]. The damping coefficient then follows

$$\gamma_g(l) = \gamma_{g0} e^{l/l_c} \ , \tag{1.5}$$

where γ_{g0} and l_c are parameters that need to be fitted in order to reproduce correctly the electron tunneling. We fit l_c using Eq. (1.4) and imposing that for the distance l_0 such that the tunneling probability calculated *ab-initio* is one percent $(T(l_0) = 0.01)$, we obtain the same value of $\gamma_g(l_0)$ using both equations (Eq. (1.4) and Eq. (1.5)):

$$\frac{\varepsilon_0 \omega_p^2}{\sigma_0(l_0)} = \gamma_{g0} e^{l_0/l_c} \ . \tag{1.6}$$

The particular choice $T(l_0) = 0.01$ to obtain the l_c parameter is somewhat arbitrary, but changing the exact condition does not modify substantially the performance of the Quantum Corrected Model (QCM)[24]. The parameter γ_{g0} in Eq. (1.5) has to be set such that at $l = 0$ we recover Eq. (1.1) giving $\gamma_{g0} = \gamma_p$. We thus obtain the expression of the gap distance dependent damping $\gamma_g(l)$ as:

$$\gamma_g(l) = \gamma_p \exp\left\{ \ln\left(\frac{\varepsilon_0 \omega_p^2}{\gamma_p \sigma_0(l_0)} \right) \frac{l}{l_0} \right\} \ . \tag{1.7}$$

Finally, with the given choice of $\gamma_g(l)$ and inserting Eq. (1.7) into Eq. (1.2), we can check that $\varepsilon_g(\omega, l) \rightarrow 1$ when $l \rightarrow \infty$. Furthermore, $\gamma_g >> \omega_p$ except for very small gap separation distances, so that, as desired, the effective material in the gap is resistive except for very short separations.

1.1.2   Generalized QCM

The model assumed above is a good approximation for metals embedded in vacuum and with illumination in the infrared. However, this model does not provide a full description of many important situations in plasmonics. For example, this model is not able to capture the effects of the interband transitions
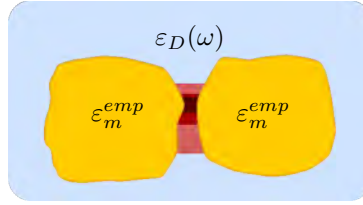
FIGURE 1.2: Two plasmonic nanoparticles with empirical permittivity ε_m^{emp} are embedded in a dielectric material with permittivity $\varepsilon_D(\omega)$ (in blue) and separated by a subnanometric gap where the effective material layers are located (in red).

in gold. Because of this, experimental values of the permittivity of metals are often used in calculations in order to reproduce the data obtained in experiments. Furthermore, many plasmonic systems with narrow gaps are not fully surrounded by vacuum, as assumed previously, but are embedded in a dielectric medium (Fig. 1.2), or a dielectric layer is placed in the gap between the nanoparticles acting as a spacer to avoid physical contact. Thus, to study more practical situations, we extend the model of the effective material to be able to include a dielectric spacer in the gap and to use experimental data for the permittivity of metals.

The permittivity of metals extracted from empirical data ε_m^{emp} can be decomposed into a contribution of a Drude-like term $\varepsilon_m^{Drude}(\omega)$ and a correction $\varepsilon_m^d(\omega)$

$$\varepsilon_m^{emp}(\omega) = \varepsilon_m^d(\omega) + \varepsilon_m^{Drude}(\omega) - 1 = \varepsilon_m^d(\omega) - \frac{\omega_p^2}{\omega(\omega + i\gamma_p)} \ , \qquad (1.8)$$

where the values of the Drude parameters ω_p and γ_p can be obtained by fitting the long wavelength part of ε_m^{emp} to a Drude function. $\epsilon_m^d(\omega)$ can then be obtained from the empirical data as $\epsilon_m^d(\omega) = \epsilon_m^{emp}(\omega) - (\epsilon_m^{Drude} - 1)$, and mostly represents the contribution from core d-electrons in the metal that participate in inter-band transitions.

To generalize the QCM we build a permittivity of the form

$$\epsilon_g(\omega, l) = \epsilon_D(\omega) + (\epsilon_m^d(\omega) - \epsilon_D(\omega))e^{-l/l_d} - \frac{\omega_p^2}{\omega(\omega + i\gamma_g(l))} \ , \qquad (1.9)$$

where ε_D is the permittivity of the dielectric filling the gap and l_d is a decay length associated with the contribution of the d-electrons to the tunneling. As a value of l_d we choose the radial decay of the 5-d orbital for gold ($l_d = 1.5 \ a.u. = 0.8$ Å)[25], as an appropriate length parameter associated with the orbitals of core electrons of the material that we are modelling, but other conventions are possible. $\gamma_g(l)$ is calculated as in the previous section, but

taking into account the presence of the dielectric in the calculation of $\sigma_0(l)$ and applying the modified boundary conditions:

- For zero gap distance ($l = 0$) the permittivity of the effective material must be equal to the empirical permittivity of the metal: $\epsilon_g(\omega, 0) = \epsilon_m^{emp}(\omega)$.

- For large separation distances ($l \to \infty$) the permittivity of the gap material must be equal to the permittivity of the medium filling the gap, $\varepsilon_g(\omega, l) \to \varepsilon_D(\omega)$.

1.1.3   QCM recipe

We have described in Sec. 1.1.1 and Sec. 1.1.2 how to build the effective material in a gap required by the Quantum Corrected Model (QCM) to mimic the effects of tunneling in plasmonic nanoparticles separated by subnanometric distances. We resume now all the necessary steps in order to provide an easy-to-follow guide.

1. Obtain $\sigma_0(l_0)$
   The distance-dependent static conductivity associated to the tunneling process is calculated at a distance l_0 using quantum mechanical methods for a simple gap system. l_0 is the gap distance such that $T(l_0) = 0.01$.

2. Obtain $\gamma_g(l_0)$

$$\gamma_g(l_0) = \frac{\varepsilon_0 \omega_p^2}{\sigma_0(l_0)} \ . \tag{1.10}$$

3. Obtain l_c
   Calculate the parameter l_c in Eq. (1.5) according to

$$l_c = l_0 \left(\ln \frac{\gamma_g(l_0)}{\gamma_p} \right)^{-1} \ . \tag{1.11}$$

After this step, combining Eq. (1.10) and Eq. (1.11) into Eq. (1.7), the description of the key $\gamma_g(l)$ parameter is known for all distances.

We also notice that if a sufficiently accurate value of $\sigma_0(l)$ is known from quantum mechanical calculations for all desired gap distances, it is also possible to build $\gamma_g(l)$ directly from Eq. (1.4).

4. Obtaining the d-electron contribution
   If we are using experimental values of the permittivity to model the metal we need to calculate $\epsilon_m^d(\omega)$:

$$\epsilon_m^d(\omega) = \epsilon_m^{emp}(\omega) - (\epsilon_m^{Drude} - 1) = \epsilon_m^{emp}(\omega) + \frac{\omega_p^2}{\omega(\omega + i\gamma_p)} \ . \qquad (1.12)$$

   If we use a pure Drude model then $\epsilon_m^d(\omega) = 1$

5. Creating the QCM effective material
   Given a surrounding/gap material with permittivity $\epsilon_D(\omega)$, the dielectric constant of the effective material is given by

$$\epsilon_g(\omega, l) = \epsilon_D(\omega) + (\epsilon_m^d(\omega) - \epsilon_D(\omega))e^{-l/l_d} - \frac{\omega_p^2}{\omega(\omega + i\gamma_g(l))} \ . \qquad (1.13)$$

1.2 Optical response within Time-Dependent Density Functional Theory

We explain in this section the details of the Time-Dependent Density Functional Theory (TDDFT) that we implement in our calculations of the nonlinear optical response of aluminium spherical nanoparticles and dimers in Ch. 4. Our objective is to introduce the main aspects of the computational method, without attempting to review the fundamental theory behind the TDDFT which is based on the Runge-Gross Theorem[58] and can be found elsewhere[59–63]. The interested reader can also find in Refs.[15, 16, 29, 64–69] examples of how some of the computational techniques discussed below can be applied to different systems. In this section all the formulas are displayed in atomic units (a.u.).

The dynamics of the space ($\mathbf{r}$) and time (t) dependent electron density $n(\mathbf{r}, t)$ of a metallic nanoparticle in response to an external perturbation can be calculated within the TDDFT framework[59]. In the Kohn-Sham (KS) scheme of TDDFT the time-dependent electron density of the many body system, $n(\mathbf{r}, t)$, is represented *via* the density of a fictitious system of non-interacting electrons represented by the KS orbitals $\Psi_j(\mathbf{r}, t)$.

$$n(\mathbf{r}, t) = \sum_{j \in occ} |\Psi_j(\mathbf{r}, t)|^2 \ , \qquad (1.14)$$

with the summation running over all the occupied KS orbitals.

The time evolution of each KS orbital in response to an external perturbation is governed by the Time-Dependent Kohn-Sham Equation (TDKSE), which is analogous to the Time-Dependent Schrödinger Equation (TDSE) for

a single electron:

$$i\frac{\partial \Psi_j(\mathbf{r},t)}{\partial t} = \{T + \underbrace{V[n](\mathbf{r},t) + V_{\text{ext}}(\mathbf{r},t) + V_{\text{abs}}(\mathbf{r})}_{V_{\text{T}}[n](\mathbf{r},t)}\} \, \Psi_j(\mathbf{r},t) \; , \qquad (1.15)$$

where $T = -\frac{1}{2}\vec{\nabla}^2$ is the kinetic energy operator, and $V_{\text{T}}[n](\mathbf{r},t)$ is the time-dependent total potential acting on the KS orbital. The total potential is given by the sum of the effective KS potential $V[n](\mathbf{r},t)$, the external time-dependent perturbation $V_{\text{ext}}(\mathbf{r},t)$, and an absorbing potential $V_{\text{abs}}(\mathbf{r})$ that can be included at the boundaries of the calculation box to avoid unphysical reflections and thus facilitate convergence. We give further details of these potentials below in this section.

Provided initial conditions $\Psi_j(\mathbf{r}, t = 0) \equiv \Psi_j^0(\mathbf{r})$, where $\Psi_j^0(\mathbf{r})$ correspond to the KS orbitals of the ground state of the system, Eq. (1.15) is numerically solved by real time propagation. Thus, prior to any TDDFT calculation we first use the standard iterative procedure within Density Functional Theory (DFT) to find the ground state KS orbitals and density $n_{\text{grnd}}(\mathbf{r})$ of the nanoobject. A practical example of the DFT approach to calculate the ground state of aluminium spheres is described in Appendix B.

The total potential $V_{\text{T}}[n](\mathbf{r},t) = V[n](\mathbf{r},t) + V_{\text{ext}}(\mathbf{r},t) + V_{\text{abs}}(\mathbf{r})$ in the TDKSE (Eq. (1.15)) is time-dependent through the explicit contribution of the external potential acting on the system ($V_{\text{ext}}(\mathbf{r},t)$) and because the effective one-electron KS potential, $V[n](\mathbf{r},t)$, is determined by the time-dependent electron density, $n(\mathbf{r},t)$. The effective KS potential is given by the sum of several contributions:

$$V[n](\mathbf{r},t) = V_{\text{H}}[n](\mathbf{r},t) + V_{\text{xc}}[n](\mathbf{r},t) + V_{\text{st}}(\mathbf{r}) \; . \qquad (1.16)$$

The Hartree potential $V_{\text{H}}[n](\mathbf{r},t)$ accounts for the Coulomb interaction of the KS electron with the rest of electrons in the system and with the positive ion cores. It can be calculated solving Poisson's equation for the electron:

$$\nabla^2 V_{\text{H}}[n](\mathbf{r},t) = +4\pi\big(n_+(\mathbf{r}) - n(\mathbf{r},t)\big) \; , \qquad (1.17)$$

where $n_+(\mathbf{r})$ is the charge density representing the positive ionic cores of the material. We choose the free-electron Jellium Model (JM) approach to represent $n_+(\mathbf{r})$ where the ionic cores are modelled as an homogeneous positive charge density[70–72]. More details on the JM implementation in our simulations are given in Sec. 4.1.

The exchange-correlation potential $V_{xc}[n](\mathbf{r}, t)$ represents the quantum electron-electron correlations in the system and we describe it within the Adiabatic Local Density Approximation (ALDA)[59,61] using the kernel of O. Gunnarsson and B. I. Lundqvist[73]

$$V_{xc}[n](\mathbf{r}, t) = -\frac{1}{2} \left(\frac{1.222}{r_s(\mathbf{r}, t)} + 0.0666 \ \ln \left(1 + \frac{11.4}{r_s(\mathbf{r}, t)} \right) \right) \ , \tag{1.18}$$

where r_s is given by

$$r_s(\mathbf{r}, t) = \left(\frac{3}{4\pi n(\mathbf{r}, t)} \right)^{1/3} \ . \tag{1.19}$$

Finally, within the so-called Stabilized Jellium Model[71], an attractive constant potential $V_{st}(\mathbf{r})$, is added inside the metal to adjust the work function of the nanoparticle to the values reported in the literature.

The explicitly time-dependent external potential $V_{ext}(\mathbf{r}, t)$ is associated with the external perturbation driving the system. From now on we consider an external potential acting on the KS electrons that only depends on the z spatial coordinate and on time t, $V_{ext}(\mathbf{r}, t) = V_{ext}(z, t)$, which corresponds to the excitation considered in the TDDFT simulations discussed in this thesis (Ch. 4).

In order to preserve the total energy of the system, the propagation method has to satisfy the time-reversal symmetry. To accomplish this objective, the time propagation of the KS orbitals is inspired on the techniques employed for the solution of the single-particle TDSE in time-dependent potentials, which can be expressed as $\Psi_j(\mathbf{r}, t) \xrightarrow{V_T[n](\mathbf{r}, t+\Delta t/2)} \Psi_j(\mathbf{r}, t+\Delta t)$. Thus, the wave function is propagated from t to $t + \Delta t$ using an intermediate time point $t + \Delta t/2$. However, while $V_{ext}(\mathbf{r}, t)$ in Eq. (1.15) can be known *a priori* at any time, the effective one-electron KS potential $V[n](\mathbf{r}, t + \Delta t/2)$ (Eq. (1.16)) requires the electron density to be computed at the intermediate time-step and thus it is not known. We use a procedure that preserves the time-reversal symmetry by calculating $V_T[n](\mathbf{r}, t + \Delta t/2)$ in an iterative manner. We define the intermediate total potential estimate of order s, $\mathcal{V}_T^{(s)}[n](\mathbf{r}, t + \Delta t/2)$, as

$$V_T[n](\mathbf{r}, t + \Delta t/2) \longrightarrow \mathcal{V}_T^{(s)}[n](\mathbf{r}, t + \Delta t/2) =$$
$$\mathcal{V}^{(s)}[n](\mathbf{r}, t + \frac{\Delta t}{2}) + V_{ext}(\mathbf{r}, t + \Delta t/2) + V_{abs}(\mathbf{r}) \ , \tag{1.20}$$

where $\mathcal{V}^{(s)}[n](\mathbf{r}, t + \Delta t/2)$ is the estimated KS effective potential of order s at time $t + \Delta t/2$ and it is defined as:

$$\mathcal{V}^{(s)}[n](\mathbf{r}, t + \frac{\Delta t}{2}) = V[n](\mathbf{r}, t) \quad \text{for} \quad s = 1 \ , \tag{1.21a}$$

$$\mathcal{V}^{(s)}[n](\mathbf{r}, t + \frac{\Delta t}{2}) = \frac{V[n](\mathbf{r}, t) + V^{(s-1)}[n](\mathbf{r}, t + \Delta t)}{2} \quad \text{for} \quad s > 1 \ . \tag{1.21b}$$

TDDFT Algorithm

$$\mathcal{V}_{\mathrm{T}}^{(s)}[n](\mathbf{r}, t + \tfrac{\Delta t}{2}) = \mathcal{V}^{(s)}[n](\mathbf{r}, t + \tfrac{\Delta t}{2})$$
$$+ V_{\mathrm{ext}}(\mathbf{r}, t + \tfrac{\Delta t}{2}) + V_{\mathrm{abs}}(\mathbf{r})$$

$\Psi_j(\mathbf{r}, t)$

$n(\mathbf{r}, t)$ $\xrightarrow{\quad s = 1 \quad}$

$V[n](\mathbf{r}, t)$

$$\begin{cases} \text{if } s = 1 : \mathcal{V}^{(s)}[n](\mathbf{r}, t + \tfrac{\Delta t}{2}) = V[n](\mathbf{r}, t) \\[2mm] \text{if } s > 1 : \mathcal{V}^{(s)}[n](\mathbf{r}, t + \tfrac{\Delta t}{2}) = \\[2mm] \qquad\qquad \frac{V[n](\mathbf{r},t) + V^{(s-1)}[n](\mathbf{r}, t + \Delta t)}{2} \end{cases}$$

$t = t + \Delta t$

Calculate $s = s + 1$

$\mathbf{p}(t + \Delta t)$

$\mathbf{j}(\mathbf{r}, t + \Delta t)$

...

if $s < s_{\mathrm{max}}$

if $s = s_{\mathrm{max}}$

$$i\frac{\partial \Psi_j(\mathbf{r}, t)}{\partial t} =$$
$$\left\{ T + \mathcal{V}_{\mathrm{T}}^{(s)}[n](\mathbf{r}, t + \frac{\Delta t}{2}) \right\} \Psi_j(\mathbf{r}, t)$$

Use WPP to propagate

$\Psi_j^{(s)}(\mathbf{r}, t + \Delta t)$

$n^{(s)}(\mathbf{r}, t + \Delta t)$ $\longleftarrow$ each KS orbital

$V^{(s)}[n](\mathbf{r}, t + \Delta t)$ $\Psi_j^{(s)}(\mathbf{r}, t + \Delta t) = \hat{U}(t, \Delta t)\Psi_j(\mathbf{r}, t)$
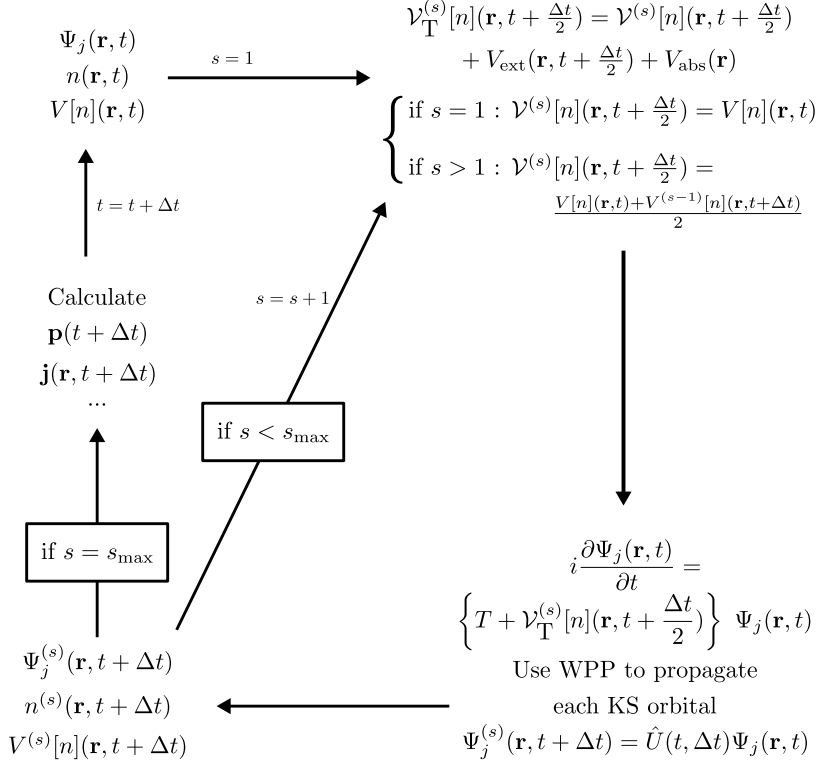
FIGURE 1.3: Scheme of the TDDFT algorithm used in the calculations. We initially consider (top-left) the KS orbitals, electron density and KS potential from which the order s approximated total potential $\mathcal{V}_{\mathrm{T}}^{(s)}[n](\mathbf{r}, t + \Delta t/2)$ is calculated (top-right). Next, the TDKSE is solved using the Wave Packet Propagation (WPP) method to propagate the KS orbitals $\Psi_j(\mathbf{r}, t)$ one time-step Δt (bottom-right). With these propagated orbitals ($\Psi_j^{(s)}(\mathbf{r}, t + \Delta t)$), the new $n^{(s)}(\mathbf{r}, t + \Delta t)$ at time $t + \Delta t$ is obtained (bottom-left). The iterative procedure on s to obtain $\mathcal{V}^{s+1}$ is continued (diagonal arrow) until the maximum number of iterations is reached. At this point the s_{max} order orbitals are taken as the propagated wavefunctions ($\Psi_j(\mathbf{r}, t + \Delta t) = \Psi_j^{(s_{\mathrm{max}})}(\mathbf{r}, t + \Delta t)$) which allows to obtain the different physical quantities of interest such as the induced dipole moment $\mathbf{p}(t + \Delta t)$ and the electronic current $\mathbf{j}(t + \Delta t)$ (centre-left). Finally, the new KS orbitals are set as the initial state of the next time step.

and $V^{(s-1)}[n](\mathbf{r}, t + \Delta t)$ is the iterative approximation of the KS potential at $t + \Delta t$ obtained from the estimate of the propagated density $n^{(s-1)}(\mathbf{r}, t + \Delta t)$, which is calculated from $\mathcal{V}^{(s-1)}(\mathbf{r}, t + \Delta t/2)$ by solving Eq. (1.15), in the iteration $s - 1$.

Figure 1.3 shows the basic scheme of the TDDFT algorithm used to obtain the time evolution of the electron density $n(\mathbf{r}, t)$. At time step t (top-left corner) we consider a set of KS orbitals, $\Psi_j(\mathbf{r}, t)$ that describe the electronic density $n(\mathbf{r}, t)$ according to Eq. (1.14), and the corresponding effective KS potential $V[n](\mathbf{r}, t)$ (Eqs. (1.16)-(1.18)). Each KS orbital is propagated from t to $t + \Delta t$ with the Wave Packet Propagation (WPP) algorithm as follows (see Sec. 1.2.2 and Sec. 1.2.3 for details):

$$\Psi_j(\mathbf{r}, t + \Delta t) = \hat{U}(t, \Delta t)\Psi_j(\mathbf{r}, t) \ , \tag{1.22}$$

which corresponds to the propagation of Eq. (1.15). The propagator $\hat{U}(t, \Delta t)$ is given by

$$\hat{U}(t, \Delta t) = e^{-i\Delta t\left(T + \mathcal{V}_{\mathrm{T}}^{(s)}[n](\mathbf{r}, t + \Delta t/2)\right)} \ , \tag{1.23}$$

and the iterative estimate of order s of the total potential at the intermediate time-step, $\mathcal{V}_{\mathrm{T}}^{(s)}[n](\mathbf{r}, t + \Delta t/2)$, is defined in Eq. (1.20) and Eq. (1.21).

Focusing on the first iteration ($s = 1$), we start using the KS potential at time t, $V[n](\mathbf{r}, t)$ (as defined in Eq. (1.21a)), to build the total approximated potential in Eq. (1.20) (top-right corner) and we then propagate each KS orbital according to Eq. (1.22) and Eq. (1.23) (bottom-right corner). We thus obtain the prediction for the KS orbitals $\Psi_j^{(1)}(\mathbf{r}, t + \Delta t)$ which allows us to calculate an iterative estimate of order 1 of the electron density and all density-dependent potentials at $t + \Delta t$ (bottom-left corner). To further refine the approximation of the estimated potential at $t + \Delta t/2$, we continue the iterative process by updating $s = s + 1$ (diagonal arrow) and thus, the estimate of the total potential at the intermediate time point $\mathcal{V}_{\mathrm{T}}^{(s)}[n](\mathbf{r}, t + \Delta t/2)$ is now obtained from Eq. (1.20) and Eq. (1.21b) (top-right corner). The propagation time step is repeated using Eq. (1.22) and Eq. (1.23) with $\mathcal{V}_{\mathrm{T}}^{(s)}[n](\mathbf{r}, t + \Delta t/2)$ to obtain an iterative estimate of order s for the KS orbitals, electron density and potentials at $t + \Delta t$ (bottom-left corner). This iterative procedure is continued until the maximum number of iterations is reached $s = s_{\max}$. Then, we admit the solutions $\Psi_j(\mathbf{r}, t + \Delta t) = \Psi_j^{(s_{\max})}(\mathbf{r}, t + \Delta t)$, calculate all relevant physical quantities such as the dipole moment or the electronic density currents (centre-left panel), update the time $t \to t + \Delta t$ and continue the time propagation starting from the top-left corner again. We found that $s_{\max} = 4$ iteration steps are sufficient to reach convergence.

The electronic density $n(\mathbf{r}, t_i)$ is thus retrieved at the discrete time points $t_i = t_0 + (i-1)\Delta t$. We discuss in more detail in the next section how to obtain all magnitudes of interest from the electronic density $n(\mathbf{r}, t)$ and KS orbitals $\Psi_j(\mathbf{r}, t)$.

1.2.1   Retrieval of the optical response from the Wave Packet Propagation (WPP)

As sketched in Fig. 1.3, at each time step several physical quantities can be retrieved to express the dynamics of the electronic density $n(\mathbf{r}, t)$. The time-dependent dipole moment induced by the excitation is given by:

$$\mathbf{p}(t) = - \int_{\mathrm{V}} n(\mathbf{r}, t) \, \mathbf{r} d^3 \mathbf{r} \, , \tag{1.24}$$

The "-" sign in Eq. (1.24) stems from the "-1" electron charge in atomic units.

Similarly, the induced current density $\mathbf{j}(\mathbf{r}, t)$ is obtained from:

$$\mathbf{j}(\mathbf{r}, t) = - \sum_{j \in occ} \left(\frac{1}{2} \left[\Psi_j^*(\mathbf{r}, t) \hat{\mathbf{p}} \Psi_j(\mathbf{r}, t) - \Psi_j(\mathbf{r}, t) \hat{\mathbf{p}} \Psi_j^*(\mathbf{r}, t) \right] + \right.$$
$$\left. \mathbf{A}(\mathbf{r}, t) \Psi_j^*(\mathbf{r}, t) \Psi_j(\mathbf{r}, t) \right) \, . \tag{1.25}$$

where $\hat{\mathbf{p}} = -i \vec{\nabla}$ is the momentum operator and $\mathbf{A}(\mathbf{r}, t)$ is the vector potential of the external electromagnetic field driving the system.

Along with the time-dependent quantities $X(t)$, frequency resolved results are used throughout Ch. 4 for quantitative and qualitative analysis. The frequency-resolved induced densities, multipole moments, currents, potentials, fields etc. are obtained applying the time-to-frequency Fourier transform to the corresponding time-dependent TDDFT data

$$X(\omega) = \frac{1}{\sqrt{2\pi}} \int_0^{t_{\max}} e^{-i\omega t} e^{-\eta t} X(t) \, dt, \tag{1.26}$$

where $t_{\max}$ is a finite but large enough propagation time, and η is an artificial damping (typically of the order of some tens of meV) introduced to account for various decay mechanisms not described with TDDFT.

Next, we explain the Wave Packet Propagation (WPP) algorithm used to propagate the KS orbitals (bottom-right in Fig. 1.3), which is at the core of the TDDFT calculations. The WPP algorithm is based on pseudo-spectral methods[74–78] (specifically we use the Fourier-Grid Hamiltonian (FGH) method[76,79–81]) where the KS-orbitals are represented on a discretized grid, and short time-step propagation schemes (Split-Operator (SO)[74,75,80] and the Crank-Nicolson[82] techniques) are employed to propagate the wavefunctions in time. We discuss the WPP for spherically (Sec. 1.2.2) and cylindrically (Sec. 1.2.3) symmetrical systems.

1.2.2 WPP algorithm in spherical coordinates

When the physical system under study is a sphere (or otherwise a spherically symmetric object), the natural choice is to use a computational mesh in spherical coordinates $\mathbf{r} = \{r, \theta, \phi\}$. This allows to take advantage of the rotational symmetry of the system and to significantly reduce the computational effort. Here, it is important to consider that the external potential may not be rotationally symmetrical itself.

In particular, in the study of Electric Field-Induced Even-Harmonic Generation (EFIEHG) in Ch. 4.4 we use an external perturbation consisting in a time-varying but spatially-constant electric field polarized along the z direction. The external potential in such a case is thus of the form $V_{\text{ext}}(r, \theta) \propto r \cdot \cos \theta$, which is azimuthally symmetric. Under those conditions, it is convenient to define the KS orbitals as:

$$\Psi_{j,m}(r, \theta, \phi, t) = \frac{1}{r} \psi_{j,m}(r, \theta, t) e^{im\phi} \ , \tag{1.27}$$

where m is the magnetic quantum number. Due to the azimuthal symmetry, m is a good quantum number that is preserved during the time-propagation. Using the definition given by Eq. (1.27), the electron density, Eq. (1.14), can be expressed as:

$$n(r, \theta, t) = \sum_{\{j, m \geq 0\} \in occ} X_m \frac{|\psi_{j,m}(r, \theta, t)|^2}{r^2} \tag{1.28}$$

where the factor X_m takes into account both the spin and the $\pm m$ degeneracy of the KS orbital ($X_m = 2$ for $m = 0$ and $X_m = 4$ for $m \neq 0$) and the summation runs over all the occupied orbitals $\{j, m \geq 0\}$. The time evolution of the $\psi_{j,m}$ and $\psi_{j,-m}$ orbitals is identical, as can be seen from the equations below.

The KS orbitals $\psi_{j,m}(r, \theta, t)$ in Eq. (1.27) are propagated according to the TDKSE (Eq. (1.15)):

$$i \frac{\partial \psi_{j,m}(r, \theta, t)}{\partial t} = \Big\{ T^m + \mathcal{V}^{(s)}[n](r, \theta, t) +$$
$$V_{\text{ext}}(r, \theta, t) + V_{\text{abs}}(r, \theta) \Big\} \ \psi_{j,m}(r, \theta, t) \tag{1.29}$$

where the different potentials were discussed previously and the kinetic energy operator T^m in spherical coordinates takes the form:

$$T^m = -\frac{1}{2} \frac{\partial^2}{\partial r^2} - \frac{1}{2r^2 \sin \theta} \frac{\partial}{\partial \theta} \left(\sin \theta \frac{\partial}{\partial \theta} \right) + \frac{m^2}{2r^2 \sin^2 \theta} \ . \tag{1.30}$$

Notably, T^m is nonlocal in the direct-space representation due to the derivative terms, which requires special treatment in the design of the time propagation scheme.

The time step propagation procedure $\psi_{j,m}(r,\theta,t) \to \psi_{j,m}(r,\theta,t+\Delta t)$ within the iterative scheme described in Fig. 1.3 requires the computation of the action of the time-evolution operator

$$
\begin{aligned}
\psi_{j,m}(r,\theta,t+\Delta t) &= \hat{U}(t,\Delta t)\psi_{j,m}(r,\theta,t) \\
&= e^{-i\Delta t(T^m + \mathcal{V}_{\mathrm{T}}[n](\mathbf{r},t+\Delta t/2))}\psi_{j,m}(r,\theta,t) \ ,
\end{aligned}
\tag{1.31}
$$

where $\mathcal{V}_{\mathrm{T}}[n](\mathbf{r},t+\Delta t/2)$ is defined by Eq. (1.20)-Eq. (1.21b) (in the following we remove the (s) superscript on the approximated total potential to ease the notation). Using the Split-Operator (SO) technique, the time propagation step can be approximated by:

$$
\begin{aligned}
\psi_{j,m}(r,\theta,t+\Delta t) &= e^{-i\frac{\Delta t}{2}\mathcal{V}_{\mathrm{T}}[n](\mathbf{r},t+\Delta t/2)}e^{-i\Delta t T^m} \times \\
& \quad e^{-i\frac{\Delta t}{2}\mathcal{V}_{\mathrm{T}}[n](\mathbf{r},t+\Delta t/2)}\psi_{j,m}(r,\theta,t) + O\big((\Delta t)^3\big) \ .
\end{aligned}
\tag{1.32}
$$

Thus, propagating each KS orbital one time step involves the computation of the action of the three exponential operators on the wavefunction. Within the present scheme of the TDDFT, the total potential is a local function of the spatial coordinates. Thus, for a wave function $\psi_{j,m}(r,\theta,t)$ represented on a mesh of points in the direct space, the action of the operator $e^{-i\frac{\Delta t}{2}\mathcal{V}_{\mathrm{T}}[n](\mathbf{r},t+\Delta t/2)}$ can be directly computed at each (r,θ) grid point. Applying the nonlocal $e^{-i\Delta t T^m}$ operator is thus the most involved step when evaluating Eq. (1.32).

To tackle the action of the nonlocal kinetic energy operator $e^{-i\Delta t T^m}$, we start by considering a general wave function $\Phi_m(r,\theta)$ in spherical coordinates. We are interested in finding $\Phi'_m(r,\theta)$ such that:

$$
\Phi'_m(r,\theta) = e^{-i\Delta t T^m}\Phi_m(r,\theta) \ .
\tag{1.33}
$$

To this end it is convenient to project $\Phi_m(r,\theta)$ on the finite basis of spherical harmonics $\mathrm{Y}_\ell^m(\theta,\phi)$ resulting in r-dependent coefficients

$$
F_{\ell,m}(r) = \langle \mathrm{Y}_\ell^m(\theta,\phi)|\Phi_m(r,\theta)e^{im\phi}\rangle, \quad m \le \ell \le L_{\max} \ .
\tag{1.34}
$$

The brackets indicate integration in $\{\theta,\phi\}$. The integration in θ is performed numerically using Gauss-Legendre quadratures[83] which implies a discrete representation of the wave function $\Phi_m(r,\theta)$ on a mesh of points in the angular θ coordinate. The set of θ_i, $(i = 1,2,...,n)$ points, abscissas of the Gauss-Legendre quadratures, is set such that the integration involving the largest order $(L_{\max})$ spherical harmonic is converged, i.e. $\langle \mathrm{Y}_{L_{\max}}^m(\theta_i,\phi)|\mathrm{Y}_\ell^m(\theta_i,\phi)\rangle = \delta_{L_{\max},\ell}$ with the desired precision. We ensure this by choosing[83] the θ_i grid points that correspond to the zeros of the $P_n(\cos(\theta))$ Legendre polynomial of the order $n = 2L_{\max} + 20$.

We can then obtain back $\Phi_m(r,\theta_i)e^{im\phi}$ from $F_{\ell,m}(r)$ according to

$$\Phi_m(r,\theta_i)e^{im\phi} = \sum_{\ell=m}^{L_{\max}} Y_\ell^m(\theta_i,\phi)F_{\ell,m}(r) \ . \qquad (1.35)$$

at each θ_i grid point. Note that, in difference to e.g. Fourier grid techniques[76,79], the transformation between the two representations $\Phi_m(r,\theta_i)$ and $F_{\ell,m}(r)$ is not unitary. However, owing to the exponential convergence of the finite basis representation with $L_{\max}$ and the exponential convergence of the Gauss-Legendre quadratures with the number of grid points, θ_i, $(i = 1,2,...,n)$, the propagation scheme involving the use of Eq. (1.34) and Eq. (1.35) is stable and the number of electrons (norm of the KS orbitals) is preserved with high precision.

Assuming a continuous variable θ and substituting $\Phi_m(r,\theta)e^{im\phi}$ given by Eq. (1.35) into Eq. (1.33) we obtain:

$$\begin{aligned}\Phi_m'(r,\theta)e^{im\phi} &= e^{-i\Delta t T^m}\sum_{\ell=m}^{L_{\max}} Y_\ell^m(\theta,\phi)F_{\ell,m}(r)\\ &= \sum_{\ell=m}^{L_{\max}} Y_\ell^m(\theta,\phi)e^{-i\Delta t T^{\ell,m}}F_{\ell,m}(r) \ ,\end{aligned} \qquad (1.36)$$

so that the pseudospectral solution on the discrete θ_i mesh is given by

$$\Phi_m'(r,\theta_i)e^{im\phi} = \sum_{\ell=m}^{L_{\max}} Y_\ell^m(\theta_i,\phi)e^{-i\Delta t T^{\ell,m}}F_{\ell,m}(r) \ , \qquad (1.37)$$

where

$$T^{\ell,m} = \left[-\frac{1}{2}\frac{\partial^2}{\partial r^2} + \frac{\ell(\ell+1)}{2r^2}\right] \ . \qquad (1.38)$$

In deriving Eq. (1.36), Eq. (1.37), and Eq. (1.38) we used the fact that the spherical harmonics are eigenfunctions of the squared momentum operator $\hat{L}^2 = -\frac{1}{\sin\theta}\frac{\partial}{\partial\theta}\left(\sin\theta\frac{\partial}{\partial\theta}\right) + \frac{m^2}{\sin^2\theta}$ with eigenvalues $\ell(\ell+1)$.

We are now left with the calculation of the terms involving derivatives in the radial coordinate. The SO technique is applied in this case too:

$$e^{-i\Delta t T^{\ell,m}}F_{\ell,m}(r) = e^{-i\frac{\Delta t}{2}\frac{\ell(\ell+1)}{2r^2}}e^{i\Delta t\frac{1}{2}\frac{\partial^2}{\partial r^2}}e^{-i\frac{\Delta t}{2}\frac{\ell(\ell+1)}{2r^2}}F_{\ell,m}(r) + O\big((\Delta t)^3\big) \ . \quad (1.39)$$

As we use the discrete representation of $F_{\ell,m}(r)$ on a mesh of equidistant points in the r-coordinate, the action of the exponential of the centrifugal potential $e^{-i\frac{\Delta t}{2}\frac{\ell(\ell+1)}{2r^2}}$ is local in each grid point. The action of the nonlocal operator $e^{i\Delta t\frac{1}{2}\frac{\partial^2}{\partial r^2}}$ is computed using the Fourier-Grid Hamiltonian (FGH) technique with fast discrete sine transform algorithms to switch between the direct space representation $\{r\}$ and the reciprocal space representation in $\{k\}$.

Briefly, given a radial wave function $\Phi_{\ell,m}(r)$, we want to calculate $\Phi_{\ell,m}'(r) = e^{i\frac{\Delta t}{2}\frac{\partial^2}{\partial r^2}}\Phi_{\ell,m}(r)$ assuming zero boundary conditions at $r = 0$ (so

that Eq. (1.27) does not diverge) and at the external boundary $r = R_{\max}$ of the r-mesh. In this case the sine transform, $\mathcal{S}$, can be used to obtain the representation of $\Phi_{\ell,m}(r)$ and $e^{i\frac{\Delta t}{2}\frac{\partial^2}{\partial r^2}}$ in the reciprocal $\{k\}$-space. Since the $\sin\left(\frac{\pi k}{R_{\max}}r\right)$, $(k = 1, 2, ...)$ is an eigenfunction of the differential operator we obtain:

$$\begin{aligned}
\Phi_{\ell,m}(r) &\to \Phi_{\ell,m}(k) = \mathcal{S}\left[\Phi_{\ell,m}(r)\right] \ , \\
e^{i\frac{\Delta t}{2}\frac{\partial^2}{\partial r^2}} &\to e^{i\frac{\Delta t}{2}\left(\frac{\pi k}{R_{\max}}\right)^2}\delta_{k,k'} \ .
\end{aligned} \tag{1.40}$$

Thus, in the $\{k\}$-space representation the matrix of the exponential operator is diagonal, and the calculation of its action on the wave function is straightforward with $\Phi'_{\ell,m}(k) = e^{i\frac{\Delta t}{2}\left(\frac{\pi k}{R_{\max}}\right)^2}\Phi_{\ell,m}(k)$. After computing the action of the operator in the $\{k\}$-representation, a second sine transform is needed to retrieve the desired wave function $\Phi'_{\ell,m}(r) = \mathcal{S}\left[\Phi'_{\ell,m}(k)\right]$ on the real-space radial mesh.

To summarize, the steps involved in the time-propagation of each KS orbital using Eq. (1.32) are:

- $\psi_{j,m}^{(1)}(r,\theta) = e^{-i\frac{\Delta t}{2}\mathcal{V}_{\mathrm{T}}[n](\mathbf{r},t+\Delta t/2)}\psi_{j,m}(r,\theta,t)$

- Given that only spherical harmonics with $\ell \geq m$ can contribute to a KS orbital with magnetic quantum number m, we apply for $\ell = m$ to $\ell = L_{\max}$:

  ⋄ $F_{j,\ell,m}^{(1)}(r) = \langle Y_\ell^m(\theta,\phi)|\psi_{j,m}^{(1)}(r,\theta)e^{im\phi}\rangle$

  ⋄ $F_{j,\ell,m}^{(2)}(r) = e^{-i\frac{\Delta t}{2}\frac{\ell(\ell+1)}{2r^2}}\,F_{j,\ell,m}^{(1)}(r)$

  ⋄ $F_{j,\ell,m}^{(2)}(k) = \mathcal{S}\left[F_{j,\ell,m}^{(2)}(r)\right]$

  ⋄ $F_{j,\ell,m}^{(3)}(k) = e^{i\Delta t\frac{(\pi k/R_{\max})^2}{2}}F_{j,\ell,m}^{(2)}(k)$

  ⋄ $F_{j,\ell,m}^{(3)}(r) = \mathcal{S}\left[F_{j,\ell,m}^{(3)}(k)\right]$

  ⋄ $F_{j,\ell,m}^{(4)}(r) = e^{-i\frac{\Delta t}{2}\frac{\ell(\ell+1)}{2r^2}}\,F_{j,\ell,m}^{(3)}(r)$

- $\psi_{j,m}^{(5)}(r,\theta) = \sum_{\ell=m}^{L_{\max}} Y_\ell^m(\theta,\phi)F_{j,\ell,m}^{(4)}(r)$

- $\psi_{j,m}(r,\theta,t+\Delta t) = e^{-i\frac{\Delta t}{2}\mathcal{V}_{\mathrm{T}}[n](\mathbf{r},t+\Delta t/2)}\psi_{j,m}^{(5)}(r,\theta)$

These steps are repeated several times within the iterative procedure explained in Sec. 1.2 (increasing order s). Once the iterative procedure reaches convergence and all the KS orbitals have been propagated one time-step, the electronic density is retrieved *via* Eq. (1.27) and Eq. (1.28).

1.2.3 WPP algorithm in cylindrical coordinates

In this section we develop the Wave Packet Propagation (WPP) for physical systems that retain only the cylindrical symmetry (e.g. conical, rod-like nanoparticles, dimers of spheres, etc.). In particular we use this method for the calculations of the nonlinear optical response of a dimer of Aluminium spheres in Sec. 4.5.

In the case of structures with axial symmetry, the description of the density dynamics of the physical system under consideration is much simplified if the Time-Dependent Kohn-Sham Equation (TDKSE), Eq. (1.15), is solved using the representation of the KS-orbitals on a grid in cylindrical coordinates $\mathbf{r} = \{\rho, z, \phi\}$. While we use mainly the same time-propagation algorithms as described in Sec. 1.2.2, specific issues linked with the choice of the cylindrical coordinate system emerge and have to be addressed. In order to give a full comprehensive explanation of the WPP algorithm we repeat all the steps involved in the calculation. Similar to Sec. 1.2.2, the main difficulty is linked with the nonlocal kinetic energy operator, here in cylindrical coordinates.

We consider a homogeneous external electromagnetic field polarized along the z-direction, so that the external potential preserves the cylindrical symmetry. This choice is consistent with the dipole approximation assumed for all TDDFT calculations in this thesis. It is then convenient to define the KS orbitals as

$$\Psi_{j,m}(\rho, z, \phi, t) = \frac{1}{\sqrt{2\pi}} \psi_{j,m}(\rho, z, t) e^{im\phi} \ . \tag{1.41}$$

As the potential does not depend on the coordinate ϕ, each KS orbital preserves its magnetic quantum number m during propagation in time. Inserting Eq. (1.41) into Eq. (1.15), leads to the TDKSE that needs to be solved:

$$i\frac{\partial \psi_{j,m}(\rho, z, t)}{\partial t} = \left\{ T^m + \mathcal{V}_\mathrm{T}[n](\rho, z, t) \right\} \psi_{j,m}(\rho, z, t) \ , \tag{1.42}$$

where $\mathcal{V}_\mathrm{T}[n](\mathbf{r}, t)$ is defined by Eq. (1.20)-Eq. (1.21b) and we remove the (s) superscript on the approximated total potential to ease the notation. The kinetic energy operator T^m in Eq. (1.42) takes the form

$$T^m = T^z + T^{m,\rho} = \underbrace{-\frac{1}{2}\frac{\partial^2}{\partial z^2}}_{T^z} \underbrace{-\frac{1}{2\rho}\frac{\partial}{\partial \rho}\rho\frac{\partial}{\partial \rho} + \frac{m^2}{2\rho^2}}_{T^{m,\rho}} \ . \tag{1.43}$$

As was already the case in Sec. 1.2.2, the time evolution of the KS orbitals characterized by $\pm m$ quantum numbers is identical. We then propagate only the $m \geq 0$ orbitals, and account for the m-degeneracy and spin degeneracy ($X_m = 2$ for $m = 0$ and $X_m = 4$ for $m \neq 0$).

Before describing the time propagation of the KS orbitals, we note a technical detail. During the development of the numerical method, it was found that using a non-uniform mesh in the ρ coordinate allows to get an improvement

in convergence. In particular a tight mesh is required around the axis ($\rho = 0$) while a sparser mesh can be used for large ρ. To achieve such distribution in ρ we use the mapping

$$\rho = f(x) = x - \frac{b}{\sqrt{a}} \arctan\left(\frac{x}{\sqrt{a}}\right) \; , \tag{1.44}$$

where a and b parametrize the family of transformations and x is defined in a uniform grid with spacing Δ. Figure 1.4 shows the function $f(x)$ used in the calculations (with $a = 700$ and $b = 595$), which generates a ρ grid that is tight around $\rho = 0$ and that transforms into an equispaced grid as ρ (or x) grows.
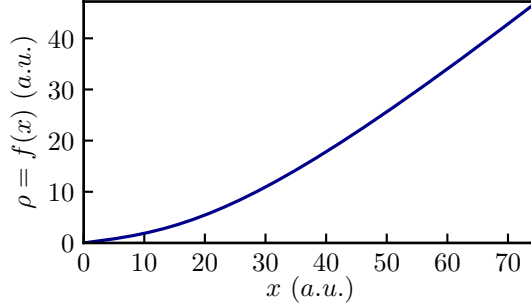
FIGURE 1.4: Mapping of equispaced x grid to the $\rho = f(x)$ coordinate as given by Eq. (1.44) with $a = 700$ and $b = 595$.

Introducing the mapping given by Eq. (1.44) into Eq. (1.42) we obtain

$$i\frac{\partial \psi_{j,m}(x,z,t)}{\partial t} = \left\{ -\frac{1}{2}\frac{\partial^2}{\partial z^2} - \frac{1}{2ff'}\frac{\partial}{\partial x}\frac{f}{f'}\frac{\partial}{\partial x} + \frac{m^2}{2f^2} \right\} \psi_{j,m}(x,z,t)$$
$$+ \mathcal{V}_{\mathrm{T}}[n](x,z,t)\ \psi_{j,m}(x,z,t) \; , \tag{1.45}$$

where we have used: $\rho = f(x) = f$, $\frac{\partial}{\partial \rho} = \frac{1}{f'}\frac{\partial}{\partial x}$ and $f' = f'(x) = \frac{df(x)}{dx}$.

If we introduce a function $\varphi_{j,m}(x,z,t)$ such that

$$\psi_{j,m}(x,z,t) = \frac{1}{\sqrt{ff'}}\ \varphi_{j,m}(x,z,t) \; , \tag{1.46}$$

and multiply both sides of Eq. (1.45) by $\sqrt{ff'}$, the TDKSE that we have to solve to propagate each KS orbital transforms to:

$$i\frac{\partial\varphi_{j,m}(x,z,t)}{\partial t} = \{T^m + V_{\mathrm{T}}[n](x,z,t)\}\,\varphi_{j,m}(x,z,t)\ , \tag{1.47a}$$

$$T^m = \underbrace{-\frac{1}{2}\frac{\partial^2}{\partial z^2}}_{T^z}\underbrace{-\frac{1}{2}\frac{1}{\sqrt{ff'}}\frac{\partial}{\partial x}\frac{f}{f'}\frac{\partial}{\partial x}\frac{1}{\sqrt{ff'}}+\frac{m^2}{2f^2}}_{T^{m,x}}\ , \tag{1.47b}$$

$$\mathcal{V}_{\mathrm{T}}[n](x,z,t) = \mathcal{V}[n](x,z,t) + V_{\mathrm{ext}}(x,z,t) + V_{\mathrm{abs}}(x,z,t)\ , \tag{1.47c}$$

where we have separated the kinetic energy operator into the z and x components $T^m = T^z + T^{m,x}$. The $T^{m,x}$ operator in Eq. (1.47b) has a symmetric form. This will be beneficial in a later step when the KS orbitals will be presented on a discrete mesh of points in (x,z) coordinates and the corresponding Hermitian matrix of the $T^{m,x}$ operator is defined.

In a similar manner to the WPP in spherical coordinates, we use a combination of FGH and SO technique to solve Eq. (1.47a). To propagate the wave function from time t, to $t+\Delta t$ we use the iterative method described in Sec. 1.2, where we need to apply the time evolution operator

$$\begin{aligned}\varphi_{j,m}(x,z,t+\Delta t) &= \hat{U}(t,\Delta t)\varphi_{j,m}(x,z,t)\\ &= e^{-i\Delta t\left(T^m + \mathcal{V}_{\mathrm{T}}[n](x,z,t+\frac{\Delta t}{2})\right)}\varphi_{j,m}(x,z,t)\ ,\end{aligned} \tag{1.48}$$

that can be evaluated with the SO technique as

$$\varphi_{j,m}(x,z,t+\Delta t) = e^{-i\frac{\Delta t}{2}\mathcal{V}_{\mathrm{T}}}e^{-i\Delta tT^m}e^{-i\frac{\Delta t}{2}\mathcal{V}_{\mathrm{T}}}\ \varphi_{j,m}(x,z,t) \tag{1.49a}$$

$$= e^{-i\frac{\Delta t}{2}\mathcal{V}_{\mathrm{T}}}e^{-i\Delta tT^z}e^{-i\Delta tT^{m,x}}e^{-i\frac{\Delta t}{2}\mathcal{V}_{\mathrm{T}}}\ \varphi_{j,m}(x,z,t)\ . \tag{1.49b}$$

where the short hand notation $\mathcal{V}_{\mathrm{T}} \equiv \mathcal{V}_{\mathrm{T}}[n](x,z,t+\Delta t/2)$ is used.

The operator $e^{-i\mathcal{V}_{\mathrm{T}}\frac{\Delta t}{2}}$ in Eq. (1.49b) is diagonal in the direct space representation of the wavefunction and its action can be evaluated locally at each point of the equidistant mesh in $\{x,z\}$-coordinates. The $e^{-i\Delta tT^z}$ operator, is diagonal in the momentum space representation. It can be treated by discretizing the wavefunction on a mesh of equidistant points in the z-coordinate and changing representation between the coordinate to momentum space with the direct and inverse discrete Fast Fourier Transform algorithms. The action of the $e^{-i\Delta tT^z}$ operator is thus calculated using the FGH technique, similar to the procedure employed in the Sec. 1.2.2 for the radial part of the kinetic energy operator.

As to the $T^{m,x}$ kinetic energy operator, $e^{-i\Delta tT^{m,x}}$, it is not diagonal in neither direct or momentum space. The calculation of the action of this operator is numerically involved and we use the Crank-Nicolson approximation[77,82].

This method can be summarized as follows. Since

$$e^{-i\Delta t T^{m,x}} = \frac{1 - \frac{1}{2}i\Delta t T^{m,x}}{1 + \frac{1}{2}i\Delta t T^{m,x}} + O\big((\Delta t)^3\big) \; , \qquad (1.50)$$

the action of the $e^{-i\Delta t T^{m,x}}$ operator on the wave function

$$\widetilde{\varphi}_{j,m}(x,z,t) = e^{-i\Delta t T^{m,x}} \varphi_{j,m}(x,z,t) \qquad (1.51)$$

is approximated by

$$\widetilde{\varphi}_{j,m}(x,z,t) = \frac{1 - \frac{1}{2}i\Delta t T^{m,x}}{1 + \frac{1}{2}i\Delta t T^{m,x}} \; \varphi_{j,m}(x,z,t) \; . \qquad (1.52)$$

In order to apply the Crank-Nicolson method we need to obtain the matrix of the $T^{m,x}$ operator represented on an equidistant grid of x-points $x_i = x_1 + \Delta(i-1)$, $i = 1,2,...,N$. With this aim, we first define several notations:

$$f_{i\pm a} = f(x_i \pm a \cdot \Delta) \;\; \text{where} \;\; a = 0, \frac{1}{2}, 1 \; , \qquad (1.53a)$$

$$f'_{i\pm a} = f'(x_i \pm a \cdot \Delta) = \left.\frac{df}{dx}\right|_{x_i \pm a \cdot \Delta} \qquad \text{where} \;\; a = 0, \frac{1}{2}, 1 \; , \qquad (1.53b)$$

$$\varphi = \varphi_{j,m}(x,z,t) \; , \qquad (1.53c)$$

$$\varphi_i = \varphi_{j,m}(x_i,z,t) \; . \qquad (1.53d)$$

We want to calculate $[T^{m,x}\varphi_{j,m}(x,z,t)]_{x=x_i}$ which can be written with this nomenclature as

$$\begin{aligned} [T^{m,x}\varphi_{j,m}(x,z,t)]_{x=x_i} &= [T^{m,x}\varphi]_i \\ &= \left[-\frac{1}{2}\frac{1}{\sqrt{ff'}}\frac{\partial}{\partial x}\frac{f}{f'}\frac{\partial}{\partial x}\frac{1}{\sqrt{ff'}}\;\varphi + \frac{m^2}{2f^2}\varphi \right]_i \end{aligned} \qquad (1.54)$$

The second term in the right-hand side of Eq. (1.54) is diagonal in the direct space representation and can be directly applied as $\left[\frac{m^2}{2f^2}\varphi\right]_i = \frac{m^2}{2f_i^2}\varphi_i$. To evaluate the derivatives in the first term we use the method of finite differences.

We start by writing the finite difference scheme

$$
-\frac{1}{2}\frac{1}{\sqrt{f_i f_i'}}\left[\frac{\partial}{\partial x}\underbrace{\left(\frac{f}{f'}\frac{\partial}{\partial x}\frac{1}{\sqrt{ff'}}\,\varphi\right)}_{\mathrm{F}}\right]_i = -\frac{1}{2}\frac{1}{\sqrt{f_i f_i'}}\left[\frac{\partial}{\partial x}\mathrm{F}\right]_{x=x_i}
$$

$$
= -\frac{1}{2}\frac{1}{\sqrt{f_i f_i'}}\frac{\mathrm{F}_{i+1/2}-\mathrm{F}_{i-1/2}}{\Delta}\ ,
$$

(1.55)

where $\mathrm{F}_{i+1/2}$ and $\mathrm{F}_{i-1/2}$ are

$$
\mathrm{F}_{i+1/2} = \frac{f_{i+1/2}}{f'_{i+1/2}}\left[\frac{\partial}{\partial x}\frac{1}{\sqrt{ff'}}\varphi\right]_{x=x_{i+1/2}}
$$

$$
= \frac{1}{\Delta}\frac{f_{i+1/2}}{f'_{i+1/2}}\left(\frac{1}{\sqrt{f_{i+1}f'_{i+1}}}\,\varphi_{i+1}-\frac{1}{\sqrt{f_i f_i'}}\,\varphi_i\right)\ ,
$$

(1.56a)

$$
\mathrm{F}_{i-1/2} = \frac{f_{i-1/2}}{f'_{i-1/2}}\left[\frac{\partial}{\partial x}\frac{1}{\sqrt{ff'}}\varphi\right]_{x=x_{i-1/2}}
$$

$$
= \frac{1}{\Delta}\frac{f_{i-1/2}}{f'_{i-1/2}}\left(\frac{1}{\sqrt{f_i f_i'}}\,\varphi_i-\frac{1}{\sqrt{f_{i-1}f'_{i-1}}}\,\varphi_{i-1}\right)\ .
$$

(1.56b)

Putting together Eq. (1.55) and Eqs. (1.56) into Eq. (1.54) we obtain

$$
[T^{m,x}\varphi]_i = -\frac{1}{2\Delta^2}\frac{1}{\sqrt{f_i f_i'}}\left\{\frac{1}{\sqrt{f_{i+1}f'_{i+1}}}\frac{f_{i+1/2}}{f'_{i+1/2}}\,\varphi_{i+1}\right.
$$

$$
+ \frac{1}{\sqrt{f_{i-1}f'_{i-1}}}\frac{f_{i-1/2}}{f'_{i-1/2}}\,\varphi_{i-1}
$$

$$
\left.- \frac{1}{\sqrt{f_i f_i'}}\left[\frac{f_{i+1/2}}{f'_{i+1/2}}+\frac{f_{i-1/2}}{f'_{i-1/2}}\right]\varphi_i\right\}+\frac{m^2}{2f_i^2}\varphi_i\ .
$$

(1.57)

which can be expressed as

$$
[T^{m,x}\varphi]_i = \sum_k T^{m,x}_{i,k}\varphi_k = T^{m,x}_{i,i-1}\varphi_{i-1}+T^{m,x}_{i,i}\varphi_i+T^{m,x}_{i,i+1}\varphi_{i+1}\ ,
$$

(1.58)

where the $T_{i,k}^{m,x}$, are the elements of the matrix $\mathbb{T}^{m,x}$ of the operator $T^{m,x}$ projected on the x-coordinate grid. We obtain a tridiagonal matrix given by

$$T_{i,i-1}^{m,x} = \qquad -\frac{1}{2\Delta^2}\frac{1}{\sqrt{f_i f_i'}}\frac{1}{\sqrt{f_{i-1}f_{i-1}'}}\frac{f_{i-1/2}}{f_{i-1/2}'}\ , \tag{1.59a}$$

$$T_{i,i}^{m,x} = \frac{1}{2\Delta^2}\frac{1}{f_i f_i'}\left[\frac{f_{i+1/2}}{f_{i+1/2}'} + \frac{f_{i-1/2}}{f_{i-1/2}'}\right] + \frac{m^2}{2f_i^2}\ , \tag{1.59b}$$

$$T_{i,i+1}^{m,x} = \qquad -\frac{1}{2\Delta^2}\frac{1}{\sqrt{f_i f_i'}}\frac{1}{\sqrt{f_{i+1}f_{i+1}'}}\frac{f_{i+1/2}}{f_{i+1/2}'}\ . \tag{1.59c}$$

The $\mathbb{T}^{m,x}$ matrix only extends over the "physical" range corresponding to $0 \le x_i \le x_{\max} = x_N$ so that $0 \le \rho \le f(x_N)$. Thus, we need to consider what happens at the limits. If the first point of the x-mesh is $x_1 = 0$ i) the $T_{1,0}^{m,x}$ matrix element in Eq. (1.59a) is not well defined as the point $f_{i-1/2}$ has no physical meaning and ii) Eq. (1.46) would diverge at the $x_1 = 0$ point. We take care of this issue defining the x-mesh such that $x_1 = \Delta/2$. Then, the matrix elements $T_{1,0}^{m,x}$, $T_{1,1}^{m,x}$ and $T_{1,2}^{m,x}$ are given by

$$T_{1,0}^{m,x} = 0 \quad \text{This matrix element lies out of the matrix,} \tag{1.60a}$$

$$T_{1,1}^{m,x} = \frac{1}{2\Delta^2}\frac{1}{f_1 f_1'}\frac{f_{1+1/2}}{f_{1+1/2}'} + \frac{m^2}{2f_1^2}\ , \tag{1.60b}$$

$$T_{1,2}^{m,x} = -\frac{1}{2\Delta^2}\frac{1}{\sqrt{f_1 f_1'}}\frac{1}{\sqrt{f_2 f_2'}}\frac{f_{1+1/2}}{f_{1+1/2}'}\ . \tag{1.60c}$$

As to the conditions at the external boundary of the mesh, $x_{\max} = x_N$, we impose zero boundary conditions, $\varphi_{N+1} = 0$, which limits the diagonal elements to $T_{N,N-1}^{m,x}$, $T_{N,N}^{m,x}$, and $T_{N-1,N}^{m,x}$.

We thus obtain the tridiagonal, symmetric, $N \times N$ matrix, $\mathbb{T}^{m,x}$, with elements given by Eq. (1.59):

$$\mathbb{T}^{m,x} = \begin{bmatrix} T_{1,1}^{m,x} & T_{1,2}^{m,x} & & & \\ \ddots & \ddots & \ddots & & \\ & T_{i,i-1}^{m,x} & T_{i,i}^{m,x} & T_{i,i+1}^{m,x} & \\ & & \ddots & \ddots & \ddots \\ & & & T_{N,N-1}^{m,x} & T_{N,N}^{m,x} \end{bmatrix}\ . \tag{1.61}$$

Once we have obtained $\mathbb{T}^{m,x}$, Eq. (1.52) can be cast in the tridiagonal form:

$$\sum_k \left(i\frac{4\Delta^2}{\Delta t}\mathbb{I}_{i,k} - \tilde{\mathbb{T}}_{i,k}^{m,x} \right) \widetilde{\varphi}_k = \sum_k \left(i\frac{4\Delta^2}{\Delta t}\mathbb{I}_{i,k} + \tilde{\mathbb{T}}_{i,k}^{m,x} \right) \varphi_k \ , \qquad (1.62)$$

where $\mathbb{I}$ is the identity matrix and $\tilde{\mathbb{T}}^{m,x} = 2\Delta^2 \, \mathbb{T}^{m,x}$. The sought $\widetilde{\varphi}$ wave function values at the grid points are obtained from the solution of the linear system of equations in Eq. (1.62) using Thomas Algorithm so that $O(N)$ operations are required. A Fortran 77 implementation of the algorithm is available in Ref. [84], pp.42-43.

To summarize, the first steps involved in any calculation are: i) define the equidistant mesh of points in z, and the mathematical mesh of equidistant points $\{x_i\}$ such that the physical mesh $\rho_i = f(x_i)$ is tight at the coordinate origin and ii) define the initial KS orbitals for the time propagation $\varphi_{j,m}(x, z, t = 0) = \sqrt{ff'}\psi_{j,m}^0(x, z)$ using the ground-state KS orbitals $\psi_{j,m}^0(x, z)$. Once these steps are completed, the time-propagation of the KS orbitals in cylindrical coordinates is done performing the time-step and the iterative procedure (explained in Sec. 1.2) according to:

- $\varphi_{j,m}^{(1)}(x, z) = e^{-i\frac{\Delta t}{2}\mathcal{V}_\mathrm{T}[n](x,z,\frac{\Delta t}{2})}\varphi_{j,m}(x, z, t)$

- For each point in z perform:
  $\left(i\frac{4\Delta^2}{\Delta t}\mathbb{I} - \tilde{\mathbb{T}}^{m,x} \right) \varphi_{j,m}^{(2)}(x, z) = \left(i\frac{4\Delta^2}{\Delta t}\mathbb{I} + \tilde{\mathbb{T}}^{m,x} \right) \varphi_{j,m}^{(1)}(x, z)$

- For each point in x:

  ◇ $\varphi_{j,m}^{(2)}(x, k_z) = \mathcal{F}\left[\varphi_{j,m}^{(2)}(x, z) \right]$

  ◇ $\varphi_{j,m}^{(3)}(x, k_z) = e^{-i\Delta t\frac{k_z^2}{2}}\varphi_{j,m}^{(2)}(x, k_z)$

  ◇ $\varphi_{j,m}^{(3)}(x, z) = \mathcal{F}^{-1}\left[\varphi_{j,m}^{(3)}(x, k_z) \right]$

- $\varphi_{j,m}(x, z, t + \Delta t) = e^{-i\frac{\Delta t}{2}\mathcal{V}_\mathrm{T}[n](x,z,t+\frac{\Delta t}{2})}\varphi_{j,m}^{(3)}(x, z)$.

Here $\mathcal{F}$ and $\mathcal{F}^{-1}$ stand for the direct and inverse discrete fast Fourier transforms respectively.

After each time step, the electronic density is computed *via* a combination of equations Eq. (1.14), Eq. (1.41) and Eq. (1.46)

$$n(\rho = f(x), z, t) = X_m \sum_{\{j,m\geq 0\}\in occ} \frac{1}{2\pi}\frac{1}{ff'}|\varphi_{j,m}(x, z, t)|^2 \ , \qquad (1.63)$$

where the factor X_m takes into account both the spin and the $\pm m$ degeneracy of the KS orbital ($X_m = 2$ for $m = 0$, and $X_m = 4$ for $m \neq 0$) and the summation runs over all the occupied orbitals defined by $\{j, m \geq 0\}$.

Chapter 2

Optoelectronic response of subnanometric plasmonic gaps

The plasmonic response of metallic gap-antennas, formed by two nanoparticles separated by a small gap, can be strongly influenced by the size of such gap, as discussed in Sec. II and Sec. IV of the introduction. Notably, closing the gap down to ≈ 1 nm separation distance produces a strong redshift of the plasmonic modes and a large enhancement of the near field in the gap. Such sensitivity to the gap size has been studied thoroughly over the past decade resulting in a good theoretical understanding[3,15,16,43,45,47,85–87] that has been supported by many experimental works[88–95].

Most of the studies used spheres or nanoparticles that are caped by a spherical end at the gap. However, the nanoparticles used in experiments usually show some degree of faceting[96–100]. When the interparticle distance is comparable with the size of the facets characterizing the gap, the exact gap morphology has an important role in the optical response of the gap-antenna, which can be expected to gain in importance as the gap closes. Special attention can be placed in the case of sub-nanometric gaps to understand the effect of electrons tunneling through the interparticle junction.

In light of the potential impact of the morphology of gaps, we study in this section the optical response of plasmonic gap-antennas with different gap-terminations, going from spherical to flat faceted, separated by very narrow gaps. We start using two elongated rods caped by spherical terminations at the gap, which behave similarly to the well known case of two spheres[45] discussed in Sec. II-Sec. IV of the introduction. We compare the behaviour of this structure with the case of antennas with flat terminations, which exhibit the coexistence of two different types of plasmonic modes, namely Longitudinal Antenna Plasmon (LAP) modes[3] that are characterized by oscillations of the electrons along the whole length of the antenna arms and Transverse Cavity Plasmon (TCP) modes[101], which are modes localized in the gap region

and that show field patterns similar to Fabry-Pérot standing waves propagating transversally to the rods arms. We discuss the properties of these modes and how, under adequate illumination and morphological conditions they show little coupling and can be independently tuned.

As pointed out, the improvement of fabrication techniques has allowed to test the behaviour of gap-antennas in the limit of subnanometric gaps, where the onset of tunneling strongly influences the response[21,22]. The tunneling current diminishes the charge accumulated at the nanoparticles surfaces facing the gap, quenches the near field and produces the appearance of Charge Transfer Plasmon (CTP) modes before physical contact[24]. We are thus particularly interested in studying the role of the gap morphology to determine the effect of tunneling of electrons in the optical response of the antennas. We are able to account for the tunneling currents in our relatively large-sized nanoantennas using the QCM implemented using the Boundary Element Method (BEM) to solve Maxwell's equations (see Sec. 1.1). We expect that rod-antennas with rounded terminations will present similar features of the tunneling regime as the dimer of spheres[22,24] i.e., quenching of the near field below a threshold distance and the appearance of a low-energy CTP that strongly blueshifts as the gap closes. However, flat-faceted antennas present a larger area of tunneling, which is expected to produce different effects in the optical response.

After comparing the optical response of the rod dimers with rounded terminations with that of the flat facet terminations, in the final section of this chapter we analyse the result of progressively changing the gap-facet size in order to observe the transition between these two limit cases. We also study the effect of changing the overall shape of the nanoparticles that form the gap-antenna, to asses the robustness of the optoelectronic response.

2.1   Role of gap morphology: spherical vs. flat-gap terminations

To understand the effects of the gap morphology in the plasmonic response, we consider the two types of nanoantennas depicted in Fig. 2.1. In both cases, the structure consists of two nanorods forming the arms of the antenna, separated by a gap distance d_{gap} measured between the closest points in the gap. Each rod has a length of L and diameter D ($D = 2R$ with R the radius of the rods), and with a flat termination at the outer end, far from the gap. The shape of the rod terminations at the gap determines the two types of antennas that we consider. In spherical-gap antennas (Fig. 2.1a), each rod is terminated at the gap by a hemispherical cap and the contact is a 0-dimensional point. In flat-gap antennas, (Fig. 2.1b), the corresponding termination is flat, with a 2-dimensional contact area. The structures are rotationally symmetric with respect to the z axis, and have mirror symmetry with respect to the $z = 0$ plane. The centre of the gap corresponds to $x = y = z = 0$. The diameter of
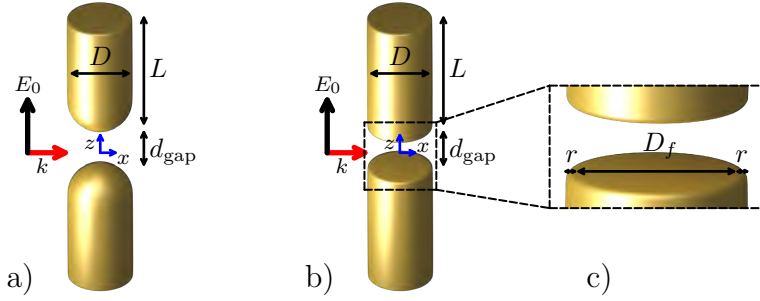
FIGURE 2.1: Schematics of the gap antennas for (a) spherical-gap and (b) flat-gap configurations used in Sec. 2.1 and Sec. 2.2. The rods forming the antennas are rotationally symmetric with respect to the z axis. The length of the rods is $L = 100$ nm from end to end and their diameter is $D = 50$ nm. The diameter of the spherical cap near the gap in (a) is also D. (c) Zoom of the flat gap-ends of the rods in panel (b). The flat facets have a diameter $D_f = 46$ nm and are rounded at the edge using a small radius of curvature r, so that $D_f = D - 2r$. The outer ends for both (a) and (b) are also flat with $D_f = 46$ nm. The dielectric constant of the metal is described by the Drude model with $\omega_p = 7.9$ eV and $\gamma_p = 0.09$ eV. The structures are illuminated laterally, with the electric field of amplitude E_0 polarized along the rod axes and the Poynting vector, indicated by a red arrow, towards positive x. The centre of the gap is at $x = y = z = 0$ and the geometry has mirror symmetry with respect to the $z = 0$ plane.

the facets of all flat ends are $D_f = D - 2r$ with r being a small edge rounding that prevents unrealistically sharp edges. When the antenna with flat facets as in Fig. 2.1b is in contact, $(d_{\mathrm{gap}} \leq 0)$, a small indentation occurs at the centre of the antenna, but this indentation has no significant effect in the optical response of the whole system.

The structure is placed in vacuum, with permittivity ε_0, and it is illuminated by a plane wave of angular frequency ω, or equivalently wavelength λ, propagating along x and with electric field of amplitude E_0 polarized along the rod axis z. Unless otherwise stated, we focus in the first part of Ch. 2 on metallic rods with $L = 100$ nm, $D = 50$ nm, with a facet $D_f = 46$ nm at the rods end that do not face the gap, and with spherical or flat $(D_f = 46$ nm$)$ gap terminations. Their metal relative permittivity ε_{m} is described using a local Drude model $\varepsilon_{\mathrm{m}} = \varepsilon_\infty - \omega_p^2/(\omega(\omega + i\gamma_p))$ with no dielectric background screening, $\varepsilon_\infty = 1$, and plasma frequency and damping constants, $\omega_p = 7.9$ eV and $\gamma_p = 0.09$ eV, respectively. These parameters correspond to a Jellium Model (JM) of gold, and describe reasonably well the Au dielectric values for large wavelengths. The simple Drude model description facilitates the interpretation of the modes at large energies, where the contribution of d-electron can suppress the plasmonic resonances for real metals. Other geometries and the experimental value of the gold permittivity is considered in Sec. 2.3.

2.1.1   Far-field and near-field optical response in the absence of electron tunneling

We first analyse the local classical optical response of the gap-antennas shown in Fig. 2.1 for gap separation $d_{\mathrm{gap}} \geq 0.5$ nm (except when otherwise indicated). Nonlocal effects are known to influence the optical response in nanometric gaps[17–19,53,54,102] but the main trends of the mode structure and spectral dispersion can be nicely described by local theories with a convenient rescaling of distances of a few Ångstroms[15,16,25], thus the local analysis serves as a good representation of the nature and tendencies of the modes. For this range of gap separations, quantum tunneling effects can be neglected[24,87]. The effect of tunneling for narrower gaps will be analysed in Sec. 2.2.

We calculate the far- and near-field response, i.e., the extinction cross section σ_{ext} and the maximum field enhancement at the central plane $|E^{\mathrm{max}}/E_0|$ (defined as the maximum amplitude of the field at the central plane $z = 0$ normalized by the amplitude of the incident plane wave), by rigorously solving Maxwell's equations using the Boundary Element Method (BEM)[36,37]. To diminish edge effects in the case of flat terminations, we evaluate the field enhancements in an area given by $x^2 + y^2 < (R - 2r)^2$.

We show the near- and far-field plasmonic response of the spherical-gap antennas for different gap separations d_{gap} in Fig. 2.2a,c. For large gap separations, the dominant feature is a broad mode at approximately $\lambda = 530$ nm that can be associated with resonances at each single nanorod that behave as coupled Fabry-Pérot-like resonances of the individual rods for plasmons propagating along the longitudinal z direction[103–106]. We denote such excitations as Longitudinal Antenna Plasmons (LAPs). As the gap separation decreases, the results follow the well-known trend for interacting sphere dimers[11,45,89,90]. The lowest-energy LAPs of each nanorod hybridize into a Bonding Dipolar Plasmon (BDP) mode and higher order bonding resonances appear. All modes redshift for decreasing separation distance, and the redshift diverges (notice the logarithmic scale for separation distances) for $d_{\mathrm{gap}} \to 0$, as a consequence of the hybridization of modes[43] induced by Coulomb coupling of the charges at the individual rods.

All observed resonances are strongly radiative and lead to increasingly large near-field enhancement for smaller d_{gap}. As a consequence, both the extinction cross-section σ_{ext} (Fig. 2.2a) and the maximum near-field enhancement $|E^{\mathrm{max}}/E_0|$ (Fig. 2.2c) exhibit similar mode structure and dispersion. For very short d_{gap}, the field enhancement, produced by a large charge density at the apex of the rods, can take very large values and is confined to a very small volume within the centre of the gap[21,45,107].

The evolution of the optical spectra of the flat-gap antennas as a function of separation, shown in Fig. 2.2b,d, is strikingly different. The main feature in the extinction cross-section of Fig. 2.2b is a broad peak appearing in the wavelength range of $\lambda \approx 575$ nm to 830 nm. Additional narrow peaks at $\lambda \approx 350$ nm and $\lambda \approx 280$ nm are also found. These three modes can be understood as LAP
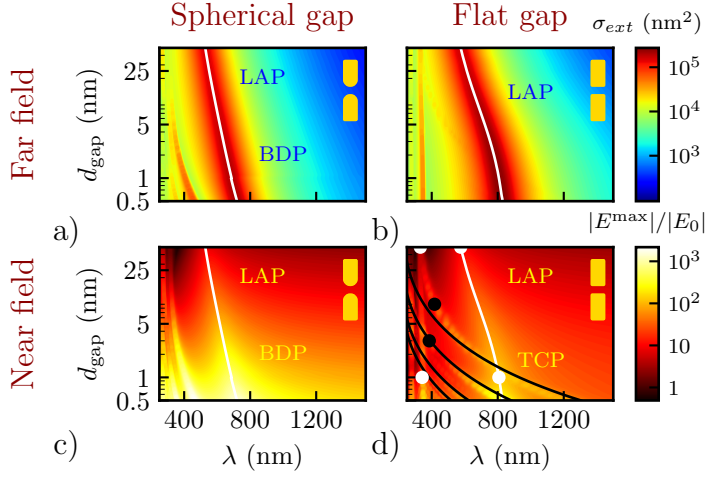
FIGURE 2.2: (a,b) Extinction cross-section σ_{ext} and (c,d) maximum near-field enhancement at the central plane $|E^{\max}/E_0|$ for (a,c) spherical-gap and (b,d) flat-gap linear metallic antennas (of dimensions $L = 100$ nm, $D = 50$ nm and $D_f = 46$ nm), as a function of incident wavelength and gap separation. The white lines correspond to extinction maxima and the black lines in (d) to the expected position of the transverse gap cavity modes ($s=1$, $m=1$ and $s=2,4,6$, $m=0$) according to the model given in the Sec. 2.1.2. Notice the logarithmic scale used for the distances and for the color scale in the figures. The white and black dots in (d) correspond to the field plots shown in Fig. 2.4 and Fig. 2.6 respectively. Modes are labelled as LAPs, TCPs and BDPs.

resonances. The coupling does not significantly affect the spectral positions of the two narrow LAP peaks at higher energy, but leads to a significant redshift with decreasing d_{gap} of the dominant, lowest-energy LAP. Critically, and in contrast with the spherical-gap terminations, the redshift saturates as the gap narrows[108,109] towards the contact $d_{\text{gap}} = 0$ limit, where the lowest-energy LAP mode for a single nanorod of length $2L$ is recovered.

Remarkably, an additional set of modes on top of the LAPs is evident in the near-field response of the flat-gap antennas in Fig. 2.2d. These modes (black lines) are spectrally narrow and exhibit a very strong dependence on gap separation. They can be clearly distinguished by the strong enhancement for narrow nanometric gaps although they radiate only weakly[110,111], thus hardly affecting the extinction cross-section in Fig. 2.2b. We denote these resonances as Transverse Cavity Plasmons (TCPs) because they can be understood as Fabry-Pérot-like resonances[104,112] of cavity plasmons propagating along the gap cavity, similar to those found in patch or related plasmonic resonators[101,113–116]. The surface plasmons excited at the metal-insulator-metal gap propagate parallel to the flat interfaces and reflect at the gap edges[117], leading to resonances
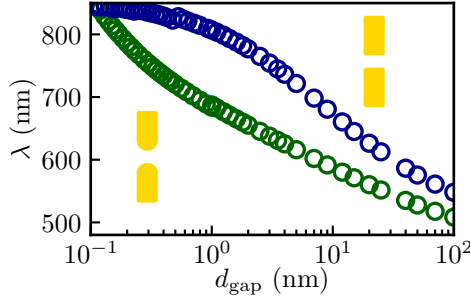
FIGURE 2.3:   Resonant wavelength as a function of gap separation d_{gap} for the lowest-energy LAP for both spherical (green) and flat gaps (blue) ($L = 100$ nm, $D = 50$ nm). These modes correspond to the white lines in Fig. 2.2a,c (spherical) and Fig. 2.2b,d (flat). All the calculations in this figure are classical, and thus do not consider the tunneling current that can be established between the rods.

with characteristic standing-wave patterns due to coherent interference (see more details in Sec. 2.1.2).

In Fig. 2.3 we can observe more clearly the distinctive dispersion of the lowest-energy LAP as $d_{\mathrm{gap}} \to 0$, where the influence of the gap morphology is emphasized. The diverging redshift for narrow spherical-gaps strongly contrasts with the saturation observed for the flat-gap antennas. To better show the trends we include in Fig. 2.3 also classical results (no electron tunneling) for very narrow gaps up to $d_{\mathrm{gap}} \approx 0.1$ nm, where electron tunneling can strongly modify the plasmonic response (this aspect will be treated in Sec. 2.2). We can understand the saturation of the LAP by a simplified model that describes the analogy of the antenna with a electric circuit in series[118–120], where the gap is represented by a capacitance and the rods by impedances. As the gap closes, the capacitance becomes divergently large and the gap can be seen as a short-circuit that does not affect the response, recovering the resonance of a single rod of twice the length. The model is described in more detail in Sec. 2.1.2.

2.1.2   Mode structure of gap-antennas with flat facets at the gap (LAPs and TCPs)

We now discuss in more detail the nature of the modes of the flat-gap antennas. All plasmon modes in this chapter (Ch. 2) can be classified using three indexes $\{\ell, s, m\}$ which determine the symmetry of their charge distribution. m describes the azimuthal symmetry of the mode, i.e. the number of nodes in the charge distribution that are present in a 180° rotation around the antenna axis. ℓ indicates the number of nodes in a rod along the antenna longitudinal direction (z-direction in Fig. 2.1). Last, s is defined as the number of charge nodes in the gap facet along a line that crosses the middle point ($x = 0$, $y = 0$)

in the direction of propagation of the incident plane wave (x-axis indicated in Fig. 2.1). LAPs are characterized by charge oscillations only along the z-axis and are classified as $\{\ell, 0, 0\}^3$. Smaller ℓ corresponds to lower energy (longer wavelength) modes. The associated charge density patterns resemble those of traditional linear antennas operating at much lower frequencies[121]. TCPs however show only oscillation in the transverse direction to the antenna axis and therefore are classified as $\{s, m\}$. In the present calculation only $m=1$ and $m=0$ modes play a role, with $m = 1$ corresponding to odd s and $m = 0$ to even s.

Longitudinal Antenna Plasmons (LAPs)

In Fig. 2.4 we summarize the characteristics of the flat-gap LAPs tracing their evolution as the gap distance is decreased and showing their symmetries in terms of the ℓ index. Figure 2.4a shows the extinction cross-section as a function of wavelength and gap distance (same as in Fig. 2.2b). The two lowest order LAPs are indicated by the white lines and the dots mark the points at which the near-field maps in Fig. 2.4d-g are calculated. The evolution of the charge distribution of the LAP$_1$ and LAP$_2$ modes is given in Fig. 2.4b,c, which show the schematic charge configuration ("+" and "−" labels) and the calculated surface charges (coloured edges). The latter are calculated in Fig. 2.4b for $d_{\text{gap}} = 50$ nm; $\lambda = 575.5$ nm (same conditions as in panel (d)) and $d_{\text{gap}} = 0$ nm; $\lambda = 807$ nm. The charge evolution shows that the lowest-energy LAP mode goes through a transition from the LAP$_1$ ($\ell = 1$, $s = 0$, $m = 0$) mode of the individual rods when the gap separation is large, to the LAP$_1$ ($\ell = 1$, $s = 0$, $m = 0$) mode of the $2L$ full antenna after contact. The simulated field enhancement maps shown in Fig. 2.4d,e, calculated for (d) $d_{\text{gap}} = 50$ nm; $\lambda = 575.5$ nm and (e) $d_{\text{gap}} = 1$ nm; $\lambda = 807$ nm, confirm this transition. For $d_{\text{gap}} = 50$ nm we observe a clear dipolar character in each of the arms of the antenna, as expected from the charge distribution in Fig. 2.4b (left). However, Fig. 2.4e shows a dipolar enhancement pattern along the whole structure characteristic of the charge distribution in Fig. 2.4b (right). Note that in Fig. 2.4e the gap is not yet totally closed ($d_{\text{gap}} = 1$ nm) and therefore a strong field enhancement and charge concentration is present at the gap but otherwise the field and charge distribution is almost identical to the contact situation ($d_{\text{gap}} = 0$).

Similarly, the second-lowest-energy LAP mode ($\ell = 2$, $m = 0, s = 0$) of the single rods (LAP$_2$) becomes the $\ell = 3$ LAP mode of the full antenna, as shown by the charge distributions in Fig. 2.4c, calculated for $d_{\text{gap}} = 50$ nm; $\lambda = 331$ nm (same conditions as in panel (f)) and $d_{\text{gap}} = 0$ nm; $\lambda = 342$ nm. In Fig. 2.4f,g we plot the corresponding near-field enhancement, in this case for (f) $d_{\text{gap}} = 50$ nm; $\lambda = 331$ nm and (g) $d_{\text{gap}} = 1$ nm; $\lambda = 342$ nm. As a general rule, the ℓ modes of the short antennas become the $2\ell - 1$ LAP mode of the large joined antenna. Significantly, the spectral position of the $\ell = 2$, 3 modes at large distance and the corresponding $2\ell - 1$ resonance of the full structure after contact is very similar in our system, so that the resulting spectral shift

Flat-gap antenna
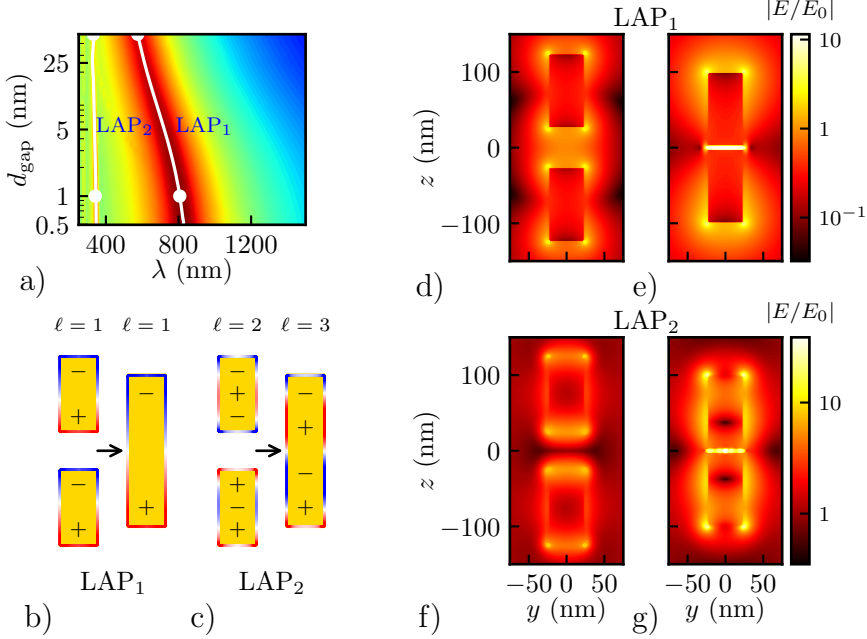
FIGURE 2.4: (a) Extinction cross-section σ_{ext} of a flat-gap antenna ($L = 100$ nm, $D = 50$ nm, $D_f = 46$ nm), as a function of wavelength and gap separation (shown also in Fig. 2.2b). White lines follow the evolution of the LAP modes and the dots mark the points where the near field in (d-g) are calculated. (b,c) Schemes of the charge distribution of the LAP$_1$ and LAP$_2$ modes before and after contact. The edges of the rods show the surface charge distribution calculated in for (b) $d_{\text{gap}} = 50$ nm; $\lambda = 575.5$ nm and $d_{\text{gap}} = 0$ nm; $\lambda = 807$ nm with saturated colours. In (c) the surface charges are calculated for $d_{\text{gap}} = 50$ nm; $\lambda = 331$ nm and $d_{\text{gap}} = 0$ nm; $\lambda = 342$ nm. (d,e) Near-field enhancement of the LAP$_1$ mode for (d) $d_{\text{gap}} = 50$ nm; $\lambda = 575.5$ nm and (e) $d_{\text{gap}} = 1$ nm; $\lambda = 807$ nm. (f,g) Near-field enhancement of the LAP$_2$ mode for (f) $d_{\text{gap}} = 50$ nm; $\lambda = 331$ nm and (g) $d_{\text{gap}} = 1$ nm; $\lambda = 342$ nm

is small. For example, the $\ell = 2$ mode at $\lambda \approx 330$ nm becomes the $\ell = 3$ mode of the joined antenna at $\lambda \approx 350$ nm. We also note that the $\ell = 2$ mode of the individual rods at $\lambda \approx 330$ nm are only excited due to their mutual interaction, as they would otherwise be symmetry forbidden under the current illumination conditions.

LAP saturation through a circuit theory model

The distinctive saturation with distance d_{gap} of the dispersion of the low-energy longitudinal antenna plasmon (LAP) of metallic flat-gap antennas (length L and radius R) can be related to the behaviour of the total displacement current along the z axis of the antenna, J_{D_z}. This magnitude can be expressed as $J_{D_z} = -i\omega\varepsilon_0\varepsilon E_z$, with ε the relative permittivity of the material ($\varepsilon = 1$ for vacuum or $\varepsilon = \varepsilon_m$ for the metal), ω the angular frequency and E_z the z component of the induced field. Figure 2.5 displays the total current I_g across the gap as a function of separation distance (blue dots), calculated as the integral $I_g \propto \left|\int J_{D_z}dS\right|$ over the surface areas defined by $x^2 + y^2 < R^2$ at the $z = 0$ plane of the gap. The calculation is performed ignoring the tunneling current across the gap.

A clear saturation of the current can be observed as the gap narrows. The insets in Fig. 2.5 display the cross-section maps of the spatial distribution of the displacement current J_{D_z} for the lowest-energy antenna mode LAP_1 as the gap narrows, showing the transition between the lowest-energy LAP mode of the individual rods to the lowest-energy LAP mode of the full $2L$ long structure. For large separation ($d_{\mathrm{gap}} = 20$ nm, inset to the right) J_{D_z} resembles the current of two coupled single rods[3,104,106]. For sufficiently narrow gaps, however, the J_{D_z} distribution inside the rods corresponds to the resonance of a single rod of twice the length, independent of the exact gap distance, as shown by the two leftmost insets in Fig. 2.5. This behaviour is also consistent with the results in Fig. 2.4.

To better understand why a very narrow gap does not affect the current distribution across the rods, we describe the impedance of the gap antenna within circuit theory[118–120], and concentrate on the behaviour of the total current I_g flowing across the gap for the lowest-energy LAP. Using a simple RC model[122] (scheme in the rightmost inset of Fig. 2.5), we can characterize the flat-gap impedance Z_c in a flat area of radius R' as $Z_c = 1/(iC_g\omega)$ with $C_g = \varepsilon_0\pi R'^2/d_{\mathrm{gap}}$ being the capacitance of the gap. The impedance of each rod is $Z_r = 0.5L/(-i\varepsilon_m\omega\pi R^2)$. The factor 0.5 in the expression of Z_r approximately takes into account the current variation[120] along z for $\ell = 1$. The antenna equivalent circuit can be expressed as a serial connection of the lump circuit elements, with the capacitor C_g in between two elements of impedance Z_r. The current through the gap would be approximately proportional to the total conductance $I_g \propto |(2L + d_{\mathrm{gap}})/(Z_c + 2Z_r)|$, where we have assumed that the total voltage drop along the whole antenna is proportional to $V \propto (2L + d_{\mathrm{gap}})E_0$. For narrow gaps Z_c becomes sufficiently low as to behave as a short circuit and thus not affect the flow of current. Under this condition ω gets close to its saturation value and I_g is approximately proportional to $1/(2Z_r)$, independently of d_{gap}.
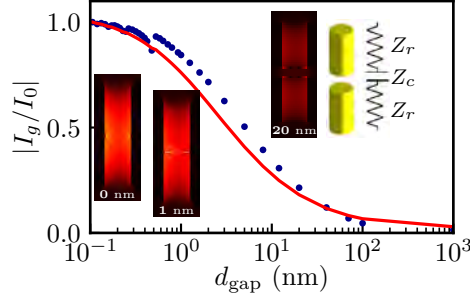
FIGURE 2.5: Evolution of the integrated displacement current I_g flowing across a flat metallic gap for the lowest-energy LAP resonance as a function of gap separation distance d_{gap}. Blue dots correspond to classical electromagnetic simulation values and the red line is the result of the RC model provided in the text and sketched in the rightmost inset. The calculations are classical, and thus ignore the tunneling current that can be established between the rods. Each curve is normalized to its value for the shortest separation distance, and the three cross-sections in the insets correspond to $|J_{D_z}|$ on the xz vertical plane ($y = 0$) for this LAP. All the cross-sections of $|J_{D_z}|$ are plotted in the same scale and the corresponding d_{gap} is indicated. The insets correspond to $\lambda = 626.5$ nm for $d_{\text{gap}} = 20$ nm (right), $\lambda = 807.0$ nm for $d_{\text{gap}} = 1$ nm (centre) and $\lambda = 851.5$ nm for $d_{\text{gap}} = 0$ nm (left).

We compare in Fig. 2.5 the dependence of the normalized I_g with d_{gap} as obtained in the simulation (blue dots) with those estimated analytically from the expression $I_g \propto |(2L + d_{\text{gap}})/(Z_c + 2Z_r)|$ (red line) for the lowest-energy LAP_1. We find a very good agreement between the calculated data and the analytical model. Furthermore, the significant similarity between the saturation of the current with d_{gap} in Fig. 2.5 and the saturation of the redshift of the LAP_1 mode in Fig. 2.3 further supports the relationship between the longitudinal displacement current and the redshift of the LAP modes as a function of the gap separation.

Transverse Cavity Plasmons (TCPs)

We focus next on the characteristics of the TCPs in Fig. 2.6 as a function of incident wavelength and gap separation. Figure 2.6a shows the maximum near-field enhancement at the gap. Many TCPs are apparent for very narrow gaps (strong interaction between the two rods), all of them characterized by a strong redshift as the gap distance is decreased. We have marked with a black line the two TCP modes to be analysed (TCP_1 and TCP_2). The black dots mark the situations that are mapped in Fig. 2.6d-g. Each TCP corresponds to a different order of plasmonic Fabry-Pérot-like cavity modes at the gap. Fabry-Pérot modes are a result of a wave that reflects back and forth in a cavity. In our case, the TCPs travel along the flat facets at the gap termination of the
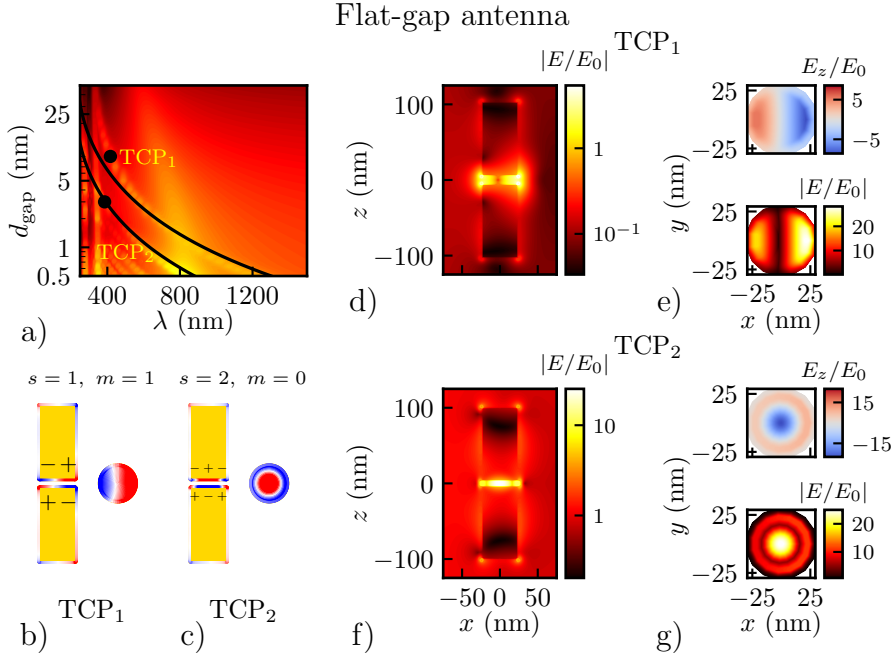
FIGURE 2.6: (a) Maximum near-field enhancement at the gap ($z = 0$) $|E^{\max}/E_0|$ for a flat-gap antenna ($L = 100$ nm, $D = 50$ nm and $D_f = 46$ nm). Black lines follow the evolution of the TCP modes and the black dots mark the points where the near field in (d-g) are calculated. Schemes of the charge distribution of the (b) TCP_1 and (c) TCP_2 modes. The edges of the sketches and the coloured flat facet show the calculated surface charge distribution (saturated) of the corresponding modes in (d) and (f). (d,e) Near-field maps of the TCP_1 mode for $d_{gap} = 9$ nm and $\lambda = 417$ nm. In (d) we plot the absolute value of the field enhancement $|E/E_0|$ in the vertical $x = 0$ plane. (e) shows the (top) imaginary part of the z-component and (bottom) absolute value of the field enhancement in the horizontal $z = 0$ plane at the centre of the gap. (f,g) same results as in (d,e) for the TCP_2 mode for $d_{gap} = 3$ nm and $\lambda = 385$ nm.

nanoparticles, getting reflected at the edges. The charge and field distribution associated with these Fabry-Pérot resonances are characterized by a standing wave pattern from the interference of waves travelling in opposite directions within the gap.

Figure 2.6d,e show the near field excited when we illuminate the gap-antenna on resonance with the TCP_1 ($d_{gap} = 9$ nm , $\lambda = 417$ nm). The vertical cut in Fig. 2.6d confirms that the fields are concentrated only at the interparticle gap. The spectrally close LAP_2 mode is likely responsible for the

weak near field observed far from the gap. Figure 2.6e show the near-field en-
hancement $|E/E_0|$ (bottom) and the amplitude of the imaginary part of the
z-component of the electric field (E_z/E_0) (top) at the central plane of the
gap $(z = 0)$. The field shows a flip of sign of the z-component of the electric
field along the propagation direction of the incoming light (x-axis), consistent
with the symmetry of the TCP_1 mode with indexes $\{s = 1, m = 1\}$. The
charge distribution of this mode is indicated in Fig. 2.6b where the coloured
edges show the calculated surface charge density They further confirm that this
mode corresponds to the TCP_1.

Similarly, Fig. 2.6f,g show the near field associated with the TCP_2 excited
at $d_{gap} = 3$ nm , $\lambda = 385$ nm. Again, the field localization at the gap is
apparent in the vertical cut in Fig. 2.6f. The fields at the gap (Fig. 2.6g)
indicate that this mode (with indexes $\{s = 2, m = 0\}$) is characterized, as
expected, by a charge distribution at the gap terminations that preserves the
rotational symmetry, with 2 nodes along the propagation direction (sketch in
Fig. 2.6c).

Flat-gap antennas can also support $m \geq 2$ modes corresponding to faster
variations of the charge density in the azimuthal direction[114], but they do not
contribute to the response in our scenario. In fact, the $m = 1$ resonances are
only excited due to retardation, which breaks the symmetry between positive
and negative values of x.

Last we note that transverse modes in nanorods often refer to resonances
that are excited by a field polarized transverse to the nanorod axis. However,
the TCPs discussed here are transverse in the sense that their surface charge
distribution has significant variation with nodes and antinodes in the transverse
direction along the gap faces. They are, however, excited by a longitudinal field.
Indeed, a pure symmetry argument indicates that the rotationally-symmetric
even s TCPs cannot be excited by a transversely polarized field. In that sense,
the TCPs must emerge as the gap closes from high-order longitudinal modes
of the separated nanorods. These TCPs become visible, among other factors,
because of the strong interparticle coupling for small gaps.

Fabry-Pérot model of the TCPs

The emergence of the TCPs can be explained and made quantitative by ap-
plying a simple Fabry-Pérot model. We first obtain the plasmonic wavelength
λ_{pl} of the cavity gap mode propagating along a thin infinite vacuum gap layer
between two semi-infinite metallic slabs[112,123,124]. When the equations of prop-
agation in this metal/insulator/metal system are solved for a given incident
wavelength λ and gap separation d_{gap} one obtains[125]:

$$\tanh\left(i\pi d_{gap}\sqrt{\frac{1}{\lambda^2} - \frac{1}{\lambda_{pl}^2}}\right) = \frac{\varepsilon_0}{\varepsilon_m}\sqrt{\frac{\varepsilon_0\lambda^2 - \varepsilon_m\lambda_{pl}^2}{\varepsilon_0\lambda^2 - \varepsilon_0\lambda_{pl}^2}} \ , \tag{2.1}$$

which could straightforwardly be generalized to account for the presence of a dielectric material in the gap by substituting the wavelength λ and the permittivity in vacuum by the respective values in the dielectric medium. A TCP appears when the incident illumination excites a plasmon with wavelength λ_{pl} that approximately satisfies the quantization condition

$$D_f/\lambda_{\mathrm{pl}} = s/2 \; , \qquad (2.2)$$

which connects λ_{pl} with the facet size D_f and the order $s \geq 1$ of the cavity mode. This quantization condition can be obtained by considering a single gap plasmon that propagates in the transverse x direction between the edges of the flat gap along a diameter of length D_f. A resonance occurs when the phase accumulated by the plasmon after a full round trip is 2π times the integer s order, $(2\pi/\lambda_{\mathrm{pl}})2D_f = 2\pi s$. Similar equations were found for other plasmonic cavities although an additional phase term was often considered to describe the reflection at the edges[104,110,112,126,127] and more complex equations have been proposed[116,128–130]. The results of the spectral position of the TCPs given by this simple analytical model for $s = 1, 2, 4$ and 6 are superimposed to the numerically calculated field enhancement in Fig. 2.2d as black solid lines. The agreement between the positions of the TCPs as predicted from the model and the calculations is remarkable and, as this simple model does not consider the excitation of LAPs, the good agreement suggests a spectral decoupling of the two types of resonances.

This simple model also explains the large sensitivity of the resonant frequency of the TCP modes to the gap separation. In the limit of no losses, $\lambda_{\mathrm{pl}} \ll \lambda$ and $\varepsilon_{\mathrm{m}}/\varepsilon_0 \approx -\lambda^2/\lambda_p^2$, then Eq. (2.1) can be reduced to $\lambda_{\mathrm{pl}}\sqrt{1 + (\lambda_{\mathrm{pl}}/\lambda_p)^2} \approx \pi d_{\mathrm{gap}}\lambda^2/\lambda_p^2$, where λ_p is the plasma wavelength associated with ω_p, $\lambda_p = 2\pi c_0/\omega_p$, and c_0 is the speed of light in vacuum. The resonant wavelength λ_{res} is then found near $\lambda_{\mathrm{res}} \approx \lambda_p\sqrt{2D_f/(\pi d_{\mathrm{gap}}s)}\left[1 + (2D_f/(s\lambda_p))^2\right]^{0.25}$. This expression shows that the resonant wavelength scales with $\lambda_{\mathrm{res}} \propto 1/\sqrt{d_{\mathrm{gap}}}$ as $d_{\mathrm{gap}} \to 0$, as numerically found in Fig. 2.2d.

Separate tunnability of LAPs and TCPs

An interesting property of the TCPs in the structures described so far is that they interact only weakly with the low-energy LAP modes. Indeed any possible anticrossing of TCPs and this LAP mode is lifted (and therefore observed as a crossing) because the losses of the modes are larger than the interaction strength. As a technical point, we notice that the wavelength saturation of the lowest-energy longitudinal mode LAP$_1$ for the flat-gap antenna appears to correlate with the wavelength where the crossing with the transverse cavity mode TCP$_1$ occurs. It would thus be tempting to ascribe this saturation to the anticrossing behaviour. However, we have extensively investigated the charge
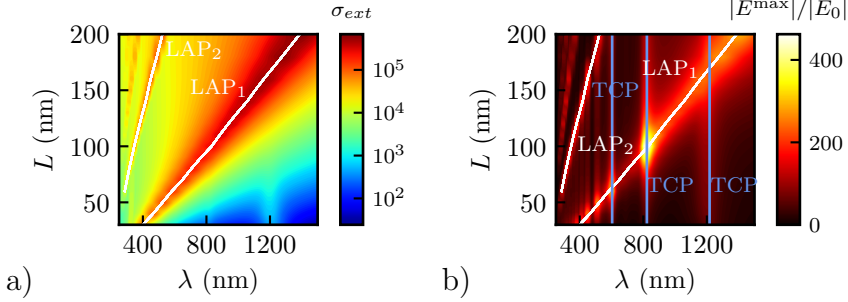
FIGURE 2.7: (a) Extinction cross-section σ_{ext} and (b) maximum near-field enhancement at the central plane $|E^{max}/E_0|$ for a flat-gap linear metallic antenna, as a function of wavelength and length of the rods L. The gap separation is $d_{\text{gap}} = 0.5$ nm, the diameter $D = 50$ nm and the facet size $D_f = 46$ nm. The lines are guides to the eye indicating the evolution of some of the LAPs (oblique white lines) and TCPs (vertical blue lines).

distributions around the crossing point and found no evidence of a change of mode symmetry that one would expect from an anticrossing.

The essentially independent behaviour of the two types of modes is supported by our previous models, which describe the LAPs (Sec. 2.1.2) and TCPs (Sec. 2.1.2) separately. It is noteworthy that although the length L of the rods critically affects the LAPs, this parameter does not influence the TCPs according to our simple model. Likewise, Fig. 2.2 showed how, for small d_{gap}, the exact gap separation distance controls the resonant position of the TCPs but does not significantly influence the LAPs. All this features suggests that the LAPs and the TCPs can be tuned independently by changing the geometry of the antenna arms and by altering the gap morphology at will.

Figure 2.7 emphasizes the very different effect of L on the two sets of modes, for a narrow $d_{\text{gap}} = 0.5$ nm gap. The far field in Fig. 2.7a shows LAPs that redshift clearly as the length increases. The effect is also visible in the near field (Fig. 2.7b). The TCPs are identified by the narrow lines in the near field enhancement (Fig. 2.7b), whose spectral position is, as expected, essentially independent on the rod lengths. In general, large enhancements are obtained for a given TCP (most notably for even TCPs), when the LAP mode overlaps the TCP, in a hint of cooperative enhancing effect of both types of modes.

Figure 2.2b,d and Fig. 2.7 thus illustrate that it is possible to tune the resonant energy of a TCP by a convenient cavity design and, at the same time, to control the strength of this mode by tuning the low energy LAP mode via the geometry of the rest of the antenna (L).
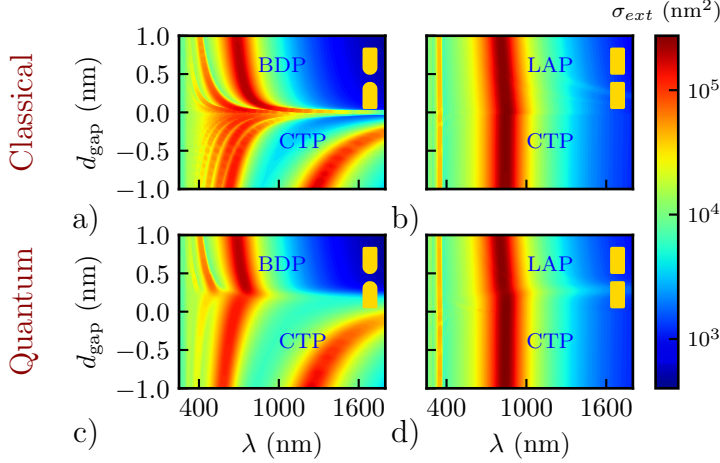
2.2 Subnanometer gaps: the tunneling regime

FIGURE 2.8: Extinction cross-section σ_{ext} of metallic gap-antennas ($L = 100$ nm, $D = 50$ nm) as a function of the wavelength λ and gap separation d_{gap} for (a,c) spherical and (b,d) flat terminations ($D_f = 46$ nm) obtained using (a,b) classical and (c,d) the QCM calculations. LAP, BDP, TCP and CTP modes are labelled in the plots. Linear separation distance scale is used in all the figures. Notice the logarithmic scale used for the colour coding in all the figures. Negative distances correspond to overlapping structures.

The results discussed up to now introduced the classical response of the nanoantennas. However, when the distance of the gap between the two antenna arms reaches subnanometric dimensions, quantum effects[131–133] such as tunneling of electrons across the gap start to play an important role for the optical response of the system[21,22,87,134]. To model this effect, we consider the same antennas as in the previous section and use the QCM[24] within a local framework. As explained in Sec. 1.1, the QCM accounts for electron tunneling *via* the insertion of an effective material in the gap, which has a conductance equivalent to that obtained from a full quantum mechanical calculation[24,25].

In Fig. 2.8 we plot the extinction cross-section for spherical-gap antennas (Fig. 2.8a,c) and flat-gap antennas (Fig. 2.8b,d) as a function of the gap separation and wavelength using both classical (Fig. 2.8a,b) and QCM (Fig. 2.8c,d) calculations. As tunneling only becomes significant for distances $d_{\text{gap}} \lesssim 0.5$ nm[24], we focus here on very narrow gaps where $d_{\text{gap}} < 1$ nm. We also consider negative separation distances, corresponding to the case of overlapping antenna arms. A negative distance d_{gap} correspond to a separation of $L - |d_{\text{gap}}|$ between the centre of the two rods.

The classical results for the spherical case (Fig. 2.8a) before contact reproduce the behaviour already observed in Fig. 2.2a for larger gap separations, emphasizing the divergent redshift of the different bonding modes as the gap closes. An unphysical discontinuity is present at contact ($d_{gap} = 0$), separating the non-touching and the overlapping regimes[45]. For $d_{gap} < 0$ Charge Transfer Plasmons (CTPs)[47,135] appear in the spectrum, blueshifting with increasing overlap. As discussed in Sec. III of the Introduction, the CTPs are plasmonic modes that emerge when charges are transferred from one antenna arm to the other. The lowest-energy CTP is excited at a characteristic low energy.

The QCM results for the spherical-termination antennas (Fig. 2.8c), display trends consistent with previous work for two gold spheres[22,29,87] that were described in detail in Sec. IV of the Introduction. In this case, instead of a discontinuity at contact, we find a gradual transition between the non-touching and the overlapping regimes with a distinctive change from modes that redshift as the gap narrows to modes that blueshift with further decrease of d_{gap}. The change occurs near a threshold distance $d_{th} \approx 0.2$ nm to 0.3 nm that can be understood as the separation where the amount of charge being transported across the gap in a fraction of the optical period is comparable to the charges induced at the metal interfaces at the gap[21,47]. For $d_{gap} \gtrsim d_{th}$ the modes are fundamentally the same as those obtained from the classical calculations. For $d_{gap} \lesssim d_{th}$, charge transfer is allowed and the modes can be considered as CTPs even if physical contact has not been established. For overlapping arms ($d_{gap} < 0$), we obtain significantly less CTPs in the presence of tunneling compared to the classical results, which can be related to a *softening* of the contact regions between the two rods due to charge transfer in the quantum treatment.

The far-field spectra for narrow flat gaps[136] in Fig. 2.8b,d behave very differently. The extinction cross-section calculated using the classical and QCM approach is very similar and insensitive to variations of the gap separation. In both cases, the gap behaves as a short circuit and the response corresponds to that of a single rod of approximately twice the length $2L$. In the classical case, this short circuit is due to physical contact ($d_{gap} < 0$) or to a large capacitance ($d_{gap} > 0$, see Sec. 2.1.2). In the QCM electron tunneling assists in reducing the gap impedance also for $d_{gap} > 0$. This result indicates that the gap morphology needs to be considered when trying to understand if a given CTP mode structure is due to quantum effects[136] in order to correctly interpret experimental results.

Figure 2.9 shows the maximum field enhancement $|E^{max}/E_0|$ for both types of antennas as a function of gap separation and wavelength, for positive separation distances $d_{gap} > 0$. The classical results display the same relationship between the near-field (Fig. 2.9a,b) and far-field (Fig. 2.8a,b) results as those in Fig. 2.2 for larger gap separations. In particular the coexistence of TCPs and LAPs for flat gaps is apparent in Fig. 2.9b,d. The field enhancement produced at the spherical gap is noticeably larger than for its flat counterpart due to a
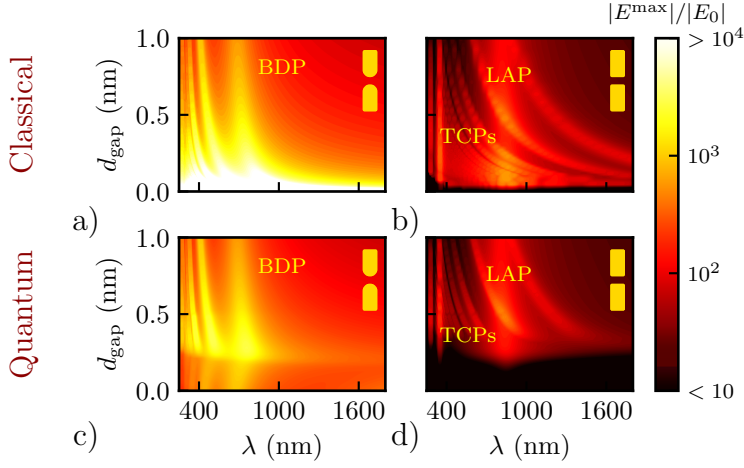
FIGURE 2.9: Maximum electric field enhancement $|E^{\max}/E_0|$ at the central plane of a metallic antenna gap ($L = 100$ nm, $D = 50$ nm) as a function of the illumination wavelength λ and the separation distance, d_{gap}, for (a,c) spherical and (b,d) flat gaps ($D_f = 46$ nm) obtained using (a,b) classical calculations and (c,d) the QCM. LAP, BDP and TCP modes are labelled in the plots. Linear separation distance scale is used in all the figures. Notice the logarithmic scale used for the colour coding in all the figures.

more pronounced concentration of the field in the spherical case (more reduced area of coupling).

The QCM results in Fig. 2.9c,d show that the electric field in the gap become quenched for gap separations below a few Ångstroms because of the onset of electron tunneling[29,87]. The charge transfer across the gap counteracts the strong charge pile-up predicted by the classical description. The electric field quenching for flat gap termination (Fig. 2.9d) occurs at longer separation distances than for the spherical case. For flat gaps the quenching of the TCPs occurs for gap separations of $d_{\text{gap}} \approx 0.4$ nm, while for spherical terminations the quenching occurs at $d_{\text{gap}} \approx 0.3$ nm, predicting a large sensitivity of the TCPs to tunneling. Thus, our results for flat narrow gaps indicate that, although the tunneling does not affect the extinction cross-section, which is dominated by the global current flow in the vertical direction, a quantum mechanical description is essential for the modeling of the local charge concentrations and thus the correct estimation of the local field enhancements.

2.3   Generalization of the results

FIGURE 2.10: Schematics of the geometries used for the general study of the effect of the size of the gaps' flat facet. (a) Gap-antenna formed by two cylindrical rods of length $L = 100$ nm, diameter $D = 50$ nm and with a facet at the gap ends of diameter D_f. S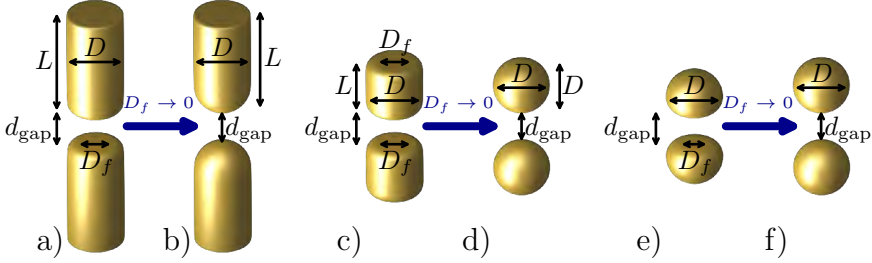tarting from $D_f = 46$ nm, the gap-antenna in (a) is progressively transformed into a (b) rod gap-antenna with rounded terminations at the gap for $D_f = 0$ nm. The outermost ends of the rods are flat with $D_f = 46$ nm. (c) Short rod gap-antenna formed by two rods of equal length and diameter $L = D = 100$ nm and with both ends of the rods caped by a facet of diameter D_f. Progressively decreasing the facets size from $D_f = 96$ nm the wide rod is transformed into a dimer of spheres (d) for $D_f = 0$ nm. (e) Faceted dimer of spheres of diameter $D = 100$ nm and with a faceted hemisphere at the gap of diameter D_f. (f) For $D_f = 0$ nm we recover a dimer of perfect spheres. All the structures are rotationally symmetric and made of gold.

In the previous sections we studied in detail the optical response of rod gap-antennas and emphasized the differences that arise when having a spherical or a flat termination at the gap. We showed that the effect of electron tunneling can be very different for flat and rounded terminations.

In this section we analyse different gap-nanoantenna systems to obtain more general conclusions. In real experimental situations, perfect control over the geometry of the nanoparticle is often not possible because of faceting that occurs in the fabrication process. We thus consider flat facets of different sizes at the gap terminations of the nanoantennas, which not only make the antennas more realistic compared to perfectly rounded terminations, but also allows us to study the transition from large flat facets to spherical terminations at the gap. We calculate the response for several geometries of the antenna arms to establish whether the different trends are robust. In all cases we consider the gold dielectric function obtained experimentally[35] to describe the metal instead of using an idealized Drude model. By doing so, we include the contribution of d-band electrons in the high energy range of the response that is important for noble metals such as gold or silver.

In Fig. 2.10 we sketch the geometries considered in this section. Figure 2.10a shows a large aspect-ratio gap-antenna with the same dimensions as the one studied in previous sections ($L = 100$ nm, $D = 50$ nm and with $D_f = 46$ nm for the rod termination away from the gap). We vary the diameter of the facet at the gap $D_f = 46$ nm, 34 nm, 24 nm, 14 nm, 0 nm ending with the geometry in Fig. 2.10b. $D_f = 46$ nm and $D_f = 0$ nm correspond to the flat and spherical termination geometries in Fig. 2.1 (here with the use of the experimental gold permittivity). The structure in Fig. 2.10c is similar but with parameters $L = D = 100$ nm and $D_f = 96$ nm, 68 nm, 44 nm, 20 nm, 0 nm. In this case, the length and the diameter are of the same size and we change the faceting at both ends of the antenna. Thus, this small aspect-ratio nanoparticle resembles a dimer of wide rods for very large facets D_f and it becomes a dimer of spheres for $D_f = 0$ nm (Fig. 2.10d). The last geometry that we study is sketched in Fig. 2.10e. The structure corresponds to a dimer of spheres of $D = 100$ nm diameter, where the regions facing the gap are faceted with $D_f = 48$ nm, 36 nm, 20 nm, 8 nm, 0 nm. A dimer of spheres is retrieved for $D_f = 0$ nm (Fig. 2.10f). In this last case we do not use very large facets because otherwise the overall spherical geometry would be distorted.

Figure 2.11 show the results for each facet size (from top to bottom $D_f = 46$ nm, 34 nm, 24 nm, 14 nm, 0 nm) for the rod gap-antennas depicted in Fig. 2.10a,b ($L = 100$ nm, $D = 50$ nm). The left column corresponds to the extinction cross-section, and the right column represents the maximum near-field enhancement at the central plane at the gap $z = 0$. The difference between the results in Figs. 2.11a,b,i,j and those in Figs. 2.8c,d and Figs. 2.9c,d are due to the contribution of the interband transitions of d-electrons to the permittivity of gold for $\lambda \lesssim 650$ nm, not considered previously. In particular, when including the d-electron contribution the plasmonic resonances only emerge for $\lambda \gtrsim 500$ nm and are significantly broadened for $\lambda \lesssim 650$ nm. For $\lambda \gtrsim 650$ nm the results become very similar to those obtained for the Drude metal.

Analysing the evolution with D_f in Fig. 2.11, we notice that the transition from the largest flat-facet to the spherical termination is continuous. For example, the far-field response clearly shows that the saturation of the lowest-energy LAP that was previously discussed for $D_f = 46$ nm (Fig. 2.11a) also occurs for $D_f = 34$ nm (Fig. 2.11c). The similarity between the spectra of these two structures can make it difficult to distinguish between both geometries from far-field spectroscopy in practical experimental realizations. For antennas with the smallest facet sizes, $D_f = 24$ nm, 14 nm, 0 nm, we observe a more marked redshift of the BDP as the gap closes.

D_f also affects strongly the resonant frequency of the lowest-energy CTP. As expected from previous results (Fig. 2.8c) , the extinction cross-section obtained in Fig. 2.11i for the spherical termination shows that the lowest-order CTP appears just before contact ($d_{\mathrm{gap}} \lesssim 1$ Å) at much lower energies than the rest of the modes ($\lambda \approx 1900$ nm) and strongly blueshifts as the particles

FIGURE 2.11: Extinction cross-section σ_{ext} (a,c,e,g,i) and maximum field enhancement at the gap $|E/E_0|_{max}$ (b,d,f,h,j) of the faceted rod gap-antenna in Fig. 2.10a,b ($L = 100$ nm $D = 50$ nm) with facets $D_f = 46$ nm (a,b), $D_f = 34$ nm (c,d), $D_f = 24$ nm (e,f), $D_f = 14$ nm (g,h), $D_f = 0$ nm (i,j), where we use the experimental dielectric permittivity function of gold. The colour plots show the changes in the spectra as a function of separation distance, with $d_{gap} < 0$ nm corresponding to overlapping nanoparticles. LAP, BDP, TCP and CTP modes are marked in the cases where they are clearly identifiable. In the case of $D_f = 24$ nm it is difficult to unambiguously identify the character of the plasmonic modes.

merge. However, the presence of even a small facet changes considerably the wavelength at which the CTP appears. For example, the far field response for $D_f = 14$ nm (Fig. 2.11g) shows a CTP that emerges at much lower wavelength ($\lambda \approx 1200$ nm) and at a slightly larger separation ($d_{\text{gap}} \approx 2.5$ Å). The difference is likely due to the larger tunneling current that flows across the full flat area compared to just the apex of a spherical termination.

The enhancement of the near field (right column of Fig. 2.11), grows as D_f decreases due to the accumulation of charges in the smaller facet region. Therefore, this calculations suggest that if a strong maximum local near field in the gap is needed, it is convenient to optimize the fabrication process to reduce the facets and obtain a spherical-gap geometry as perfect as possible (see Sec. 3.2 for longer discussion in the case of chains). However, gap-antennas with larger facet sizes present a more complex mode structure with the combination of LAPs and TCPs. The TCPs are observable for facet sizes of $D_f = 46$ nm and 34 nm, with more modes for the largest facets. As D_f becomes smaller but still with a moderate value ($D_f \sim 24$ nm), it is harder to distinguish if a given mode is a TCP, a LAP or a resonance that is a combination of both.

Figure 2.12 show that increasing the diameter to obtain the wide rod with $L = D = 100$ nm (sketch in Fig. 2.10c) does not significantly affect the main qualitative features of the far-field (left column) or near-field (right column) properties. There is also a continuous transition of the optical response (top to bottom) from large facets, where the saturation of the LAP (far field) and a large number of TCPs (near field) are observed, to the dimer of spheres, where we find the typical fading of the BDPs and the emergence of CTPs as tunneling is established at a threshold distance of $d_{\text{gap}} \approx 0.25$ nm. The main difference of this geometry is the lower resonance energy of a given TCP for a fixed d_{gap}, due to the larger D_f (Eq. (2.2)). Interestingly, these TCP modes are slightly more radiative than for the $D = 50$ nm rods (compare Fig. 2.12a with 2.11a, for example).

The strong qualitative similarity between Fig. 2.11 and Fig. 2.12 suggests that, for ultranarrow gaps, the influence of the exact gap morphology in the optical response is robust with respect to the exact entenna geometry. In particular, both nanoantennas show a different effect of tunneling in the optical response for large facets vs. spherical gaps. This is further emphasized by studying the optical response of the faceted-sphere dimer of diameter $D = 100$ nm (sketch in Fig. 2.10e,f), shown in Fig. 2.13. In this case, the geometry is similar to the wide rod geometry in the gap region but very different far from it. The results are very similar to those of the wide rods in Fig. 2.12, as observed for example, by comparing Figs. 2.13e,f with Figs. 2.12g,h, where both structures have the same $D_f = 20$ nm gap facet (notice that in Fig. 2.13 we consider values of D_f only up to 48 nm). The similarity emphasizes that for structures of equivalent size, the far-field and the near-field response depend much more strongly on the characteristics of the gap rather than on the overall shape of the nanoparticles.
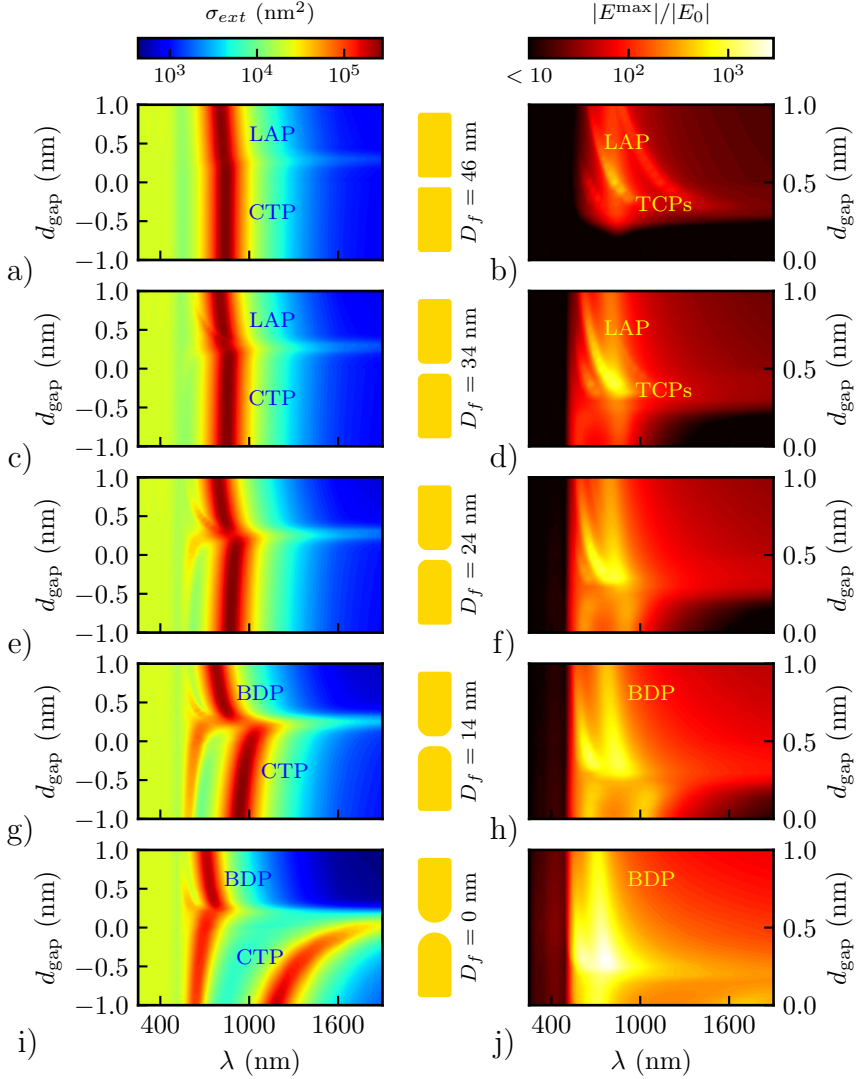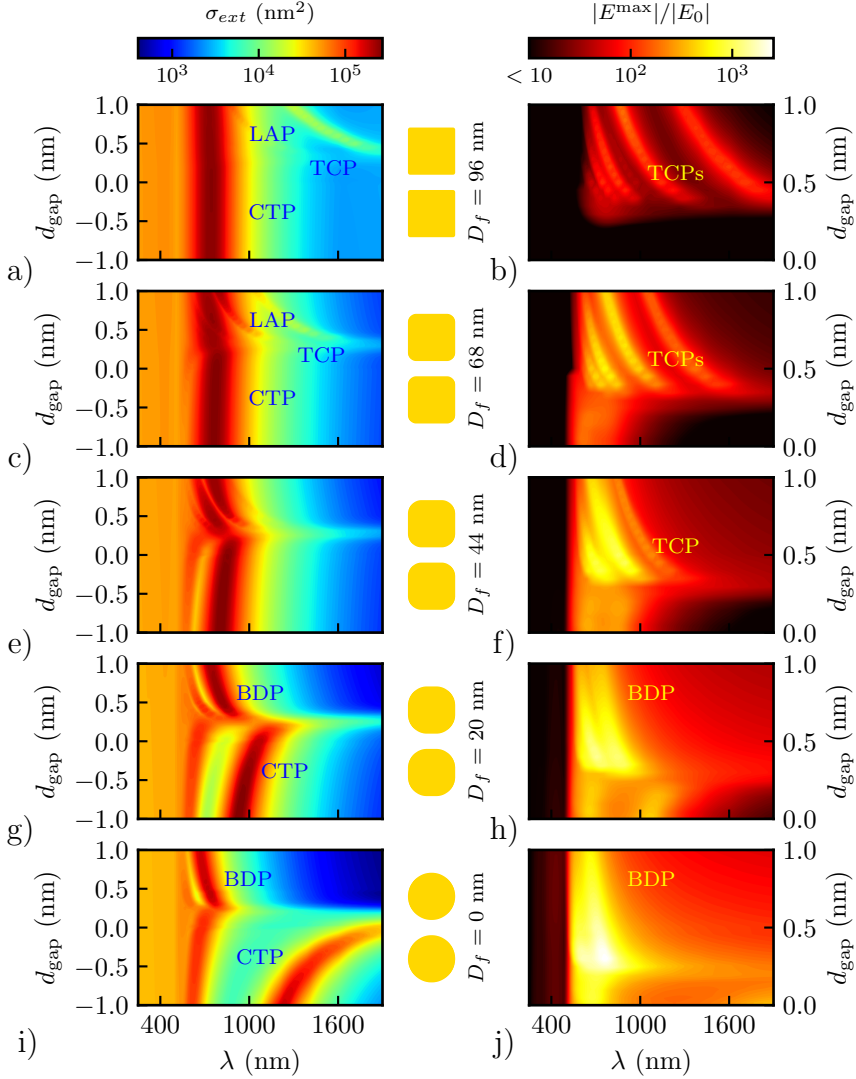
FIGURE 2.12: Extinction cross-section σ_{ext} (a,c,e,g,i) and maximum field enhancement at the gap $|E/E_0|_{max}$ (b,d,f,h,j) of the faceted wide rod gap-antenna in Fig. 2.10c,d ($L = 100$ nm $D = 100$ nm) with facets $D_f = 96$ nm (a,b), $D_f = 68$ nm (c,d), $D_f = 44$ nm (e,f), $D_f = 20$ nm (g,h), $D_f = 0$ nm (i,j) using the experimental dielectric permittivity function of gold. The colour plots show the changes in the spectra as a function of separation distance, with $d_{gap} < 0$ nm corresponding to overlapping nanoparticles. LAP, BDP, TCP and CTP modes are marked in the cases where they are clearly identifiable. In the case of $D_f = 44$ nm is difficult to unambiguously identify the character of the plasmonic modes.
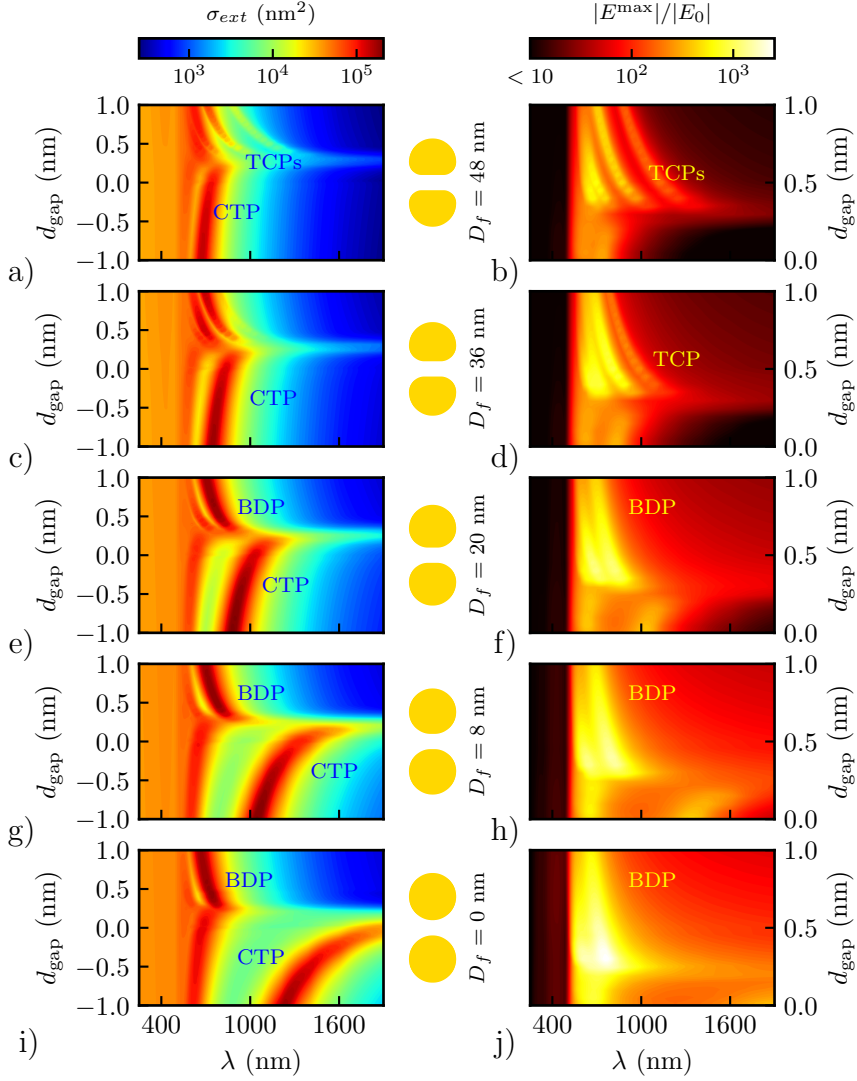
FIGURE 2.13: Extinction cross-section σ_{ext} (a,c,e,g,i) and maximum field enhancement at the gap $|E/E_0|_{max}$ (b,d,f,h,j) of faceted sphere dimers in Fig. 2.10e,f ($D = 100$ nm) with facets $D_f = 48$ nm (a,b), $D_f = 36$ nm (c,d), $D_f = 20$ nm (e,f), $D_f = 8$ nm (g,h), $D_f = 0$ nm (i,j) using the experimental dielectric permittivity function of gold. The colour plots show the changes in the spectra as a function of separation distance, with $d_{gap} < 0$ nm corresponding to overlapping nanoparticles. LAP, BDP, TCP and CTP modes are marked in the cases where they are clearly identifiable.

2.4   Summary and Discussion

The behaviour of metallic gap-antennas with flat faceted terminations and ultra-narrow gaps has been studied in detail in this chapter, paying special attention to the differences in the optical response of flat vs. spherical terminations at the gaps. We have found that the morphology of the gap is critical to understand the optical response not only for distances where classical calculations are appropriate ($d_{\mathrm{gap}} > 0.5$ Å), but also for $d_{\mathrm{gap}} < 0.5$ Å. Interestingly, the emergence of electron transfer in these ultra-narrow gaps affects very differently the optical response depending on the size of the facet D_f and the type of electromagnetic fields addressed (far or near field). This shows the complex role of electron tunneling in the optoelectronic response of plasmonic systems with ultra-narrow gaps.

The results obtained for gap-antennas with spherical terminations is similar to that of dimers composed by spherical particles, with a set of bonding modes that strongly redshift with narrowing gaps and that are observable in both the near- and the far-field response[45]. Once the gap-antenna enters the tunneling regime, for subnanometric gaps, the optical response is modified[21,22]. The redshifting BDP fade away, blueshifting CTPs appear before physical contact, and the near field in the gap is quenched. Once the gap is closed and the merging process takes place, the CTPs continue blueshifting as the particles merge deeper.

In contrast, for flat-gap antennas with large facets, we find two different sets of modes[137–139], Longitudinal Antenna Plasmons (LAPs) and Transverse Cavity Plasmons (TCPs). The LAPs are present in the far- and near-field spectra, redshifting as the gap gets closed but saturate spectrally for narrow gaps. The saturation is not linked to the tunneling of electrons through the gap since it is already observed for gap distances where tunneling is not relevant and when tunneling is ignored. This can be qualitatively understood using a model based in circuit theory, where the flat gap is modelled as a capacitor whose impedance tends to zero for ultra-narrow gaps (behaving as a short circuit) and therefore the resonance wavelength no longer depends on d_{gap}. In contrast. the TCPs are very sensitive to the separation distance d_{gap} showing a very strong redshift as the gap closes. These modes can can be described using a simple Fabry-Pérot-like model originated from the interference of a wave travelling back and forth along the flat gap surfaces. When tunneling sets on, the near field in the flat gap region quenches faster than in the spherical case, due to the larger area of tunneling.

In the case of large aspect-ratio antennas with large facets, the TCPs are essentially dark modes[140] that have a negligible effect on the far-field optical properties. We also find that the TCPs and the LAPs can be tuned independently for this geometry, with both modes contributing strongly to the enhancement of the near-field response. The flexibility on the independent control of

LAP and TCP resonances can be advantageous to finely tune the near- and far-field properties of this plasmonic system. On the other hand, structures with smaller aspect-ratios, in particular the faceted dimers of spheres, show a significant radiation of TCPs in the far field. Studies of related structures[130] have shown that conveniently designed plasmonic structures can present significant coupling between LAPs and TCPs.

Given the robustness of the results obtained in Sec. 2.3, we believe that the cavity modes can be supported by any plasmonic junction presenting flat areas, assuming that the lateral dimensions of the cavity are comparable to the plasmonic wavelength in the gap (see Eq. (2.2)), and that the separation distance is relatively small and remains approximately constant along the entire gap. On the other hand, due to the sensitivity of the spectral position of the TCPs to the gap distance, even small local variations on the gap separation may suppress the formation of these modes, or confine them to particular regions within the gap.

These results can contribute to address discrepancies and inconsistencies in experimental results where the fine details of the morphology of a plasmonic nanocavity are often not known. The qualitative differences between flat and spherical terminations are robust regarding the overall shape of the nanoantennas. However, the exact resonance frequencies are very sensitive to morphological changes of the cavities at the nanometric level. Thus, a small variation in the gap facets can quantitatively modify the performance of a particular optoelectronic process providing an explanation for the frequent variability in experimental results. Fabrication technologies with fine control over the nanoparticle shape are thus key to produce systematic experimental output[22,141]. The exact field distribution in a plasmonic cavity also determines the performance of many field-enhanced spectroscopies, such as in Tip-Enhanced Raman Spectroscopy (TERS)[142,143], or in scattering-type Scanning Near-field Optical Microscopy (s-SNOM)[144]. The variation of the morphology of the tip-on-substrate cavities in these spectroscopies could indeed explain the large variability in signal quality and spectral behaviour, often found in experiments from tip to tip[145]. Similarly, modifications of the gap can also determine the yields and properties of many optoelectronic processes such as in photoemission[146,147] or in nonlinear plasmonics[148].

Furthermore, the sensitivity to the fine details of the cavity, even reaching down to atomic-scale variations within the gap, is not always detrimental. If controlled, as for example in a particle-on-mirror geometry[149], the dependence on the faceting can serve as an optical monitor of complex photochemical processes[48,150] or to trace transport properties at optical frequencies[48,136], thus allowing the access to information that cannot be reached by other techniques.

Last, experimental realizations that seek to study the tunneling regime should also consider the differences that the faceting of the gap termination or the exact atomic structure of the nanoparticle introduce[28,151,152]. Identification of the tunneling regime through far-field methods might become a very difficult

task if the geometry of the plasmonic system presents large facets.

The results presented in this chapter stress the importance of the morphology of the gap for applications in nanophotonics. The possibility of independent control of the two types of modes (LAPs and TCPs) for adequately engineered nanoantennas provides a valuable mean to control the far-field and near-field properties separately. Flat gap termination antennas may also find applications beyond the manipulation of light under plane-wave illumination. The faceted gap geometry may also be an adequate morphology to achieve strong coupling with self-assembled molecules[153,154] extended over the entire gap. For applications exploiting subnanometric gaps it is necessary to consider the importance of tunneling, and particularly the quenching of the near field. The possibilities of the flat gap morphology could thus open new venues for simultaneous and independent control of the near-field and far-field responses in nanophotonics.

Chapter 3

Multi-gap plasmonic structures

In the previous chapters we have studied plasmonic systems with a single gap and discussed the influence of electron tunneling and gap morphology in the linear optical response. However, plasmonic systems with more than 2 particles and thus separated by multiple gaps can present a richer variety of plasmonic resonances and offer additional opportunities for tuning the response due to the hybridization of the modes of all the nanoparticles[155,156].

We first consider the optical mode structure of trimers. In the introduction and in Ch. 2 we have focused on modes of electric character sustained by a dimer. Furthermore, we always illuminated the system using linearly polarized plane waves, thus exciting bright modes, i.e. resonances with net dipole moment that are excitable by a conventional laser. Nevertheless, magnetic and dark modes (plasmonic resonances that cannot be directly excited by paraxial light owing to their lack of a net dipole moment) can also be excited in more complex configurations. For example, magnetic resonances at optical frequencies have been shown to improve the sensitivity of circular dichroism spectroscopy[157,158] as well as to enable tunable permeability for novel metamaterials[159–163]. Dark modes are also of interest in the development of ultrasensitive molecular detectors[156,164] due to the narrow spectral widths typical of these resonances.

The influence of quantum effects on these modes remained unexplored, largely due to the challenges associated with fabricating and simulating sub-nanometer features in complex nanoparticle geometries[5,155]. In Sec. 3.1 we thus use the trimer 'metamolecule' (three nanospheres arranged in a triangular shape) to investigate theoretically and experimentally the influence of tunneling in electric, magnetic and dark plasmonic modes. In this study we consider perfectly spherical particles.

On the other hand, we have seen in Ch. 2 that the details of the gap morphology can strongly influence the optical response of plasmonic dimers with narrow gaps. In Sec. 3.2 we consider chains of nanoparticles separated by

nanometre gaps, and systematically change the gap morphology of the constituents to explore how the faceting influences the optical response of such chains. This results can be used to understand the optical behaviour of self-assembled aggregates, as it has been demonstrated that the plasmonic response of these aggregates can be often described as the combination of plasmonic chain resonances[165].

3.1 The trimer metamolecule: effect of electron tunneling in electric, magnetic and dark modes

In this section, we investigate theoretically (with experimental support by Jennifer Dionne's group in Stanford) nanoparticle trimers as one of the most basic plasmonic "metamolecules" that support a rich variety of resonances of different fundamental character[155,156,166–169]. We focus on tracking electric, magnetic, and dark plasmonic modes as the trimer geometry evolves from a situation with very narrow gaps between the nanoparticles to a situation where the nanoparticles have established physical contact, allowing to observe the transition from the classical to the quantum regime[23].

We choose silver nanoparticles as the constituents of the trimer owing to their relatively low losses, strong electric polarizability and capacity to interact strongly with each other. These properties enable the formation of distinct modes with relatively narrow spectral linewidths. We theoretically model the dielectric function of the nanospheres using experimental bulk dielectric functions[35] and perform rigorous 3-dimensional electromagnetic calculations using the MNPBEM solver developed by the group of Prof. U. Hohenerster[37,170,171] The effect of tunneling is introduced using the Quantum Corrected Model (QCM)[23] (see Sec. 1.1). Figure 3.1 presents a sketch of the metamolecule geometries that are analysed throughout the section. Figure 3.1a shows three spheres of diameter $D = 25$ nm whose centres are at the vertex of an equilateral triangle. The three gaps between the particles have the same dimensions. In Fig. 3.1b we have sketched the coalesced equilateral configuration. As in panel (a) the centres of the three $D = 25$ nm spheres are located at the vertex of an equilateral triangle but now the gap between the particles has been decreased and the spheres are in contact. In the last example in Fig. 3.1c, the top particle has contacted the bottom ones while the later remain separated. In this configuration the centres of the particles are located at the vertex of an isosceles triangle. The spheres are surrounded by vacuum and excited by an 80 keV electron beam with a spatial width of 0.2 nm.

To experimentally access the quantum regime, a combination of Scanning Transmission Electron Microscopy (STEM) and Electron Energy-Loss Spectroscopy (EELS) is implemented. Both techniques use an electron beam that
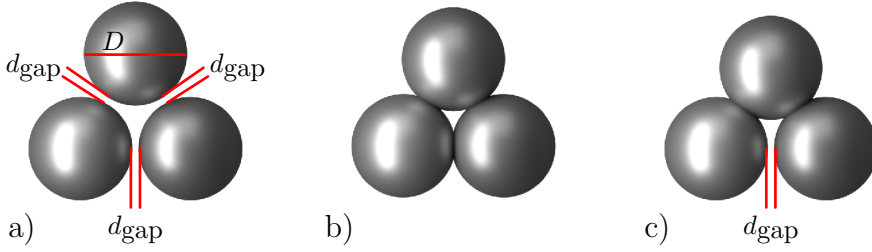
FIGURE 3.1: Representation of the trimer metamolecule composed by three Ag spheres of diameter $D = 25$ nm and surrounded by vacuum. (a) Fully separated trimer with equilateral configuration: the three gaps have the same dimensions (d_{gap}). (b) Coalesced trimer with equilateral configuration: Starting from the geometry in (a), the three gaps have closed reducing the distance between the centres on the nanoparticles. (c) Coalesced trimer with isosceles configuration: Starting from the geometry in (a), the top particle has contacted the bottom ones while the bottom gap remains unaltered (d_{gap}).

is focused on the sample to extract information about the system. STEM allows to obtain images of the nanoparticles with sub-nanometric resolution[172] by scanning the sample with the electron probe and recording the transmission of electrons at each step. EELS generates spectral information about the optical resonances in the system by measuring the energy that the electrons loose when they pass through or nearby the sample, for example due to the excitation of plasmons. Additionally, the focused electron beam can be used to induce particle motion, allowing dynamic modification of the interparticle separation. This phenomena is likely a combination of coulombic attraction and surface diffusion: the electron beam can induce polarization of the particles into aligned, attractive dipoles[173,174] as well as facilitate the diffusive movement of the surface atoms of the nanoparticles[172,175–177]. Spheres of 25 nm diameter are selected for this study because they are sufficiently large to exhibit a detectable plasmonic magnetic mode EELS signal and at the same time small enough to be responsive to electron beam manipulation. The particles are synthesized according to a previously reported[178] colloidal chemistry procedure.

The electron-beam-induced merging phenomenon is illustrated in Fig. 3.2, where a series of silver nanosphere trimer TEM images depict decreasing interparticle separation distances. Initially, the 25-nm-diameter spheres self-assemble into an equilateral triangle trimer with gap sizes of ~ 1 nm (Fig. 3.2a). After interaction with a focused electron beam, the particles proceed to converge and achieve Ångström-scale separations (Fig. 3.2b). Upon further coalescence, physical connections are established (Fig. 3.2c), which ultimately broaden and recrystallize to create fully-merged aggregates (Fig. 3.2d). This final form remains relatively stable and is no longer substantially affected by the electron beam. More details on the nanoparticle's synthesis methodology
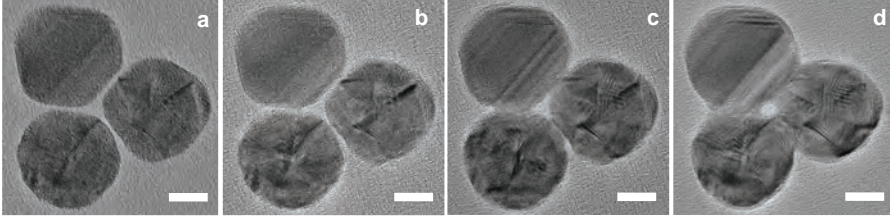
FIGURE 3.2: Aberration-corrected STEM images of a silver nanosphere trimer with particles converging and coalescing under the influence of the electron beam. The particles are 25 nm in diameter and supported on an 8 nm-thick SiO$_2$ membrane substrate. The electron beam induces particle convergence from a separation of 1 nm (a) down through sub-nm gaps (b) until particle contact (c) and ultimate recrystallization into a single entity (d). Scale bars equal 10 nm. Experiments performed by Dionne's group in Stanford.

as well as in the STEM-EELS experimental set-up are discussed in Ref. [23].

For the comparison between theory and experiments a few considerations are needed. The simulations consider perfectly spherical nanoparticles suspended in vacuum while in the experiments the trimers are deposited on a SiO$_2$ substrate that redshifts the resonances. Furthermore, the theoretical simulations assume a perfectly monochromated electron beam, while the experimental spectra have a small, ~ 0.1 eV, energy spread in the incident electrons, which results in the experimental spectra showing broader resonances than in the theory. Finally, the experimental spheres show faceting (not modelled in the calculation), which as discussed in Ch. 2 also shifts and broadens the resonances.

In the following, by analysing the experimental and theoretical plasmonic spectra (EELS) for well characterized trimer structures of known geometry (STEM), we discover prominent quantum effects on the electric and magnetic modes of trimers at the smallest separation distances but purely classical behaviour for the radially-symmetric dark mode.

3.1.1 Characterization of the plasmonic modes

Before exploring the modal evolution as the particles coalesce and electron tunneling becomes important, we study in Fig. 3.3 the plasmonic response of the trimer to electron excitation for the classical regime (≥ 0.5 nm gap sizes). We use an equilateral configuration of the nanoparticles with 0.5 nm gaps separating them and we place the EELS electron beam at the vertex (Fig. 3.3a-d), edge (Fig. 3.3e-h) and centre (Fig. 3.3i-k). The vertex position excites electric modes equivalent to the ones studied in previous chapters, while

the edge and centre excitations gives access to magnetic and dark plasmonic modes respectively.

As a first example of trimer excitation, the EELS simulation spectra for the beam situated at the vertex position is depicted in Fig. 3.3a. The plot features two primary resonance peaks at ~ 2.75 eV (blue circle) and ~ 3.5 eV (green triangle) together with a narrow peak at ~ 3.3 eV. To understand the specific nature of the observed ~ 2.75 eV and ~ 3.5 eV plasmonic resonances, simulated field maps are generated at the energies corresponding to the spectral peaks. The field maps are accompanied by arrows depicting the direction of the field at a given time snapshot. All the arrows in this chapter are normalized to have the same length in three dimensions; accordingly, smaller arrows indicate the presence of out-of-plane field components. As seen in Fig. 3.3b, the lower energy resonance of Fig. 3.3a can primarily be attributed to the electric bonding mode between the top and each of the bottom particles, in which the field directions exhibit a dominant vertical component and produces a strong near-field enhancement in the gap between the top and the bottom particles. This dipolar coupling in similar to the BDP resonance of dimers[22] (Introduction and Ch. 2). The higher energy peaks (3.5 eV) in the simulation correspond to a more complex combination of higher-order modes where the electric fields concentrate mainly next to the electron probe, as illustrated in Fig. 3.3c. This mode is often referred to as the pseudomode[179]. Figure 3.3d shows the experimental EELS spectrum that presents two peaks at ~ 2.6 eV and ~ 3.5 eV in excellent agreement with the calculated spectrum in panel (a). The main difference between the experiments and the calculations is that the latter shows the additional narrow peak at ~ 3.3 eV, which does not appear in the experimental spectrum probably due to the broadening of the two main peaks.

The calculated spectra of a second trimer system in this case with edge excitation at the right side of the top sphere is presented in Fig. 3.3e. As with the vertex excitation of Fig. 3.3a, electric bonding (blue circle at ~ 2.75 eV) and higher-order modes (pseudomode marked by the green triangle at ~ 3.5 eV) are observed, but unlike the vertex excitation, a third, weaker resonance at lower energy (purple square at ~ 2.5 eV) emerges. According to the simulated field maps at ~ 2.5 eV energy (Fig. 3.3f), the displacement current associated to the electric field (depicted with the arrows) circulates around the three-particles in a loop, which creates a magnetic field in the middle of the trimer normal to the plane of the figure (as will be explicitly shown in Fig. 3.6). This field distribution indicates that this resonance corresponds to a magnetic mode. The near-field map of the high-energy mode at ~ 3.5 eV is plotted in Fig. 3.3g. As in Fig. 3.3c, the combination of higher order modes strongly concentrates the near field in the area close to the electron beam. Good agreement is again obtained between the theoretical (Fig. 3.3e) and the experimental EELS spectrum in Fig. 3.3h, where the main difference is that the measured magnetic resonance peak at ~ 2.5 eV appears as a shoulder to the electric bonding mode.

BEM Field Map

Classical theory
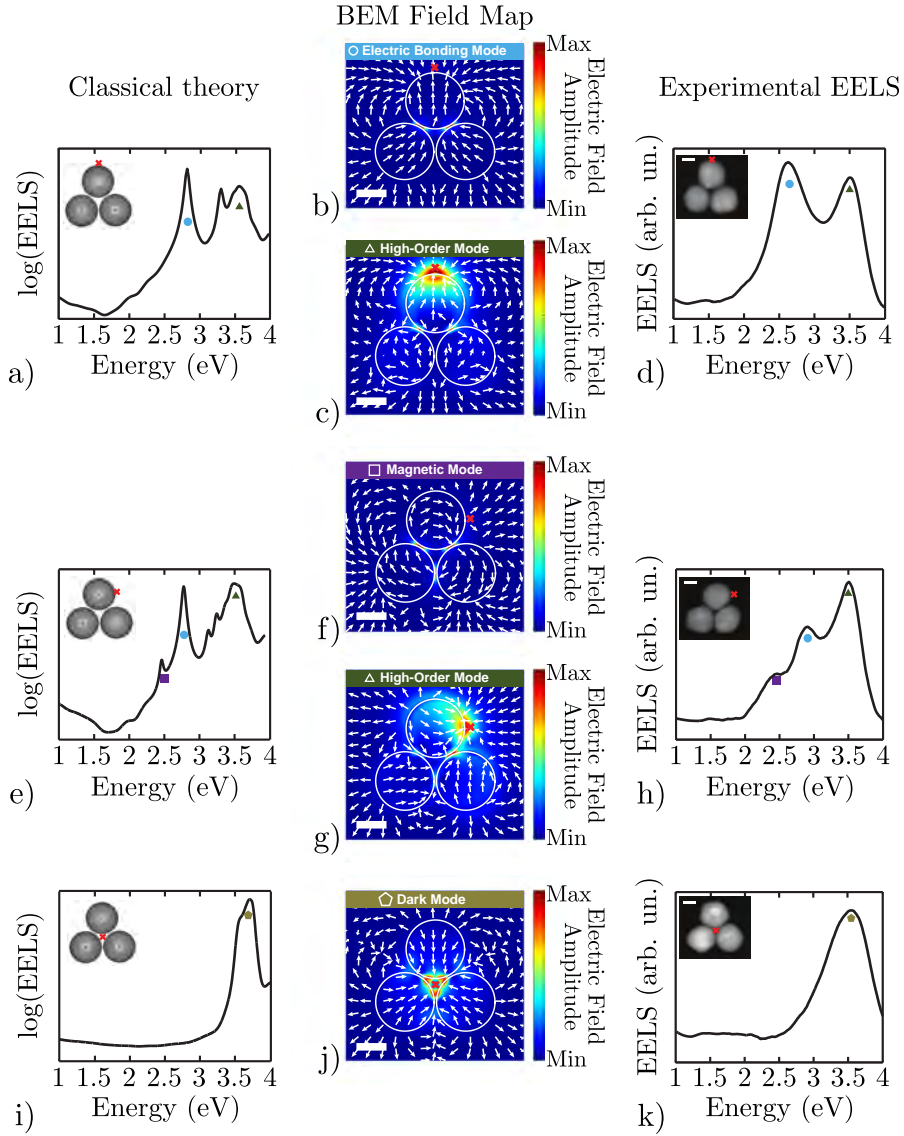
Experimental EELS

FIGURE 3.3: Optical response of trimers with vertex (a-d), edge (e-h), and centre (i-k) excitations (beam position indicated with a red cross in the field maps) are depicted with their BEM simulation spectra (a, e, i) and their experimental STEM-EELS (d, h, k). The nature of the resonance peak modes are identified with classical BEM field maps and arrows depicting a time snapshot of field direction (b, c, f, g, j). The prominent resonances include electric bonding mode (blue circle), magnetic mode (purple square), higher-order modes (green triangle), and dark modes (gold pentagon). All scale bars equal 10 nm. Classical calculations and experiments performed by Dionne's group in Stanford.

In Fig. 3.3i the third electron excitation position at the trimer's centre reveals a unique EELS resonance profile containing a primary, intense peak at ∼ 3.5 eV (gold pentagon) in both the calculation (Fig. 3.3i) and the experiment (Fig. 3.3k). The near-field map associated to the peak in Fig. 3.3j shows that the induced electric field in each nanoparticle is directed towards the centre of the trimer. Thus, the combination of the induced dipoles in each nanoparticle creates zero net-dipole moment making the mode not excitable with paraxial light[156]. This dark mode can, however, be accessed by the electron beam, as shown here.

We study next in Fig. 3.4 the case of a merged trimer under edge electron excitation. As observed in Fig. 3.4a the top sphere has contacted the two bottom spheres (effective distance between the centres of the top and bottom particles is $= (D - 0.5)$ nm.) while the bottom ones remain separated by a 0.5 nm gap. To perform the calculations a tangent toroidal surface (inner radius $= 0.5$ nm) is applied at the contact points to reduce the sharpness of the connection, ease the convergence of the calculations and avoid the unphysical strong shift of the resonances that was found in Fig. 6b of the Introduction. In this merged situation charge transfer occurs through the contact bridge and the classical treatment is a good approximation (as far as the edges are rounded). This approach has been used in previous studies to simplify particle merging evolution[22,45].

The peaks in the experimental EELS spectrum (Fig. 3.4c) are broader than the calculated ones in Fig. 3.4b, but otherwise the two spectra show very good correspondence, with 3 principal resonances around 1 eV, 2 eV and 3.5 eV. The main differences between the calculated and the experimental spectra are that the calculated narrow peak at ∼ 3.4 eV is likely to correspond to the shoulder of the high-energy pseudomode in the experimental spectrum and that the weak and narrow peak at ∼ 2.75 eV in Fig. 3.4b is not resolved in the experiment. The latter resonance is a post-merged gap mode similar to a BDP due to the interaction between the bottom particles[23] and will not be further discussed.

To analyse the nature of the main coalesced trimer resonances, we plot the calculated electric field maps for the main peaks in panels d-f. For the peak at ∼ 1 eV (red hexagon in Fig. 3.4b) the electric field (Fig. 3.4d) circulates around the three nanoparticles and therefore the mode is a magnetic-Charge Transfer Plasmon (mCTP) similar to the magnetic mode at ∼ 2.5 eV that we observed in the separated trimer (Fig. 3.3f), but at much lower energies. Due to the merging of the spheres, electrons can now circulate freely between the top and bottom spheres but cannot cross the bottom gap, thus creating stronger near field in this region. Figure 3.4e corresponds to a dipolar electric-CTP mode located at energy ∼ 2 eV, (orange rhomboid). The field lines flow from the bottom particles to the top sphere in a very similar manner as for the dipolar electric-bonding mode in Fig. 3.3b. However, in the coalesced trimer charges can freely flow between the top and bottom particles (similart to the CTPs studied in the introduction and Ch. 2). Last, Fig. 3.4f
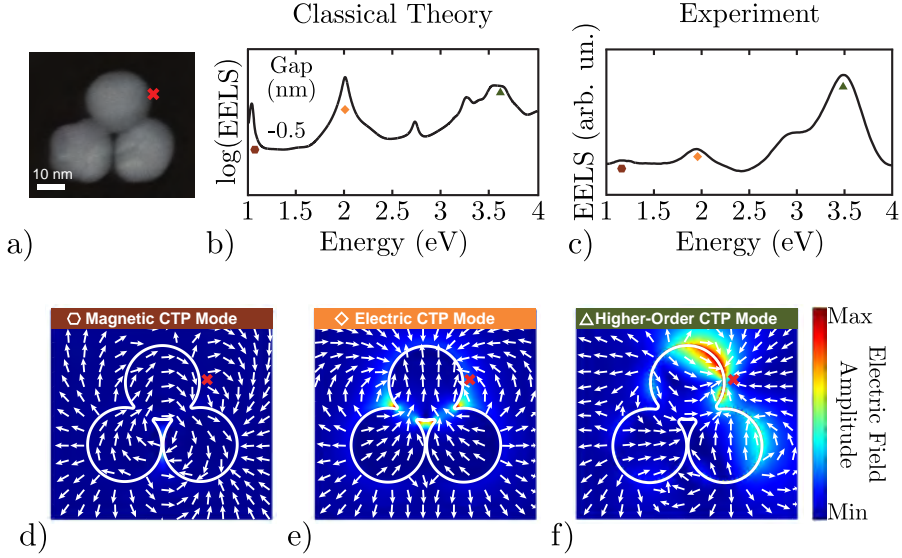
FIGURE 3.4: Modal structure of a coalesced trimer subjected to edge exci-
tation. (a) STEM image of a trimer where the top sphere has coalesced
into the two bottom ones. (b) Simulated EELS spectra of the trimer.
(c) Experimental EELS of the situation in panel (a). The marked peaks cor-
respond to the induced near-field maps showing (d) magnetic-CTP located
around ~ 1 eV, (e) electric-CTP at ~ 2 eV and (f) high-order CTP mode
at ~ 3.5 eV of the contacted trimer. Experiments and classical calculations
performed by Dionne's group in Stanford.

shows a complex field distribution for the pseudomode at ~ 3.5 eV energy (cor-
responding to a combination of high-order modes) which closely resembles the
behaviour of the high-energy peak of the separated trimer (Fig. 3.3g).

With this understanding of the classical modes for the separated and the
merged trimers, we can now follow up the coalescence through the sub-nm gap-
size regime. We calculate the evolution of the trimer modes as the particles
coalesce using a purely classical approach as well as the semiclassical Quantum
Corrected Model (QCM). As discussed in Sec. 1.1, the QCM incorporates the
effect of tunneling in the calculations. We then compare these results with the
EELS data collected while the trimer dimensions are altered. Our observations,
described below, indicate the emergence of non-classical plasmonic behaviour
for a select set of trimer modes, while others maintain a purely classical be-
haviour.

3.1.2 Evolution of plasmonic modes as the trimer coalesces

As shown in Figs. 3.3e-h and Fig. 3.4, placing the electron beam at the edge of the top particle excites both electric and magnetic modes in a fully separated trimer and in the coalesced isosceles configuration. We study next the evolution of the different plasmonic modes as the coalescence takes place. The trimer merging process is depicted in the leftmost panel of Fig. 3.5. The trimer evolves from a a situation where all the particles are well separated at the bottom (same structure as in Fig. 3.3h) to the final coalesced geometry at the top of the panel where the top sphere has contacted the bottom ones while the later remain separated (as in Fig. 3.4a and the sketch in Fig. 3.1c). A negative gap d_{gap} means that the distance between the centre of the top and bottom particles is $D - |d_{\mathrm{gap}}|$.

We first analyse the modal evolution using classical calculations in Fig. 3.5a. As the top two gaps decrease from 0.5 nm (lower spectrum) to 0.1 nm, the magnetic mode (purple square) and electric bonding mode (blue circle) shift to lower energies. Meanwhile, the dominant higher-order resonance at 3.5 eV remains at constant energy throughout the merging process.

Once the particles touch (separation distances ≤ 0 nm), the classical simulations predict that the bonding electric and magnetic modes disappear. Simultaneously, new modes emerge, as electrons can freely move between particles through the physical connection. The modes for $d_{\mathrm{gap}} = -0.5$ nm were already identified in Fig. 3.4. They correspond to a mCTP at ~ 1 eV, a dipolar electric-CTP at ~ 2 eV and a pseudomode at ~ 3.5 eV. Figure 3.5a also reveals that the dipolar electric-CTP blueshifts as the particles coalesce.

On the other hand, from the discussion in Ch. 2 and from other works in the literature[21;22;24] it is known that for gap distances below ~ 0.5 nm, electron tunneling modifies the plasmonic response and the classical calculation fails to reproduce the modal structure. We use the QCM (see Sec. 1.1) to effectively incorporate the effect of the tunneling currents between the top and bottom spheres (Fig. 3.5b). In the QCM calculations, no tangent surface is required after contact in order to converge the calculations (see description of Fig. 3.4), as the presence of the distance-dependent effective medium avoids spatial discontinuities at sharp interfaces. To make a better comparison between the classical and the QCM results, the QCM negative separation distances are considered to be equivalent to those of the classical model when the areas of the contact junction necks between the particles are the same.

By comparing Fig. 3.5a and Fig. 3.5b, it can be seen that the QCM simulations display a close correspondence with classical calculations for separation distances $d_{\mathrm{gap}} \geq 0.4$ nm and $d_{\mathrm{gap}} \leq 0$ nm. This can be explained since for large gaps electron tunneling is exponentially small and after contact the electron transfer is dominated by the classical conduction across the relatively wide junction neck.
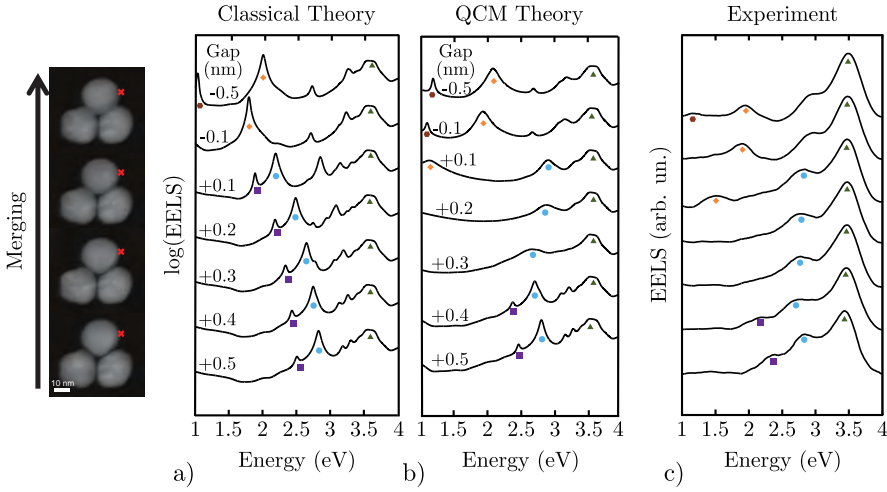
FIGURE 3.5: (a) Spectral series comparing the plasmonic mode evolution in the classical theory, (b) QCM calculations and (c) experimental EELS as the particles merge. Experiments and classical calculations performed by Dionne's group in Stanford. The trimer is excited with the electron beam at the edge position (red cross at a distance < 1 nm from the top particle) and induces merging of the two top junctions. The prominent resonant modes are monitored, including magnetic mode (purple square), electric bonding mode (blue circle), higher-order modes (green triangle), electric charge transfer mode (orange rhombus) and magnetic charge transfer mode (brown hexagon). Experiments and classical calculations performed by Dionne's group in Stanford.

For the smallest (positive) gap region, the QCM calculations strongly diverge from the classical model. The magnetic and electric bonding resonances do not redshift as the distance decreases. Instead, the magnetic mode becomes quenched and the electric bonding resonance disappears and transforms into a blueshifting higher-order charge transfer plasmon mode. Similar electric mode phenomena have been predicted in the introduction and in Ch. 2 for dimers in the quantum regime[24]. The QCM simulations also predict that the lowest-energy electric-CTP emerges at a gap of ≈ +0.1 nm, before the particles physically come into contact. This feature has been reported in dimers[22,24,56] and is produced when the quantum tunneling probability is sufficiently high to facilitate interparticle conductivity[47]. Finally, it can be observed that the introduction of the tunneling current does not influence the pseudomode at ∼ 3.5 eV.

The experimental STEM-EELS data are plotted in Fig. 3.5c. We observe that, while the classical calculations are only able to reproduce the experiment in the regime where the nanoparticles are well separated or in physical contact, the QCM calculations satisfactorily reproduce the STEM-EELS spectra in the

Magnetic Field Amplitude   Electric Field Amplitude
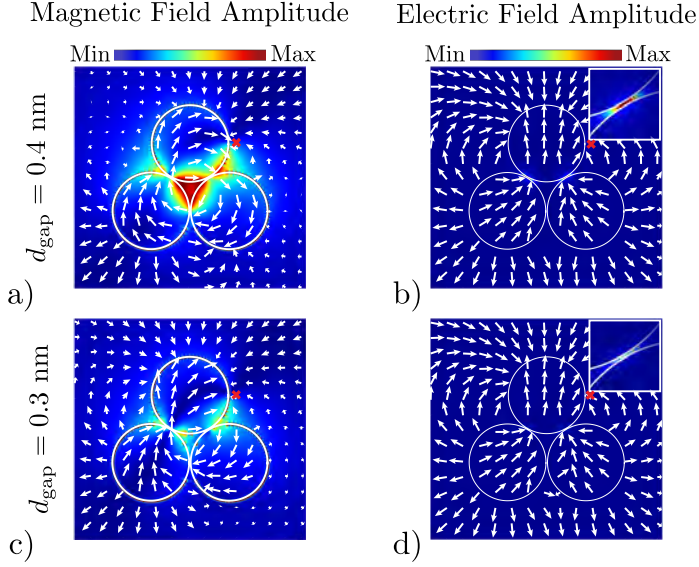
FIGURE 3.6: Electric and magnetic simulated field maps before and after the onset of quantum tunneling. Quantum-corrected model simulations of 25-nm-diameter silver nanosphere trimers with edge excitation (red crosses) are generated at 0.4 nm gap distances (a,b), outside the quantum regime, and at 0.3 nm gap distances (c,d), where quantum tunneling is substantially stronger. As indicated by the electric field direction arrows, the magnetic mode at ≈ 2.5 eV is displayed at left (a,c), while the electric bonding mode is shown at right (b,d). The insets in (b) and (d) display a zoomed view of the electric fields in the gap regions. The quantum effects at the smaller separation distances result in a significant decrease in the magnetic and electric field amplitude for their corresponding modes. Classical calculations performed by Dionne's group in Stanford.

whole range of gap distances. Notably, both the QCM calculation and the experiment show a quenching of the magnetic mode, the transformation of the redshifting electric bonding mode into a higher order CTP mode, and the appearance of the lowest-energy electric-CTP before physical contact.

To better illustrate the evolution of the magnetic and electric resonances at these Ångström-scale separation distances, Fig. 3.6 shows the distribution of electric and magnetic field amplitudes and electric field directions for the relevant modes as the gap sizes diminish. The first column plots the magnetic field amplitude of the pre-merging magnetic mode while the second column shows the electric field amplitude of the electric bonding mode. Upper (a,b) and lower (c,d) rows correspond to gap separation distances of 0.4 nm and 0.3 nm, before and after reaching the quantum tunneling threshold, respectively.

For d_{gap} = 0.4 nm (Figs. 3.6a,b), quantum tunneling still does not substantially impact the response of the system, and both electric and magnetic modes present the expected classical bonding behaviour. The magnetic mode (Fig. 3.6a) generates a strong magnetic field at the centre of the system as a result of the circulating displacement currents across the three particle loop. The electric dipole mode instead presents intense electric fields at the particle gaps as a result of the large coupling between the modes of the individual particles.

In contrast, the d_{gap} = 0.3 nm separation distance (Fig. 3.6c,d) is sufficiently small to allow a high-frequency tunneling current between the particles to be established. To use a similar circuit model analogy as in Ch. 2, at this threshold, the gap impedance acquires an increasingly resistive character (from the electron tunneling). Furthermore, the capacitive bonding nature of the modes loses strength, resulting in the damping and quenching of the bonding electric and magnetic modes. Consequently, the magnetic field amplitude map (Fig. 3.6c) indicates a substantial drop in the magnetic field concentration at the centre of the particle loop, and the electric fields in the interparticle gaps of the electric mode are similarly reduced (Fig. 3.6d).

While the resonance energy of the magnetic mode and the bonding electric mode display distinct non-classical behaviour, other plasmonic modes are not equally affected by quantum phenomena in the sub-nm regime. This contrast is seen when a trimer is excited through the centre and the three particles symmetrically merge (all connections occurring simultaneously). The dark mode resonance, as seen in the classical simulations of Fig. 3.7a, initially occurs at 3.5 eV with 0.5 nm gap size and remains constant throughout the entire particle merging.

The experimental EELS spectra in Fig. 3.7b also reveal virtually identical resonance energy trends with separation distance, as the dark gap mode in Fig. 3.7c evolves into a dark merged trimer mode (Fig. 3.7d) with similar field orientation. This similarity between experimental data and classical simulations indicates that quantum effects do not influence the energy of the dark mode resonance behaviour, even at the smallest interparticle dimensions.

Why does the dark mode energies remain constant in both experiment and classical theory while the magnetic and bonding electric gap modes show substantial differences? The discrepancy between dark and bright modes is caused by the orientation of electric fields and charge distribution at the junctions associated with the dark mode polarizations. In the magnetic and electric bonding modes, charges with opposite polarity are induced at the interparticle interfaces, creating a strong local field through the gap and further facilitating electron tunneling between the nanospheres. The radially-symmetric dark mode, in contrast, has identical charge polarity at the junctions, reducing the electric field and hindering electron transport between particles. Note that this result should also be applicable to other dark-modes of metamolecule assemblies, including the antibonding longitudinal modes of nanoparticle dimers.
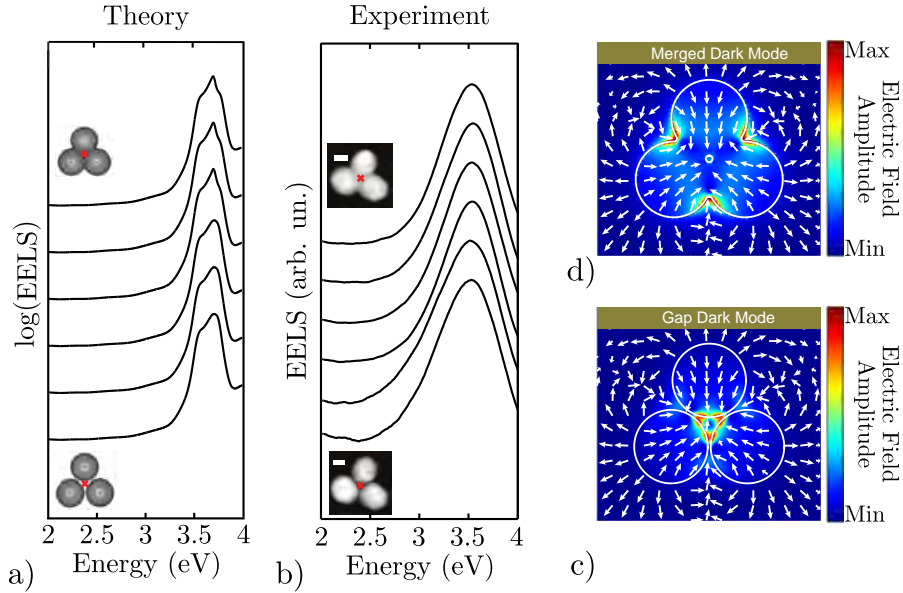
FIGURE 3.7: Spectral series comparing experimental EELS and classical simulations for a merging trimer with centre electron beam excitation. The beam positions are indicated by red crosses. Both experimental (a) and classical simulations (b) indicate a dominant peak that remains at the same energy throughout the merging process. (c) Electric field map of the dark gap mode of the separated trimer. (d) Electric field map of the dark mode of the merged trimer. All scale bars equal 10 nm. Experimental data and classical calculations obtained by Dionne's group in Stanford.

3.1.3 Summary and Discussion

To summarize, we have analysed the response and selective excitation of hybridized trimer metamolecule modes excited by electron beams through classical and QCM simulations. Furthermore we have verified the predictions of our model by comparing them with experimental STEM-EELS with the use of sub-nm imaging, spectral analysis, and electron-beam manipulation of the nanoparticles. Combined, these methods have allowed to explore fundamental trimer modes and their progression in particles with interparticle gap sizes in the sub-nanometer regime. The plasmonic mode evolution during merging reveals that classical electrodynamics correctly captures the behaviour of typically antibonding cases (*e.g.* radially-symmetric dark mode), but is insufficient to describe other types of modes (*i.e.* electric bonding and magnetic modes) in which quantum phenomena are revealed. These spectral features, including resonance quenching and relative blueshifting, provide strong indication of electron tunneling between particles. Consideration of quantum features can play an important role in the design of future multi-particle metamolecules

with sub-nm gaps and brings up new interdisciplinary exploration bridging molecular electronics, nonlinear optics, and plasmonics.

3.2   Plasmonic chain resonances

We have considered up to now structures with 2 or 3 particles where the different parameters (position, size, ...) are well controlled. Such control however, is experimentally demanding when fabricating complex plasmonic systems with multiple nanoparticles. A promising approach is to use self-assembled aggregates of small nanoparticles[8], where molecular linkers allow to achieve consistent gap separations[180] down to $\approx$ 1 nm. The particles can self-assemble to form chain-like structures[181] or more complex 3-dimensional aggregates, where the position of each particle is essentially stochastic[165,180]. Interestingly, this stochasticity does not prevent to obtain a reproducible overall plasmonic response even for quite complex aggregates, and to control the response by changing the size and shape of the particles and the conditions of aggregation[8,182]. Furthermore, it has been demonstrated that the optical response of these aggregates can be described by the combination of plasmonic chain resonances[165].

Figure 3.8a sketches a typical situation of self-assembled spherical particles aggregated in the Diffusion-Limited Regime. We consider that a small molecular linker fixes the interparticle distance, a situation that is possible to achieve using wet chemistry synthesis[8,183]. The optical response of such an aggregate can be tuned by modifying the self-assembly conditions (particle size, material, linker, concentrations,...). The resulting aggregate presents a branched configuration of particles separated by well defined nanometer gaps[165,180]. It has been argued in previous works[165,184] that much of the resulting plasmonic response can be understood by modelling the system as an ensemble of relatively straight chains of adequate lengths (Fig. 3.8). Thus, understanding the case of straight chains[185,186] is a critical step to optimize these complex systems, as also to predict the optical response when mixed independent chains are directly synthesized.

Indeed, chains of spherical particles interacting across nanometre gaps have received considerable attention[42,45,87,165,187–191]. The optical response of these chains (blue line in Fig. 3.8e) shows a strong dipolar Longitudinal Chain Plasmon (LCP) mode, which redshifts as the number of particles in the chain increases and is characterized by the generation of very strong and localized near fields in the gap regions, thus making them interesting for enhanced spectroscopy.

Nonetheless, the redshift of the LCP with increasing number of particles in the chain saturates for chains formed by $\sim$ 10 spherical particles[188,192–195]. This saturation limits the tunability of the system, making it necessary to use relatively large spheres and very narrow gaps when resonances in the infrared are sought[196–198], as for example when working in the biological transparency window[199,200]. To increase the tunability, a straightforward possibility is to

change the morphology of the particles. Nonetheless, the results for chains of rods suggest that, as far as the terminations remain spherical, the redshift can be larger than for spheres, but the response still saturates with the number of particles[183]. Furthermore, the self-assembly process may become challenging for elongated or very complex particle morphologies.

On the other hand, chemically-synthesized particles in self-assembled aggregates present flat facets either by design or due to unavoidable reconfiguration processes inherent to the chemical synthesis[96–98] (see also Refs. [99, 100] and references therein for a discussion on growth of gold nanoparticles). Thus addressing theoretically the effects that the presence of facets induces in the plasmonic response of self-assembled aggregates can have direct implications in the interpretation of experimental results. It has been shown in Sec. 2.1 that rod dimers terminated by a flat surface present a very different behaviour as compared to spherically capped rods[56]. It is argued below that such flat facets can be advantageous for applications based on self-assembled systems, notably by improving the tunability of the optical response of the system. Large facets are able to accommodate a larger number of molecules in the gap, a situation beneficial for applications which do not require to work at the single molecule level[48].

Figure 3.8 shows the main idea for the analysis in this section. In the absence (Fig. 3.8a,b) and in the presence (Fig. 3.8c,d) of faceting in the particle units, branched aggregates (Fig. 3.8a,c) are considered to behave as an ensemble of non-interacting straight chains (Fig. 3.8b,d), an approach supported by previous studies that showed how chain calculations can nicely and effectively reproduce the optical response of the full aggregate[165]. For linearly polarized light, the polarization of the external field selects the excitation of particular chain modes parallel to the incident field (Fig. 3.8a,c). On the other hand, if unpolarized light is used, plasmonic modes can be efficiently excited in chains that are oriented in all directions perpendicular to the propagation direction of the excitation beam.

The faceting at each particle unit within a straight chain strongly affects the optical response (Fig. 3.8e). For the same number and size of particles, the resulting resonances are found at larger wavelengths for chains of particles with large facets compared to chains of spheres (red line for flat-faceted particles chain vs. blue line for spheres in Fig. 3.8e). In the following theoretical work, a systematic analysis of the behaviour of chains of different length and facet size is presented. In particular, special attention is paid to the influence of the size of the facets on the tunability of resonances and the field enhancement in the gap regions, with direct implications for surface-enhanced spectroscopy and sensing at infrared frequencies.

3.2.1   Chain configuration

We simulate 1-dimensional chains (Fig. 3.8b and Fig. 3.8d) composed by cylindrical gold nanoparticles described by the experimental permittivity of gold[35]
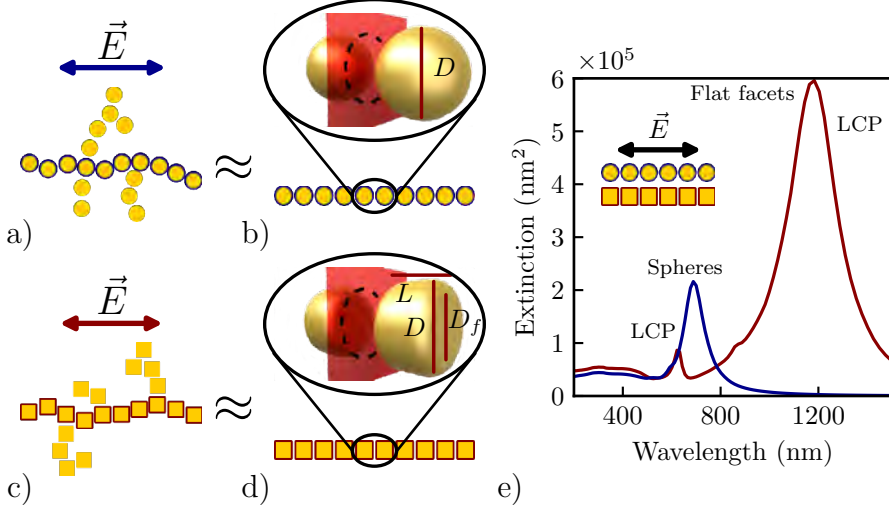
FIGURE 3.8: Scheme of aggregates of (a) spherical and (c) flat-faceted particles under plain wave illumination with electric field $\vec{E}$. The incoming illumination mainly excites longitudinal plasmon modes in chains that extend along the polarization direction (chains delimited in the scheme by thick blue and red lines, respectively). We thus focus on the optical response of chains of (b) spherical or (d) flat-faceted particles. Zooms in (b) and (d) illustrate the dimensions of the particles composing the chains. In both cases the particles are rotationally symmetric with respect to the chain axis. We notice that the complex flat-faceted aggregates in (c) would require breaking the rotational symmetry to have more than 2 flat facets per particle. The spheres (b) are defined by their diameter $D = 50$ nm. The flat-faceted particles (d) are rods defined by 3 parameters, the length L (in the direction along the chain axis), the diameter D (in the orthogonal direction) and the facet diameter D_f. We fix $L = D = 50$ nm and we vary D_f from $D_f = 0$ nm, corresponding to a sphere, to $D_f = 46$ nm, a cylindrical rod with almost completely flat facets. In Fig. 3.11, Fig. 3.12 and Fig. 3.13 the fields are evaluated in the central plane of the gaps, in an area corresponding to a circle of radius 25 nm. We mark this region for one gap in the insets of (b) and (d) as the region of the central red plane delimited by the dashed circular line. (e) Calculated extinction spectrum of a chain of $N_p = 10$ gold spherical particles in blue and a chain of 10 flat-faceted particles with $D_f = 46$ nm in red for incident light with the electric field polarized along the chain direction. All the structures considered in this study are cylindrically symmetric.

and surrounded by vacuum. For simplicity, the full structure is rotationally symmetric, even if the more complex 3-dimensional aggregates with flat facets in Fig. 3.8c would require less symmetrical particles. The nanoparticles are a smaller version of the wide rods studied in Sec. 2.3. The length of the particles along the chain axis is $L = 50$ nm, their diameter along the plane orthogonal to the chain axis is also $D = 50$ nm and the separation in the gaps is $d_{\text{gap}} = 1$ nm. The rods are capped by a flat surface of diameter D_f, with the radius of the rounded edge $r_{edge} = \frac{D - D_f}{2}$ (see zoom of Fig. 3.8d). We vary the diameter of these gap facets from $D_f = 0$ nm to $D_f = 46$ nm, where the former corresponds to the limit situation of a sphere of diameter $D = 50$ nm (zoom in Fig. 3.8b). Plane wave illumination at wavelength λ with the electric field of amplitude E_0 polarized along the chain axis is used to excite the strong longitudinal plasmonic resonance of the system. We then analyse the optical response of the plasmonic chains in the far-field and in the near-field as a function of the number of particles in the chain (N_p) and the facet diameter (D_f). The gap distance ($d_{\text{gap}} = 1$ nm) is short enough that nonlocal effects might introduce some modification in the exact resonance frequency and strength of the plasmonic modes. However, previous studies have shown that considering nonlocality in calculations of gold systems is equivalent to assuming a slightly shifted surface interface inside the metal by about 0.9 to 1.5 Å.[16] This effective displacement of the interfaces creates an effective gap distance which is about 1.7-3 Å larger than in the local treatment. To simplify the discussion of the properties of the chain modes and focus on the dependence on the morphology, we develop all our study within the local description.

To analyse the near-field properties in the gaps, we calculate the near-field enhancement in the central plane of all gaps, for a region corresponding to a circle of 25 nm of radius centred in the chain axis (area inside the dashed circle in the zoom of Fig. 3.8b and Fig. 3.8d). We then evaluate two different quantities. On the one hand we study the maximum near-field enhancement, $|E/E_0|_{\text{max}}$, which corresponds to the maximum field enhancement produced in the gaps. On the other hand we consider the average field enhancement, $|E/E_0|_{\text{avr}}$, by averaging the near-fields calculated in all the gaps of a particular chain. To obtain the far-field and near-field response we solve Maxwell's equations using the Boundary Element Method (BEM)[10,36] optimized for cylindrically symmetric systems.

3.2.2 Far-field response in metallic particle chains

In order to show the strong impact of faceting in the optical response of metallic chains, Fig. 3.8e shows the extinction cross section of chains formed by $N_p = 10$ particles composed by spheres (blue) and by $D_f = 46$ nm flat-faceted particles (red). The presence of the flat facets strongly influences the spectral position of the lowest-energy plasmon resonance by shifting it to longer wavelengths.
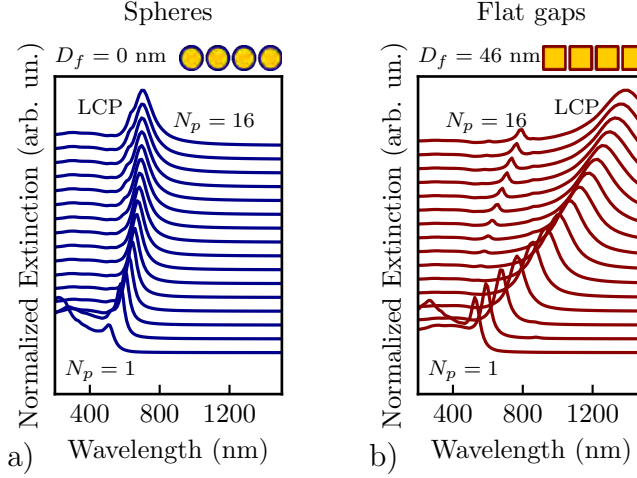
FIGURE 3.9:   (a),(b) Waterfall plot of the normalized extinction cross-section calculated as a function of wavelength for a chain of Au particles for (a) $D_f = 0$ nm (spheres) and (b) rods with $D_f = 46$ nm facets for increasing number of particles $N_p = 1 - 16$. Shorter chains are plotted at the bottom. All the structures considered in this study are cylindrically symmetric, and the different spectra are shifted vertically for clarity. The LCP mode is clearly observed in all the spectra.

For a more detailed analysis of the far-field response of the system, Fig. 3.9 shows the normalized extinction cross-section for chains of different length, both considering spherical particles ($D_f = 0$ nm, Fig. 3.9a) as well as particles with the largest flat termination considered ($D_f = 46$ nm, Fig. 3.9b). All the spectra are characterized by a dominant plasmonic peak ($\lambda > 500$ nm) associated with the lowest-energy LCP of dipolar character, which redshifts as the number of particles increases. For spherical particles (Fig. 3.9a) the plasmon energy shift saturates for chains with $N_p \sim 10$ particles, and the maximum LCP energy difference with respect to the resonance of a single sphere is relatively small[188,192–195]. In contrast, in the case of flat-terminated particles (Fig. 3.9b) the saturation of the redshift is less pronounced. Even for chains formed by up to $N_p \sim 16$ particles, the resonance wavelength of the LCP continues to increase with chain length. It is thus possible to tune the response of flat-faceted particles over a much larger spectral range than for spherical ones. Additionally, for flat-gap chains formed by $N_p \gtrsim 10$ particles, a higher order longitudinal mode that redshifts with increasing N_p is also excited at lower wavelengths ($\lambda \approx 625$ nm).

    Further insight into the strong influence of the gap morphology on the optical response can be obtained by observing the evolution of the lowest-energy longitudinal chain plasmon resonance (λ_{LCP}) with increasing number of particles in the chain, N_p (Fig. 3.10a, dots) and for different sizes of the
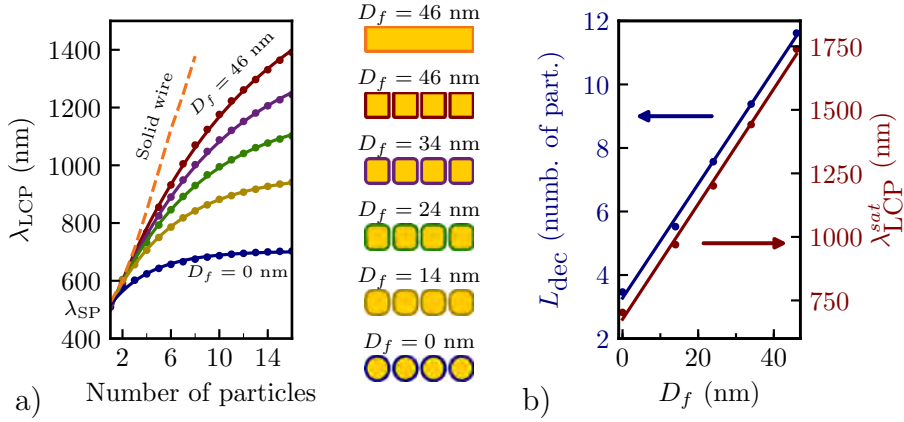
FIGURE 3.10: (a) Spectral position of the lowest-energy longitudinal chain plasmon (λ_{LCP}) calculated as a function of the number of particles in the chain N_p, for different diameters D_f of the flat facet forming the gaps (top to bottom, $D_f = 46$ nm, 34 nm, 24 nm, 14 nm, 0 nm). The different colours in the plot indicate the corresponding structure in the central panel (recall that the particles are cylindrically symmetric). The calculated values (dots) are fitted to an exponential function (solid lines) as indicated in the text. λ_{SP} labels the wavelength of the dipolar resonance of a single spherical particle at $\lambda_{\text{SP}} \approx 510$ nm. The results for a rod of length $N_p \cdot L$ (orange dashed line) are also shown. (b) Parameters of the exponential fit for each facet diameter corresponding to the saturation wavelength $\lambda_{\text{LCP}}^{sat}$ (red, right axis) and the decay length L_{dec} (blue, left axis). Dots are the calculated values and lines are a linear fit.

gap facet ($D_f = 46$ nm, 34 nm, 24 nm, 14 nm, 0 nm, top to bottom). For comparison, Fig. 3.10a also shows the dipolar plasmon resonance of a rod of diameter $D = 50$ nm and increasing length, capped by flat terminations with $D_f = 46$ nm (orange dashed line). The resonant shift of the LCP for small chains is similar for all the facet morphologies. However, D_f strongly affects how λ_{LCP} evolves as the chain gets longer. The shift for the chain of spheres deviates from the general trend for very small number of particles in the chain ($N_p \approx 3$), saturating for a smaller N_p, and thus the maximum shift with respect to the single particle resonance wavelength $\lambda_{\text{SP}} \approx 510$ nm remains comparatively small ($\lambda_{\text{LCP}} - \lambda_{\text{SP}} \approx 200$ nm, bottom line in Fig. 3.10a). As the facet size increases, the shift of the dipolar LCP reaches saturation for longer chains (upper lines in Fig. 3.10a) so that larger energy shifts are possible. In the case of $D_f = 46$ nm we obtain $\lambda_{\text{LCP}} - \lambda_{\text{SP}} \approx 800$ nm for $N_p = 16$, a length still far from saturation. This behaviour can be connected with the response of a rod dimer with flat gap terminations[56], where the narrow flat gap con be considered as a capacitor[119] whose capacitance becomes larger as the gap closes and eventually behaves as a short-circuit (see Sec. 2.1.2). Thus,

the chains with $D_f = 46$ nm and very narrow gaps approach the behaviour of a single "connected" rod of the same length, characterized by strong, and approximately linear plasmon energy shift with the length of the structure[3,104] (orange dashed line in Fig. 3.10a). We have indeed verified that the similarity between the single rod and the $D_f = 46$ nm chain increases if the gap distance is decreased.

The LCP redshift follows quite closely an exponential dependence with N_p for all facets considered, which generalizes the tendencies observed in previous works for spheres[188]. The solid lines in Fig. 3.10a correspond to a fit of the calculated data (dots) using the dependence:

$$\lambda_{\text{LCP}} = \lambda_{\text{LCP}}^{sat} - \beta e^{-N_p/L_{\text{dec}}} \ , \tag{3.1}$$

where $\lambda_{\text{LCP}}^{sat}$ is the saturation wavelength of the longitudinal chain plasmon and L_{dec} is the decay length (measured in number of particles). The fit is very satisfactory in all the cases. In Fig. 3.10b we analyse the fitting parameters, L_{dec} and $\lambda_{\text{LCP}}^{sat}$, obtained from the calculations in Fig. 3.10a as a function of the facet diameter D_f. The red dots (right axis) show how the saturation wavelength $\lambda_{\text{LCP}}^{sat}$ increases for larger facet size, going from $\lambda_{\text{LCP}}^{sat} = 705$ nm for spheres, to $\lambda_{\text{LCP}}^{sat} = 1760$ nm for $D_f = 46$ nm particles. The redshift with respect to the single particle resonance ($\lambda_{\text{LCP}}^{sat} - \lambda_{\text{SP}}$) is thus a factor of ~ 6 larger for the large flat facets than for spheres. A similar behaviour is observed for the decay length L_{dec} (blue dots and left axis in Fig. 3.10b), which increases monotonously from $L_{\text{dec}} = 3.5$ particles for spheres to $L_{\text{dec}} = 11.8$ particles for $D_f = 46$ nm flat-faceted particles. Interestingly, the evolution of both $\lambda_{\text{LCP}}^{sat}$ and L_{dec} with N_p can be fitted very satisfactorily by a simple linear relationship (solid lines in Fig. 3.10b), which makes it straightforward to determine the particular flatness D_f and particle number N_p to obtain a resonance at a desired energy.

To understand the linear dependence of $\lambda_{\text{LCP}}^{sat}$ with D_f we consider an infinite chain, ignoring losses. Similarly as in Sec. 2.1.2 we model the infinite chain as an electrical circuit where each unit cell of the resulting periodic structure can be modelled as a inductance $\mathbb{L}$ characterizing the metallic particle and a capacitance C associated to the inter-particle gaps, leading to a total impedance $Z = i\mathbb{L}\omega + \frac{1}{i\omega C}$ where ω is the (angular) frequency and i is the imaginary unit[49,122,201]. The resonant frequency thus corresponds to $\omega_{res}^\infty = \frac{1}{\sqrt{\mathbb{L}C}}$. Using the capacitance of two parallel plates of area A separated by the gap distance d_{gap}, $C = \frac{\varepsilon_0 \varepsilon A}{d_{\text{gap}}}$, where ε is the relative dielectric constant of the material between the plates and ε_0 is the permittivity of vacuum, and substituting A by the facet area, we get $\omega_{res}^\infty = \left(\mathbb{L}\varepsilon_0\varepsilon\pi(D_f/2)^2/d_{\text{gap}}\right)^{-1/2} \propto 1/D_f$. Therefore, $\lambda_{\text{LCP}}^{sat} = \lambda_{res}^\infty \propto 1/\omega_{res}^\infty \propto D_f$ reproducing the linear proportionality with D_f found in Fig. 3.10b. This simple model thus exhibits the trends found for $\lambda_{\text{LCP}}^{sat}$. Nonetheless, a full understanding of more subtle details might require more complex modelling. For example, this simple equation wrongly predicts

that $\lambda_{\mathrm{LCP}}^{sat} \to 0$ for $D_f \to 0$, which may be the consequence of neglecting the intrinsic capacitance of the metallic particles and the contribution to the gap capacitance of the region outside the flat facets.

3.2.3 Near-field response in metallic particle chains

Spheres   Flat gaps

a)   b)
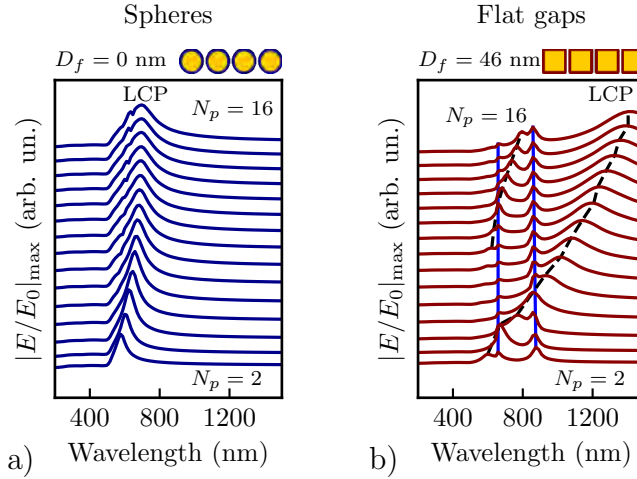
FIGURE 3.11: Waterfall plot of the maximum near-field enhancement at the gaps of a chain of Au particles with (a) $D_f = 0$ nm and b) $D_f = 46$ nm facets calculated as a function of wavelength and number of particles $N_p = 2 - 16$. Shorter chains are plotted at the bottom. In (b) black dashed lines trace the position of the LCP resonances while blue lines correspond to the position of the TCPs. All the structures considered in this study are cylindrically symmetric, and the different spectra are shifted vertically for clarity.

We analyse next the evolution of the maximum near-field enhancement $|E/E_0|_{\max}$ at the gaps as a function of the number of particles in the chain, N_p, obtained by evaluating the fields in the middle plane of the gaps as described in Sec. 3.2.1, both for spherical particles (Fig. 3.11a) and for flat-terminated particles with $D_f = 46$ nm (Fig. 3.11b). For spherical particles we observe the same predominant lowest-energy LCP mode found in the far-field response, which redshifts with increasing N_p until it saturates. $|E/E_0|_{\max}$ reaches values of the order of several hundreds for this resonance. For large N_p we also observe a small narrow peak at a lower wavelength, which corresponds to a higher order LCP. On the other hand, chains formed by flat-faceted particles support two distinct sets of modes, revealing the existence of non-radiative modes that were not excited in the far-field spectrum[56,137]. First, we can readily identify the strongly radiant LCP modes on the near-field response (black dashed lines) because their spectral evolution is known from the analysis of the extinction

peaks in Fig. 3.9b. As pointed out, a new set of modes emerges in the field enhancement spectra, as revealed by the maximum at wavelengths $\lambda \approx 650$ nm and $\lambda \approx 850$ nm (blue vertical lines). The resonant energy of these modes is not significantly affected by changing the length of the chain and, consistently with Ch. 2, we identify them as Transverse Cavity Plasmons (TCPs) (see Sec. 2.1.2). The resonant position of the LCPs and the TCPs at the gap behave essentially independently, as enphasized by the guiding lines in Fig. 3.11b (blue and black dashed lines). These modes do not show any clear sign of avoided crossing[56], although more interplay between these type of modes was found in Fig. 2.12 and Fig. 2.13 for dimers and for other morphologies by Tserkezis *et al* in Ref. [130]. When the two modes are simultaneously excited (spectral match), the enhancement produced by both of the resonances leads to larger enhancement values.

For a more direct comparison of the effects of the morphology on the maximum field enhancement, Fig. 3.12a shows $|E/E_0|_{max}$ at the wavelength of the dipolar (lowest-energy) LCP peak ($|E_{LCP}/E_0|_{max}$) as a function of N_p, for the same values of D_f considered earlier. As expected, chains of spheres lead to the strongest enhancements of $|E_{LCP}/E_0|_{max} \approx 470$, which is found for chains of 6 spheres. Nevertheless, for $N_p \gtrsim 6$ spheres, $|E_{LCP}/E_0|_{max}$ starts to drop off due to the emergence of significant radiative losses[184,202,203]. Particles with small facets follow the same trend as the spherical ones but the local fields are weaker, $|E_{LCP}/E_0|_{max} \approx 345$ for $N_p = 4$ and $D_f = 14$ nm. Finally, short particle chains with larger flat facets exhibit comparatively small $|E_{LCP}/E_0|_{max}$, with some oscillations when increasing N_p, due to the crossing of the LCP and the TCPs. The maximum enhancement increases continuously reaching $|E_{LCP}/E_0|_{max} \approx 180$ for the largest facets and longest chains.

Although chains of spheres produce larger maximum near-fields than flat-faceted particles, the enhancement remains of the same order of magnitude. Furthermore, for specific applications in spectroscopy and sensing, it is convenient to enhance the field over large areas. Notably, while studies of single molecules placed at the optimal location are sensitive to the maximum near field, large average fields are interesting for applications where a considerable number of molecules are probed or characterized simultaneously, or when the position of the molecules is randomly distributed as in wet chemistry synthesis. Figure 3.12b shows the average field enhancement in the gaps for the LCP mode, $|E_{LCP}/E_0|_{avr}$, as a function of the number of particles and D_f. The average is calculated as described in Sec. 3.2.1. For $N_p \lesssim 5$, $|E_{LCP}/E_0|_{avr}$ generally grows as the chain gets longer. The largest average enhancement is produced for particles with $D_f = 14$ nm, whereas spheres and particles with $D_f = 46$ nm generate the weakest average fields in these short chains. For long chains of spherical particles and particles with $D_f = 14$ nm, $|E_{LCP}/E_0|_{avr}$ diminishes as N_p grows. In contrast, for particles with large facets ($D_f = 46$ nm and $D_f = 34$ nm) $|E_{LCP}/E_0|_{avr}$ keeps growing significantly with increasing chain length up to $N_p \approx 14 - 16$. As a consequence, spherical particles are
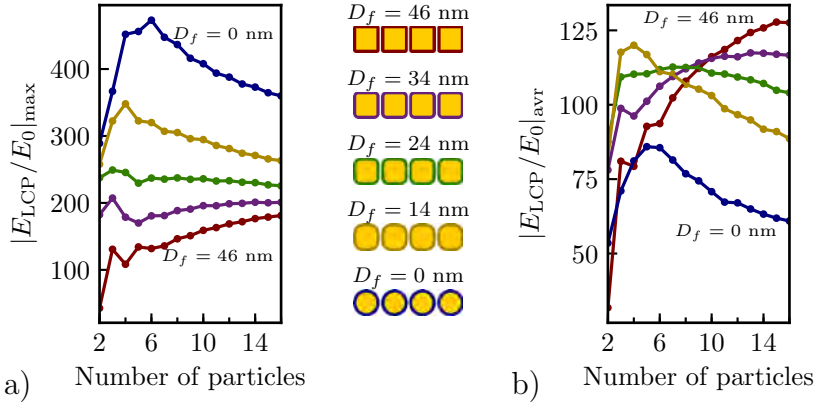
FIGURE 3.12: (a) Maximum near-field enhancement $|E_{\mathrm{LCP}}/E_0|_{\max}$ of the lowest-energy LCP mode calculated as a function of the number of particles in the chain N_p, for different diameters D_f (bottom to top , $D_f = 46$ nm, 34 nm, 24 nm, 14 nm, 0 nm). (b) Average near-field enhancement $|E_{\mathrm{LCP}}/E_0|_{\mathrm{avr}}$ of the lowest-energy LCP mode as a function of the number of particles in the chain N_p, for the same diameters D_f as in (a). The different colours in the plot indicate the structure under study, as given by the schematics in the central panel of the figure. All the particles are cylindrically symmetric.

found not to be optimal to maximize the average field enhancement. To that end, particles with small but non-zero D_f are preferred in short chains, and so are particles with large facets in the case of long chains. We emphasize that, although the dependence of the results in Fig. 3.12b on the chain length and on the facet diameter are relatively complex, strong average fields can nicely be obtained for all types of particle terminations.

3.2.4 Field localization

In any plasmonic structure it is important to understand how the distribution of field enhancements associated to a plasmonic resonance around the structure is related with the actual localization of the incident light. To that end, we analyse the field distribution near the gaps of the different structures studied in the previous subsections. In Fig. 3.13a-e we plot the field enhancement $|E/E_0|$ in the central gap of a $N_p = 8$ particle chain for the wavelength of the dipolar LCP and for each facet diameter studied. Particles with flat facets exhibit less intense near fields but distributed over a larger flat area in contrast with the stronger localization and more intense fields at the gaps formed by spherical particles, corroborating the results of Fig. 3.12a. The analysis of the field localization can be made more quantitative by using the normalized mode
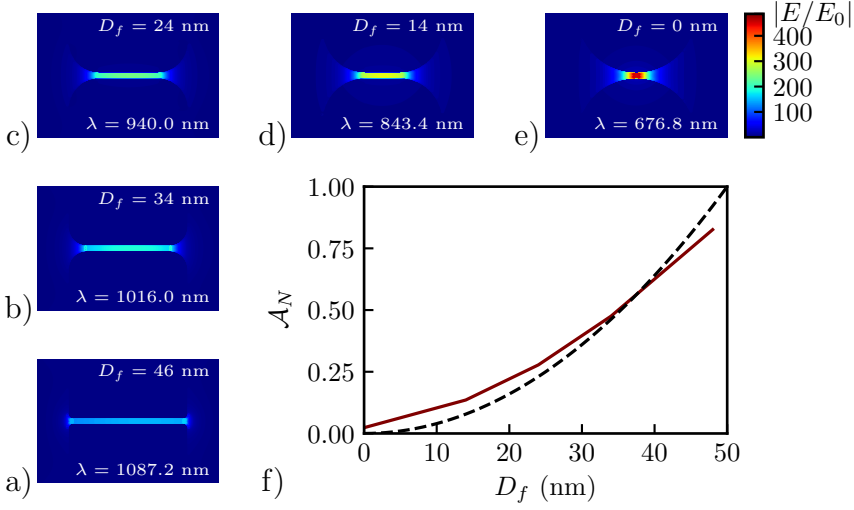
FIGURE 3.13:   Near-field maps of the LCP mode, calculated near the central gap of a chain formed by $N_p = 8$ particles with faceted diameter (a) $D_f = 46$ nm, (b) $D_f = 34$ nm, (c) $D_f = 24$ nm, (d) $D_f = 14$ nm and (e) $D_f = 0$ nm. (f) The solid red line show the calculated LCP normalized mode area $\mathcal{A}_N$ as a function of facet diameter D_f. The dashed black line indicate the normalized area D_f^2/D^2 for each structure considered. All the structures considered in this study are cylindrically symmetric.

area $\mathcal{A}_N$,

$$\mathcal{A}_N = \frac{1}{\pi(D/2)^2} \int_S \frac{|E(\mathbf{r})|^2}{|E^{max}|^2} dS \; , \tag{3.2}$$

where $|E(\vec{r})|^2$ is the square modulus of the induced field at position $\mathbf{r}$ in the central plane of the gap, $|E^{max}|^2$ is the maximum of $|E(\mathbf{r})|^2$. This quantity is normalized by the particles geometrical cross-section, $\pi(D/2)^2$. The integral extends over the same 25 nm radius region as described in Sec. 3.2.1 (dashed circle in the central plane in Fig. 3.8b,d). We have verified that integrating over a circle of 50 nm radius does not significantly affect the results.

$\mathcal{A}_N$ gives a measure of the confinement of the near-fields in the gap. A value of $\mathcal{A}_N = 0$ would mean that the field is localized at a single point whereas a value $\mathcal{A}_N = 1$ is obtained when the near-field is uniform across the integration area (particle cross-section) and zero outside. Figure 3.13f shows that $\mathcal{A}_N$ monotonously increases as the facet diameter D_f gets larger (red solid line), evolving from $\mathcal{A}_N = 0.024$ for spherical gaps to $\mathcal{A}_N = 0.83$ for larger D_f. Two limiting situations are helpful to understand these results. Adopting the quasistatic approximation[107], the near-field between two spherical nanoparticles of diameter D separated by a gap d_{gap} is confined to a circle of radius $\approx \sqrt{(D/2)d_{\text{gap}}}$, giving $\mathcal{A}_N \approx 2d_{\text{gap}}/D$ (to be compared to the value

$\mathcal{A}_N = 1.2 d_{\text{gap}}/D$ obtained in the calculations). In the case of large facets, Fig. 3.13a-c indicate that the near-field is approximately homogeneous at the gap region between the flat facets and much weaker outside. This would correspond to $\mathcal{A}_N = D_f^2/D^2$, which is represented in Fig. 3.13f by the black dashed line. As observed, the agreement between the normalized area obtained with this simple expression and that obtained from the calculation is very good for intermediate and large facets.

3.2.5   Summary and Discussion

The analysis of the optical response of metallic chains of particles has shown that the exact facet morphology of the particles plays a key role in determining the near-field and far-field properties of plasmonic chains of particles separated by ~ 1 nm gaps, as those obtained by chemical self-assembly. We argue that these results might be also extended to more complex branched aggregates[165,204], whose optical response can be dominated by plasmonic modes supported by chain-like subunits. The description of the optical response of complex aggregates of spherical nanoparticles as the combination of the response of linear chains of plasmonic spheres was validated comparing theoretical and experimental results[165]. We expect it to be valid also in aggregates formed by flat-faceted units, at least if the gaps are formed between well-aligned flat facets. Significantly, although the inherent disorder found in self-assembled aggregates modifies to some extent the plasmonic modes, the overall properties of the plasmonic response have been found to be robust with respect to disorder[165,198,205,206]. The experimental realization of such 2 or 3-dimensional aggregates would require particles with more than two flat facets. Multiple facets often occur naturally when synthesizing spherical particles[207], and it is possible to modify the synthesis process to optimize the level of faceting as required for a given application. Notably, for instance, cubes have already been synthesized[208].

   The key result of this section is the much larger tunability of the Longitudinal Chain Plasmon (LCP) obtained when using flat-capped cylindrical particles compared to spherical ones. All the geometries studied in this section exhibit an exponential redshift of the LCP as the chain gets longer, with a decay length L_{dec} and a saturation wavelength $\lambda_{\text{LCP}}^{sat}$ increasing linearly as the diameter of the facets become larger. In particular, the resonant energy for the case of flat-capped cylindrical particles extends from $\lambda_{\text{SP}} \approx 525$ nm for a single particle to a saturation wavelength (as defined in Eq. (3.1)) $\lambda_{\text{LCP}}^{sat} \approx 1760$ nm, which covers the whole near-infrared biological window[199,200] and the corresponding decay length is $L_{\text{dec}} = 11.8$ particles. In comparison, $\lambda_{\text{LCP}}^{sat} \approx 705$ nm and $L_{\text{dec}} = 3.4$ particles for spherical particles. Chains of flat-faceted particles are thus a promising alternative in field-enhanced spectroscopy and sensing, which could compete with other self-assembled structures such as chains of rods[183] to improve their performance at large wavelengths.

Last, we found that flat-faceted particles exhibit near-field enhancements of the same order of magnitude as spheres but distributed over a larger area at the gaps. This larger region of strong enhancement can be used to accommodate more molecules and to facilitate a less precise distribution of molecules in the gaps in field-enhanced spectroscopies. Chains of flat-faceted particles thus seem suitable for experiments requiring optical tunability over a wide spectral range without losing the strong near-field enhancements characteristic of chains of spherical particles.

Chapter 4

High-harmonic generation in nanoplasmonics: Single antenna and nanogaps

In previous chapters we have focused on the linear optical response of plasmonic systems. On the other hand, the nonlinear response of materials also plays an important role in numerous applications of nanophotonics devoted to information transfer[46,209–213]. Moreover, frequency conversion and generation of high harmonics can be used for (bio-)imaging[214–217], metrology and sensing[218–221], and generation of atto-second XUV laser pulses[222,223]. The latter allowed spectacular progress in direct time-domain access to electronic processes in atoms, molecules, and solids[223,224].

However, optical nonlinearities are usually weak, and therefore the nonlinear responses associated to them are orders of magnitude smaller than the linear ones. Plasmonics offers a way to overcome this difficulty since many experimental and theoretical works have shown relevant plasmon-enhanced nonlinear effects at metallic surfaces, nanoparticles and in artificially created nanomaterials[46,213,225–237]. Recent developments also demonstrate the role of plasmon excitations in the nonlinear response of graphene nanostructures[238–240]. The common understanding provided by these works is that the plasmonic enhancement of the near fields in the proximity of metallic surfaces can be utilized to boost nonlinear effects.

Increased interest in nonlinear plasmonics have been driven by the technological progress that allows nowadays to engineer nanostructures with the desired optical properties[227,241]. Along with a "passive" tailoring during the fabrication process, the ability to actively modify the linear and nonlinear response of plasmonic nanostructures opens new capabilities of paramount importance in nanophotonics. In particular, electrical control of the optical response of metallic building nanoblocks, similar to that available in two-dimensional (2D) materials[242], would allow their integration into optoelectronic devices providing compact signal processing and information transfer.

In this context, classical electromagnetic theory is routinely applied to explain many of the experimental data and to predict the nonlinear properties of nanostructures using perturbative and model approaches. It has been shown that an efficient frequency conversion can be obtained by fulfilling appropriate symmetry constraints, and choosing the frequency of the fundamental incident wave or its corresponding high harmonic in resonance with a suitable plasmonic mode of the system[232–237,243–256]. Beyond classical electromagnetic theory, hydrodynamic methods recently demonstrated the impact of nonlocal screening on the nonlinear response of individual nanoparticles[52,255,257,258]. On the other hand, Time-Dependent Density Functional Theory (TDDFT) (see Sec. 1.2), which allows to elucidate the rich variety of effects in plasmonic systems and the contribution of the different mechanisms driving the optical frequency conversion is a convenient methodology to theoretically study the nonlinear plasmonic response within a parameter-free approach. This quantum framework can facilitate the design of efficient nonlinear devices by increasing our understanding of the respective role of the field enhancement, plasmon resonances, intrinsic nonlinearity of metal nanoparticles and, in the case of closely separated dimers (Sec. 4.5), of the nonlinear electron transport through narrow plasmonic gaps. As we will see, this approach also allows to study active control of the nonlinearity. Therefore TDDFT calculations present a very compelling opportunity to study how the dynamics of conduction electrons in plasmonic nanoparticles influence the nonlinear optical response.

In Sec. 4.1 we first introduce some details about the Jellium Model (JM) implementation that is used to characterize the Al and Na nanoparticles. In Sec. 4.2 we give a brief explanation of the nonlinear processes investigated in this chapter, paying special attention to the mechanism that enables the generation of even harmonics in centrosymmetric structures. In Sec. 4.3 we describe how we retrieve the frequency-domain nonlinear plasmonic response from the TDDFT calculation and in Sec. 4.4 and Sec. 4.5 we present the final results. More in detail, in Sec. 4.4 we study the case of a plasmonic sphere which, without the action of an external perturbation that breaks its centrosymmetry, does not generate signal at the even harmonics of the illumination laser. By applying an external polarizing electric field, we show that it is possible to produce radiation at the second and fourth harmonic frequencies and to control the intensity of this radiation *via* the strength of this external field. In Sec. 4.5 we explore the harmonic generation process in plasmonic dimers with sub-nanometer gaps. In these structures each nanoparticle contributes to the nonlinear response as in Sec. 4.4, but the tunneling currents introduce an additional source of nonlinearity. We observe that under appropriate conditions, the harmonic generation can be enhanced by orders of magnitude thanks to the existence of nonlinear tunneling currents. The final discussion and conclusions are described in Sec. 4.6. This work was performed in close collaboration with A.G. Borisov and D.C. Marinica from the Approches théoriques en dynamique quantique group at the Institut des Sciences Moléculaires d'Orsay, who led the

calculations on Na nanoparticles. We use atomic units (a.u.) throughout this chapter unless otherwise stated.

4.1 Jellium model approach within TDDFT

In this chapter we use TDDFT calculations, which allow us to trace the nonlinear quantum-mechanical dynamics of conduction electrons in metallic nanoparticles, and are well suited to describe the nonlinear response of nanostructures at a quantum level[259]. The details on the numerical implementation used throughout the chapter can be found in Sec. 1.2. Using TDDFT calculations allows us to qualitatively and quantitatively determine the dynamics of relevant physical quantities and their dependence on the plasmon modes of the system, as well as on the applied electric field or on the gap distance separating a dimer of nanoparticles. Retardation effects are neglected because of the small particle sizes that we consider in Sec. 4.4 and Sec. 4.5. We study the valence electron dynamics in individual Aluminium spherical nanoparticles (Sec. 4.4), dimers of Al spheres and dimers of Na cylinders (Sec. 4.5). In all the cases, the particles are placed in vacuum. The effect of the surrounding aluminium oxide shell typically formed in ambient conditions[260] is not considered here. We adopt Aluminium and Sodium for our study because these are two prototypes of free-electron metals well described by the Jellium Model (JM)[70,261]. Aluminium nanoparticles offer several advantages because of their strong nonlinearity[229,262], and the presence of a Mie plasmon resonance in the ultra-violet[260,263,264], so that the nonlinear signal can be resonantly enhanced using a pump laser in the visible or near infrared range of the spectrum. On the other hand, Sodium is characterized by a lower electron density than Al, so that the Na metal nanoparticles feature plasmon modes in a frequency range similar to that of gold and silver nanoparticles and therefore have been often used as a prototype to study quantum effects in plasmonics[15,29,72,265].

Within the JM the lattice ions are represented by a uniform positive background charge of density $n_+ = \left[\frac{4\pi}{3}r_s^3\right]^{-1}$, with r_s being the Wigner-Seitz radius. We use the value $r_s = 2.07$ a_0 which corresponds to the Al metal (Sec. 4.4 and Sec. 4.5), and $r_s = 4$ a_0 for the Na metal (Sec. 4.5). Here $a_0 = 0.053$ nm is the Bohr radius.

Similar to the hydrodynamic treatments[52,255,257,258], the JM approach does not describe excitations involving electrons from the localized bands, as e.g. the d-band in the case of noble metals. However, and despite its simplicity, the JM correctly captures the collective behaviour of the conduction electrons and allows to address linear and nonlinear effects in plasmonic structures[29,72,87]. In particular, the JM along with the TDDFT approach allow to account for the electron spill-out, tunneling, nonlocal response, and photo-assisted transport, effects of paramount importance for electron-photon coupling in narrow gaps. For all the above, the JM has been often considered to elucidate robust quantum

effects in the linear and nonlinear plasmon response as confirmed by ab-initio and experimental results[15,21,22,29,72,87,133,265–269].

4.2   Description of the nonlinear response of plasmonic nanoparticles

The nonlinear response of a nanostructure much smaller than the wavelength of light can be described by means of its induced dipole $\mathbf{p}$. Let us consider a nanostructure made of centrosymmetric material, with a geometry characterised by a reflection symmetry plane set as the (x, y)-plane. For a combination z-polarized incident electromagnetic fields oscillating at different frequencies, the induced dipole at frequency ω is given by[14]

$$\mathbf{p}(\omega; t) = \sum_i \hat{e}_i \left[\alpha_{iz}^{(1)}(\omega) E_\omega + \alpha_{izzz}^{(3)}(\omega; \omega_o, \omega_k, \omega_m) E_{\omega_o} E_{\omega_k} E_{\omega_m} + \ldots \right], \quad (4.1)$$

where the sub-index i indicates the spatial direction $i = \{x, y, z\}$, $\hat{e}_i$ is the unit length vector in the corresponding direction and ω_o, ω_k, ω_m are three different illumination frequencies. The $\alpha^{(n+1)}$, $(n = 0, 2, 4, 6, ...)$ are the linear and nonlinear hyperpolarizability tensors of the system, where only the odd orders are nonzero because of the centrosymmetry, and $\omega = \omega_o + \omega_k + \omega_m$. The angular frequency of the different fields are indicated by the subindex and the short-hand notation $E_\omega \equiv E_\omega(t)$ has been used. If the system is illuminated by only one frequency, $\omega_o = \omega_k = \omega_m = \omega$, the combination of the different terms in Eq. (4.1) shows that only odd-order harmonics can be generated.

We illuminate the system by a z-polarized plane-wave of amplitude E_0 such as:

$$\mathbf{E}_\omega(t) = E_0 \cos(\omega t) \hat{e}_z , \quad (4.2)$$

The induced nonlinear dipoles oscillating at 3ω and 5ω can be obtained from Eq. (4.1) in a scalar form as:

$$p(3\omega; t) = \alpha^{(3)}(3\omega) \left[E_\omega^3(t) \right]_{3\omega} , \quad (4.3a)$$

$$p(5\omega; t) = \alpha^{(5)}(5\omega) \left[E_\omega^5(t) \right]_{5\omega} , \quad (4.3b)$$

where we used the simplified notations:

$$\alpha^{(3)}(3\omega) \equiv \alpha^{(3)}(3\omega; \omega, \omega, \omega) , \quad (4.4a)$$

$$\alpha^{(5)}(5\omega) \equiv \alpha^{(5)}(5\omega; \omega, \omega, \omega, \omega, \omega) , \quad (4.4b)$$

and where $[\ldots]_{n\omega}$ indicates that, when taking the nth power of $E_\omega(t)$, we only retain the contribution that oscillates at frequency $n\omega$. Only lower order contributions to the nonlinear dipole are considered.

From the nonlinear dipole:

$$p_{n\omega} = \mathcal{F}\left[p(n\omega; t)\right] \quad (n = 3, 5, ...) , \tag{4.5}$$

where $\mathcal{F}$ indicates the time-to-frequency Fourier transform, the power radiated by the nanostructure at the harmonic frequency, $\mathcal{I}_{n\omega}$, can be obtained as:

$$\mathcal{I}_{n\omega} = \frac{(n\omega)^4}{3c^3}|p_{n\omega}|^2, \tag{4.6}$$

where c is the speed of light in vacuum.

Even-order harmonics can be obtained if, along with the incident electromagnetic wave, the nanostructure is subjected to a polarizing static electric field $\mathbf{E}_p = \hat{e}_z E_p$ that breaks the centrosymmetry. In this case the total electric field (optical + static) acting on the nanosystem is given by:

$$\mathbf{E}(t) = \mathbf{E}_p + \mathbf{E}_\omega(t) = \left(E_p + E_0 \cos(\omega t)\right)\hat{e}_z . \tag{4.7}$$

For a centrosymmetric system illuminated by such an electromagnetic field, the corresponding nonlinear dipoles can be obtained from Eq. (4.1) in a scalar form as:

$$p(2\omega; t) = \alpha^{(3)}(2\omega)\left[E_\omega^2(t)\right]_{2\omega} E_p , \tag{4.8a}$$

$$p(4\omega; t) = \alpha^{(5)}(4\omega)\left[E_\omega^4(t)\right]_{4\omega} E_p , \tag{4.8b}$$

where we used:

$$\alpha^{(3)}(2\omega) \equiv \alpha^{(3)}(2\omega; \omega, \omega, 0) , \tag{4.9a}$$

$$\alpha^{(5)}(4\omega) \equiv \alpha^{(5)}(4\omega; \omega, \omega, \omega, \omega, 0) . \tag{4.9b}$$

Again, only lower order contributions to the nonlinear dipole are considered.

Using Eq. (4.6) and the Fourier transform of the nonlinear dipole in Eq. (4.8), it follows that the intensities of the even-order harmonics can be actively controlled by means of the polarizing field E_p:

$$\mathcal{I}_{n\omega} = \frac{(n\omega)^4}{3c^3}|\alpha^{(n+1)}(n\omega)E_0^n|^2 E_p^2, \ n = 2, 4, 6, ..., \tag{4.10}$$

where $\frac{c}{4\pi}|E_\omega|^2$ is the intensity of the excitation source.

The TDDFT calculations performed to obtain the results that will be discussed in Sec. 4.4 and Sec. 4.5 require the use of a Gaussian pulse as the illumination. Therefore, instead of the plane-waves of Eq. (4.2) and Eq. (4.7), we illuminate the plasmonic nanoparticles using a Gaussian of width $2 * \tau$ and

centred at t_0 given by:

$$\mathbf{E}_\omega(t) = E_0 \cos(\omega t) e^{-\left(\frac{t-t_0}{\tau}\right)^2} \hat{e}_z \ , \tag{4.11a}$$

$$\mathbf{E}(t) = \mathbf{E}_p + \mathbf{E}_\omega(t) = \left(E_p + E_0 \cos(\omega t) e^{-\left(\frac{t-t_0}{\tau}\right)^2}\right)\hat{e}_z \ , \tag{4.11b}$$

For the quantitative assessment of the hyperpolarisability ($\alpha^{(n)}$), Eq. (4.3) and Eq. (4.8) are used. A careful Fourier analysis is used to correctly take into account that the illumination is a finite pulse (Eq. (4.11a) and Eq. (4.11b)). The method is described in Appendix C.

In a practical situation, metallic nanoparticles are typically deposited at the substrate and are not perfectly spherical so that the inversion symmetry is generally broken. This symmetry breaking leads to a "background" even-order harmonic signal, observed experimentally[270,271], which will add-up to the generation of the even-order harmonic signal controlled by the applied polarizing electric field. In this work we address only the latter process (Electric Field-Induced Even-Harmonic Generation (EFIEHG)) assuming that its contribution can be distinguished from the former by varying the strength of the applied polarizing electric field[270,271].

Simple model to understand the physical origin of the even harmonics

In order to develop a better understanding of the origin of the even harmonics in centrosymmetric systems we present here a simplified model. Starting from the expression of the third harmonic dipole $p_{3\omega}(t)$ in Eq. (4.3), and assuming that the hyperpolarizability $\alpha^{(3)}$ is a scalar that does not depend on the frequency of the illumination and scattered fields, we can write

$$p(t) = \alpha^{(3)} E_\omega^3(t) \ . \tag{4.12}$$

If the optical field $E(t)$ is given by Eq. (4.2) and we use the trigonometric identity $\cos^3(x) = \left(3\cos(x) + \cos(3x)\right)/4$, we observe that only odd harmonics are excited.

However, if we insert the electric field in Eq. (4.7), which has a static and an oscillatory term, into Eq. (4.12), developing $E^3(t)$ gives us a contribution ($p'(t)$) to the total dipole proportional to $E_\omega^2(t)E_p$:

$$p'(t) = \alpha^{(3)} E_\omega^2(t) E_p = E_0^2 E_p \cos^2(\omega t) \ , \tag{4.13}$$

which using the trigonometric identity $\cos^2(x) = \left(1 + \cos(2x)\right)/2$ provide us with the harmonic term oscillating at 2ω:

$$p(2\omega; t) = \frac{1}{2}\alpha^{(3)} E_0^2 \cos(2\omega t) E_p \ . \tag{4.14}$$

and the rectification term with $\omega = 0$

$$p_{\text{rect}} = \frac{1}{2}\alpha^{(3)}E_0^2 E_p \ . \tag{4.15}$$

4.3 Retrieval of physical quantities in the frequency domain
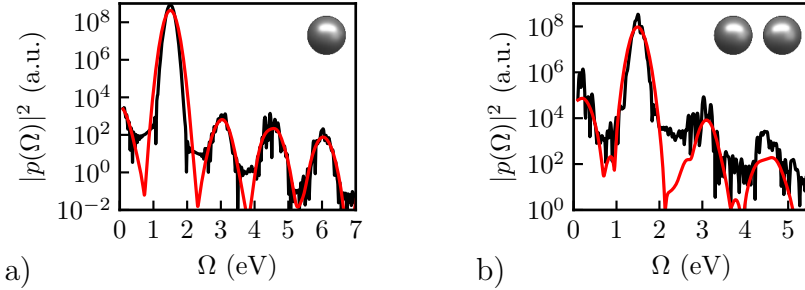
FIGURE 4.1: Spectrum of the dipolar response of (a) a single Al sphere polarised by a $E_p = 0.843$ V/nm static electric field and (b) a dimer of Al spheres separated by a gap $d_{\text{gap}} = 2.1$ Å and polarised by a $E_p = 0.535$ V/nm static electric field. In both cases the spheres are illuminated by a pulse of frequency $\omega = 1.5$ eV and $\mathcal{I} = 10^{11}$ W/nm^2. The black line represents the spectrum obtained using Eq. (4.16) with $\tau = \infty$ and the red line the corresponding result after applying the filter with τ equal to the width of the pulse.

In Sec. 4.4 and Sec. 4.5 we use frequency-resolved quantities such as the z-component of the induced dipole p_ω, the z-component of the induced field in the middle of the junction E_ω^g, the current through the middle of the junction I_ω, the current density $\mathbf{j}_\omega(\mathbf{r})$, or the induced charge density $n_\omega(\mathbf{r})$ for the analysis of the results. As TDDFT is a time-domain method that retrieves the electron dynamics in the nanoparticles, the physical quantities in the frequency domain are obtained from the corresponding time-dependent ones using the time-to-frequency Fourier transform (see Eq. (1.26)). Considering that the relevant sizes of the dimers under study are much smaller than the optical wavelength, the nonlinear response of the nanostructure can be adequately described by the z-component dipole induced at the corresponding frequency $p_{n\omega}$ (in our case with $n = 2$ and $n = 3$), given by

$$p_{n\omega} = \int_0^T e^{in\omega t} e^{-\left(\frac{t-t_0}{\Delta}\right)^2} p(t)dt \ , \tag{4.16}$$

In what follows we do not use the vector notations for the dipoles because for symmetry reasons only the dipole along the z-axis can be induced in the systems considered in this chapter. In Eq. (4.16) T is a large enough (though finite) propagation time, and $p(t)$ is the time-dependent dipole of the nanostructure

$$p(t) = - \int z \ n(\mathbf{r}, t) \ d^3\mathbf{r} \ , \qquad (4.17)$$

which is obtained from the induced electron density $n(\mathbf{r}, t)$ produced by the incident electromagnetic pulse, calculated with TDDFT. Alternatively, $p_{n\omega}$ can be obtained from the TDDFT result of the z-component of the harmonic current density[272] $j_{z,n\omega}(\mathbf{r})$:

$$n\omega \ p_{n\omega} = i \int \ j_{z,n\omega}(\mathbf{r}) \ d^3\mathbf{r} \ . \qquad (4.18)$$

where the $\exp(-in\omega t)$ time evolution of $p_{n\omega}$ is assumed. We have explicitly checked that Eq. (4.16) and Eq. (4.18) yield the same result.

We use a Gaussian filter of width $\Delta \geq \tau$ in Eq. (4.16) when performing the Fourier analysis of the time dependent quantities. This approach allows one to improve the convergence of the single nanoparticle and the dimer, and it is particularly appropriate for the excitation of the nanoparticles far from the plasmon resonance where the dipolar polarisation is only induced during the duration of the optical pulse (in practice we set $\Delta = \tau$, see Eq. (4.11a) and Eq. (4.11b)). In the cases where the harmonic frequency matches some plasmon mode of the dimer, the nonlinear dipole is enhanced, and it can be reliably extracted without using the filter (Δ parameter is then set to infinity in Eq. (4.16)). Figure 4.1 shows the effect of the filter on the dipolar spectrum of a single Al nanoparticle (Fig. 4.1a) and a dimer of Al spheres with gap distance $d_{\mathrm{gap}} = 2.1$ Å (Fig. 4.1b). In both cases the nanoparticles are illuminated at $\omega = 1.5$ eV and a static polarizing field is applied to produce even harmonics. The black line is the Fourier transform of the time evolution of the dipole $p(t)$ while the red line corresponds to the results obtained once the filter is applied. We can observe that the principal effect of the filtering is to remove the noise, which allows for an easier analysis of the results.

4.4 Electric Field-Induced Even-Harmonic Generation in Al spherical nanoparticles

In Sec. 4.2 we have introduced the possibility of active control of even harmonics by means of an externally applied polarizing static field. Indeed, a variety of strategies of active control of the optical response of plasmonic systems by externally applied perturbations have been proposed in the linear regime[226,273–275],

and the possibility of electrical tuning of plasmon resonances by means of different physical mechanisms has been recently demonstrated[65,276–284]. However, with the exception of optical rectification[285–287], active control in the nonlinear regime remains largely unexplored. It is only recently that experimental evidence of electrically controlled 2nd harmonic generation has been reported in planar metamaterials and plasmonic nanocavities filled with nonlinear materials[270,271].

Here we use the Time-Dependent Density Functional Theory (TDDFT) methodology (see Sec. 1.2) along with the JM for metal nanoparticles to retrieve the generation of even-order and odd-order harmonics in small spherical Al plasmonic nanoparticles of radius $R_{cl} = 13.86$ Å (containing $N_e = 2018$ electrons). We study harmonic generation and its dependence on the externally applied electric field and on the plasmon resonances. We find a robust field-induced 2nd harmonic generation[270,271,288–291] in centrosymmetric nanostructures and demonstrate the possibility of a controllable and efficient generation of higher harmonics under practical experimental conditions.

4.4.1 Active control of even-harmonic generation in single nanoparticles

To access the nonlinear response of the system we use a Gaussian incident electromagnetic pulse that launches the electron density dynamics. The electric field of the incident pulse has an amplitude E_0 and it is polarized along the direction of the applied static field E_p (Eq. (4.11b)). The pulse duration 2τ is set large enough (typically 6 laser periods, or 10-20 fs) so that well-resolved harmonics can be observed in the spectrum of the induced dipole[255]. We use optical pulses of intensity $\mathcal{P} = 10^{11}$ W/cm^2 and $\mathcal{P} = 10^{12}$ W/cm^2 so that $E_0 = 1.51 \times 10^{-3}$ a.u. and $E_0 = 4.8 \times 10^{-3}$ a.u.. Here "a.u." stands for atomic units (1 a.u., $= 514$ V/nm), respectively. A sketch of the system considered is presented in Fig. 4.2a.

The effect of the polarising field E_p on the nonlinear response of the spherical Al nanoparticle is shown in Fig. 4.2b. The intensity spectrum $|p(\omega)|^2$ of the dipole induced by the electromagnetic pulse is presented for the cases with and without polarising field. $p(\omega)$ is obtained by the time-to-frequency Fourier transform of the induced dipole $p(t)$ calculated with TDDFT upon substraction of the static polarisation produced by E_p. Without the polarising field only the odd-order harmonics are excited as expected from the symmetry of the system (blue dots). We clearly distinguish up to the 5th harmonic in the spectrum where the finite size of the harmonics peaks reflects the gaussian profile of the incident optical pulse[255] (see Eq. (4.11b)). When the static field is applied to the nanoparticle, even-order harmonics at 2ω and 4ω emerge (red lines). A static polarization is also produced in this case via processes involving $\alpha^{(3)}(0; \omega, -\omega, 0)$. Calculations performed with different powers of the
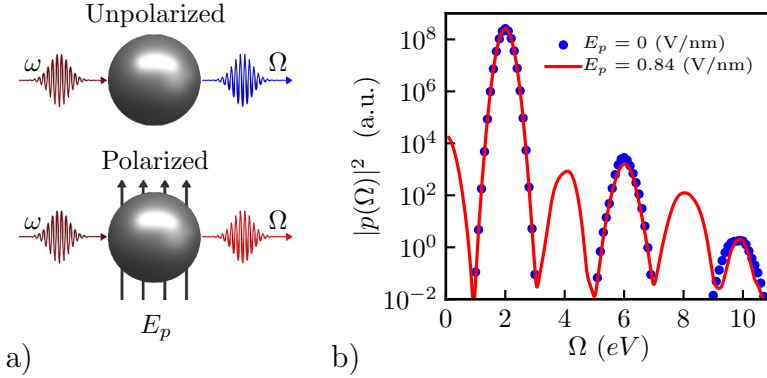
FIGURE 4.2: (a) Sketch of the spherical aluminium nanoparticle subjected to an optical pulse of frequency Ω (shown in brown) and emitting at frequency ω. Unpolarized/Polarized case refers to the situation without/with the presence of an applied static field E_p. (b) Intensity spectrum of the induced dipole $|p_\omega|^2$ (in atomic units, a.u.) for a spherical aluminium nanoparticle of radius $R_{cl} = 13.86$ Å excited by an optical pulse of intensity $\mathcal{I} = 10^{12}$ W/cm^2, frequency $\omega = 2$ eV (620 nm), and polarized along E_p. The blue dots and the red line indicate the results obtained for the "Unpolarized" and "Polarized" cases, respectively.

electromagnetic pulse confirm that the intensities of harmonics at $n\omega$ vary as $\mathcal{I}^n$.

The analysis of the electrical control of the even-order harmonic generation using a spherical Al nanoparticle is presented in Fig. 4.3. We show the nonlinear dipole induced at the 2nd ($|p_{2\omega}|^2$), and the 4th ($|p_{4\omega}|^2$) harmonic of the incident optical pulse with frequency $\omega = 2.18$ eV (wavelength 568.7 nm). The optical frequency is set such that the 4th harmonic is at resonance with the dipolar plasmon mode of the Al nanosphere, $4\omega = \Omega_{\mathrm{DP}}$. The energy of the dipolar plasmon $\Omega_{\mathrm{DP}} = 8.72$ eV (142.2 nm) is defined as the position of the maximum of the optical absorption cross section calculated here with TDDFT (see red dashed lines in Fig. 4.4). The resonance condition results in a strong increase of the nonlinear signal as we discuss in more detail in Sec. 4.4.2. In agreement with Eq. (4.8) and Eq. (4.10) the calculated nonlinearity (symbols) shows the $|p_{n\omega}|^2 \propto E_p^2$ dependence with the applied static field E_p as follows from the comparison to the analytical quadratic fit given by the corresponding dashed lines. A 10^4 increase in the intensities of the emitted harmonics is obtained within the studied range of E_p. The two orders of magnitude difference in the 2nd harmonic intensity obtained with incident pulses of intensity $\mathcal{I} = 10^{12}$ W/cm^2 and $\mathcal{I} = 10^{11}$ W/cm^2 reflects the $\mathcal{I} \propto |p_{n\omega}|^2$ scaling of the nonlinear signal (see Eq. (4.10)).

The TDDFT results in Fig. 4.3 span the 0.02 V/nm $\leq E_p \leq 1$ V/nm $(4 \times 10^{-5}$ a.u. $\leq E_p \leq 2 \times 10^{-3}$ a.u.) range, so that the relative strength of the
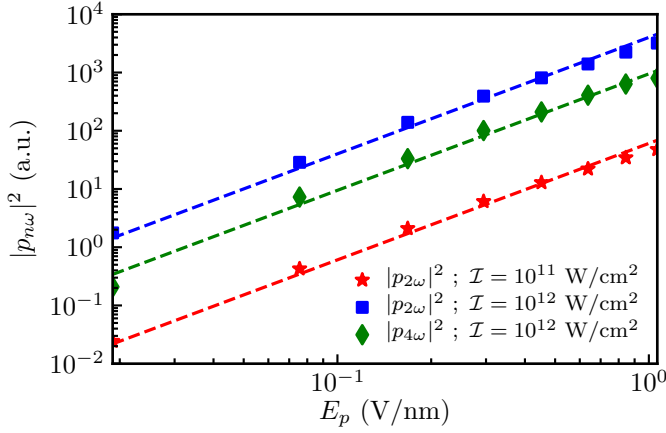
FIGURE 4.3: TDDFT results of the nonlinear response of a $R_{cl} = 13.86$ Å spherical Al nanoparticle. The intensities of nonlinear dipoles at the 2nd ($|p_{2\omega}|^2$) and 4th ($|p_{4\omega}|^2$) harmonic frequencies are presented as a function of the strength of the applied static field E_p. Symbols: TDDFT results; dashed lines: fits to a quadratic dependence. The incident optical pulse with frequency $\omega = 2.18$ eV (568.7 nm) is polarized along the direction of E_p. Results are shown for two intensities of the incident pulse: $\mathcal{I} = 10^{12}$ W/cm^2, and $\mathcal{I} = 10^{11}$ W/cm^2. For further details see the legend.

optical and applied static fields is $0.01 \leq E_p/E_0 \leq 1$. While one can a priori use Eq. (4.8) and extrapolate the data to even smaller E_p, in the TDDFT calculations of the nanoparticle considered, even-order harmonics are only resolved for applied static fields above 0.02 V/nm. These values of the polarizing field require that the nanostructure is placed in metallic nanogaps such as break junctions or gaps of electrically connected dimer antennas[285,287,292,293]. In this case an applied bias of a few volts can create strong enough static fields across the nanogap. An additional benefit of using an electrically connected dimer antenna is that the incident optical field acting on the Al nanostructure and/or the emitted second harmonic can be resonantly enhanced thus increasing frequency conversion efficiency.

The analytical fit of the TDDFT results with Eq. (4.8) allows to extract the hyperpolarisabilities of the nanosphere $|\alpha^{(3)}(2\omega; \omega, \omega, 0)| = 2.62 \times 10^7$ a.u. (1.3×10^{-32} esu), and $|\alpha^{(5)}(4\omega; \omega, \omega, \omega, \omega, 0)| = 2.5 \times 10^{12}$ a.u. (4.1×10^{-42} esu), as well as the respective effective susceptibilities (polarisability per unit volume) $|\chi^{(3)}(2\omega; \omega, \omega, 0)| = 1.2 \times 10^{-12}$ esu and $|\chi^{(5)}(4\omega; \omega, \omega, \omega, \omega, 0)| = 10^{-22}$ esu. We also obtain that $|\alpha^{(3)}(3\omega; \omega, \omega, \omega)|$ driving the third harmonic generation process is of the same order of magnitude as $|\alpha^{(3)}(2\omega; \omega, \omega, 0)|$. The values above are given for $\omega = 2.18$ eV (568.7 nm) such that the 4ω frequency coincide with the plasmon resonance. The third-order nonlinearity calculated

here for an Al nanosphere is typically 4 orders of magnitude lower than
the theoretical results reported for graphene nanostructures[239], and it is
comparable to the typical values for gold[244,245,294] and silver[254]. Note however
that in this latter case and in contrary to the situation considered here,
$|\chi^{(3)}(3\omega; \omega, \omega, \omega)| = 2 \times 10^{-9}$ esu was reported for the fundamental frequency
$\omega = 2.95$ eV (420 nm) at resonance with the Ag nanoparticle plasmon[253].

4.4.2   Plasmon enhancement of harmonic generation

The possibility of strong enhancement of the nonlinear signal when the sought
harmonic matches the plasmon resonance of the nanostructure represents a
major advantage when using plasmonic nanoparticles. This effect is usually
discussed for the 2nd or 3rd harmonic generation[230,235,239,243–245,253–255,295,296].
In this respect Al nanoparticles offer appealing possibilities because of the high
density of conduction electrons which lead to plasmon frequencies in the ultra-
violet in small nanoparticles. Thus, the resonance condition can be reached for
the 4th or higher harmonics of typical lasers.
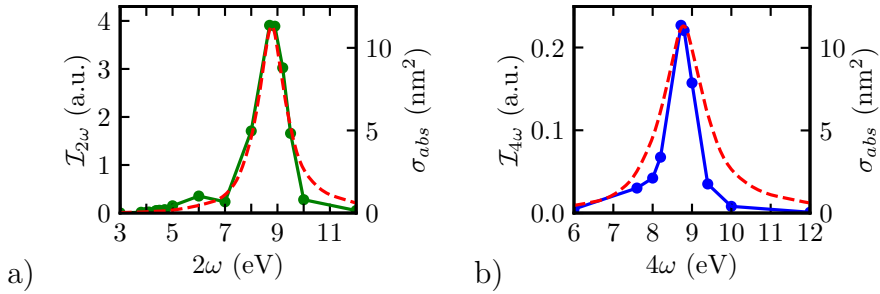
FIGURE 4.4: TDDFT results for the linear and nonlinear responses of a
$R_{cl} = 13.86$ Å Al spherical nanoparticle. The data is shown as a function of
(a) the 2nd harmonic frequency 2ω and (b) 4th harmonic frequency 4ω. The
green line with circles in panel (a) traces the intensity $\mathcal{I}_{2\omega}$ radiated at the
2nd harmonic. The blue line with circles in panel (b) traces the intensity $\mathcal{I}_{4\omega}$
radiated at the 4th harmonic. The incident optical pulse at frequency ω has an
intensity $\mathcal{I} = 10^{12}$ W/cm^2, and a static field $E_p = 0.843$ V/nm (0.0016 a.u.)
is applied. The dashed red line represents the optical absorption cross-section
of the individual Al nanoparticle $\sigma_{abs}(2\omega)$ (panel a), and $\sigma_{abs}(4\omega)$ (panel b).

We can link the linear and nonlinear response of Al nanoparticles with help
of the results shown in Fig. 4.4. In this figure, the red dashed lines represent
the absorption cross section at the harmonic frequency ($\sigma_{abs}(2\omega)$ in Fig. 4.4a
and $\sigma_{abs}(4\omega)$ in Fig. 4.4b). The solid lines show the radiated power $\mathcal{I}_{n\omega}$ at the
2nd (Fig. 4.4a) or 4th (Fig. 4.4b) harmonic frequency (Eq. (4.10)) produced by
an incident electromagnetic pulse when a static field with $E_p = 0.843$ V/nm
is applied. Since the static field and the amplitude of the optical field are

constant, the data in Fig. 4.4 show equivalently the frequency evolution of the hyperpolarizabilities as follows from Eq. (4.10).

The absorption cross-section features the dipolar plasmon resonance at $\Omega_{\mathrm{DP}} = 8.72$ eV (142.2 nm). Excitation of this mode affects the nonlinear response of the nanosphere. In both panels of Fig. 4.4 the frequency range is chosen to demonstrate that the intensity radiated by the plasmonic nanoparticle present a peak when the harmonic frequency overlaps with the dipolar plasmon resonance $\Omega_{\mathrm{DP}} = 8.72$ eV. To quantify the enhancement produced by the plasmon resonance we compare the intensity radiated when $n\omega = \Omega_{\mathrm{DP}}$ with the intensity radiated when $n\omega = 6$ eV, which corresponds to a frequency such that the absorption cross section $\sigma_{abs}(\omega = 6 \text{ eV}) \approx 0.05\sigma_{abs}(\Omega_{\mathrm{DP}})$. We obtain 1 order of magnitude increase for the 2nd harmonic and 2 orders of magnitude increase for the 4th harmonic radiated intensity.

4.5 Role of electron tunneling in the nonlinear response of plasmonic nanodimers

We have considered so far the nonlinear response of single nanoparticles. Plasmonic systems with narrow gaps have also received a much attention as platforms to efficiently support nonlinear optical processes because of their ability to strongly enhance electromagnetic fields in the gap region[46,148,230–233,243–246,270,295–301]. In this context, the quantum regime of plasmonics where the atomic scale becomes relevant, is an interesting benchmark to explore nonlinear responses. As discussed in previous chapters, the linear optical response of dimer plasmonic antennas with nanometer and sub-nanometer gaps is sensitive to quantum effects such as nonlocal screening and electron tunneling between the constituent nanoparticles[15,17,19,21,22,29,53,72,87,102,133,265–269]. This brings the question about the impact of quantum effects on the nonlinear processes in plasmonic structures with (sub-)nanometer gaps, and their eventual ability to strengthen the associated nonlinear optical response.

The coupling of tunneling electrons with photons is known to provide ultra-compact sources for light and plasmon generation in tunneling configurations[293,302–304]. This effect can become a source of frequency conversion due to the strong sensitivity of the tunneling process to the potential barrier across the junction and to the variation of the tunneling barrier with the optical bias. Optical rectification, as studied in narrow plasmonic gaps formed by STM configurations, or functionalised with molecules, or break junctions[285,286,298,305], is one of the examples of nonlinearity associated to the tunneling current and, a priori, it is accompanied by second-harmonic generation.

The presence of the high harmonics in the tunneling current has been studied in the context of the theory of Photo-Assisted electron Transport (PAT)[306–310], particularly well developed in the THz frequency range for semiconductor structures. At optical frequencies, the nonlinearity of the tunneling current was demonstrated using Time-Dependent Density Functional Theory (TDDFT) calculations for the case of a plasmonic dimer formed by spherical nanoparticles[29,72], and model studies based on the theory of PAT addressed the effect of tunneling in the nonlinear response of the gap nanoantenna[291,311–313].

The present work aims at clarifying the contributions of the rich variety of effects sustained in nanogap plasmonic systems to the nonlinear optical response. To that end we use TDDFT[59,63] calculations to retrieve the 2nd and 3rd harmonic generation from plasmonic dimer nanoantennas with narrow gaps. By considering a variety of geometries, different materials, and a wide range of junction sizes, we isolate different regimes of frequency conversion in structures with narrow plasmonic gaps. We analyse in detail the 2nd and 3rd harmonic generation in such situation, and show that under certain conditions the nonlinear tunneling current through the potential barrier between nanoparticles can provide a dominant contribution to the nonlinear response with up to 2 orders of magnitude increase in the frequency conversion efficiency. However, we also demonstrate that because of the role of the plasmon resonances, the dimer configuration does not always provide a gain in efficiency of the nonlinear process as compared to the pair of non-interacting nanoparticles.

4.5.1　Plasmonic systems considered

To reveal the role of tunneling effects, field enhancement, and plasmon modes in the generation of frequency conversion, we perform TDDFT calculations of the nonlinear optical response in dimers of metallic nanostructures separated by a vacuum gap and with different geometries, as sketched in Fig. 4.5a,b. The width of the gap, d_{gap}, is varied to cover all the interaction regimes, from a touching geometry to well-separated, weakly-coupled nanoparticles. We consider a spherical nanoparticle dimer (Fig. 4.5a) and a dimer formed by infinitely long cylindrical nanowires (Fig. 4.5b). The field of the fundamental incident wave is polarised along the dimer z-axis, as sketched in the figure. The spherical nanoparticle and the cylindrical nanowire dimer geometries allow for a strong field enhancement in the junction and feature Bonding Plasmon (BP) and Charge Transfer Plasmon (CTP) modes[15,17,29,45,53,72,87,265,314] discussed in previous chapters.

As in Sec. 4.4 the system is excited by an incident Gaussian electromagnetic pulse given by Eq. (4.11b) polarized along the dimer axis (z-direction). The pulse amplitude is E_0 and the static polarizing field is denoted by E_p. The pulse duration, 2τ, is again set large enough (typically 6 laser periods) to resolve the harmonic peaks. The results presented in this section are obtained with a field amplitude $E_0 = 1.5 \times 10^{-3}$ a.u. which corresponds to an intensity of the
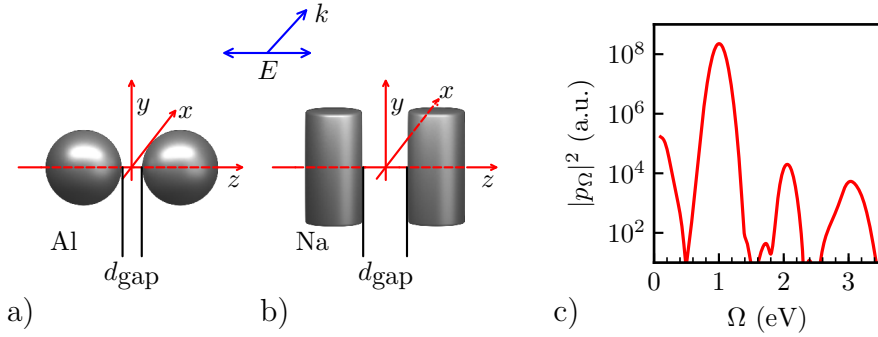
FIGURE 4.5: (a) Spherical Al nanoparticle dimer. Each individual nanosphere has a radius of $R_{sph} = 11$ Å and comprises 1012 electrons. (b) Dimer of Na cylinders, infinite along y-axis. An individual cylinder has a radius $R_{cyl} = 30.7$ Å and comprises 800 electrons per 1 nm length. In both cases the origin of coordinates is at the middle of the junction and the dimer z-axis is such that the $(x, y, z = 0)$-plane is the symmetry plane of the system. The incident electromagnetic field is a plane wave polarized along the z-axis and propagating along the x-axis. (c) Spectral analysis of the z-component of the induced dipole for a dimer of spherical Al nanoparticles separated by a junction of $d_{gap} = 2.1$ Å width. Results of the TDDFT calculations are shown as function of the emission frequency ω. The incident Gaussian electromagnetic pulse has carrier frequency $\omega = 1.0$ eV and the dimer is subjected to a static polarising field $E_p = 1.05 \times 10^{-4}$ a.u.

incident pulse of 10^{11} W/cm^2. Different values of E_0 were also used to confirm the $\mathcal{I}_{n\omega} \propto E_0^{2n}$ scaling of the intensity $\mathcal{I}_{n\omega}$ of the n-th harmonic.

For a dimer formed by identical free-electron metal nanoparticles, the 2nd harmonic generation is a symmetry-forbidden process[233,300,301]. However, as shown in Sec. 4.4, this process can be induced using a polarising field, E_p,[270,289,290] which allows to actively control the intensity of the 2nd harmonic generation. The results shown below for the 2nd harmonic generation of the Al dimer of spheres are obtained for a polarising field $E_p = 1.05 \times 10^{-4}$ a.u. In the calculations of the 3rd harmonic no dc polarising field is applied, $E_p = 0$.

In Fig. 4.5c we show an example of the spectral analysis of the dipolar polarisation of a spherical nanoparticle dimer separated by a junction of $d_{gap} = 2.1$ Å width. The dimer is polarized by a static electric field of $E_p = 1.05 \times 10^{-4}$ a.u. and the incident Gaussian electromagnetic pulse has a frequency $\omega = 1.0$ eV. The main peak in Fig. 4.5c corresponds to the induced dipole at the fundamental frequency. The 2nd and 3rd harmonics are also clearly distinguishable in the spectrum.

4.5.2   Linear response

Understanding the main phenomena underlying the dependence of the nonlinear response on the frequency of the fundamental wave and on the size of the gap first requires characterisation of the linear optical properties of the system. The linear optical response of a dimer configuration including the effects of quantum tunneling and nonlocality[15,17,29,45,53,72,87,265,314] has been addressed in great detail in the introduction and in Ch. 2 of this thesis. Therefore, we just summarize here the results for the two systems considered here.

The optical absorption cross section σ_{abs} calculated with TDDFT for the Na nanowire dimer and the Al nanosphere dimer in vacuum are shown in Fig. 4.6a,b as a function of the width of the gap d_{gap} and the frequency ω of the incident z-polarized plane wave. In Fig. 4.6c we show the d_{gap} dependence of the field enhancement, and of the ac electron current across the middle of the junction of the Na cylinder dimer. Results are presented for several relevant frequencies. The field enhancement is defined as $\mathrm{R_E} = |E_\omega^g/E_\omega|$, where E_ω and E_ω^g are given by the Fourier transforms of the incident pulse, and of the field induced by the nanostructure in the middle of the junction, respectively. The ac electron current through the middle of the junction is given by

$$I_\omega = \hat{e}_z \int dx \int dy \, \mathbf{j}_\omega(x, y, z = 0) \, . \tag{4.19}$$

In Fig. 4.6c the current is normalized to the field of the incident pulse ($|I_\omega/E_\omega|$ quantity is shown).

For large gap widths (capacitive coupling between nanoparticles), the absorption resonances correspond to the excitation of the bonding plasmon modes (Bonding Dipolar Plasmon (BDP), Bonding Quadrupolar Plasmon (BQP), etc) that are formed by the hybridization between the dipolar and higher momentum plasmon modes of the individual nanoparticles[314]. As the width of the gap d_{gap} decreases, we observe the redshift experienced by the bonding plasmons due to the attractive interaction between the charges of opposite sign induced at facing metal surfaces across the junction. The induced charges also lead to the enhancement of the electromagnetic field in the gap between nanoparticles. The field enhancement, $\mathrm{R_E}$, increases with decreasing d_{gap} and can reach very high values at bonding plasmon resonance frequencies[15,45]. However, the enhancement at low frequencies, out of resonance, is also considerable, as observed in Fig. 4.6c.

When d_{gap} is reduced down to a few Å, the absorption resonances owing to the bonding plasmon modes progressively disappear, and the field enhancement is first saturated and then quenched. This effect is attributed to the establishment of the ac tunneling current across the junction, I_ω, at optical frequencies. Because of the electron transfer through the potential barrier separating the nanoparticles, the lowest (CTP) and higher energy (CTP') charge transfer plasmon modes emerge. The nanoparticles thus become conductively
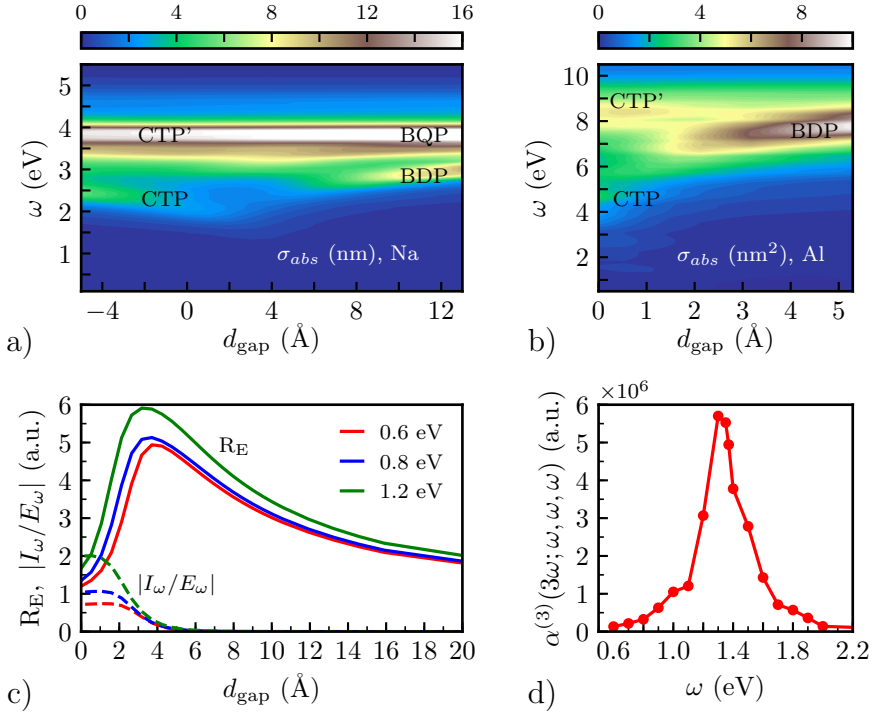
FIGURE 4.6: Colour plots of the optical absorption cross section σ_{abs} of (a) a dimer of cylindrical Na wires and (b) a dimer of spherical Al nanoparticles. TDDFT results are presented as a function of the size of the gap between nanoparticles d_{gap} and frequency of the incident plane wave ω. Labels indicate the plasmon modes responsible for the absorption resonances: Bonding Dipolar Plasmon (BDP), Bonding Quadrupolar Plasmon (BQP), the lowest-energy (dipole) Charge Transfer Plasmon (CTP), and the higher energy CTP'. (c) Gap-size dependence of the enhancement of the incident field $R_E = |E_\omega^g/E_\omega|$ (solid lines) and of the amplitude of the normalized ac current $|I_\omega/E_\omega|$ (dashed lines) between nanoparticles for the cylindrical Na dimer. The TDDFT results are obtained in the middle of the gap for different frequencies of the linearly polarised incident electromagnetic wave $\omega = 0.6$ eV ($\lambda = 2066$ nm), $\omega = 0.8$ eV ($\lambda = 1550$ nm), and $\omega = 1.2$ eV ($\lambda = 1033$ nm). Here, E_ω is the incident field, E_ω^g is the induced ac field in the middle of the gap and I_ω is the electron current across the gap at the optical frequency. (d) Hyper-polarisability $\alpha^{(3)}(3\omega)$ of an individual Na nanowire. The values are given in atomic units (a.u.). The relation 1 esu = 0.1985×10^{40} a.u. can be used for conversion of the third-order hyper-polarisability to electrostatic units (esu).

coupled prior to direct geometrical contact between their surfaces. The establishment of I_ω can be identified in Fig. 4.6c for the dimer of Na cylinders. As d_{gap} decreases, the ac current between nanoparticles I_ω grows exponentially (tunneling regime). However, starting from $d_{\mathrm{gap}} \simeq 2$ Å the potential barrier separating the nanoparticles decreases enough so that the electrons close to the Fermi level can move quasi-freely across the junction. In this situation I_ω is stabilised at a nearly constant value.

Qualitatively, the results obtained for the Al spherical dimer and for the Na nanowires dimer are very similar, except for the relevant frequency and distance ranges. Because of the lower electron density, the dipolar plasmon resonance of an individual Na cylinder is at $\omega = 4$ eV compared to the dipolar plasmon resonance of an individual Al sphere at $\omega = 8.7$ eV. Regarding the relevant distances, the effects of electron tunneling require smaller d_{gap} to be apparent in the Al case. Indeed, the tunneling barrier of the junction is larger in this case because of its higher work function. Note also that because of the much larger radii, the plasmon resonances are better defined for the Na nanowires. In the case of Al, the strong interaction between collective (plasmon) and one-particle electron-hole pair excitations leads to the broadening of the plasmon modes[315].

Among the effects influencing the nonlinear response of metal nanostructures, the situations where the incident wave, or the frequency-converted signal (second or third harmonic for example) are in resonance with the plasmon mode of the system have been identified as particularly effective[232–237,243–255]. We already discussed this resonance enhancement in Sec. 4.4.2 for the case of Al spherical nanoparticles (see Fig. 4.4). This resonant effect is further illustrated in Fig. 4.6d with the example of an individual Na cylinder in vacuum. The third-order hyper-polarisability, $\alpha^{(3)}(3\omega)$, increases by more than one order of magnitude when the frequency of the 3rd harmonic matches the dipolar plasmon resonance of the individual cylinder, $3\omega = 4$ eV. Similarly, a strong resonant increase of the nonlinear response is also obtained for the dimer, as discussed below in Sec. 4.5.4.

4.5.3   Nonlinear response in off-resonant conditions

To facilitate the analysis of the different mechanisms involved in the nonlinear response and reveal the effect of electron tunneling across the gap of the nanoantenna, we focus first, in Fig. 4.7, on the situation where the illuminating laser and the studied harmonic are detuned with respect to the plasmonic resonances. Specifically, we use $\omega \leq 0.8$ eV for the Na nanowire dimer and $\omega \leq 2.5$ eV for Al nanospheres, which places the 2nd or 3rd harmonic frequencies below the energies of the plasmon modes of the system (see Fig. 4.6a,b). It is also noteworthy that considering low frequencies for the incident wave allows for a more direct comparison between the results of the TDDFT calculations and the qualitative analytical trends obtained within the theory of PAT[306–308]. After the contribution of tunneling to the nonlinear response is unveiled, we
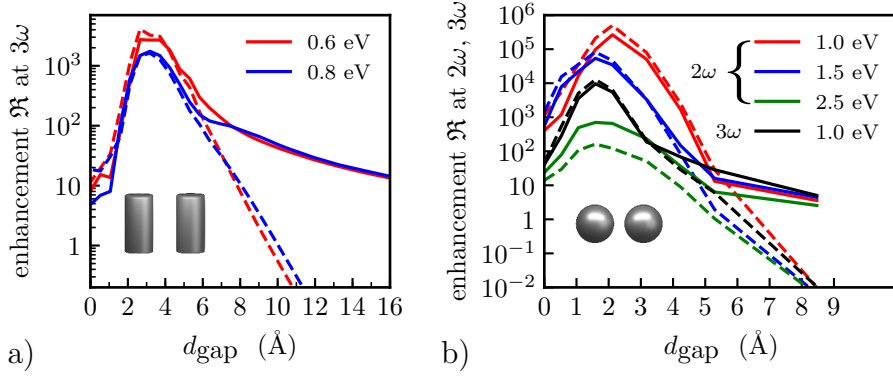
FIGURE 4.7: Nonlinear response of a dimer of (a) cylindrical Na, and (b) spherical Al nanoparticles. Results of the TDDFT calculations are shown as a function of the size of the gap between nanoparticles, d_{gap}. Solid lines represent the enhancement of the intensity of the nonlinear dipole $\mathfrak{R}_n = |p_{n\omega}|^2 / (4 |p_{n\omega}^i|^2)$ at the 2$^{\text{nd}}$ ($n = 2$) and 3$^{\text{rd}}$ ($n = 3$) harmonic frequency. Dashed lines represent the scaled ac current through the middle of the junction $\beta |I_{n\omega}|^2 / (4 |p_{n\omega}^i|^2)$ calculated at the 2$^{\text{nd}}$ and 3$^{\text{rd}}$ harmonic frequency. Different colours correspond to results obtained with different frequencies ω of the incident fundamental wave, as detailed in the legends.
For further details, including the definition of β, see the main text.

will extend our analysis to the results obtained at higher frequencies which show resonance effects.

In Fig. 4.7 we show the enhancement $\mathfrak{R}$ of the nonlinear response for the dimer configuration (solid lines). This enhancement is defined as the ratio between the intensity of the 2$^{\text{nd}}$ ($n = 2$) or 3$^{\text{rd}}$ ($n = 3$) harmonic emitted by the dimer and the intensity of the corresponding nonlinear signal obtained from the pair of non-interacting nanoparticles:

$$\mathfrak{R}_n = |p_{n\omega}|^2 / (4 |p_{n\omega}^i|^2), \tag{4.20}$$

where $p_{n\omega}$ is the induced nonlinear dipole of the dimer, and $p_{n\omega}^i$ is the non-linear dipole of the corresponding individual nanoparticle. Along with the enhancement $\mathfrak{R}_n$, we also show the scaled ac current through the middle of the junction, $\beta |I_{n\omega}|^2 / (4 |p_{n\omega}^i|^2)$, calculated at the 2$^{\text{nd}}$ and 3$^{\text{rd}}$ harmonic frequency (dashed lines). β is a scaling parameter that will be defined below in this section. Calculations have been performed for the dimer of cylindrical Na nanowires (Fig. 4.7a) and for the Al nanospheres dimer (Fig. 4.7b). The results of these calculations are shown as a function of the width of the gap for several frequencies of the incident pulse, as indicated in the insets of the figures.

In this off-resonant situation the same general trends are obtained overall for both dimer geometries. The nonlinear conversion is much more efficient for a

dimer configuration than for non-interacting nanoparticles. The intensity of the nonlinear signal progressively increases from large separation distances, as the width of the gap d_{gap} decreases. This increase is due to the field enhancement in the gap of the dimer (see Fig. 4.6c), so that each nanoparticle of the dimer is subjected to a stronger field leading to its larger nonlinear polarisation. The TDDFT results obtained here for low ω thus confirm the advantage of using a dimer nanoantenna configuration as a platform for enhancing nonlinear effects.

At first glance, the main trends in the dependence of the frequency conversion on d_{gap} (Fig. 4.7a and Fig. 4.7b) seem to correspond to the dependence of the field enhancement with the gap width (see Fig. 4.6c). In particular, the decrease of the nonlinearity for narrow gaps correlates with the quenching of the field enhancement due to the establishment of the optically induced ac current, I_ω, across the junction (see Fig. 4.6c). It is then tempting to consider that the nonlinear response of the dimer can be explained on the basis of the nonlinear response of the individual nanoparticles subjected to the corresponding enhanced fields. However, a careful inspection of the data obtained for the gap widths of $d_{\text{gap}} < 4 - 6$ Å shows additional features that might point at a different explanation:

All the TDDFT results for the *nonlinear response* shown in Fig. 4.7 feature the same trend when the width of the gap is reduced to a few Å range where the electron transport across the junction strongly affects the *linear response* of the system (see Fig. 4.6a,b). Namely, the efficiency of the frequency conversion reaches a maximum at $d_{\text{gap}} = 2 - 3$ Å (depending on the metal), distances which correspond to the strongest electron transport via an ac-tunneling current through the potential barrier separating the nanoparticles, and before establishment of ballistic transport. For even smaller d_{gap}, as the conductive contact is fully established across the junction, the conversion efficiency $\mathfrak{R}$ drops off by several orders of magnitude. The dimer evolves towards a single, albeit larger, joint nanoparticle.

At first glance, the main trends in the dependence of the frequency conversion on d_{gap} (Fig. 4.7a and Fig. 4.7b) seem to correspond to the dependence of the field enhancement with the gap width (see Fig. 4.6c). In particular, the decrease of the nonlinearity for narrow gaps correlates with the quenching of the field enhancement due to the establishment of the optically induced ac current, I_ω, across the junction (see Fig. 4.6c). It is then tempting to consider that the nonlinear response of the dimer can be explained on the basis of the nonlinear response of the individual nanoparticles subjected to the corresponding enhanced fields. However, a careful inspection of the data obtained for the gap widths of $d_{\text{gap}} < 4 - 6$ Å shows additional features that might point at a different explanation:

- The smooth variation of the nonlinearity when decreasing d_{gap} at large separations is replaced by a sharp growth at a separation distance of $d_{\text{gap}} \approx 4 - 6$ Å, which correlates with the fast increase of the ac electron tunneling across the gap.

- The change in the behaviour of the nonlinear response at $d_{\text{gap}} \approx 4 - 6$ Å, and the overall dependence of $\mathfrak{R}(d_{\text{gap}})$ in the tunneling region matches the dependence on d_{gap} of the corresponding n-th harmonic of the (tunneling) current across the junction, $|I_{nw}|^2$, marked with dashed lines in Fig. 4.7a and in Fig. 4.7b.

In what follows, on the basis of a detailed analysis of the TDDFT results we show that while for large d_{gap} the nonlinear response of the dimer is that of individual nanoparticles subjected to enhanced fields, the electron tunneling, and more generally electron transport through the junction, plays a key role

dimer configuration than for non-interacting nanoparticles. The intensity of the nonlinear signal progressively increases from large separation distances, as the width of the gap d_{gap} decreases. This increase is due to the field enhancement in the gap of the dimer (see Fig. 4.6c), so that each nanoparticle of the dimer is subjected to a stronger field leading to its larger nonlinear polarisation. The TDDFT results obtained here for low ω thus confirm the advantage of using a dimer nanoantenna configuration as a platform for enhancing nonlinear effects.

All the TDDFT results for the *nonlinear response* shown in Fig. 4.7 feature the same trend when the width of the gap is reduced to a few Å range where the electron transport across the junction strongly affects the *linear response* of the system (see Fig. 4.6a,b). Namely, the efficiency of the frequency conversion reaches a maximum at $d_{\text{gap}} = 2 - 3$ Å (depending on the metal), distances which correspond to the strongest electron transport via an ac-tunneling current through the potential barrier separating the nanoparticles, and before establishment of ballistic transport. For even smaller d_{gap}, as the conductive contact is fully established across the junction, the conversion efficiency $\mathfrak{R}$ drops off by several orders of magnitude. The dimer evolves towards a single, albeit larger, joint nanoparticle.

At first glance, the main trends in the dependence of the frequency conversion on d_{gap} (Fig. 4.7a and Fig. 4.7b) seem to correspond to the dependence of the field enhancement with the gap width (see Fig. 4.6c). In particular, the decrease of the nonlinearity for narrow gaps correlates with the quenching of the field enhancement due to the establishment of the optically induced ac current, I_ω, across the junction (see Fig. 4.6c). It is then tempting to consider that the nonlinear response of the dimer can be explained on the basis of the nonlinear response of the individual nanoparticles subjected to the corresponding enhanced fields. However, a careful inspection of the data obtained for the gap widths of $d_{\text{gap}} < 4 - 6$ Å shows additional features that might point at a different explanation:

- The smooth variation of the nonlinearity when decreasing d_{gap} at large separations is replaced by a sharp growth at a separation distance of $d_{\text{gap}} \approx 4 - 6$ Å, which correlates with the fast increase of the ac electron tunneling across the gap.

- The change in the behaviour of the nonlinear response at $d_{\text{gap}} \approx 4 - 6$ Å, and the overall dependence of $\mathfrak{R}(d_{\text{gap}})$ in the tunneling region matches the dependence on d_{gap} of the corresponding n-th harmonic of the (tunneling) current across the junction, $|I_{nw}|^2$, marked with dashed lines in Fig. 4.7a and in Fig. 4.7b.

In what follows, on the basis of a detailed analysis of the TDDFT results we show that while for large d_{gap} the nonlinear response of the dimer is that of individual nanoparticles subjected to enhanced fields, the electron tunneling, and more generally electron transport through the junction, plays a key role

in the formation of the nonlinear response of the dimer structures with narrow gaps ($d_{\text{gap}} < 4 - 6$ Å).

Nonlinear tunneling currents

Electron tunneling through the junction can influence the nonlinear response due to its effect on the distribution of the fields inside the particles, as well as due to the nonlinearity of the tunneling process itself[29,291,311,312]. The latter can be qualitatively argued using a semi-classical approach as follows: high harmonics in the tunneling current between nanoparticles, $I_{n\omega}$, arise because of the nonlinearity in the current-voltage characteristic, $I(V)$, of the junction: $I_{n\omega} \propto \frac{\partial^n I}{\partial V^n} (U_{\text{opt}})^n$, where $U_{\text{opt}} = d_{\text{gap}} E_\omega^g$ is the optical potential (bias) across the gap[285,298], with E_ω^g the corresponding local field in it. Going beyond this simple approach, the quantum theory of photon-assisted tunneling provides a closed-form expression for the time-dependent tunneling current in terms of the complex response function of the junction $\mathfrak{J}$[306,309]:

$$I(t) = \text{Im}\left(\sum_{n,m} J_n(\alpha) J_{n+m}(\alpha) \, e^{im\omega t} \, \mathfrak{J}(V_p + n\omega)\right), \qquad (4.21)$$

where $\text{Im}(x)$ stands for the imaginary part of x, J_k is the Bessel function of order k , and $\alpha = \frac{U_{\text{opt}}}{\omega}$. Assuming that α is small, $J_k(\alpha) \propto \left(\frac{U_{\text{opt}}}{\omega}\right)^k$. Under these conditions, and in agreement with a simple semi-classical approach, it follows from Eq. (4.21) that the high harmonics in the tunneling current between nanoparticles are given by $I_{nw} \propto (d_{\text{gap}} E_\omega^g/\omega)^n$. We find, that the relative weight of high harmonics in the ac tunneling current through the junction calculated with TDDFT indeed increases as $I_{n\omega}/I_\omega \propto (E_\omega^g d_{\text{gap}})^{(n-1)}$ with increasing separation between nanoparticles. For the Na cylinder dimer at large d_{gap}, $I_{3\omega}$ becomes comparable to the ac tunneling current at the frequency of the fundamental wave I_ω. Obviously, both tunneling currents are exponentially small in this case.

To further analyse the origin of the nonlinear response, we show in Fig. 4.8c colour maps of the absolute value of the z-component of the current density at the 3$^{\text{rd}}$ harmonic frequency $|j_{z,3\omega}(y,z)|$ for a Na cylindrical dimer nanoantenna (Fig. 4.8a), calculated in the (x,z)-plane perpendicular to the cylinders axis. The frequency of the fundamental wave is $\omega = 0.6$ eV. Note that because of the strong variation of the nonlinearity with d_{gap} the colour scale is set separately for each panel. Assuming an $\exp(-i\omega t)$ time dependence, the total z-oriented nonlinear dipole per unit length can be obtained from the relationship[272]

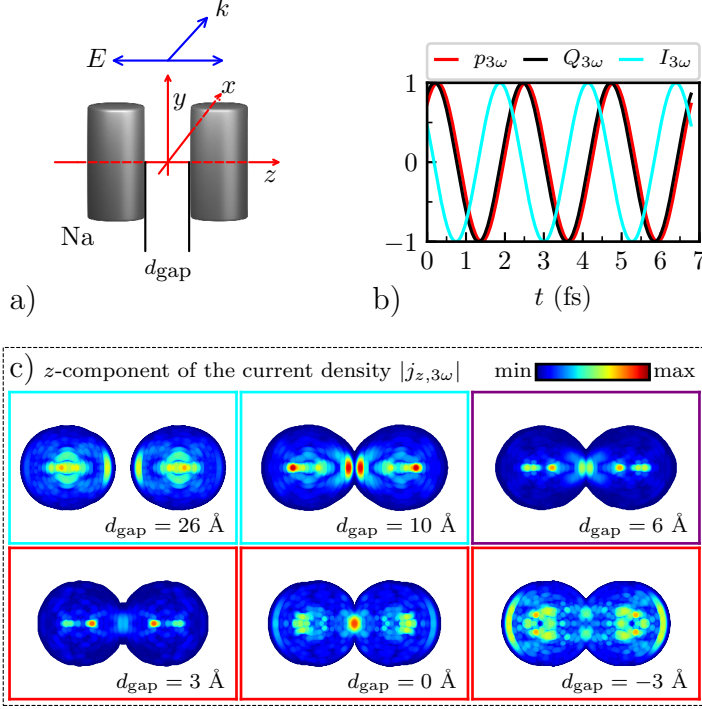$$3\omega \, p_{3\omega} = i \int dy \int dz \, j_{z,3\omega}(y,z). \qquad (4.22)$$

FIGURE 4.8: Analysis of the nonlinear response of the Na cylindrical dimer for the frequency of the fundamental wave $\omega = 0.6$ eV. (a) Sketch of the geometry of the system and of the polarisation of the fundamental wave. (b) Time evolution of the nonlinear dipole $\mathrm{Re}\!\left(e^{-i3\omega t}\, p_{3\omega}\right)$ (red), charge transferred between nanoparticles $\mathrm{Re}\!\left(e^{-i3\omega t}\, Q_{3\omega}\right)$ (black), and current through the junction $\mathrm{Re}\!\left(e^{-i3\omega t}\, I_{3\omega}\right)$ (cyan) at the 3rd harmonic frequency. Results are shown for $d_{\mathrm{gap}} = 3$ Å, which corresponds to the maximum enhancement of the 3rd harmonic intensity. Here, $\mathrm{Re}(x)$ stands for the real part of x. All the quantities are scaled to 1 at the maximum. (c) Colour plots of the the current density $\mathbf{j}_{3\omega}$ induced at the 3rd harmonic frequency calculated for several sizes of the gap d_{gap}. The absolute value of the z-component of $\mathbf{j}_{3\omega}$, $|j_{z,3\omega}| \equiv |\hat{e}_z\, \mathbf{j}_{3\omega}|$ is shown in the (x,z)-plane. Blue frames indicate a regime of capacitive coupling between nanoparticles, and red frames indicate a conductive coupling regime. A violet frame is used for an intermediate situation at $d_{\mathrm{gap}} = 6$ Å.

Thus, the results in Fig. 4.8 allow us to visualize the relative contributions of the nonlinear currents to $p_{3\omega}$ in the different regions of space. In particular, it is interesting to know how the relative weight of the nonlinear tunneling current evolves with d_{gap}.

For well-separated cylinders ($d_{\mathrm{gap}} = 26$ Å, and $d_{\mathrm{gap}} = 10$ Å) the nonlinear current is predominantly excited in the volume of each nanoparticle as well as at the portion of its surface oriented in the direction along the electric field of the incident pulse. Thus, we observe the (strong) volume and (weaker) surface contributions to the nonlinear polarisation[255]. At these sizes of the gap the total dipole $p_{3\omega}$ is built as a sum of the polarisations of individual cylinders. Note that the nonlinear surface currents are stronger at the surfaces facing the gap because of the field enhancement at the junction. A decrease of the gap width to $d_{\mathrm{gap}} = 10$ Å leads to larger fields in the gap region so that the contribution of the metal surfaces facing the gap becomes more pronounced.

For $d_{\mathrm{gap}} \leq 8$ Å the coupling between cylindrical nanowires evolves from capacitive to conductive. In this situation electron tunneling through the junction strongly affects the optical absorption cross section σ_{abs} as shown in Fig. 4.6a,c. Along with its effect on the linear response, the electron transport through the junction contributes to the nonlinear polarisation of the dimer. Indeed, simultaneously to the presence of the surface currents, the 3rd harmonic current through the junction becomes visible for $d_{\mathrm{gap}} = 6$ Å, and the regions with the strongest nonlinear current density within the nanoparticle volume shift towards the junction. Note that the volume current density also contains the contribution of the tunneling current. This is because the electrons transferred through the potential barrier of the junction continue to move towards the inner part of the nanoparticle while suffering inelastic scattering and dephasing due to the collisions with the valence electrons[316,317]. Thus, it is impossible to explicitly separate the tunneling current contribution to the build up of the total nonlinear polarisation.

A gap width of $d_{\mathrm{gap}} = 3$ Å corresponds to the situation with the strongest enhancement of the nonlinear conversion in the system (see Fig. 4.7a). In this case the 3rd harmonic of the tunneling current in the junction region is essential while the surface nonlinear currents are not distinguishable at the scale of the figure. By further decreasing the width of the gap, at geometrical contact between the cylinders ($d_{\mathrm{gap}} = 0$ Å) the junction becomes metallic. The tunneling barrier for the electrons moving along the dimer axis disappears, the field is expelled outside the junction neck created by the metallic conductive path, and the field enhancement in the gap is quenched. Interestingly, the nonlinear currents in the gap remain strong relative to the other regions. It is worth stressing however that the total nonlinear polarisation and 3rd harmonic currents between nanoparticles are orders of magnitude smaller than that in the tunneling regime at $d_{\mathrm{gap}} = 3$ Å (see Fig. 4.7a). In this case of conductive contact we ascribe the strong nonlinear current through the gap region to the evolution of the system towards the limit of a single elongated peanut-shape
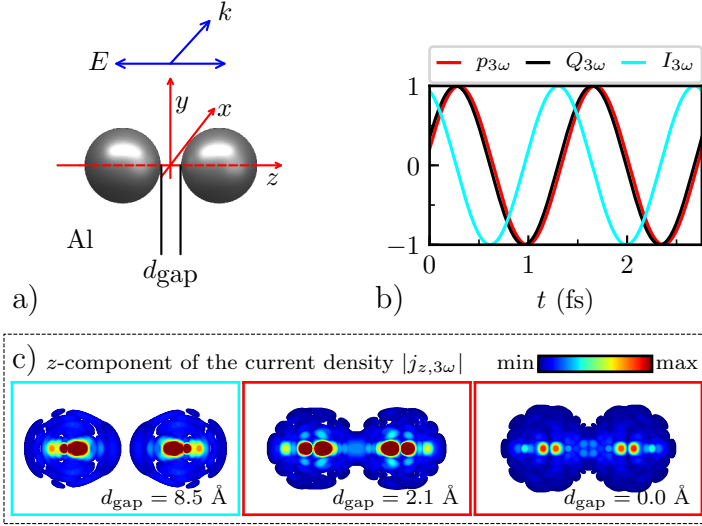
FIGURE 4.9: Analysis of the nonlinear response of an Al spherical dimer for a frequency of the fundamental wave $\omega = 1$ eV. (a) Sketch of the geometry of the system and of the polarisation of the fundamental wave. (b) Time evolution of the nonlinear dipole $\mathrm{Re}\left(e^{-i3\omega t}\,p_{3\omega}\right)$ (red), charge transferred between nanoparticles $\mathrm{Re}\left(e^{-i3\omega t}\,Q_{3\omega}\right)$ (black), and current through the junction $\mathrm{Re}\left(e^{-i3\omega t}\,I_{3\omega}\right)$ (cyan) at the 3rd harmonic frequency. Results are shown for $d_{\mathrm{gap}} = 2.1$ Å, which corresponds to the maximum enhancement of the 3rd harmonic intensity All the quantities are scaled to 1 at the maximum. (c) Colour plots of the current density $\mathbf{j}_{3\omega}$ induced at the 3rd harmonic frequency calculated for several sizes of the gap d_{gap}. The absolute value of the z-component of $\mathbf{j}_{3\omega}$, $|j_{z,3\omega}| \equiv |\hat{e}_z\,\mathbf{j}_{3\omega}|$ is shown in the (x, z)-plane. Blue frames indicate a regime of capacitive coupling between the nanoparticles and red frames indicate a conductive coupling regime.

nanowire. The formation of the nonlinear dipole involves the charge separation between left and right parts of this compound nanoparticle which results in electron currents through the junction. Because of the small cross-section of the latter relatively high currents might be reached. In the fully overlapping geometry ($d_{\mathrm{gap}} = -3$ Å) the role of the nonlinear currents at the bulk of the particles and at the surfaces increases, with the corresponding decrease of the contribution at the junction itself. This is consistent with a recovery of the nonlinear response based on the intrinsic bulk and surface nonlinearity of the full connected system.

In Fig. 4.9 we perform the same analysis as in Fig. 4.8 but for a dimer of Al spheres as sketched in Fig. 4.9a. Figure 4.9c shows the absolute value of the z-component of the current density at the 3rd harmonic frequency $|j_{z,3\omega}| \equiv |\hat{e}_z\,\mathbf{j}_{3\omega}|$ when the dimer is illuminated at a frequency $\omega = 1$ eV

and for three different gap distances d_{gap}. The plots show similar trends to the ones obtained for the dimer of cylinders in Fig. 4.8c. In the capacitive regime (blue panel) the nonlinear currents concentrate in the volume of the nanoparticles. When the gap is reduced and the system enters the conductive regime (red panels), an electron current at the 3rd harmonic frequency is developed across the gap. The central panel shows the current density map for a tunneling gap distance ($d_{\text{gap}} = 2.1$ Å) corresponding to the peak of the induced nonlinear dipole (see Fig. 4.7b). In this case a strong nonlinear current across the gap is observed in addition to the currents in the volume. When the particles touch, the nonlinear current flow between the nanoparticles owing to the direct conductive contact and the nonlinear current at the bulk dominates.

Nonlinear currents through the junction and build up of the nonlinear response of the dimer

The nonlinear current through the middle of the junction,

$$I_{n\omega} = \iint j_{z,n\omega}(x, y, z = 0) dx dy, \tag{4.23}$$

transfers a charge $Q_{n\omega} = iI_{n\omega}/(n\omega)$ between the nanoparticles and polarizes the system. Here the relationship $I_{n\omega} = dQ_{n\omega}/dt = -in\omega Q_{n\omega}$ is used assuming harmonic signals. The resulting charge-transfer dipole can be expressed as $DQ_{n\omega} = iDI_{n\omega}/(n\omega)$, with D the (unknown) effective separation between the charges $\pm Q_{n\omega}$ induced in the nanoparticles. In Fig. 4.8b we show the dynamics of the total nonlinear dipole $p_{3\omega}$, the transferred charge $Q_{3\omega}$, and the current $I_{3\omega}$ calculated for the dimer of Na cylinder illuminated by a electromagnetic wave of fundamental frequency $\omega = 0.6$ eV, and $d_{\text{gap}} = 3$ Å. These conditions correspond to the maximum enhancement of the 3rd harmonic generation by the dimer nanoantenna. The width of the gap is such that the system is in the tunneling regime, i.e., electron transport through the junction corresponds to the tunneling through the potential barrier between nanoparticles. The total nonlinear dipole evolves in phase with the transferred charge and its time evolution is shifted by a quarter of an optical period with respect to that of the current, i.e. the dynamics of the total nonlinear dipole is equivalent to that of the charge transfer dipole. This result is consistent with a likely important role played by the charge transfer dipole and thus by the electron transport through the junction in the build up of the total nonlinear polarisation.

One might consider that for the Na nanowire dimer the increase of nonlinear response for tunneling distances is connected with an effect of proximity of the frequency of the 3rd harmonic to the CTP. For $d_{\text{gap}} = 1 - 2$ Å this is indeed the case at low frequencies of the fundamental wave $\omega = 0.6$ eV and $\omega = 0.8$ eV, and this could further increase the role of the electron transport across the gap. However, the same qualitative results in the behaviour of the nonlinear current and the charge transfer are obtained in the case of an Al spherical

dimer for the frequency of the fundamental wave $\omega = 1$ eV and $d_{\mathrm{gap}} = 2.1$ Å. These results are shown in Fig. 4.9b, where we plot again the evolution of the 3rd harmonic nonlinear dipole ($p_{3\omega}$), transferred charge ($Q_{3\omega}$) and current trough the middle of the junction ($I_{3\omega}$) as they evolve in time. We observe again that the dipole and the transferred charge oscillate in phase while the nonlinear current is dephased a quarter optical period. In this situation the 3rd harmonic frequency is well below any resonant excitation in the system (see Fig. 4.6b), which points towards a non-resonant effect, intrinsically associated with the nonlinear tunneling current and therefore supports the robustness of the influence of the tunneling current as a key aspect of the nonlinear response.

Intrinsic versus tunneling contributions

As explained above, the tunneling, volume, and surface components of the total nonlinear current calculated with TDDFT cannot be explicitly separated so that the respective contributions to the nonlinear response cannot be straightforwardly obtained using Eq. (4.18) or Eq. (4.22). Similarly, the effective separation D between the charges transferred across the junction is *a priori* unknown. To quantify the role of the electron transport through the junction in the nonlinear response we implement the following procedure. Let us write the nonlinear dipole of the dimer in the form:

$$p_{n\omega} = 2p_{n\omega}^{\mathrm{np}} + p_{n\omega}^{\mathrm{CT}}, \qquad (4.24)$$

where the intrinsic nonlinear polarisation of each nanoparticle excluding the effects of nonlinear electron transport through the junction is denoted as $p_{n\omega}^{\mathrm{np}}$, and $p_{n\omega}^{\mathrm{CT}} \equiv iDI_{n\omega}/(n\omega)$ is the nonlinear dipole induced by the nonlinear current between nanoparticles. If the charge-transfer polarisation $p_{n\omega}^{\mathrm{CT}}$ provides the main contribution to the total nonlinear dipole, i.e., if $p_{n\omega}^{\mathrm{CT}} \gg p_{n\omega}^{\mathrm{np}}$, then the quantity $\tilde{D} = -in\omega p_{n\omega}/I_{n\omega}$ should be real valued and nearly independent on the width of the gap (we assume $d_{\mathrm{gap}} << D$). This is indeed what we obtain from $p_{n\omega}$ and $I_{n\omega}$ calculated with TDDFT at small widths of the gap for both the Na nanowire (below 6 Å) and for the Al nanosphere dimer (below 4 Å). Thus, $\tilde{D}$ can be used to find an effective separation $D = \mathrm{Re}(\tilde{D})$ between the charges induced at the nanoparticles at the corresponding n^{th}-harmonic frequency because of the electron transport across the junction.

We find that for the Al nanosphere dimer the effective separation D is very close to $2R_{sph}$ for both the 2nd and 3rd harmonic cases. The transferred charge is effectively located close to the centre of the nanoparticles as one would expect considering the symmetry and the small size of the Al spheres. For the Na nanowire dimer, because of the relatively large cylinder radii, the nonlocal screening effects become important. Depending on the frequency, we find an effective separation distance D within $15 - 50$ Å, i.e. $D < 2R_{cyl}$. For all the systems, at large widths of the gap, the quantity $\tilde{D}$ diverges. This is because the tunneling current $I_{n\omega}$ becomes exponentially small in such a situation, and

the intrinsic polarisation $p_{n\omega}^{\mathrm{np}}$ of each particle provides the leading contribution to the total nonlinear dipole.

We adopt the definition of D above and fix its value to that obtained for the junction of small width. We can estimate in this way the frequency conversion enhancement $\tilde{\mathfrak{R}}$ owing exclusively to the charge-transfer dipole $p_{n\omega}^{\mathrm{CT}}$, which is given by: $\tilde{\mathfrak{R}} = \beta \left|I_{n\omega}\right|^2 / 4 \left|p_{n\omega}^i\right|^2$, where $\beta = (D/n\omega)^2$. The charge transfer contribution $\tilde{\mathfrak{R}}$ is shown in Fig. 4.7a and Fig. 4.7b with dashed lines. In the range of gap widths where the electron transfer across the gap is efficient, the agreement between the TDDFT result shown in Fig. 4.7 with solid lines and the prediction obtained by considering only the charge transfer between cylinders is remarkable. This points at the dominant role of the nonlinear currents in the gap as responsible for the frequency conversion by the dimer. In particular, as follows from Fig. 4.6c and Fig. 4.7, the maximum of the frequency conversion is reached in the tunneling regime, prior to the establishment of the conductive contact between nanoparticles introducing the possibility of ballistic electron transport through the junction.

The results in Fig. 4.7 also help to visualise the transition between "tunneling" and "intrinsic" regimes of the nonlinearity with increasing d_{gap}. As the width of the junction increases, and the tunneling effects become exponentially low, the enhancement $\mathfrak{R}$ dependence on d_{gap} (solid lines) changes to a substantially smoother variation. At these large widths of the gap the total nonlinear dipole is built by intrinsic polarisations of the nanoparticles, which are determined by the field enhancement in the system and decrease relatively slowly with increasing d_{gap}.

It is noteworthy that an efficient generation of the 2$^{\mathrm{nd}}$ and 3$^{\mathrm{rd}}$ harmonics in the tunneling current and thus the build up of the nonlinear dipole due to the charge transferred between nanoparticles is possible in the spherical and cylindrical dimer configurations owing to the field enhancement in the junction. As follows from Eq. (4.21), the harmonics in the tunneling current between nanoparticles $I_{n\omega}$ are determined by the enhanced fields in the junction $I_{n\omega} \propto (E_{\omega}^g)^n$. In this respect, $I_{n\omega}$ should be more sensitive to the field enhancement than the intrinsic polarisation representing the integral over the nanoparticle volume.

4.5.4 Role of resonant plasmonic modes

While a dimer nanoantenna generally enables a more efficient frequency conversion as compared to the corresponding independent nanoparticles, this "rule of thumb" is subject to specific conditions determined by the width of the junction, and by the respective role of the electron transport across the gap and of the plasmon modes of the nanoantenna. Depending on whether one seeks for the strongest gain of the nonlinearity as compared to the single nanoparticle (relative efficiency), or for the largest intensity of the nonlinear signal (absolute efficiency), the choice of the dimer structure might differ, as revealed by the
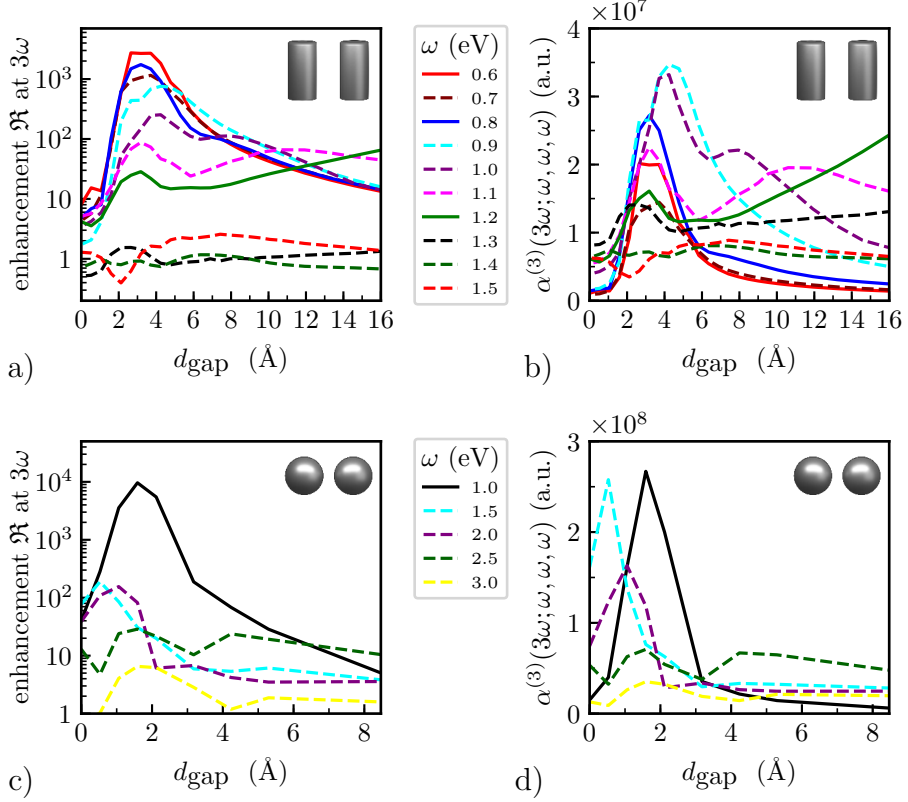
FIGURE 4.10: 3rd harmonic generation in a Na cylinder dimer and Al sphere dimer. TDDFT results are presented as a function of the size of the gap between nanoparticles d_{gap}. (a,c) Enhancement of the intensity of the emitted 3rd harmonic, $\mathfrak{R}$, for a dimer of (a) Na cylinders and (c) Al spheres as compared to the case of the individual non-interacting nanoparticles. For the exact definition of $\mathfrak{R}$ see Eq. (4.20). (b,d) Hyperpolarisability, $\alpha^{(3)}(3\omega)$, of the (b) Na cylinder dimer and (d) Al sphere dimer. The values are given in atomic units (a.u.). The relation 1 esu $= 0.1985 \times 10^{40}$ a.u. can be used for conversion of the third-order hyper-polarisability to electrostatic units (esu). Different colours correspond to results obtained with different frequencies ω of the incident fundamental wave, as detailed in the legends between the panels.

TDDFT results shown in Fig. 4.10. The $3^{\rm rd}$ harmonic generation in the Na cylinder dimer and the Al sphere dimer are analysed in this figure for a wide range of gap widths and different frequencies ω of the incident fundamental wave. The main difference between the left and right panels in Fig. 4.10 is that the former shows the effect of the response of the dimer as a whole relative to the independent individual nanoparticles, while the latter provides the information on the absolute value of the nonlinear response.

We focus first on the Na cylinder. The dependence of the enhancement of the intensity of the emitted $3^{\rm rd}$ harmonic, $\mathfrak{R}$, on the width of the junction is shown in Fig. 4.10a. The solid lines in red and blue correspond to the same cases as those analysed in Fig. 4.7a where the fundamental ($\omega = 0.6$ eV and $\omega = 0.8$ eV) and harmonic frequencies are far from the plasmonic resonances. As discussed earlier, the enhancement increases as the gap distance $d_{\rm gap}$ is reduced, reaching a maximum at the point of maximum tunneling current. If one focuses on the data for a fundamental frequency at $\omega = 1.2$ eV (solid green line) the situation changes dramatically. For this frequency, the $3^{\rm rd}$ harmonic ($3\omega = 3.6$ eV) is in resonance with the red-shifted BDP for well-separated nanowires, at $d_{\rm gap} = 21$ Å. Decreasing the width of the gap below this value red shifts the BDP frequency. The resonance condition is lost in that situation thereby reducing the nonlinearity despite that larger fields at ω are reached for this smaller $d_{\rm gap}$. However, when the width of the gap is further reduced down to the tunneling regime, the $3^{\rm rd}$ harmonic intensity increases again.

The largest $3^{\rm rd}$ harmonic enhancement (nearly four orders of magnitude) is reached at low frequencies of the fundamental wave in the tunneling regime (tunneling enhancement (TE), in narrow gaps) because of the nonlinear electron transport across the gap. As the frequency of the incident fundamental wave is increased, the gain in the $3^{\rm rd}$ harmonic intensity because of the dimer structure as compared to the two individual non-interacting nanoparticles becomes smaller. This is because of (i) the overall decrease in the nonlinearity of the tunneling current (see Eq. (4.21)) and (ii) the enhancement of the $3^{\rm rd}$ harmonic intensity from the single nanoparticle since 3ω approaches its dipolar plasmon resonance (see Fig. 4.6). For the frequencies of the fundamental wave ω above 1.2 eV, no noticeable effect of the tunneling enhancement can be observed.

Together with the main maximum of the nonlinear enhancement in the tunneling regime at $d_{\rm gap} = 3 - 4$ Å, the results obtained for larger frequencies of the fundamental wave, at $\omega = 0.9$ eV, 1.0 eV, 1.1 eV, and 1.2 eV also show an additional, weaker, feature at larger $d_{\rm gap}$. This corresponds to a resonant process (resonant enhancement (RE)). At these frequencies of the fundamental wave, the corresponding $3^{\rm rd}$ harmonic frequency is below the dipolar plasmon mode of the individual cylinder (see Fig. 4.6d). However, the plasmon coupling[314] in a dimer configuration red-shifts the dipolar plasmon frequency so that at a given $d_{\rm gap}$ the $3^{\rm rd}$ harmonic can be at resonance with the BDP plasmon mode of the dimer. This leads to the RE of the nonlinear polarisation.

The red shift of the BDP frequency with decreasing d_{gap} translates into the corresponding shift of the RE maximum which appears at smaller d_{gap} when decreasing ω.

At frequencies of the fundamental wave $\omega =$1.3 eV, 1.4 eV, and 1.5 eV, the 3$^{\mathrm{rd}}$ harmonic spans the high frequency wing of the RE for the individual cylinder owing to the dipolar plasmon mode (see Fig. 4.6d). Since the interaction between the particles for short distances redshifts the BDP out of resonance and because of the relatively small TE at high frequencies, $\mathfrak{R}$ decreases by several orders of magnitude, reaching values close to unity, i.e. the dimer performs equally good as the noninteracting cylinders in these circumstances. This is despite the fact that the field enhancement in the gap between nanoparticles *a priori* should increase the nonlinear response, however, the resonance effects outperform the effects of the field enhancement.

A similar behaviour is found for the 3$^{\mathrm{rd}}$ harmonic frequency of the dimer of Al spheres presented in Fig. 4.10c. The black solid line corresponds to the result analysed in Sec. 4.5.3 (Fig. 4.7b) for the illumination frequency $\omega = 1$ eV. For the dimer of spheres we also find that the strongest enhancement ($\mathfrak{R}$) is produced when the fundamental and the harmonic frequencies are below the plasmon resonance (black solid line). As the frequency of the illumination is increased, the enhancement $\mathfrak{R}$ decreases. Furthermore, for large frequencies the RE produced by the plasmonic modes gains importance again. In particular, for the fundamental frequency $\omega = 2.5$ eV (green dashed line), the 3$^{\mathrm{rd}}$ harmonic frequency is close to the BDP resonance of the dimer at a distance $d_{\mathrm{gap}} \approx 4.5$ Å (see Fig. 4.6b), which leads to a maximum on $\mathfrak{R}$. Interestingly, for the fundamental frequencies $\omega = 1.5$ eV and $\omega = 2.0$ eV we find a peak for particularly small gaps $d_{\mathrm{gap}} \lesssim 1.5$ Å. The shift of the peak to those short separation distances might be related to the excitation of the emerging low-energy CTP.

Thus, at low frequency of the fundamental wave the field enhancement and tunneling effects in the gap between nanoparticles result in the strongest gain of the frequency conversion obtained with a dimer, as compared to individual nanoparticles. At the same time, reaching the maximum absolute value of the nonlinear response might not necessarily require the same conditions, as follows from Fig. 4.10b,d. In these plots the TDDFT results for the hyperpolarisability, $\alpha^{(3)}(3\omega)$, of the dimer are shown as a function of the width of the junction for different frequencies of the fundamental wave. In the case of the cylinder dimer (Fig. 4.10b), the maximum value of $\alpha^{(3)}(3\omega)$ is obtained for a narrow junction, not at the lowest frequencies but at an intermediate frequency range between $\omega = 0.9$ eV and $\omega = 1.0$ eV, where tunneling and resonance effects overlap. Comparable high nonlinear hyperpolarisability is obtained at $\omega = 1.2$ eV for a wide gap of $d_{\mathrm{gap}} = 21$ Å, where the 3$^{\mathrm{rd}}$ harmonic frequency is at resonance with the BDP plasmon mode of the dimer. At even higher frequencies, the hyperpolarisability $\alpha^{(3)}(3\omega)$ shows only mild variations with d_{gap} and its frequency dependence is mainly determined by the plasmon resonance of the individual

cylinders.

In the case of the sphere dimer (Fig. 4.10d) we observe that the difference between values of the hyperpolarisability at relatively large $\omega = 2.0$ eV and $d_{\mathrm{gap}} \approx 1.5$ Å becomes of the same order of magnitude than for short $\omega = 1.0$ eV and $d_{\mathrm{gap}} \approx 2.0$ Å (notice that (c) is in logarithmic scale and (d) in linear scale). This is also the case for $\omega = 1.5$ eV and $d_{\mathrm{gap}} \approx 1.0$ Å, which showed two orders of magnitude smaller enhancement $\mathfrak{R}$ than the $\omega = 1.0$ eV maximum, while both cases show similar absolute hyperpolarisability. However in contrast to the results of the sodium cylinder dimer, the RE of the BDP mode does not increase substantially the absolute hyperpolarizability for $\omega = 2.5$ eV and $d_{\mathrm{gap}} \approx 4.0$ Å. Notice, however, that the maximum for $\omega = 1.5$ eV and $d_{\mathrm{gap}} \approx 1.0$ Å may be caused by the RE due to the lowest-energy CTP.

One remark is in order before closing this section. We intentionally did not perform calculations with higher frequencies of the fundamental wave in resonance with the plasmon modes of the system. While this situation is known to provide strong enhancement of the nonlinearity[46,233,243,247,255,256,295,296], the nonlinear tunneling effects would be small at these relatively high frequencies, and thus difficult to reveal. Moreover, since the incident pulse needed to observe nonlinear effects is intense, a frequency match with the plasmon resonance in the absorption cross section would result in strong electron emission. Precisely, this efficient conversion of the optical energy into electron-hole pairs via an intermediate plasmon excitation has made plasmonics a very attractive tool for solar energy harvesting or for photochemical applications[318–324]. However, in the present case, hot electron emission would result in a spread of the electron density over the entire computational grid, leading to the loss of precision.

4.6 Summary and Discussion

In this chapter first-principles calculations have been used to study the nonlinear response of plasmonic single nanoparticles and nanoparticle dimers. This quantum approach goes beyond the classical and hydrodynamic descriptions of high harmonic generation and allows for qualitative and quantitative assessment of the role of an externally applied field, spectral matching of the harmonic frequency with plasmon resonances and the nonlinear tunneling across narrow gaps.

In Sec. 4.4 we have focused on single Al nanoparticles to show the promise of plasmonic systems for the realisation of controllable even-order high-harmonic generation via an applied dc electric field. The necessary conditions for frequency conversion can be reached, for instance, by placing an Al nanosystem in a break junction or in a gap of an electrically driven plasmonic gold nanoantenna[293]. The latter should be particularly efficient as might enable to reach a double resonance condition, where the fundamental frequency is resonant with the gold nanoantenna and the high-order harmonic is at resonance with the plasmon mode of the Al nanostructure. Indeed, for the particle sizes

considered here we have shown that for the fundamental frequency in the visible, the 4th or higher harmonics can be set into resonance with the plasmon mode of the Al nanostructure, resulting is a strong enhancement of the nonlinear response. Thus, small Al nanoparticles are a promising system for the generation of actively-controlled radiation in the ultraviolet.

In Sec. 4.5 we study dimer plasmonic systems separated by ultranarrow gaps. Both dimers of Na cylinders and dimers of spherical Al nanoparticles were analysed to test the robustness of the results. We found that depending on the main contributions to the nonlinear response, three interaction regimes can be identified in a dimer nanoantenna with small gap distance separation d_{gap}:

(i) At large widths of the gap between nanoparticles, $d_{\mathrm{gap}} > 6 - 8$ Å (separated nanoparticles), the total nonlinear polarisation of the dimer is given by the sum of the nonlinear polarizations of the individual nanoparticles. The coupling between the nanoparticles in the dimer, and, in particular, the field enhancement in the gap increases the overall nonlinear response.

(ii) In the tunneling distance range of 2 Å$< d_{\mathrm{gap}} < 6 - 8$ Å, the harmonic components of the ac electron tunneling current through the gap between nanoparticles build the nonlinear charge-transfer dipole. Along with the response of the individual nanoparticles, this charge-transfer dipole contributes to the total nonlinear polarisation of the dimer. At low frequencies (0.6-1.5 eV depending on the metal) of the fundamental incident wave, the nonlinear tunneling current across the junction determines and governs the nonlinear response of the dimer. This nonlinear current might lead to orders of magnitude increase of the frequency conversion.

(iii) Finally, for a situation of geometrical overlap between nanoparticle surfaces, a conductive contact is established. The nonlinear response of the dimer evolves to that of a single nanoparticle, albeit of the larger size. The strong gap-induced enhancement of the nonlinear signal is quenched in this situation, consistent with experimental observations[148,266].

The three ranges of gap widths pointed out above are defined with respect to the transport properties of the junction. In that respect, they are very similar to the definition proposed on previous work, based on the quantum effects in the linear response[55].

It is worth to stress that the incident field enhancement in the gap of the dimer structure is at the origin of the strong nonlinear effects due to both the nonlinear polarizations of individual nanoparticles and the nonlinear electron tunneling mechanisms. In the former case it leads to an overall increase of the fundamental field seen by each nanoparticle, while in the latter case it results in the high optical bias across the junction producing the strong nonlinear current between nanoparticles.

It is thus possible to conclude that if one seeks for the best performance of the dimer compared to the non-interacting nanoparticles, the low frequency range and the tunneling regime might provide an appropriate solution. At the

same time, if the largest absolute value of the emitted harmonic is sought, either using the tunneling regime at small gap width, or setting the emission frequency in resonance with the bonding plasmon mode at large gap width, can be similarly efficient. It is noteworthy that, as shown in previous works, setting the main signal in resonance with the plasmon mode of the system also allows to reach the manifold enhancement on the frequency conversion. However, because of numerical constrains this regime could not be addressed in the present study.

The present quantum treatment enabled the theoretical study of the mechanisms involved in the generation of the harmonics of the fundamental frequency in single nanoparticles and dimer nanoantennas with subnanometer gaps. While this work addresses small-size plasmonic nanoparticles, the demonstration of active control by an externally applied static field of the enhancement of nonlinear emission due to plasmon resonances and of the importance of the nonlinear tunneling currents in small gaps is of relevance for larger systems. Considering the current experimental capabilities to build plasmonic nanoparticles and dimers with junctions that reach subnanometre scale[21,22,133,148,244,266–269,285,286,298,305], the understanding of the mechanisms of the nonlinear response of plasmonic systems with and without narrow gaps is of paramount importance. The qualitative and quantitative study in this chapter not only offers the appropriate quantum theoretical treatment of nonlinear processes in plasmonic systems, but it also establishes an effective platform to design and exploit electrically controllable nonlinear devices for optoelectronics and extreme ultraviolet generation.

Conclusions

In this thesis we have studied the optical response of plasmonic systems with ultranarrow gaps. The use of classical, semi-classical and quantum mechanical calculations has allowed to rigorously address the diverse phenomena that arise in the capacitive and in the conductive coupling regimes of plasmonic nanometre and subnanometre gaps.

Varying the gap morphology allowed us to address the strong influence that particle faceting has in the mode structure of nanoantennas with nanometre gaps. While gap antennas with spherical gap terminations show qualitatively the same optical response as the widely studied dimers of spherical particles, the presence of flat facets at the gap surfaces strongly changes the optical response. Large flat gaps allow for the formation of two sets of mostly independent modes, namely Longitudinal Antenna Plasmons (LAPs) and Transverse Cavity Plasmons (TCPs). A main characteristic that distinguishes the LAPs in flat-gap antennas from typical Bonding Plasmons (BPs) in dimers with spherical terminations, is the saturation of the redshift of the resonance energy of the mode as the gap is closed, so that the response of a single longer rod is recovered. This saturation can be understood by modelling the gap as a capacitance that short-circuits for very small gaps. In contrast, the energy of the TCPs strongly redshifts as the gap is closed. These modes can show a very intricate near-field patterns in the gap. Generally, the LAPs control the far-field properties of the plasmonic response while the TCPs control the near-field distribution in the gap region. Both types of modes can be independently tuned, which allows to separately engineer the far-field and near-field properties of such a gap antenna.

When the gap is reduced, reaching subnanometre scale, we also observe that the faceting determines how electron tunneling affects the optical response. Spherical gaps again follow the expected optical behaviour of spherical dimers for closing gaps: quenching of the near field in the gap and a far field characterized by a progressive fading of the BP resonances and the emergence of blueshifting Charge Transfer Plasmons (CTPs) before physical contact. As one evolves from the spherical gap-termination to a completely flat one, the lowest-energy CTP initially appears at a blueshifted energy. In the limiting case when the gap termination is practically flat, we observe that electron tunneling does not affect the far-field response as we close the gap because the addition of the tunneling conductivity to a short-circuited gap does not impact the response. Therefore, there is no distinction between the LAPs and CTPs in the far field. We finally observe that all the different gap morphologies show a strong quenching of the near field in the gap. Our results show that some

features associated with he tunneling regime are common for all types of gaps (near-field quenching), but others can be strongly affected by the presence of faceted gaps. Therefore, experiments seeking to demonstrate or exploit the properties of tunneling gaps in plasmonics require a very precise control not only of the separation between the particles but also of the gap morphology. Importantly, a badly fabricated gap presenting large facets can completely hinder the far-field signature of electron tunneling even for set-ups with a perfect control of the gap distance.

Electron tunneling affects the optical response of BP resonances because it allows the transport of the charges accumulated at facing surfaces across the gap. Using a trimer plasmonic metamolecule configuration, and together with the experimental group of Jennifer Dionne at Stanford, we demonstrate that electron tunneling affects in a similar manner different types of plasmon resonances, as long as they present charges of opposite sign at facing surfaces across the gap. Using an adequately placed electron beam as a probe, it is possible to induce a merging process in the trimer geometry while, at the same time, the evolution of the plasmon resonances is characterized. We experimentally observe and theoretically confirm that magnetic plasmon resonances, which present a charge distribution that results in a displacement current circulating around the metamolecule, are strongly affected by tunneling currents. Magnetic resonances display a charge distribution with charges of opposite sign at facing surfaces of each of the gaps in the trimer and thus, electron tunneling produces a similar effect in these types of modes as that in electric BP resonances. In contrast to magnetic and electric plasmon modes, dark modes that display a zero total dipole moment and that can be excited placing the electron beam in the centre of the trimer metamolecule, are not affected by tunneling. The reason is that the dark mode is characterized by a dipole moment at each nanoparticle that points to the centre of the trimer and therefore the surfaces across the gaps display charges of the same sign.

As already discussed, the gap morphology can modify the modal structure of plasmonic resonances. With this idea in mind we have explored the advantages that flat facets might have to build plasmonic devices. Chains of plasmonic nanoparticles present a large amount of gaps and therefore they might be a good platform for field-enhanced spectroscopies or sensing applications. Furthermore, the optical response of chains can be representative of more complex self-assembled aggregates. We explored the far-field and near-field properties of chains of cylindrical particles separated by a gap of 1 nm and with flat facets of different sizes in the gap region, and compare the results with those obtained for an equivalent chain of spheres. All chains show a dominant Longitudinal Chain Plasmon (LCP) whose resonance energy redshifts and saturates as the number of particles in the chain increases. We find that the maximum redshift obtained for a chain of flat-faceted particles is ~ 4 times larger that for a chain of spherical particles. Regarding the near-field intensity achievable in the gap region we observe that, as expected, the chain of spheres produces the largest

fields. However, chains of flat-faceted particles generate only slightly weaker fields and they are distributed over a much larger region. The combination of the large tunnability of the LCP resonance and intense near field in the gaps distributed over large volumes indicates that flat-faceted particles might be a very good platform for spectroscopy/sensing applications, particularly is the case where molecular layers are employed or when the position of the molecules to be analysed is not well controlled.

All the results discussed so far deal with the linear optical response of plasmonic systems with (sub)nanometre gaps and how electron tunneling affects them. In this context, the quenching of the near field in the gap due to electron tunneling is usually seen as a limiting feature for plasmonic devices, as many applications try to maximize the electric field in the gap. However, electron tunneling is a highly nonlinear process and thus, it might be relevant in the nonlinear optical response of plasmonic systems. In collaboration with A.G. Borisov and D.C. Marinica from the Approches théoriques en dynamique quantique group at the Institut des Sciences Moléculaires d'Orsay, we investigated the nonlinear response of small nanoparticles and dimers subjected to intense electromagnetic illumination from first principles simulations. We started exploring the response of a single aluminium sphere that is polarized by an external static electric field and illuminated by a short light pulse. As a metallic sphere is a centrosymmetric structure, only odd harmonics are generated when no polarizing field is applied. Increasing the polarizing electric field breaks the symmetry and allows to actively control the emission of light at even-harmonic frequencies due to a nonlinear process of $3^{\rm rd}$ order, which offers the opportunity of creating a compact and controllable source of harmonic light. We show that illuminating the nanoparticle with a driving frequency such that the harmonic one is on resonance with the plasmon mode results in one order of magnitude increase in the nonlinear light emission. Using Aluminium as the material of the particles has the additional advantage that they display the Dipolar Plasmon (DP) resonance in the ultraviolet. Therefore, setting the $4^{\rm th}$ harmonic to be in resonance with the plasmonic mode results in a source of ultraviolet light that can be actively controlled by an applied electric field.

To study the effect of tunneling in the nonlinear response of plasmonic gaps we also used a dimer of Aluminium spheres and a dimer of Sodium cylinders. We tracked the $2^{\rm nd}$ and $3^{\rm rd}$ harmonic generation while the gap is progressively closed. If one illuminates the system so that the driving frequency and the harmonic one are off resonance, we observed that the harmonic generation progressively increases due to the enhanced-electric field acting on each particle and a peak is found at gap distances where the tunneling current is maximum. By analysing the nonlinear currents at the harmonic frequency, we were able to link the strong enhancement of the harmonic-generation process to the nonlinear tunneling current. If the illumination is such that the harmonic frequency is resonant with a BP mode of the dimer at a given separation distance $d_{\rm gap}$, it can be more efficient to have a well separated dimer (where the resonance

condition is fulfilled) rather than to reduce the gap to tunneling distances (losing the resonance condition) where the nonlinear tunneling currents dominate the harmonic emission. All these results show that the effect of tunneling in the nonlinear optical properties of plasmonic gaps is very complex. Depending on the available driving laser frequency and on the mode structure of the plasmonic system, the optimal harmonic generation can be found at large d_{gap} or at distances where the tunneling current is maximum.

The results presented in this thesis show the rich optical response of plasmonic subnanometre gaps. We investigated in detail the effect that the shape of the surfaces facing the gap and the electron tunneling have in the linear and nonlinear optical response of plasmonic particles with extremely narrow gaps. However many interesting questions are still open in the field of (sub)nanometre-gap plasmonics. Additionally to the quantum dynamics of conduction electrons, atomic-scale features can be crucial to understand subtle effects in the plasmonic response of subnanometre gaps[28,151,152] and thus, advances in the atomistic description of large-scale metallic nanoparticles are crucial to continue exploring the subnanometre gap regime. On the other hand, the Quantum Corrected Model (QCM) is a powerful alternative to extend the computationally intensive quantum calculations to large plasmonic systems, but the approximations made within it do not completely capture the complexity of the quantum tunneling process[27]. Therefore it would be desirable to further develop the QCM to better capture the full complex value the tunneling conductivity as well as to extend its validity to the nonlinear regime. Finally, experimentally reaching tunneling distances and controlling them with high accuracy is a very challenging task. Other alternative mechanisms can be explored to produce charge transfer between the nanoparticles. Molecular linkers for example can be used to stabilize the gap distance and at the same time, to exploit the properties of a molecule to control the charge transfer between nanoparticles[69]. Another option is to open the gap to distances large enough so that current fabrication techniques can reliably control these distances and thus induce charge transfer from photo-emitted electrons[147,325].

Appendixes

A Relationship between permittivity and conductivity of a material

For a general material that responds linearly to a external electric field and that is nonlocal in time and space, the dielectric displacement, $\mathbf{D}(\mathbf{r}, t)$, and the induced current in the material, $\mathbf{J}(\mathbf{r}, t)$, can be related to the external electric field driving the system, $\mathbf{E}(\mathbf{r}, t)$, as

$$\mathbf{D}(\mathbf{r}, t) = \varepsilon_0 \iint \varepsilon(\mathbf{r} - \mathbf{r}', t - t')\mathbf{E}(\mathbf{r}', t')dt'\mathbf{dr}' \,, \tag{A.1a}$$

$$\mathbf{J}(\mathbf{r}, t) = \iint \sigma(\mathbf{r} - \mathbf{r}', t - t')\mathbf{E}(\mathbf{r}', t')dt'\mathbf{dr}' \,, \tag{A.1b}$$

where ε is defined as the relative dielectric permittivity of the material and σ is defined as the conductivity of the material.

The linear macroscopic interaction of a metal with electromagnetic fields can be studied using the dielectric permittivity ε or the conductivity σ. Both options are equivalent and thus there should be a relationship between them. It is common in optics to use the permittivity to model the optical response of the materials of a given system. On the other hand, the objective of the Quantum Corrected Model (QCM) introduced in Sec. 1.1 is to build an effective material to mimic the conductive properties of a narrow gap where electron tunneling is possible. The conductivity thus appears naturally within the QCM. In this appendix we briefly review the connection between the ε and σ[30].
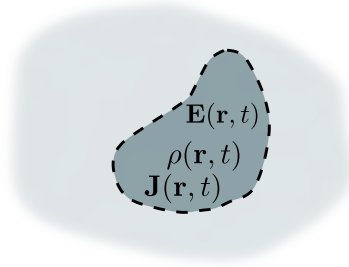

FIGURE A.1: Schematic representation of the system under consideration. Charge $\rho(\mathbf{r}, t)$ and current $\mathbf{J}(\mathbf{r}, t)$ densities are excited in a particle (dark blue) by an electric field $\mathbf{E}(\mathbf{r}, t)$.

Figure A.1 represents the system that will be discussed. In dark blue a particle is embedded in an isotropic and homogeneous medium. The electromagnetic field $\mathbf{E}(\mathbf{r}, t)$ exciting the system induces a charge density $\rho(\mathbf{r}, t)$ and current density $\mathbf{J}(\mathbf{r}, t)$ in the particle.

We aim at obtaining a relationship $\varepsilon = f(\sigma)$. To that end, we start from one of the Maxwell's equations which involves the dielectric displacement $\mathbf{D}(\mathbf{r}, t)$:

$$\nabla \cdot \mathbf{D}(\mathbf{r}, t) = \rho_{ext}(\mathbf{r}, t) = 0 \ , \tag{A.2}$$

where $\rho_{ext}(\mathbf{r}, t)$ is the external charge density of the particle that we consider to be 0.

The dielectric displacement $\mathbf{D}(\mathbf{r}, t)$ is linked to the electric field $\mathbf{E}(\mathbf{r}, t)$ *via* the polarization of the material $\mathbf{P}(\mathbf{r}, t)$:

$$\mathbf{D}(\mathbf{r}, t) = \varepsilon_0 \mathbf{E}(\mathbf{r}, t) + \mathbf{P}(\mathbf{r}, t) \ . \tag{A.3}$$

We next use the Gauss theorem in differential form[272]:

$$\nabla \cdot \mathbf{E}(\mathbf{r}, t) = \frac{\rho(\mathbf{r}, t)}{\varepsilon_0} \ . \tag{A.4}$$

Using Eq. (A.2), Eq. (A.3) and Eq. (A.4) we obtain

$$\nabla \cdot \mathbf{P}(\mathbf{r}, t) = -\rho(\mathbf{r}, t) \ . \tag{A.5}$$

Next, requiring charge conservation in the system[272], we get to:

$$\frac{\partial \rho(\mathbf{r}, t)}{\partial t} + \nabla \cdot \mathbf{J}(\mathbf{r}, t) = 0 \ , \tag{A.6}$$

and inserting Eq. (A.5) into Eq. (A.6) we get

$$\nabla \cdot \left(\mathbf{J}(\mathbf{r}, t) - \frac{\partial \mathbf{P}(\mathbf{r}, t)}{\partial t} \right) = 0 \ . \tag{A.7}$$

If we now come back to the general expressions where we defined the dielectric permittivity (Eq. (A.1a)) and the conductivity (Eq. (A.1b)) we find that working with these expressions in the direct space $\{\mathbf{r}, t\}$ is in general complicated. However, if we decompose the fields into their plane-wave components of frequency ω and wave-vector $\mathbf{k}$ by doing a Fourier transform , Eqs. (A.1) transform into:

$$\mathbf{D}(\mathbf{k}, \omega) = \varepsilon_0 \varepsilon(\mathbf{k}, \omega) \mathbf{E}(\mathbf{k}, \omega) \ , \tag{A.8a}$$
$$\mathbf{J}(\mathbf{k}, \omega) = \sigma(\mathbf{k}, \omega) \mathbf{E}(\mathbf{k}, \omega) \ . \tag{A.8b}$$

Furthermore, all the previous equations (Eq. (A.2)-Eq. (A.7)) are easily transformed to the frequency domain by taking into account that the derivatives in direct space get transformed as $\partial / \partial t \to -i\omega$ and $\nabla \to i\mathbf{k}$, in Fourier space.

From Eq. (A.7) and Eq. (A.8b) we obtain

$$\mathbf{P}(\mathbf{k}, \omega) = \frac{i\sigma(\mathbf{k}, \omega)}{\omega} \mathbf{E}(\mathbf{k}, \omega) \ , \tag{A.9}$$

and finally from Eq. (A.3), Eq. (A.8a) and Eq. (A.9) the relationship between the permittivity of a material and its conductivity is obtained

$$\varepsilon(\mathbf{k}, \omega) = 1 + i \frac{\sigma(\mathbf{k}, \omega)}{\varepsilon_0 \omega} \tag{A.10}$$

If the medium is not spatially dispersive, Eq. (A.10) is transformed to the local version:

$$\boxed{\varepsilon(\omega) = 1 + i \frac{\sigma(\omega)}{\varepsilon_0 \omega}} \tag{A.11}$$

which corresponds to the expression adopted in the Quantum Corrected Model.

B Density Functional Theory: Ground state calculation

The Time-Dependent Density Functional Theory (TDDFT) calculations discussed in Sec. 1.2 require as an input the ground state Kohn-Sham (KS) orbitals and density of the system. Here we briefly describe how Density Functional Theory (DFT) is used to calculate the ground state of a spherical Al nanoparticle. The method described here relays on the same principles as the WPP method (Sec. 1.2). We use atomic units throughout this appendix. Similarly to the TDDFT calculations, we focus on the stabilized Jellium Model (JM) approach[70,71] (Sec. 4.1) with closed-shell electronic structure. The sphere is characterized by the uniform positive background with charge density n_+ given by

$$n_+ = \left(\frac{4\pi}{3}r_{\rm s}^3\right)^{-1} , \tag{B.1}$$

where the Wigner-Seitz radius $r_{\rm s}$ of Al is set to the value $r_{\rm s} = 2.07$ a$_0$ where a$_0$ is the Bohr radius ($r_{\rm s} = 1.1$ Å). A sphere containing $N_{\rm e}$ electrons (or atoms) has then a radius

$$R_{\rm cl} = r_{\rm s}N_{\rm e}^{1/3} , \tag{B.2}$$

as each Al atom contributes with one conduction electron to the system.

Because of the central symmetry of the problem we work in spherical coordinates $\mathbf{r} = \{r, \theta, \phi\}$. The Kohn-Sham (KS) orbitals are sought in the form $\Psi_{k,\ell,m}^0(\mathbf{r}) = \frac{1}{r}\psi_{k,\ell}^0(r)Y_{\ell m}(\theta, \phi)$, where $Y_{\ell m}(\theta, \phi)$ are the spherical harmonics, and k, ℓ, m are radial, angular, and magnetic quantum numbers, respectively. Superscript s stands for "stationary". The electronic density is then given by:

$$n_{\rm grnd}(r) = 2 \sum_{(k,\ell)\in occ.} \frac{2\ell+1}{r^2} \left|\psi_{k,\ell}^0(r)\right|^2 , \tag{B.3}$$

where spin and m degeneracy is taken into account. The sum in Eq. (B.3) runs over the occupied orbitals: $E_{k,\ell} \leq E_{\rm F}$, where $E_{\rm F}$ is the energy of the Fermi level.

The orbitals $\psi_{k,\ell}^0(r)$ satisfy the KS equation:

$$H\psi_{k,\ell}^0(r) = \left[-\frac{1}{2}\frac{\partial^2}{\partial r^2} + \frac{\ell(\ell+1)}{2r^2} + V[n](r)\right]\psi_{k,\ell}^0(r) = E_{k,\ell}\,\psi_{k,\ell}^0(r) , \tag{B.4}$$

where the potential $V[n](r)$ is the sum of Hartree, exchange-correlation, and stabilization potentials

$$V(r) = V_{\rm H}[n](r) + V[n]_{\rm xc}(r) + V_{\rm st}(r) . \tag{B.5}$$

The exchange-correlation potential $V_{\rm xc}(r)$ is treated in the Local Density

Approximation with the exchange-correlation functional of Gunnarson and Lundqvist[73] defined in Eq. (1.18) of Sec. 1.2. The Hartree potential V_{H} is found solving the Poisson equation in radial form:

$$\frac{\partial^2}{\partial r^2}(r\, V_{\mathrm{H}}(r)) = 4\pi\left[n_+(r) - n_{\mathrm{grnd}}(r)\right] \tag{B.6}$$

with zero boundary conditions. Last, the attractive stabilization potential $V_{\mathrm{st}}(r) = -3.1$ eV is added inside the nanosphere to obtain the work function value close to the $\Phi = 4.4$ eV as reported for Al(100) surface[326].

An iterative procedure is employed to find the ground state KS orbitals. Equation. (B.4) is solved with zero boundary conditions on the radial mesh of equidistant points

$$\psi^0_{k,\ell}(0) = 0 \;, \tag{B.7}$$

$$\psi^0_{k,\ell}(R_{\max}) = 0 \;, \tag{B.8}$$

via diagonalization of the Fourier-Grid Hamiltonian (FGH)[74,76,81,327]. We use a FGH generated by the $\sin(\pi k r / R_{\max})$ basis functions, where k is an integer[327]. In each iteration the obtained KS orbitals are used to build the electronic density *via* Eq. (B.3). The new electronic density is employed to obtain a better estimation of the KS potential in Eq. (B.5), which allows construct a more accurate Hamiltonian matrix in Eq. (B.4), and thus to find a more converged solution of the KS orbitals $\psi^0_{k,\ell}(r)$. Typically, the size of the radial mesh comprising 256 equidistant points has been set as $R_{\max} = R_{\mathrm{cl}} + 25$ a$_0$. To solve Eq. (B.6) the FGH of the differential operator is constructed on the same mesh and the potential $V_{\mathrm{H}}(r)$ is obtained *via* direct inversion.

C   Quantitative estimation of the nonlinear hyperpolarisabilities $\alpha^{(n)}$

The quantitative estimation of the nonlinear hyperpolarisabilities given in Ch. 4 follows the method described in this appendix. If the illumination were a plane-wave, Eqs. (4.3) or Eqs. (4.8) could be used to obtain the hyperpolarisabilities $\alpha^{(n)}$ in a straightforward manner: $\alpha^{(3)}(2\omega)$ and $\alpha^{(3)}(3\omega)$ would be calculated as

$$\alpha^{(3)}(2\omega) = p_{2\omega}/(E_0^2 E_p) \ , \tag{C.1a}$$

$$\alpha^{(3)}(3\omega) = p_{3\omega}/E_0^3 \ , \tag{C.1b}$$

where $p_{n\omega}$ is the Fourier transform of the total induced dipole evaluated at $n\omega$. We use the short-hand notation $\alpha^{(3)}(2\omega) \equiv \alpha^{(3)}(2\omega; \omega, \omega, 0)$ and $\alpha^{(3)}(3\omega) \equiv \alpha^{(3)}(3\omega; \omega, \omega, \omega)$.

However, as mentioned in Sec. 4.2, to perform the calculations of the non-linear response, the plasmonic systems are subjected to a polarizing static field and illuminated by a Gaussian pulse of frequency ω:

$$E(t) = E_p + E_\omega(t) = \left(E_p + E_0 \cos(\omega t) e^{-\left(\frac{t-t_0}{\tau}\right)^2} \right) . \tag{C.2}$$

The Gaussian envelope is characterized by a half-width $\tau = 3\frac{2\pi}{\omega}$ and it is centred at t_0. The pulse and the static field are linearly polarized along the z-direction. The finite time profile of the illumination in the calculation (Eq. (C.2)) requires a more involved analysis to calculate the hyperpolarisabilities. In the following, the case of $\alpha^{(3)}(2\omega)$ is discussed. A similar procedure can be applied to obtain any of the other hyperpolarisabilities.

Illuminating the system with the electric field given by Eq. (C.2), the induced dipole oscillating at 2ω can be expressed as (see Eq. (4.8a)):

$$p(2\omega; t) = \alpha^{(3)}(2\omega) \left[E_\omega^2(t)\right]_{2\omega} E_p \ e^{-\left(\frac{t-t_0}{\tau}\right)^2} . \tag{C.3}$$

The $[\ ]_{2\omega}$ notation indicates that only the term oscillating at frequency 2ω is retained when evaluating the square of $E_\omega(t)$. The last exponential factor in Eq. (C.3) is the Gaussian filter (with the same parameters as the illumination) that we apply as explained in Sec. 4.3. Inserting the expression for $E_\omega(t)$ (see Eq. (C.2)) into Eq. (C.3):

$$\begin{aligned} p(2\omega; t) &= \alpha^{(3)}(2\omega) E_0^2 E_p e^{-3\left(\frac{t-t_0}{\tau}\right)^2} \left[\cos^2(\omega t)\right]_{2\omega} \\ &= \frac{1}{2}\alpha^{(3)}(2\omega) E_0^2 E_p e^{-3\left(\frac{t-t_0}{\tau}\right)^2} \cos(2\omega t) \ . \end{aligned} \tag{C.4}$$

Defining:

$$\psi(t) = e^{-3\left(\frac{t-t_0}{\tau}\right)^2} \, , \tag{C.5a}$$

$$\phi(t) = \cos(2\omega t) \, , \tag{C.5b}$$

the spectrum profile of the induced dipole oscillating at 2ω:

$$
\begin{aligned}
p_{2\omega}(\Omega) = \mathcal{F}\big[p(2\omega;t)\big] &= \frac{1}{2}\alpha^{(3)}(2\omega)E_0^2 E_p \mathcal{F}\left[\psi(t)\phi(t)\right] \\
&= \frac{1}{2}\alpha^{(3)}(2\omega)E_0^2 E_p \mathcal{F}\left[\psi(t)\right] * \mathcal{F}\left[\phi(t)\right] \, ,
\end{aligned}
\tag{C.6}
$$

where $\mathcal{F}[\ ]$ stands for the Fourier transform and $*$ denotes the convolution operation defined as:

$$\left[f*g\right](x) = \int_{-\infty}^{\infty} f(X)g(x-X)dX \, . \tag{C.7}$$

Let us calculate now the two Fourier transforms in Eq. (C.6). If we write

$$e^{-3\left(\frac{t-t_0}{\tau}\right)^2} = e^{-ax^2} \, , \tag{C.8}$$

with $a = 3/\tau^2$ and $x = t - t_0$,

$$\psi(\Omega) = \mathcal{F}\left[\psi(t)\right] = \mathcal{F}\left[e^{-ax^2}\right] = \sqrt{\frac{\pi}{a}}e^{-\Omega^2/4a} \, , \tag{C.9}$$

and

$$\phi(\Omega) = \mathcal{F}\left[\phi(t)\right] = \mathcal{F}\left[\cos(2\omega t)\right] = \frac{1}{2}\Big(\delta(\Omega - 2\omega) + \delta(\Omega + 2\omega)\Big) \, , \tag{C.10}$$

where $\delta(x)$ is de Delta function.

The convolution of Eq. (C.9) and Eq. (C.10) is:

$$
\begin{aligned}
\psi(\Omega) * \phi(\Omega) &= \int_{-\infty}^{\infty} \sqrt{\frac{\pi}{a}}e^{-\Omega'^2/4a}\frac{1}{2}\Big(\delta(\Omega - 2\omega - \Omega') + \delta(\Omega + 2\omega - \Omega')\Big)d\Omega' \\
&= \frac{1}{2}\sqrt{\frac{\pi}{a}}\left(e^{-(\Omega - 2\omega)^2/4a} + e^{-(\Omega + 2\omega)^2/4a}\right) \, .
\end{aligned}
\tag{C.11}
$$

Inserting Eq. (C.11) in Eq. (C.6) we obtain:

$$p_{2\omega}(\Omega) = \frac{1}{4}\alpha^{(3)}(2\omega)E_0^2 E_p\sqrt{\frac{\pi}{3}}\tau\left(e^{-(\Omega - 2\omega)^2\tau^2/12} + e^{-(\Omega + 2\omega)^2\tau^2/12}\right) \, . \tag{C.12}$$

We used $a = 3/\tau^2$.

Following a similar procedure we can obtain the spectral profile of the Gaussian pulse illuminating the system (oscillating term in Eq. (C.2)) as:

$$E_\omega(\Omega) = \frac{1}{2} E_0 \sqrt{\pi} \tau \left(e^{-(\Omega-\omega)^2\tau^2/4} + e^{-(\Omega+\omega)^2\tau^2/4} \right) . \qquad \text{(C.13)}$$

If we now evaluate Eq. (C.12) at $\Omega = 2\omega$ and Eq. (C.13) at $\Omega = \omega$, in both cases the first term in the parenthesis is equal to 1 and the second term is ≈ 0. Dividing one by the other we obtain:

$$\frac{p_{2\omega}(2\omega)}{E_\omega(\omega)} = \frac{1}{2\sqrt{3}} \alpha^{(3)}(2\omega) E_0 E_p . \qquad \text{(C.14)}$$

Equation. (C.14) allows to finally obtain the hyperpolarisability $\alpha^{(3)}(2\omega)$. The left-hand side of the equation is obtained directly from the calculation by doing the Fourier transform of the time-dependent total induced dipole and of the illumination field. The right-hand side parameters (E_0 and E_p) are set for each calculation.

Applying the same procedure described here to the 3$^{\text{rd}}$ harmonic leads to the expression for $\alpha^{(3)}(2\omega)$.

$$\frac{p_{3\omega}(3\omega)}{E(\omega)} = \frac{1}{2} \alpha^{(3)}(3\omega) E_0^2 . \qquad \text{(C.15)}$$

Bibliography

[1] J. D. Joannopoulos, P. R. Villeneuve, and S. Fan, "Photonic crystals: putting a new twist on light", Nature **386**, 143 (1997).

[2] H. Xu, E. J. Bjerneld, M. Käll, and L. Börjesson, "Spectroscopy of single hemoglobin molecules by surface enhanced Raman scattering", Physical Review Letters **83**, 4357 (1999).

[3] J. Aizpurua, G. W. Bryant, L. J. Richter, F. G. De Abajo, B. K. Kelley, and T Mallouk, "Optical properties of coupled metallic nanorods for field-enhanced spectroscopy", Physical Review B **71**, 235420 (2005).

[4] A. Sundaramurthy, K. Crozier, G. Kino, D. Fromm, P. Schuck, and W. Moerner, "Field enhancement and gap-dependent resonance in a system of two opposing tip-to-tip Au nanotriangles", Physical Review B **72**, 165409 (2005).

[5] J. Alegret, T. Rindzevicius, T. Pakizeh, Y. Alaverdyan, L. Gunnarsson, and M. Käll, "Plasmonic properties of silver trimers with trigonal symmetry fabricated by electron-beam lithography", Journal of Physical Chemistry C **112**, 14313–14317 (2008).

[6] S. S. Acimovic, M. P. Kreuzer, M. U. González, and R. Quidant, "Plasmon near-field coupling in metal dimers as a step toward single-molecule sensing", ACS Nano **3**, 1231–1237 (2009).

[7] L. M. Liz-Marzán, "Tailoring surface plasmons through the morphology and assembly of metal nanoparticles", Langmuir **22**, 32–41 (2006).

[8] M. Grzelczak, J. Vermant, E. M. Furst, and L. M. Liz-Marzán, "Directed self-assembly of nanoparticles", ACS Nano **4**, 3591–3605 (2010).

[9] G. González-Rubio, P. Díaz-Núñez, A. Rivera, A. Prada, G. Tardajos, J. González-Izquierdo, L. Bañares, P. Llombart, L. G. Macdowell, M. A. Palafox, et al., "Femtosecond laser reshaping yields gold nanorods with ultranarrow surface plasmon resonances", Science **358**, 640–644 (2017).

[10] F. G. De Abajo and J Aizpurua, "Numerical simulation of electron energy loss near inhomogeneous dielectrics", Physical Review B **56**, 15873 (1997).

[11] H. Xu, J. Aizpurua, M. Käll, and P. Apell, "Electromagnetic contributions to single-molecule sensitivity in surface-enhanced Raman scattering", Physical Review E **62**, 4318 (2000).

[12] D. M. Solis, J. M. Taboada, F. Obelleiro, L. M. Liz-Marzan, and F. J. Garcia de Abajo, "Toward ultimate nanoplasmonics modeling", ACS Nano **8**, 7559–7570 (2014).

[13] D. M. Solís, J. M. Taboada, F. Obelleiro, L. M. Liz-Marzan, and F. J. Garcia de Abajo, "Optimization of nanoparticle-based SERS substrates through large-scale realistic simulations", ACS Photonics **4**, 329–337 (2017).

[14] R. W. Boyd, *Nonlinear optics* (Academic press, 2003).

[15] T. V. Teperik, P. Nordlander, J. Aizpurua, and A. G. Borisov, "Quantum effects and nonlocality in strongly coupled plasmonic nanowire dimers", Optics Express **21**, 27306–27325 (2013).

[16] T. V. Teperik, P. Nordlander, J. Aizpurua, and A. G. Borisov, "Robust subnanometric plasmon ruler by rescaling of the nonlocal optical response", Physical Review Letters **110**, 263901 (2013).

[17] F. J. García de Abajo, "Nonlocal effects in the plasmons of strongly interacting nanoparticles, dimers, and waveguides", The Journal of Physical Chemistry C **112**, 17983–17987 (2008).

[18] J. M. McMahon, S. K. Gray, and G. C. Schatz, "Optical properties of nanowire dimers with a spatially nonlocal dielectric function", Nano Letters **10**, 3473–3481 (2010).

[19] C. Ciracì, R. T. Hill, J. J. Mock, Y. Urzhumov, A. I. Fernández-Domínguez, S. A. Maier, J. B. Pendry, A. Chilkoti, and D. R. Smith, "Probing the ultimate limits of plasmonic enhancement", Science **337**, 1072–1074 (2012).

[20] C. Ciraci, J. B. Pendry, and D. R. Smith, "Hydrodynamic model for plasmonics: a macroscopic approach to a microscopic problem", ChemPhysChem **14**, 1109–1116 (2013).

[21] K. J. Savage, M. M. Hawkeye, R. Esteban, A. G. Borisov, J. Aizpurua, and J. J. Baumberg, "Revealing the quantum regime in tunnelling plasmonics", Nature **491**, 574–577 (2012).

[22] J. A. Scholl, A. García-Etxarri, A. L. Koh, and J. A. Dionne, "Observation of quantum tunneling between two plasmonic nanoparticles", Nano Letters **13**, 564–569 (2013).

[23] J. A. Scholl, A. Garcia-Etxarri, G. Aguirregabiria, R. Esteban, T. C. Narayan, A. L. Koh, J. Aizpurua, and J. A. Dionne, "Evolution of plasmonic metamolecule modes in the quantum tunneling regime", ACS Nano **10**, 1346–1354 (2015).

[24] R. Esteban, A. G. Borisov, P. Nordlander, and J. Aizpurua, "Bridging quantum and classical plasmonics with a quantum-corrected model", Nature Communications **3**, 825 (2012).

[25] R. Esteban, A. Zugarramurdi, P. Zhang, P. Nordlander, F. J. García-Vidal, A. G. Borisov, and J. Aizpurua, "A classical treatment of optical tunneling in plasmonic gaps: extending the quantum corrected model to practical situations", Faraday Discussions **178**, 151–183 (2015).

[26] D. Knebl, A. Hörl, A. Trügler, J. Kern, J. R. Krenn, P. Puschnig, and U. Hohenester, "Gap plasmonics of silver nanocube dimers", Physical Review B **93**, 081405 (2016).

[27] U. Hohenester and C. Draxl, "Ab initio approach for gap plasmonics", Physical Review B **94**, 165418 (2016).

[28] M. Barbry, P. Koval, F. Marchesin, R. Esteban, A. G. Borisov, J. Aizpurua, and D. Sánchez-Portal, "Atomistic near-field nanoplasmonics: reaching atomic-scale resolution in nanooptics", Nano Letters **15**, 3410–3419 (2015).

[29] D. C. Marinica, A. K. Kazansky, P. Nordlander, J. Aizpurua, and A. G. Borisov, "Quantum plasmonics: nonlinear effects in the field enhancement of a plasmonic nanoparticle dimer", Nano Letters **12**, 1333–1339 (2012).

[30] S. A. Maier, *Plasmonics: fundamentals and applications* (Springer Science & Business Media, 2007).

[31] L. Novotny and B. Hecht, *Principles of nano-optics* (Cambridge university press, 2012).

[32] A. Derkachova, K. Kolwas, and I. Demchenko, "Dielectric function for gold in plasmonics applications: size dependence of plasmon resonance frequencies and damping rates for nanospheres", Plasmonics **11**, 941–951 (2016).

[33] A. Otto, "Excitation of nonradiative surface plasma waves in silver by the method of frustrated total reflection", Zeitschrift für Physik **216**, 398–410 (1968).

[34] E. Kretschmann and H. Raether, "Radiative decay of non radiative surface plasmons excited by light", Zeitschrift für Naturforschung A **23**, 2135–2136 (1968).

[35] P. B. Johnson and R.-W. Christy, "Optical constants of the noble metals", Physical Review B **6**, 4370 (1972).

[36] F. G. De Abajo and A Howie, "Retarded field calculation of electron energy loss in inhomogeneous dielectrics", Physical Review B **65**, 115418 (2002).

[37] U. Hohenester and A. Trügler, "MNPBEM - A Matlab toolbox for the simulation of plasmonic nanoparticles", Computer Physics Communications **183**, 370–381 (2012).

[38] M. Pelton, J. Aizpurua, and G. Bryant, "Metal-nanoparticle plasmonics", Laser & Photonics Reviews **2**, 136–159 (2008).

[39] R. Vogelgesang and A. Dmitriev, "Real-space imaging of nanoplasmonic resonances", Analyst **135**, 1175–1181 (2010).

[40] L. Novotny and N. Van Hulst, "Antennas for light", Nature Photonics **5**, 83–90 (2011).

[41] E. Prodan, C. Radloff, N. J. Halas, and P. Nordlander, "A hybridization model for the plasmon response of complex nanostructures", Science **302**, 419–422 (2003).

[42] E. Prodan and P. Nordlander, "Plasmon hybridization in spherical nanoparticles", The Journal of Chemical Physics **120**, 5444–5454 (2004).

[43] P. Nordlander, C. Oubre, E. Prodan, K. Li, and M. I. Stockman, "Plasmon hybridization in nanoparticle dimers", Nano Letters **4**, 899–903 (2004).

[44] P. Mühlschlegel, H.-J. Eisler, O. J. F. Martin, B. Hecht, and D. W. Pohl, "Resonant optical antennas", Science **308**, 1607–1609 (2005).

[45] I. Romero, J. Aizpurua, G. W. Bryant, and F. J. G. De Abajo, "Plasmons in nearly touching metallic nanoparticles: singular response in the limit of touching dimers", Optics Express **14**, 9988–9999 (2006).

[46] M. Kauranen and A. V. Zayats, "Nonlinear plasmonics", Nature Photonics **6**, 737–748 (2012).

[47] O. Pérez-González, N. Zabala, A. G. Borisov, N. J. Halas, P. Nordlander, and J. Aizpurua, "Optical spectroscopy of conductive junctions in plasmonic cavities", Nano Letters **10**, 3090–3095 (2010).

[48] F. Benz, C. Tserkezis, L. O. Herrmann, B. De Nijs, A. Sanders, D. O. Sigle, L. Pukenas, S. D. Evans, J. Aizpurua, and J. J. Baumberg, "Nanooptics of molecular-shunted plasmonic nanojunctions", Nano Letters **15**, 669–674 (2014).

[49] F. Benz, B. De Nijs, C. Tserkezis, R. Chikkaraddy, D. O. Sigle, L. Pukenas, S. D. Evans, J. Aizpurua, and J. J. Baumberg, "Generalized circuit model for coupled plasmonic systems", Optics Express **23**, 33255–33269 (2015).

[50] K. Gottfried and T.-M. Yan, *Quantum mechanics: fundamentals* (Springer Science & Business Media, 2013).

[51] B. Voigtländer, *Scanning probe microscopy: atomic force microscopy and scanning tunneling microscopy* (Springer, 2016).

[52] N. Crouseilles, P.-A. Hervieux, and G. Manfredi, "Quantum hydrodynamic model for the nonlinear electron dynamics in thin metal films", Physical Review B **78**, 155412 (2008).

[53] A. I. Fernández-Domínguez, A. Wiener, F. J. García-Vidal, S. A. Maier, and J. B. Pendry, "Transformation-optics description of nonlocal effects in plasmonic nanostructures", Physical Review Letters **108**, 106802 (2012).

[54] Y. Luo, A. Fernandez-Dominguez, A. Wiener, S. A. Maier, and J. Pendry, "Surface plasmons and nonlocality: a simple model", Physical Review Letters **111**, 093901 (2013).

[55] W. Zhu, R. Esteban, A. G. Borisov, J. J. Baumberg, P. Nordlander, H. J. Lezec, J. Aizpurua, and K. B. Crozier, "Quantum mechanical effects in plasmonic structures with subnanometre gaps", Nature Communications **7** (2016).

[56] R. Esteban, G. Aguirregabiria, A. G. Borisov, Y. M. Wang, P. Nordlander, G. W. Bryant, and J. Aizpurua, "The morphology of narrow gaps modifies the plasmonic response", ACS Photonics **2**, 295–305 (2015).

[57] E. D. Palik, *Handbook of optical constants of solids*, Vol. 3 (Academic press, 1998).

[58] E. Runge and E. K. U. Gross, "Density-functional theory for time-dependent systems", Physical Review Letters **52**, 997 (1984).

[59] M. A. Marques and E. Gross, "Time-dependent density functional theory", Annual Review of Physical Chemistry **55**, 427–455 (2004).

[60] M. E. Casida, "Time-dependent density-functional theory for molecules and molecular solids", Journal of Molecular Structure: THEOCHEM **914**, 3–18 (2009).

[61] K. Burke, J. Werschnik, and E. Gross, "Time-dependent density functional theory: past, present, and future", The Journal of Chemical Physics **123**, 062206 (2005).

[62] C. A. Ullrich, "Time-dependent density-functional theory beyond the adiabatic approximation: insights from a two-electron model system", The Journal of Chemical Physics **125**, 234108 (2006).

[63] R. E. Stratmann, G. E. Scuseria, and M. J. Frisch, "An efficient implementation of time-dependent density-functional theory for the calculation of excitation energies of large molecules", The Journal of Chemical Physics **109**, 8218–8224 (1998).

[64] A. G. Borisov, J. P. Gauyacq, and S. V. Shabanov, "Wave packet propagation study of the charge transfer interaction in the F—Cu (111) and–Ag (111) systems", Surface Science **487**, 243–257 (2001).

[65] D. C. Marinica, M. Zapata, P. Nordlander, A. K. Kazansky, P. M. Echenique, J. Aizpurua, and A. G. Borisov, "Active quantum plasmonics", Science Advances **1**, e1501095 (2015).

[66] T. V. Teperik, A. K. Kazansky, and A. G. Borisov, "Electron tunneling through water layer in nanogaps probed by plasmon resonances", Physical Review B **93**, 155431 (2016).

[67] D.-C. Marinica, J. Aizpurua, and A. G. Borisov, "Quantum effects in the plasmon response of bimetallic core-shell nanostructures", Optics Express **24**, 23941–23956 (2016).

[68] M. Z. Herrera, A. K. Kazansky, J. Aizpurua, and A. G. Borisov, "Quantum description of the optical response of charged monolayer–thick metallic patch nanoantennas", Physical Review B **95**, 245413 (2017).

[69] D. C. Marinica, A. K. Kazansky, and A. G. Borisov, "Electrical control of the light absorption in quantum-well functionalized junctions between thin metallic films", Physical Review B **96**, 245407 (2017).

[70] W. A. de Heer, P. Milani, and A. Chtelain, "Nonjellium-to-jellium transition in aluminum cluster polarizabilities", Physical Review Letters **63**, 2834 (1989).

[71] J. P. Perdew, H. Q. Tran, and E. D. Smith, "Stabilized jellium: structureless pseudopotential model for the cohesive and surface properties of metals", Physical Review B **42**, 11627 (1990).

[72] A. Varas, P. García-González, J. Feist, F. García-Vidal, and A. Rubio, "Quantum plasmonics: from jellium models to ab initio calculations", Nanophotonics **5**, 409–426 (2016).

[73] O. Gunnarsson and B. Lundqvist, "Exchange and correlation in atoms, molecules, and solids by the spin-density-functional formalism", Physical Review B **13**, 4274 (1976).

[74] M. D. Feit, J. A. Fleck, and A. Steiger, "Solution of the Schrödinger equation by a spectral method", Journal of Computational Physics **47**, 412–433 (1982).

[75] M. D. Feit and J. A. Fleck Jr, "Solution of the Schrödinger equation by a spectral method ii: vibrational energy levels of triatomic molecules", The Journal of Chemical Physics **78**, 301–308 (1983).

[76] R. Kosloff, "Quantum molecular dynamics on grids", Dynamics of molecules and chemical reactions, 185–230 (1996).

[77] W. Schweizer, *Numerical quantum dynamics*, Vol. 9 (Springer Science & Business Media, 2001).

[78] B. Shizgal, *Spectral methods in chemistry and physics: applications to kinetic theory and quantum mechanics*, Vol. 1 (Springer Netherlands, 2015).

[79] D. Kosloff and R. Kosloff, "A Fourier method solution for the time dependent Schrödinger equation as a tool in molecular dynamics", Journal of Computational Physics **52**, 35–53 (1983).

[80] R. Kosloff, "Time-dependent quantum-mechanical methods for molecular dynamics", The Journal of Physical Chemistry **92**, 2087–2100 (1988).

[81] C. C. Marston and G. G. Balint-Kurti, "The Fourier grid hamiltonian method for bound state eigenvalues and eigenfunctions", The Journal of Chemical Physics **91**, 3571–3576 (1989).

[82] A. Goldberg, H. M. Schey, and J. L. Schwartz, "Computer-generated motion pictures of one-dimensional quantum-mechanical transmission and reflection phenomena", American Journal of Physics **35**, 177–186 (1967).

[83] K. Atkinson, "Numerical integration on the sphere", The ANZIAM Journal **23**, 332–347 (1982).

[84] W. H. Press, S. A. Teukolsky, W. T. Vetterling, and B. P. Flannery, *Numerical recipes in fortran (2nd ed.): the art of scientific computing* (Cambridge University Press, New York, NY, USA, 1992).

[85] T. Jensen, L. Kelly, A. Lazarides, and G. C. Schatz, "Electrodynamics of noble metal nanoparticles and nanoparticle clusters", Journal of Cluster Science **10**, 295–317 (1999).

[86] N. Large, M. Abb, J. Aizpurua, and O. L. Muskens, "Photoconductively loaded plasmonic nanoantenna as building block for ultracompact optical switches", Nano Letters **10**, 1741–1746 (2010).

[87] J. Zuloaga, E. Prodan, and P. Nordlander, "Quantum description of the plasmon resonances of a nanoparticle dimer", Nano Letters **9**, 887–891 (2009).

[88] H. Tamaru, H. Kuwata, H. T. Miyazaki, and K. Miyano, "Resonant light scattering from individual Ag nanoparticles and particle pairs", Applied Physics Letters **80**, 1826–1828 (2002).

[89] K.-H. Su, Q.-H. Wei, X Zhang, J. Mock, D. R. Smith, and S Schultz, "Interparticle coupling effects on plasmon resonances of nanogold particles", Nano Letters **3**, 1087–1090 (2003).

[90] W. Rechberger, A. Hohenau, A. Leitner, J. R. Krenn, B. Lamprecht, and F. R. Aussenegg, "Optical properties of two interacting gold nanoparticles", Optics Communications **220**, 137–141 (2003).

[91] T. Atay, J.-H. Song, and A. V. Nurmikko, "Strongly interacting plasmon nanoparticle pairs: from dipole- dipole interaction to conductively coupled regime", Nano Letters **4**, 1627–1631 (2004).

[92] P. J. Schuck, D. P. Fromm, A. Sundaramurthy, G. S. Kino, and W. E. Moerner, "Improving the mismatch between light and nanoscale objects with gold bowtie nanoantennas", Physical Review Letters **94**, 017402 (2005).

[93] L. Gunnarsson, T. Rindzevicius, J. Prikulis, B. Kasemo, M. Käll, S. Zou, and G. C. Schatz, "Confined plasmons in nanofabricated single silver particle pairs: experimental observations of strong interparticle interactions", The Journal of Physical Chemistry B **109**, 1079–1087 (2005).

[94] O. Muskens, V Giannini, J. A. Sánchez-Gil, and J. G. Rivas, "Optical scattering resonances of single and coupled dimer plasmonic nanoantennas", Optics Express **15**, 17736–17746 (2007).

[95] P. Ghenuche, S. Cherukulappurath, T. H. Taminiau, N. F. van Hulst, and R. Quidant, "Spectroscopic mode mapping of resonant plasmon nanoantennas", Physical Review Letters **101**, 116805 (2008).

[96] K. G. Thomas, S. Barazzouk, B. I. Ipe, S. S. Joseph, and P. V. Kamat, "Uniaxial plasmon coupling through longitudinal self-assembly of gold nanorods", The Journal of Physical Chemistry B **108**, 13066–13068 (2004).

[97] P. Y. Kim, J.-W. Oh, and J.-M. Nam, "Controlled co-assembly of nanoparticles and polymer into ultralong and continuous one-dimensional nanochains", Journal of the American Chemical Society **137**, 8030–8033 (2015).

[98] A. Klinkova, H. Thérien-Aubin, A. Ahmed, D. Nykypanchuk, R. M. Choueiri, B. Gagnon, A. Muntyanu, O. Gang, G. C. Walker, and E. Kumacheva, "Structural and optical properties of self-assembled chains of plasmonic nanocubes", Nano Letters **14**, 6314–6321 (2014).

[99] C. J. Murphy, L. B. Thompson, A. M. Alkilany, P. N. Sisco, S. P. Boulos, S. T. Sivapalan, J. A. Yang, D. J. Chernak, and J. Huang, "The many faces of gold nanorods", The Journal of Physical Chemistry Letters **1**, 2867–2875 (2010).

[100] N. Ortiz and S. E. Skrabalak, "On the dual roles of ligands in the synthesis of colloidal metal nanostructures", Langmuir **30**, 6649–6659 (2014).

[101] R. Esteban, T. Teperik, and J.-J. Greffet, "Optical patch antennas for single photon emission using surface plasmon resonances", Physical Review Letters **104**, 026802 (2010).

[102] G. Toscano, S. Raza, A.-P. Jauho, N. A. Mortensen, and M. Wubs, "Modified field enhancement and extinction by plasmonic nanowire dimers due to nonlocal response", Optics Express **20**, 4176–4188 (2012).

[103] H. Ditlbacher, A. Hohenau, D. Wagner, U. Kreibig, M. Rogers, F. Hofer, F. R. Aussenegg, and J. R. Krenn, "Silver nanowires as surface plasmon resonators", Physical Review Letters **95**, 257403 (2005).

[104] L. Novotny, "Effective wavelength scaling for optical antennas", Physical Review Letters **98**, 266802 (2007).

[105] G. W. Bryant, F. J. García de Abajo, and J. Aizpurua, "Mapping the plasmon resonances of metallic nanoantennas", Nano Letters **8**, 631–636 (2008).

[106] J. Dorfmuller, R. Vogelgesang, W. Khunsin, C. Rockstuhl, C. Etrich, and K. Kern, "Plasmonic nanowire antennas: experiment, simulation, and theory", Nano Letters **10**, 3596–3603 (2010).

[107] V. Lebedev, S. Vergeles, and P. Vorobev, "Giant enhancement of electric field between two close metallic grains due to plasmonic resonance", Optics Letters **35**, 640–642 (2010).

[108] H. Fischer and O. J. Martin, "Engineering the optical response of plasmonic nanoantennas", Optics Express **16**, 9144–9154 (2008).

[109] N. Grillet, D. Manchon, F. Bertorelle, C. Bonnet, M. Broyer, E. Cottancin, J. Lermé, M. Hillenkamp, and M. Pellarin, "Plasmon coupling in silver nanocube dimers: resonance splitting induced by edge rounding", ACS Nano **5**, 9450–9462 (2011).

[110] J. Yang, C. Sauvan, A. Jouanin, S. Collin, J.-L. Pelouard, and P. Lalanne, "Ultrasmall metal-insulator-metal nanoresonators: impact of slow-wave effects on the quality factor", Optics Express **20**, 16880–16891 (2012).

[111]S.-H. Kwon, "Deep subwavelength plasmonic whispering-gallery-mode cavity", Optics Express **20**, 24918–24924 (2012).

[112]S. I. Bozhevolnyi and T. Søndergaard, "General properties of slow-plasmon resonant nanostructures: nano-antennas and resonators", Optics Express **15**, 10869–10877 (2007).

[113]J. Jung, T. Søndergaard, and S. I. Bozhevolnyi, "Gap plasmon-polariton nanoresonators: scattering enhancement and launching of surface plasmon polaritons", Physical Review B **79**, 035401 (2009).

[114]M. Kuttge, F. J. García de Abajo, and A. Polman, "Ultrasmall mode volume plasmonic nanodisk resonators", Nano Letters **10**, 1537–1541 (2009).

[115]J. B. Lassiter, F. McGuire, J. J. Mock, C. Ciracì, R. T. Hill, B. J. Wiley, A. Chilkoti, and D. R. Smith, "Plasmonic waveguide modes of film-coupled metallic nanocubes", Nano Letters **13**, 5866–5872 (2013).

[116]F. Minkowski, F. Wang, A. Chakrabarty, and Q.-H. Wei, "Resonant cavity modes of circular plasmonic patch nanoantennas", Applied Physics Letters **104**, 021111 (2014).

[117]R. Gordon, "Light in a subwavelength slit in a metal: propagation and reflection", Physical Review B **73**, 153405 (2006).

[118]A. Alù and N. Engheta, "Input impedance, nanocircuit loading, and radiation tuning of optical nanoantennas", Physical Review Letters **101**, 043901 (2008).

[119]A. Alù and N. Engheta, "Tuning the scattering response of optical nanoantennas with nanocircuit loads", Nature Photonics **2**, 307–310 (2008).

[120]A. Locatelli, C. De Angelis, D. Modotto, S. Boscolo, F. Sacchetto, M. Midrio, A.-D. Capobianco, F. M. Pigozzo, and C. G. Someda, "Modeling of enhanced field confinement and scattering by optical wire antennas", Optics Express **17**, 16792–16800 (2009).

[121]C. A. Balanis, *Antenna theory: analysis and design* (John Wiley & Sons, 2016).

[122]M. Staffaroni, J. Conway, S. Vedantam, J. Tang, and E. Yablonovitch, "Circuit analysis in metal-optics", Photonics and Nanostructures-Fundamentals and Applications **10**, 166–176 (2012).

[123]H. T. Miyazaki and Y. Kurokawa, "Squeezing visible light waves into a 3-nm-thick and 55-nm-long plasmon cavity", Physical Review Letters **96**, 097401 (2006).

[124]J. Park, H. Kim, I.-M. Lee, S. Kim, J. Jung, and B. Lee, "Resonant tunneling of surface plasmon polariton in the plasmonic nano-cavity", Optics Express **16**, 16903–16915 (2008).

[125]J. A. Dionne, L. A. Sweatlock, H. A. Atwater, and A. Polman, "Plasmon slot waveguides: towards chip-scale propagation with subwavelength-scale localization", Physical Review B **73**, 035407 (2006).

[126]T. Søndergaard, J. Beermann, A. Boltasseva, and S. I. Bozhevolnyi, "Slow-plasmon resonant-nanostrip antennas: analysis and demonstration", Physical Review B **77**, 115420 (2008).

[127]E. S. Barnard, J. S. White, A. Chandran, and M. L. Brongersma, "Spectral properties of plasmonic resonator antennas", Optics Express **16**, 16529–16537 (2008).

[128]R. Filter, J. Qi, C. Rockstuhl, F. Lederer, et al., "Circular optical nanoantennas: an analytical theory", Physical Review B **85**, 125429 (2012).

[129]C. Ciracì, J Britt Lassiter, A. Moreau, and D. R. Smith, "Quasi-analytic study of scattering from optical plasmonic patch antennas", Journal of Applied Physics **114**, 163108 (2013).

[130]C. Tserkezis, R. Esteban, D. O. Sigle, J. Mertens, L. O. Herrmann, J. J. Baumberg, and J. Aizpurua, "Hybridization of plasmonic antenna and cavity modes: extreme optics of nanoparticle-on-mirror nanogaps", Physical Review A **92**, 053811 (2015).

[131]Z. Jacob and V. M. Shalaev, "Plasmonics goes quantum", Science **334**, 463–464 (2011).

[132]M. S. Tame, K. McEnery, Ş. Özdemir, J Lee, S. Maier, and M. Kim, "Quantum plasmonics", Nature Physics **9**, 329–340 (2013).

[133]H. Cha, J. H. Yoon, and S. Yoon, "Probing quantum plasmon coupling using gold nanoparticle dimers with tunable interparticle distances down to the subnanometer range", ACS Nano **8**, 8554–8563 (2014).

[134]L. Mao, Z. Li, B. Wu, and H. Xu, "Effects of quantum tunneling in metal nanogap on surface-enhanced Raman scattering", Applied Physics Letters **94**, 243102 (2009).

[135]M. Schnell, A. Garcia-Etxarri, A. J. Huber, K. Crozier, J. Aizpurua, and R. Hillenbrand, "Controlling the near-field oscillations of loaded plasmonic nanoantennas", Nature Photonics **3**, 287–291 (2009).

[136]S. F. Tan, L. Wu, J. K. Yang, P. Bai, M. Bosman, and C. A. Nijhuis, "Quantum plasmon resonances controlled by molecular tunnel junctions", Science **343**, 1496–1499 (2014).

[137]B. P. Joshi and Q.-H. Wei, "Cavity resonances of metal-dielectric-metal nanoantennas", Optics Express **16**, 10315–10322 (2008).

[138]J. Kern, S. Großmann, N. V. Tarakina, T. Hackel, M. Emmerling, M. Kamp, J.-S. Huang, P. Biagioni, J. C. Prangsma, and B. Hecht, "Atomic-scale confinement of resonant optical fields", Nano Letters **12**, 5504–5509 (2012).

[139]R. Alaee, C. Menzel, U. Huebner, E. Pshenay-Severin, S. Bin Hasan, T. Pertsch, C. Rockstuhl, and F. Lederer, "Deep-subwavelength plasmonic nanoresonators exploiting extreme coupling", Nano Letters **13**, 3482–3486 (2013).

[140] Y.-C. Chang, S.-M. Wang, H.-C. Chung, C.-B. Tseng, and S.-H. Chang, "Observation of absorption-dominated bonding dark plasmon mode from metal–insulator–metal nanodisk arrays fabricated by nanospherical-lens lithography", ACS Nano **6**, 3390–3396 (2012).

[141] R. Zhang, Y. Zhang, Z. C. Dong, S. Jiang, C. Zhang, L. G. Chen, L. Zhang, Y. Liao, J. Aizpurua, Y. E. Luo, and J. Yang, "Chemical mapping of a single molecule by plasmon-enhanced Raman scattering", Nature **498**, 82–86 (2013).

[142] A. Hartschuh, E. J. Sánchez, X. S. Xie, and L. Novotny, "High-resolution near-field Raman microscopy of single-walled carbon nanotubes", Physical Review Letters **90**, 095503 (2003).

[143] T. Deckert-Gaudig and V. Deckert, "Ultraflat transparent gold nanoplates—ideal substrates for tip-enhanced Raman scattering experiments", Small **5**, 432–436 (2009).

[144] A. García-Etxarri, I. Romero, F. J. G. de Abajo, R. Hillenbrand, and J. Aizpurua, "Influence of the tip in near-field imaging of nanoparticle plasmonic modes: weak and strong coupling regimes", Physical Review B **79**, 125439 (2009).

[145] B. Pettinger, P. Schambach, C. J. Villagómez, and N. Scott, "Tip-enhanced Raman spectroscopy: near-fields acting on a few molecules", Annual Review of Physical Chemistry **63**, 379–399 (2012).

[146] M. I. Stockman, M. F. Kling, U. Kleineberg, and F. Krausz, "Attosecond nanoplasmonic-field microscope", Nature Photonics **1**, 539–544 (2007).

[147] P. Dombi, A. Horl, P. Racz, I. Marton, A. Trugler, J. R. Krenn, and U. Hohenester, "Ultrafast strong-field photoemission from plasmonic nanoparticles", Nano Letters **13**, 674–678 (2013).

[148] M. Danckwerts and L. Novotny, "Optical frequency mixing at coupled gold nanoparticles", Physical Review Letters **98**, 026104 (2007).

[149] F. Benz, M. K. Schmidt, A. Dreismann, R. Chikkaraddy, Y. Zhang, A. Demetriadou, C. Carnegie, H. Ohadi, B. de Nijs, R. Esteban, et al., "Single-molecule optomechanics in "picocavities"", Science **354**, 726–729 (2016).

[150] L. O. Herrmann, V. K. Valev, C. Tserkezis, J. S. Barnard, S. Kasera, O. A. Scherman, J. Aizpurua, and J. J. Baumberg, "Threading plasmonic nanoparticle strings with light", Nature Communications **5** (2014).

[151] F. Marchesin, P. Koval, M. Barbry, J. Aizpurua, and D. Sánchez-Portal, "Plasmonic response of metallic nanojunctions driven by single atom motion: quantum transport revealed in optics", ACS Photonics **3**, 269–277 (2016).

[152] M. Urbieta, M. Barbry, Y. Zhang, P. Koval, D. Sánchez-Portal, N. Zabala, and J. Aizpurua, "Atomic-scale lightning rod effect in plasmonic picocavities: a classical view to a quantum effect", ACS nano **12**, 585–595 (2018).

[153] J. Bellessa, C. Bonnand, J. C. Plenet, and J. Mugnier, "Strong coupling between surface plasmons and excitons in an organic semiconductor", Physical Review Letters **93**, 036404 (2004).

[154] S. Savasta, R. Saija, A. Ridolfo, O. Di Stefano, P. Denti, and F. Borghese, "Nanopolaritons: vacuum rabi splitting with a single quantum dot in the center of a dimer nanoantenna", ACS Nano **4**, 6369–6376 (2010).

[155] J. A. Fan, C. Wu, K. Bao, J. Bao, R. Bardhan, N. J. Halas, V. N. Manoharan, P. Nordlander, G. Shvets, and F. Capasso, "Self-assembled plasmonic nanoparticle clusters", Science **328**, 1135–1138 (2010).

[156] D. E. Gómez, Z. Q. Teo, M. Altissimo, T. J. Davis, S. Earl, and A. Roberts, "The dark side of plasmonics.", Nano Letters **13**, 3722–3728 (2013).

[157] A. García-Etxarri and J. A. Dionne, "Surface-enhanced circular dichroism spectroscopy mediated by nonchiral nanoantennas", Physical Review B **87**, 235409 (2013).

[158] Z. Fan, H. Zhang, and A. O. Govorov, "Optical properties of chiral plasmonic tetramers: circular dichroism and multipole effects", Journal of Physical Chemistry C **117**, 14770–14777 (2013).

[159] V. M. Shalaev, W. Cai, U. K. Chettiar, H.-K. Yuan, A. K. Sarychev, V. P. Drachev, and A. V. Kildishev, "Negative index of refraction in optical metamaterials", Optics Letters **30**, 3356–3358 (2005).

[160] C. Enkrich, M. Wegener, S. Linden, S. Burger, L. Zschiedrich, F. Schmidt, J. F. Zhou, T. Koschny, and C. Soukoulis, "Magnetic metamaterials at telecommunication and visible frequencies", Physical Review Letters **95**, 203901 (2005).

[161] A. Alù and N. Engheta, "The quest for magnetic plasmons at optical frequencies", Optics Express **17**, 5723–5730 (2009).

[162] A. Vallecchi, M. Albani, and F. Capolino, "Effect of irregularities of nanosatellites position and size on collective electric and magnetic plasmonic resonances in spherical nanoclusters", Optics Express **21**, 7667–7685 (2013).

[163] A. C. Atre, A. García-Etxarri, H. Alaeian, and J. A. Dionne, "A Broadband negative index metamaterial at optical frequencies", Advanced Optical Materials **1**, 327–333 (2013).

[164] A. Baldi, T. C. Narayan, A. L. Koh, and J. A. Dionne, "In situ detection of Hydrogen-induced phase transitions in individual Palladium nanocrystals.", Nature Materials **13**, 1143–1148 (2014).

[165] R. Esteban, R. W. Taylor, J. J. Baumberg, and J. Aizpurua, "How chain plasmons govern the optical response in strongly interacting self-assembled metallic clusters of nanoparticles", Langmuir **28**, 8881–8890 (2012).

[166] Y. A. Urzhumov, G. Shvets, J. A. Fan, F. Capasso, D. Brandl, and P. Nordlander, "Plasmonic nanoclusters: A path towards negative-index metafluids.", Optics Express **15**, 14129–14145 (2007).

[167] D. W. Brandl, N. A. Mirin, and P. Nordlander, "Plasmon modes of nanosphere trimers and quadrumers.", Journal of Physical Chemistry B **110**, 12302–12310 (2006).

[168] L. Chuntonov and G. Haran, "Trimeric plasmonic molecules: the role of symmetry", Nano Letters **11**, 2440–2445 (2011).

[169] N. Zohar, L. Chuntonov, and G. Haran, "The simplest plasmonic molecules: metal nanoparticle dimers and trimers", Journal of Photochemistry and Photobiology C **21**, 26–39 (2014).

[170] U. Hohenester, "Simulating electron energy loss spectroscopy with the MNPBEM toolbox", Computer Physics Communications **185**, 1177–1187 (2014).

[171] J. Waxenegger, A. Trügler, and U. Hohenester, "Plasmonics simulations with the MNPBEM toolbox: consideration of substrates and layer structures", Computer Physics Communications **193**, 138–150 (2015).

[172] M. A. Asoro, D. Kovar, Y. Shao-Horn, L. F. Allard, and P. J. Ferreira, "Coalescence and sintering of Pt nanoparticles: in situ observation by aberration-corrected HAADF STEM.", Nanotechnology **21**, 025701 (2010).

[173] A. Reyes-Coronado, R. Barrera, P. Batson, P. Echenique, A. Rivacoba, and J. Aizpurua, "Electromagnetic forces on plasmonic nanoparticles induced by fast electron beams", Physical Review B **82**, 235429 (2010).

[174] P. E. Batson, A. Reyes-Coronado, R. G. Barrera, A. Rivacoba, P. M. Echenique, and J. Aizpurua, "Plasmonic nanobilliards: controlling nanoparticle movement using forces induced by swift electrons.", Nano Letters **11**, 3388–3393 (2011).

[175] M. José-Yacaman, C. Gutierrez-Wing, M. Miki, D.-Q. Yang, K. N. Piyakis, and E. Sacher, "Surface diffusion and coalescence of mobile metal nanoparticles.", Journal of Physical Chemistry B **109**, 9703–9711 (2005).

[176] Y. Chen, R. E. Palmer, and J. P. Wilcoxon, "Sintering of passivated gold nanoparticles under the electron beam.", Langmuir **22**, 2851–2855 (2006).

[177] T. H. Lim, D. McCarthy, S. C. Hendy, K. J. Stevens, S. A. Brown, and R. D. Tilley, "Real-time TEM and kinetic monte carlo studies of the coalescence of decahedral gold nanoparticles.", ACS Nano **3**, 3809–3813 (2009).

[178] T. Dadosh, "Synthesis of uniform silver nanoparticles with a controllable size", Materials Letters **63**, 2236–2238 (2009).

[179] A. Delga, J. Feist, J. Bravo-Abad, and F. J. Garcia-Vidal, "Quantum emitters near a metal nanoparticle: strong coupling and quenching", Physical Review Letters **112**, 253601 (2014).

[180] T.-C. Lee and O. A. Scherman, "Formation of dynamic aggregates in water by cucurbit [5] uril capped with gold nanoparticles", Chemical Communications **46**, 2438–2440 (2010).

[181]Y. Kang, K. J. Erickson, and T. A. Taton, "Plasmonic nanoparticle chains via a morphological, sphere-to-string transition", Journal of the American Chemical Society **127**, 13800–13801 (2005).

[182]M. Grzelczak, J. Pérez-Juste, P. Mulvaney, and L. M. Liz-Marzán, "Shape control in gold nanoparticle synthesis", Chemical Society Reviews **37**, 1783–1791 (2008).

[183]S. T. Jones, R. W. Taylor, R. Esteban, E. K. Abo-Hamed, P. H. Bomans, N. A. Sommerdijk, J. Aizpurua, J. J. Baumberg, and O. A. Scherman, "Gold nanorods with sub-nanometer separation using cucurbit [n] uril for SERS applications", Small **10**, 4298–4303 (2014).

[184]R. W. Taylor, R. Esteban, S. Mahajan, J. Aizpurua, and J. J. Baumberg, "Optimizing SERS from gold nanoparticle clusters: addressing the near field by an embedded chain plasmon model", The Journal of Physical Chemistry C **120**, 10512–10522 (2016).

[185]A. Alù and N. Engheta, "Theory of linear chains of metamaterial/plasmonic particles as subdiffraction optical nanotransmission lines", Physical Review B **74**, 205436 (2006).

[186]A. F. Koenderink and A. Polman, "Complex response and polariton-like dispersion splitting in periodic metal nanoparticle chains", Physical Review B **74**, 033402 (2006).

[187]P. Ghenuche, I. G. Cormack, G. Badenes, P. Loza-Alvarez, and R. Quidant, "Cavity resonances in finite plasmonic chains", Applied Physics Letters **90**, 041109 (2007).

[188]N. Harris, M. D. Arnold, M. G. Blaber, and M. J. Ford, "Plasmonic resonances of closely coupled gold nanosphere chains", The Journal of Physical Chemistry C **113**, 2784–2791 (2009).

[189]C. Girard, E. Dujardin, M. Li, and S. Mann, "Theoretical near-field optical properties of branched plasmonic nanoparticle networks", Physical Review Letters **97**, 100801 (2006).

[190]M. I. Stockman, L. N. Pandey, L. S. Muratov, and T. F. George, "Giant fluctuations of local optical fields in fractal clusters", Physical Review Letters **72**, 2486 (1994).

[191]V. M. Shalaev, R. Botet, D. P. Tsai, J. Kovacs, and M. Moskovits, "Fractals: localization of dipole excitations and giant optical polarizabilities", Physica A: Statistical Mechanics and its Applications **207**, 197–207 (1994).

[192]S. J. Barrow, A. M. Funston, D. E. Gómez, T. J. Davis, and P. Mulvaney, "Surface plasmon resonances in strongly coupled gold nanosphere chains from monomer to hexamer", Nano Letters **11**, 4180–4187 (2011).

[193]L. S. Slaughter, B. A. Willingham, W.-S. Chang, M. H. Chester, N. Ogden, and S. Link, "Toward plasmonic polymers", Nano Letters **12**, 3967–3972 (2012).

[194]T. Chen, M. Pourmand, A. Feizpour, B. Cushman, and B. M. Reinhard, "Tailoring plasmon coupling in self-assembled one-dimensional Au nanoparticle chains through simultaneous control of size and gap separation", The Journal of Physical Chemistry Letters **4**, 2147–2152 (2013).

[195]Z. Li, S. Butun, and K. Aydin, "Touching gold nanoparticle chain based plasmonic antenna arrays and optical metamaterials", ACS Photonics **1**, 228–234 (2014).

[196]D. Citrin, "Plasmon polaritons in finite-length metal-nanoparticle chains: the role of chain length unravelled", Nano Letters **5**, 985–989 (2005).

[197]M. D. Arnold, M. G. Blaber, M. J. Ford, and N. Harris, "Universal scaling of local plasmons in chains of metal spheres", Optics Express **18**, 7528–7542 (2010).

[198]R. W. Taylor, R. Esteban, S. Mahajan, R. Coulston, O. A. Scherman, J. Aizpurua, and J. J. Baumberg, "Simple composite dipole model for the optical modes of strongly-coupled plasmonic nanoparticle aggregates", The Journal of Physical Chemistry C **116**, 25044–25051 (2012).

[199]A. M. Smith, M. C. Mancini, and S. Nie, "Bioimaging: second window for in vivo imaging", Nature Nanotechnology **4**, 710–711 (2009).

[200]M.-F. Tsai, S.-H. G. Chang, F.-Y. Cheng, V. Shanmugam, Y.-S. Cheng, C.-H. Su, and C.-S. Yeh, "Au nanorod design as light-absorber in the first and second biological near-infrared windows for in vivo photothermal therapy", ACS Nano **7**, 5330–5342 (2013).

[201]N. Engheta, A. Salandrino, and A. Alù, "Circuit elements at optical frequencies: nanoinductors, nanocapacitors, and nanoresistors", Physical Review Letters **95**, 095504 (2005).

[202]E. C. Le Ru, W. R. Somerville, and B. Auguié, "Radiative correction in approximate treatments of electromagnetic scattering by point and body scatterers", Physical Review A **87**, 012504 (2013).

[203]Z. B. Wang, B. S. Luk'yanchuk, W. Guo, S. P. Edwardson, D. J. Whitehead, L. Li, Z. Liu, and K. G. Watkins, "The influences of particle number on hot spots in strongly coupled metal nanoparticles chain", The Journal of Chemical Physics **128**, 094705 (2008).

[204]S. Lin, M. Li, E. Dujardin, C. Girard, and S. Mann, "One-dimensional plasmon coupling by facile self-assembly of gold nanoparticles into branched chain networks", Advanced Materials **17**, 2553–2559 (2005).

[205]L. S. Slaughter, L.-Y. Wang, B. A. Willingham, J. M. Olson, P. Swanglap, S. Dominguez-Medina, and S. Link, "Plasmonic polymers unraveled through single particle spectroscopy", Nanoscale **6**, 11451–11461 (2014).

[206] C. Hanske, M. Tebbe, C. Kuttner, V. Bieber, V. V. Tsukruk, M. Chanana, T. A. König, and A. Fery, "Strongly coupled plasmonic modes on macroscopic areas via template-assisted colloidal self-assembly", Nano Letters **14**, 6863–6871 (2014).

[207] L. Chuntonov, M. Bar-Sadan, L. Houben, and G. Haran, "Correlating electron tomography and plasmon spectroscopy of single noble metal core–shell nanoparticles", Nano Letters **12**, 145–150 (2011).

[208] M. Zhu, P. Chen, W. Ma, B. Lei, and M. Liu, "Template-free synthesis of cube-like Ag/AgCl nanostructures via a direct-precipitation protocol: highly efficient sunlight-driven plasmonic photocatalysts", ACS Applied Materials & Interfaces **4**, 6386–6392 (2012).

[209] J. E. Sharping, K. F. Lee, M. A. Foster, A. C. Turner, B. S. Schmidt, M. Lipson, A. L. Gaeta, and P. Kumar, "Generation of correlated photons in nanoscale silicon waveguides", Optics Express **14**, 12388–12393 (2006).

[210] M. A. Foster, A. C. Turner, M. Lipson, and A. L. Gaeta, "Nonlinear optics in photonic nanowires", Optics Express **16**, 1300–1320 (2008).

[211] M. Schultze, E. M. Bothschafter, A. Sommer, S. Holzner, W. Schweinberger, M. Fiess, M. Hofstetter, R. Kienberger, V. Apalkov, V. S. Yakovlev, et al., "Controlling dielectrics with the electric field of light", Nature **493**, 75 (2013).

[212] C. Argyropoulos, P.-Y. Chen, F. Monticone, G. D'Aguanno, and A. Alù, "Nonlinear plasmonic cloaks to realize giant all-optical scattering switching", Physical Review Letters **108**, 263905 (2012).

[213] V. J. Sorger, R. F. Oulton, R.-M. Ma, and X. Zhang, "Toward integrated plasmonic circuits", MRS bulletin **37**, 728–738 (2012).

[214] A. Zoumi, A. Yeh, and B. J. Tromberg, "Imaging cells and extracellular matrix in vivo by using second-harmonic generation and two-photon excited fluorescence", Proceedings of the National Academy of Sciences **99**, 11014–11019 (2002).

[215] P. J. Campagnola, A. C. Millard, M. Terasaki, P. E. Hoppe, C. J. Malone, and W. A. Mohler, "Three-dimensional high-resolution second-harmonic generation imaging of endogenous structural proteins in biological tissues", Biophysical Journal **82**, 493–508 (2002).

[216] V. Kravtsov, R. Ulbricht, J. M. Atkin, and M. B. Raschke, "Plasmonic nanofocused four-wave mixing for femtosecond near-field imaging", Nature Nanotechnology **11**, 459 (2016).

[217] A. Horneber, K. Braun, J. Rogalski, P. Leiderer, A. J. Meixner, and D. Zhang, "Nonlinear optical imaging of single plasmonic nanoparticles with 30 nm resolution", Physical Chemistry Chemical Physics **17**, 21288–21293 (2015).

[218] R. M. Corn and D. A. Higgins, "Optical second harmonic generation as a probe of surface chemistry", Chemical Reviews **94**, 107–125 (1994).

[219] J. Butet and O. J. Martin, "Nonlinear plasmonic nanorulers", ACS Nano **8**, 4931–4939 (2014).

[220] A. Hohenau, J. R. Krenn, J. Beermann, S. I. Bozhevolnyi, S. G. Rodrigo, L. Martin-Moreno, and F. Garcia-Vidal, "Spectroscopy and nonlinear microscopy of Au nanoparticle arrays: experiment and theory", Physical Review B **73**, 155404 (2006).

[221] M. Mesch, B. Metzger, M. Hentschel, and H. Giessen, "Nonlinear plasmonic sensing", Nano Letters **16**, 3155–3159 (2016).

[222] M. Lewenstein, P. Balcou, M. Y. Ivanov, A. L'huillier, and P. B. Corkum, "Theory of high-harmonic generation by low-frequency laser fields", Physical Review A **49**, 2117 (1994).

[223] F. Krausz and M. Ivanov, "Attosecond physics", Reviews of Modern Physics **81**, 163 (2009).

[224] L. Gallmann, C. Cirelli, and U. Keller, "Attosecond science: recent highlights and future trends", Annual Review of Physical Chemistry **63**, 447–469 (2012).

[225] G. A. Wurtz and A. V. Zayats, "Nonlinear surface plasmon polaritonic crystals", Laser & Photonics Reviews **2**, 125–135 (2008).

[226] K. F. MacDonald, Z. L. Sámson, M. I. Stockman, and N. I. Zheludev, "Ultrafast active plasmonics", Nature Photonics **3**, 55–58 (2009).

[227] H. Husu, R. Siikanen, J. Makitalo, J. Lehtolahti, J. Laukkanen, M. Kuittinen, and M. Kauranen, "Metamaterials with tailored nonlinear optical response", Nano Letters **12**, 673–677 (2012).

[228] J. Y. Suh and T. W. Odom, "Nonlinear properties of nanoscale antennas", Nano Today **8**, 469–479 (2013).

[229] M. Castro-Lopez, D. Brinks, R. Sapienza, and N. F. van Hulst, "Aluminum for nonlinear plasmonics: resonance-driven polarized luminescence of Al, Ag, and Au nanoantennas", Nano Letters **11**, 4674–4678 (2011).

[230] P.-Y. Chen, C. Argyropoulos, and A. Alù, "Enhanced nonlinearities using plasmonic nanoantennas", Nanophotonics **1**, 221–233 (2012).

[231] G. Grinblat, M. Rahmani, E. Cortés, M. Caldarola, D. Comedi, S. A. Maier, and A. V. Bragas, "High-efficiency second harmonic generation from a single hybrid ZnO nanowire/Au plasmonic nano-oligomer", Nano Letters **14**, 6660–6665 (2014).

[232] T. Hanke, G. Krauss, D. Träutlein, B. Wild, R. Bratschitsch, and A. Leitenstorfer, "Efficient nonlinear light emission of single gold optical antennas driven by few-cycle near-infrared pulses", Physical Review Letters **103**, 257404 (2009).

[233] J. Butet, P.-F. Brevet, and O. J. Martin, "Optical second harmonic generation in plasmonic nanostructures: from fundamental principles to advanced applications", ACS Nano **9**, 10545–10562 (2015).

[234] M. Lippitz, M. A. van Dijk, and M. Orrit, "Third-harmonic generation from single gold nanoparticles", Nano Letters **5**, 799–802 (2005).

[235] R. Czaplicki, J. Mäkitalo, R. Siikanen, H. Husu, J. Lehtolahti, M. Kuittinen, and M. Kauranen, "Second-harmonic generation from metal nanoparticles: resonance enhancement versus particle geometry", Nano Letters **15**, 530–534 (2014).

[236] B. Metzger, M. Hentschel, and H. Giessen, "Probing the near-field of second-harmonic light around plasmonic nanoantennas", Nano Letters **17**, 1931–1937 (2017).

[237] Y. Zhang, A. Manjavacas, N. J. Hogan, L. Zhou, C. Ayala-Orozco, L. Dong, J. K. Day, P. Nordlander, and N. J. Halas, "Toward surface plasmon-enhanced optical parametric amplification (SPOPA) with engineered nanoparticles: a nanoscale tunable infrared source", Nano Letters **16**, 3373–3378 (2016).

[238] A. Gorbach, "Nonlinear graphene plasmonics: amplitude equation for surface plasmons", Physical Review A **87**, 013830 (2013).

[239] J. D. Cox and F. J. G. De Abajo, "Electrically tunable nonlinear plasmonics in graphene nanoislands", Nature Communications **5** (2014).

[240] H. Rostami, M. I. Katsnelson, and M. Polini, "Theory of plasmonic effects in nonlinear optics: the case of graphene", Physical Review B **95**, 035416 (2017).

[241] N. C. Lindquist, P. Nagpal, K. M. McPeak, D. J. Norris, and S.-H. Oh, "Engineering metallic nanostructures for plasmonics and nanophotonics", Reports on Progress in Physics **75**, 036501 (2012).

[242] F. H. Koppens, D. E. Chang, and F. J. García de Abajo, "Graphene plasmonics: a platform for strong light–matter interactions", Nano Letters **11**, 3370–3377 (2011).

[243] K. Thyagarajan, S. Rivier, A. Lovera, and O. J. Martin, "Enhanced second-harmonic generation from double resonant plasmonic antennae", Optics Express **20**, 12860–12865 (2012).

[244] J. B. Lassiter, X. Chen, X. Liu, C. Ciracì, T. B. Hoang, S. Larouche, S.-H. Oh, M. H. Mikkelsen, and D. R. Smith, "Third-harmonic generation enhancement by film-coupled plasmonic stripe resonators", ACS Photonics **1**, 1212–1217 (2014).

[245] M. S. Nezami, D. Yoo, G. Hajisalem, S.-H. Oh, and R. Gordon, "Gap plasmon enhanced metasurface third-harmonic generation in transmission geometry", ACS Photonics **3**, 1461–1467 (2016).

[246] M. Celebrano, X. Wu, M. Baselli, S. Großmann, P. Biagioni, A. Locatelli, C. De Angelis, G. Cerullo, R. Osellame, B. Hecht, and L. Duò, "Mode matching in multiresonant plasmonic nanoantennas for enhanced second harmonic generation", Nature Nanotechnology **10**, 412 (2015).

[247] M. Hentschel, T. Utikal, H. Giessen, and M. Lippitz, "Quantitative modeling of the third harmonic emission spectrum of plasmonic nanoantennas", Nano Letters **12**, 3778–3782 (2012).

[248] A. Slablab, L. Le Xuan, M. Zielinski, Y. de Wilde, V. Jacques, D. Chauvat, and J.-F. Roch, "Second-harmonic generation from coupled plasmon modes in a single dimer of gold nanospheres", Optics Express **20**, 220–227 (2012).

[249] J. Butet, S. Dutta-Gupta, and O. J. Martin, "Surface second-harmonic generation from coupled spherical plasmonic nanoparticles: eigenmode analysis and symmetry properties", Physical Review B **89**, 245449 (2014).

[250] S. Fomichev, S. Popruzhenko, D. Zaretsky, and W Becker, "Laser-induced nonlinear excitation of collective electron motion in a cluster", Journal of Physics B: Atomic, Molecular and Optical Physics **36**, 3817 (2003).

[251] B. Metzger, T. Schumacher, M. Hentschel, M. Lippitz, and H. Giessen, "Third harmonic mechanism in complex plasmonic fano structures", ACS Photonics **1**, 471–476 (2014).

[252] M. Ethis de Corny, N. Chauvet, G. Laurent, M. Jeannin, L. Olgeirsson, A. Drezet, S. Huant, G. Dantelle, G. Nogues, and G. Bachelier, "Wave-mixing origin and optimization in single and compact aluminum nanoantennas", ACS Photonics **3**, 1840–1846 (2016).

[253] K. Uchida, S. Kaneko, S. Omi, C. L. Hata, H. Tanji, Y. Asahara, A. J. Ikushima, T. Tokizaki, and A. Nakamura, "Optical nonlinearities of a high concentration of small metal particles dispersed in glass: copper and silver particles", Journal of the Optical Society of America B **11**, 1236–1243 (1994).

[254] T.-M. Liu, S.-P. Tai, C.-H. Yu, Y.-C. Wen, S.-W. Chu, L.-J. Chen, M. R. Prasad, K.-J. Lin, and C.-K. Sun, "Measuring plasmon-resonance enhanced third-harmonic $\chi(3)$ of Ag nanoparticles", Applied Physics Letters **89**, 043122 (2006).

[255] P. Ginzburg, A. V. Krasavin, G. A. Wurtz, and A. V. Zayats, "Nonperturbative hydrodynamic model for multiple harmonics generation in metallic nanostructures", ACS Photonics **2**, 8–13 (2014).

[256] J. Hurst, F. Haas, G. Manfredi, and P.-A. Hervieux, "High-harmonic generation by nonlinear resonant excitation of surface plasmon modes in metallic nanoparticles", Physical Review B **89**, 161111 (2014).

[257] C. Ciracì, M. Scalora, and D. R. Smith, "Third-harmonic generation in the presence of classical nonlocal effects in gap-plasmon nanostructures", Physical Review B **91**, 205403 (2015).

[258] A. V. Krasavin, P. Ginzburg, G. A. Wurtz, and A. V. Zayats, "Nonlocality-driven supercontinuum white light generation in plasmonic nanostructures", Nature Communications **7** (2016).

[259] F. Calvayrac, P.-G. Reinhard, E. Suraud, and C. A. Ullrich, "Nonlinear electron dynamics in metal clusters", Physics Reports **337**, 493–578 (2000).

[260] R. G. Hobbs, V. R. Manfrinato, Y. Yang, S. A. Goodman, L. Zhang, E. A. Stach, and K. K. Berggren, "High-energy surface and volume plasmons in nanopatterned sub-10-nm aluminum nanostructures", Nano Letters (2016).

[261] N. Lang and W Kohn, "Theory of metal surfaces: work function", Physical Review B **3**, 1215 (1971).

[262] P. Narang, R. Sundararaman, A. S. Jermyn, W. A. Goddard III, and H. A. Atwater, "Cubic nonlinearity driven up-conversion in high-field plasmonic hot carrier systems", The Journal of Physical Chemistry C **120**, 21056–21062 (2016).

[263] M. W. Knight, N. S. King, L. Liu, H. O. Everitt, P. Nordlander, and N. J. Halas, "Aluminum for plasmonics", ACS Nano **8**, 834–840 (2013).

[264] G. Maidecchi, G. Gonella, R. Proietti Zaccaria, R. Moroni, L. Anghinolfi, A. Giglia, S. Nannarone, L. Mattera, H.-L. Dai, and M. Canepa, "Deep ultraviolet plasmon resonance in aluminum nanoparticle arrays", ACS Nano **7**, 5834–5841 (2013).

[265] P. Zhang, J. Feist, A. Rubio, P. García-González, and F. García-Vidal, "Ab initio nanoplasmonics: the impact of atomic structure", Physical Review B **90**, 161407 (2014).

[266] G. Hajisalem, M. S. Nezami, and R. Gordon, "Probing the quantum tunneling limit of plasmonic enhancement by third harmonic generation", Nano Letters **14**, 6651–6654 (2014).

[267] W. Zhu and K. B. Crozier, "Quantum mechanical limit to plasmonic enhancement as observed by surface-enhanced Raman scattering", Nature Communications **5** (2014).

[268] H. Jung, H. Cha, D. Lee, and S. Yoon, "Bridging the nanogap with light: continuous tuning of plasmon coupling between gold nanoparticles", ACS Nano **9**, 12292–12300 (2015).

[269] D. Xiang, J. Wu, and R. Gordon, "Coulomb blockade plasmonic switch", Nano Letters **17**, 2584–2588 (2017).

[270] W. Cai, A. P. Vasudev, and M. L. Brongersma, "Electrically controlled nonlinear generation of light with plasmonics", Science **333**, 1720–1723 (2011).

[271] L. Kang, Y. Cui, S. Lan, S. P. Rodrigues, M. L. Brongersma, and W. Cai, "Electrifying photonic metamaterials for tunable nonlinear optics", Nature Communications **5** (2014).

[272] J. D. Jackson, *Classical electrodynamics* (Wiley, 1999).

[273] R. A. Pala, K. T. Shimizu, N. A. Melosh, and M. L. Brongersma, "A nonvolatile plasmonic switch employing photochromic molecules", Nano Letters **8**, 1506–1510 (2008).

[274] T. Nikolajsen, K. Leosson, and S. I. Bozhevolnyi, "Surface plasmon polariton based modulators and switches operating at telecom wavelengths", Applied Physics Letters **85**, 5833–5835 (2004).

[275] F. Huang and J. J. Baumberg, "Actively tuned plasmons on elastomerically driven Au nanoparticle dimers", Nano Letters **10**, 1787–1792 (2010).

[276] K. Chu, C. Chao, Y. Chen, Y. Wu, and C.-C. Chen, "Electrically controlled surface plasmon resonance frequency of gold nanorods", Applied Physics Letters **89**, 103107 (2006).

[277] P. Mulvaney, J. Pérez-Juste, M. Giersig, L. M. Liz-Marzán, and C. Pecharromán, "Drastic surface plasmon mode shifts in gold nanorods due to electron charging", Plasmonics **1**, 61–66 (2006).

[278] S. Vivekchand, C. J. Engel, S. M. Lubin, M. G. Blaber, W. Zhou, J. Y. Suh, G. C. Schatz, and T. W. Odom, "Liquid plasmonics: manipulating surface plasmon polaritons via phase transitions", Nano Letters **12**, 4324–4328 (2012).

[279] A. M. Brown, M. T. Sheldon, and H. A. Atwater, "Electrochemical tuning of the dielectric function of Au nanoparticles", ACS Photonics **2**, 459–464 (2015).

[280] C. P. Byers, H. Zhang, D. F. Swearer, M. Yorulmaz, B. S. Hoener, D. Huang, A. Hoggard, W.-S. Chang, P. Mulvaney, E. Ringe, et al., "From tunable core-shell nanoparticles to plasmonic drawbridges: active control of nanoparticle optical properties", Science Advances **1**, e1500988 (2015).

[281] A. Emboras, J. Niegemann, P. Ma, C. Haffner, A. Pedersen, M. Luisier, C. Hafner, T. Schimmel, and J. Leuthold, "Atomic scale plasmonic switch", Nano Letters **16**, 709–714 (2015).

[282] K. Chen, G. Razinskas, T. Feichtner, S. Grossmann, S. Christiansen, and B. Hecht, "Electromechanically tunable suspended optical nanoantenna", Nano Letters **16**, 2680–2685 (2016).

[283] S. Dong, K. Zhang, Z. Yu, and J. A. Fan, "Electrochemically programmable plasmonic antennas", ACS Nano **10**, 6716–6724 (2016).

[284] Y.-W. Huang, H. W. H. Lee, R. Sokhoyan, R. A. Pala, K. Thyagarajan, S. Han, D. P. Tsai, and H. A. Atwater, "Gate-tunable conducting oxide metasurfaces", Nano Letters **16**, 5319–5325 (2016).

[285] D. R. Ward, F. Hüser, F. Pauly, J. C. Cuevas, and D. Natelson, "Optical rectification and field enhancement in a plasmonic nanogap", Nature Nanotechnology **5**, 732–736 (2010).

[286] R. Arielly, A. Ofarim, G. Noy, and Y. Selzer, "Accurate determination of plasmonic fields in molecular junctions by current rectification at optical frequencies", Nano Letters **11**, 2968–2972 (2011).

[287] A. Stolz, J. Berthelot, M.-M. Mennemanteuil, G. Colas des Francs, L. Markey, V. Meunier, and A. Bouhelier, "Nonlinear photon-assisted tunneling transport in optical gap antennas", Nano Letters **14**, 2330–2338 (2014).

[288] R. Terhune, P. Maker, and C. Savage, "Optical harmonic generation in calcite", Physical Review Letters **8**, 404 (1962).

[289] C. H. Lee, R. K. Chang, and N. Bloembergen, "Nonlinear electroreflectance in silicon and silver", Physical Review Letters **18**, 167 (1967).

[290] O. A. Aktsipetrov, A. A. Fedyanin, E. D. Mishina, A. N. Rubtsov, C. W. Van Hasselt, M. A. C. Devillers, and T. Rasing, "Dc-electric-field-induced second-harmonic generation in si (111)-sio 2-cr metal-oxide-semiconductor structures", Physical Review B **54**, 1825 (1996).

[291] J. W. Haus, D. de Ceglia, M. A. Vincenti, and M. Scalora, "Nonlinear quantum tunneling effects in nanoplasmonic environments: two-photon absorption and harmonic generation", Journal of the Optical Society of America B **31**, A13–A19 (2014).

[292] J. C. Prangsma, J. Kern, A. G. Knapp, S. Grossmann, M. Emmerling, M. Kamp, and B. Hecht, "Electrically connected resonant optical antennas", Nano Letters **12**, 3915–3919 (2012).

[293] J. Kern, R. Kullock, J. Prangsma, M. Emmerling, M. Kamp, and B. Hecht, "Electrically driven optical antennas", Nature Photonics **9**, 582–586 (2015).

[294] R. W. Boyd, Z. Shi, and I. De Leon, "The third-order nonlinear optical susceptibility of gold", Optics Communications **326**, 74–79 (2014).

[295] H. Harutyunyan, G. Volpe, R. Quidant, and L. Novotny, "Enhancing the nonlinear optical response using multifrequency gold-nanowire antennas", Physical Review Letters **108**, 217403 (2012).

[296] H. Aouani, M. Navarro-Cia, M. Rahmani, T. P. Sidiropoulos, M. Hong, R. F. Oulton, and S. A. Maier, "Multiresonant broadband optical antennas as efficient tunable nanosources of second harmonic light", Nano Letters **12**, 4997–5002 (2012).

[297] D. de Ceglia, M. A. Vincenti, and M. Scalora, "On the origin of third harmonic light from hybrid metal-dielectric nanoantennas", Journal of Optics **18**, 115002 (2016).

[298] A. Bouhelier, M. Beversluis, A. Hartschuh, and L. Novotny, "Near-field second-harmonic generation induced by local field enhancement", Physical Review Letters **90**, 013903 (2003).

[299] H. Aouani, M. Rahmani, M. Navarro-Cía, and S. A. Maier, "Third-harmonic-upconversion enhancement from a single semiconductor nanoparticle coupled to a plasmonic antenna", Nature Nanotechnology **9**, 290 (2014).

[300] J. Berthelot, G. Bachelier, M. Song, P. Rai, G. C. Des Francs, A. Dereux, and A. Bouhelier, "Silencing and enhancement of second-harmonic generation in optical gap antennas", Optics Express **20**, 10498–10508 (2012).

[301] L.-J. Black, P. R. Wiecha, Y. Wang, C. De Groot, V. Paillard, C. Girard, O. L. Muskens, and A. Arbouet, "Tailoring second-harmonic generation in single L-shaped plasmonic nanoantennas from the capacitive to conductive coupling regime", ACS Photonics **2**, 1592–1601 (2015).

[302] J. K. Gimzewski, B. Reihl, J. H. Coombs, and R. R. Schlittler, "Photon emission with the scanning tunneling microscope", Zeitschrift für Physik B Condensed Matter **72**, 497–501 (1988).

[303] R. Berndt, J. K. Gimzewski, and P. Johansson, "Inelastic tunneling excitation of tip-induced plasmon modes on noble-metal surfaces", Physical Review Letters **67**, 3796 (1991).

[304] W. Du, T. Wang, H.-S. Chu, and C. A. Nijhuis, "Highly efficient on-chip direct electronic–plasmonic transducers", Nature Photonics **11**, 623 (2017).

[305] M. Lenner, P. Rácz, P. Dombi, G. Farkas, and N. Kroó, "Field enhancement and rectification of surface plasmons detected by scanning tunneling microscopy", Physical Review B **83**, 205428 (2011).

[306] J. R. Tucker and M. J. Feldman, "Quantum detection at millimeter wavelengths", Reviews of Modern Physics **57**, 1055 (1985).

[307] M. Grifoni and P. Hänggi, "Driven quantum tunneling", Physics Reports **304**, 229–354 (1998).

[308] G. Platero and R. Aguado, "Photon-assisted transport in semiconductor nanostructures", Physics Reports **395**, 1–157 (2004).

[309] M. H. Pedersen and M. Büttiker, "Scattering theory of photon-assisted electron transport", Physical Review B **58**, 12993 (1998).

[310] I. Urdaneta, A. Keller, O. Atabek, and V. Mujica, "Laser-induced nonlinear response in photoassisted resonant electronic transport", The Journal of Chemical Physics **127**, 154110 (2007).

[311] M. Scalora, M. A. Vincenti, D. de Ceglia, and J. W. Haus, "Nonlocal and quantum-tunneling contributions to harmonic generation in nanostructures: electron-cloud-screening effects", Physical Review A **90**, 013831 (2014).

[312] P.-Y. Chen, K. Q. Le, and A. Alù, "Nonlinear nanocircuitry based on quantum tunneling effects", MRS Communications **5**, 565–571 (2015).

[313] P.-Y. Chen, R. Salas, and M. Farhat, "Generation of high-power terahertz radiation by nonlinear photon-assisted tunneling transport in plasmonic metamaterials", Journal of Optics **19**, 124012 (2017).

[314] N. J. Halas, S. Lal, W.-S. Chang, S. Link, and P. Nordlander, "Plasmons in strongly coupled metallic nanostructures", Chemical Reviews **111**, 3913–3961 (2011).

[315] E. Prodan, P. Nordlander, and N. J. Halas, "Electronic structure and optical properties of gold nanoshells", Nano Letters **3**, 1411–1415 (2003).

[316] I. Campillo, J. M. Pitarke, A. Rubio, E. Zarate, and P. M. Echenique, "Inelastic lifetimes of hot electrons in real metals", Physical Review Letters **83**, 2230 (1999).

[317] V. P. Zhukov, E. V. Chulkov, and P. M. Echenique, "GW+T theory of excited electron lifetimes in metals", Physical Review B **72**, 155109 (2005).

[318] G. Baffou and R. Quidant, "Nanoplasmonics for chemistry", Chemical Society Reviews **43**, 3898–3907 (2014).

[319] H. A. Atwater and A. Polman, "Plasmonics for improved photovoltaic devices.", Nature Materials **9**, 205–213 (2010).

[320] C. Clavero, "Plasmon-induced hot-electron generation at nanoparticle/metal-oxide interfaces for photovoltaic and photocatalytic devices", Nature Photonics **8**, 95–103 (2014).

[321] M. L. Brongersma, N. J. Halas, and P. Nordlander, "Plasmon-induced hot carrier science and technology", Nature Nanotechnology **10**, 25–34 (2015).

[322] S. Linic, U. Aslam, C. Boerigter, and M. Morabito, "Photochemical transformations on plasmonic metal nanoparticles", Nature Materials **14**, 567 (2015).

[323] R. G. Hobbs, W. P. Putnam, A. Fallahi, Y. Yang, F. X. Kartner, and K. K. Berggren, "Mapping photoemission and hot-electron emission from plasmonic nanoantennas", Nano Letters **17**, 6069–6076 (2017).

[324] P. Narang, R. Sundararaman, and H. A. Atwater, "Plasmonic hot carrier dynamics in solid-state and chemical systems for energy conversion", Nanophotonics **5**, 96–111 (2016).

[325] T. Rybka, M. Ludwig, M. F. Schmalz, V. Knittel, D. Brida, and A. Leitenstorfer, "Sub-cycle optical phase control of nanotunnelling in the single-electron regime", Nature Photonics **10**, 667 (2016).

[326] C. Fall, N Binggeli, and A Baldereschi, "Anomaly in the anisotropy of the aluminum work function", Physical Review B **58**, R7544 (1998).

[327] D. T. Colbert and W. H. Miller, "A novel discrete variable representation for quantum mechanical reactive scattering via the s-matrix kohn method", The Journal of Chemical Physics **96**, 1982–1991 (1992).